Doctoral theses at NTNU, 2023:192

Frida Hemstad Danmo

Oxygen absorption in hexagonal manganites

Doctoral thesis

NTNU
Norwegian University of Science and Technology
Thesis for the Degree of
Philosophiae Doctor
Faculty of Natural Sciences
Department of Materials Science and Engineering

NTNU
Norwegian University of
Science and Technology

Frida Hemstad Danmo

Oxygen absorption in hexagonal manganites

Thesis for the Degree of Philosophiae Doctor

Trondheim, June 2023

Norwegian University of Science and Technology
Faculty of Natural Sciences
Department of Materials Science and Engineering

NTNU
Norwegian University of
Science and Technology

NTNU
Norwegian University of Science and Technology

Thesis for the Degree of Philosophiae Doctor

Faculty of Natural Sciences
Department of Materials Science and Engineering

ISBN 978-82-326-7086-4 (printed ver.)
ISBN 978-82-326-7085-7 (electronic ver.)
ISSN 1503-8181 (printed ver.)
ISSN 2703-8084 (online ver.)

Doctoral theses at NTNU, 2023:192

Printed by NTNU Grafisk senter

Preface

This dissertation has been submitted to the Norwegian University of Science and Technology (NTNU) in partial fulfillment of the requirements for the academic degree of Philosophiae Doctor.

The doctoral studies were performed at the Functional Materials and Materials Chemistry Research Group (FACET) at the Department of Materials Science and Engineering, NTNU, Trondheim, Norway. The supervision of the work was lead by Prof. Sverre Magnus Selbach, with co-supervisors Prof. Tor Grande and Prof. Julia Glaum.

The work was funded by the Department of Materials Science and Engineering, and by NTNU through "Rektors ekstratildeling".

Frida Hemstad Danmo
Trondheim, April 2023

Acknowledgements

With this thesis, over 4.5 years of work is nearing its end. It has been quite a journey, with many experiences and opportunities I had not imagined when I started this PhD in August, 2018. The work condensed into this book would not have been achievable without the help of others, and I would therefore like to take this opportunity to express my gratitude towards everyone who have helped me and supported me throughout these last years.

First of all, I want to sincerely thank my main supervisor Sverre Magnus Selbach. Your passion for everything related to hexagonal manganites has been an unending source of motivation for me throughout the almost 6 years we have collaborated. Together, we have faced all the joys, challenges, and surprises that emerge when working with hexagonal manganites. Thank you for your thorough feedback, brilliant ideas, and for reminding me to keep doing the things that give me energy. I would also like to give a big thanks to my co-supervisors Julia Glaum and Tor Grande, for all your help and feedback throughout this work. Julia, thanks for supporting me through the difficult spring of 2020, and for providing your valuable outside opinion on my research. Tor, thank you for sharing your thermodynamic knowledge, and for letting me know you always had time for me if I needed it.

A huge thanks goes out to all of the engineers at the department who has helped me with all my big and small problems in the lab. To Kristin, Maria and Elvia, thank you for helping me with the elaborate X-ray diffraction experiments I have run over the years. I also want to give a big thank you to everyone in the technical

and administrative staff, especially Eli, Anita, Elin, Johannes, Pei Na, Ida and Marthe, for giving me such a warm welcome when I entered the team as the HSE coordinator for 4 months, and for giving me the support I needed as I dove head first into unknown waters. I also want to thank my wonderful master students Sigmund, Embla, Iman, and Aamund for all your valuable work, and our fruitful discussions. It was a pleasure to supervise you all, and I have really appreciated sharing the experimental ups and downs with you.

These last years would not have been the same without all my good friends and colleagues at IMA. The entertaining lunch conversations we have had throughout the years have been the highlight of my workday. An extra shout-out goes to the "K2 gang", especially Håvard, Frode, Jacob and Elise, for all our fun times both at and outside of work. And to my dear 4th-floor-almost-office-mates Vilde and Harald, thank you for all our long coffee breaks, rants, wine tastings, and fun evenings. I will always cherish the times we have shared together.

I have been extremely fortunate to have met so many great people during my time here in Trondheim, and I am honored to have all of you as my friends. Kristine and Amalie, I am so glad to have met you two, and I am definitely looking forward to even more laughter-filled evenings in the future. Solveig, I will miss our regular cinnamon bun breaks. Thank you also to my dear friends Sindre, Haakon, Eskild, Adnan, Hanne, Fredrik and Silje. I would not have gotten through all these years in Trondheim without all of you, and all the good times were have shared. To my long time friend Rebecca, thank you for always having waffles ready, and for making me feel like not a single day had passed no matter how long it had been since we last met. And to all my good friends in Level Up, thank you for giving me a space where I can be creative, and let my other worries rest for a moment.

To my family back home, thank you for supporting me and cheering me on, every step of the way. To my parents, Vivi and Knut Birger, thank you for always showing such enthusiasm for everything I do, no matter how big or small an achievement. Thank you to my cats, Zoey and Nyx, for bringing cuddles (and chaos) to my life. And finally, to Petter, my love, I cannot express my thanks to you enough. Thank you for always being there for me and making me laugh, no matter how hard the day has been. I wouldn't be who and where I am today if it wasn't for you.

"Be curious on your journey!"
Nomai,
Outer Wilds

The author’s contribution

The following scientific works are included in this dissertation

I: F. H. Danmo, B. A. D. Williamson, D. R. Småbråten, N. H. Gaukås, E. R. Østli, T. Grande, J. Glaum, and S. M. Selbach, "Oxygen absorption in nanocrystalline h-RMnO$_3$ (R = Y, Ho, Dy) and the effect of Ti donor doping", *Chemistry of Materials, under review*, 2023.

Contributions: F.H.D. synthesized the samples, not including the YMTO21 sample which was made by E.R.Ø. F.H.D. conducted experiments, prepared figures, and made the thermodynamic model. DFT calculations were carried out by B.A.D.W. The data was analysed by F.H.D. and S.M.S. F.H.D. wrote the paper, with feedback from all co-authors.

II: F. H. Danmo, I.-E. Nylund, A. Westermoen, K. P. Marshall, D. Stoian, T. Grande, J. Glaum, and S. M. Selbach, "Oxidation kinetics of nanocrystalline h-RMn$_{1\text{-x}}$Ti$_\text{x}$O$_3$ (R = Ho, Dy)", *Submitted*, 2023.

Contributions: F.H.D. conducted the synthesis, thermogravimetric measurements, in-house X-ray diffraction measurements, and prepared figures. I.-E.N. took TEM and STEM images. Synchrotron measurements were carried out by F.H.D, A.W. and S.M.S., with technical support by K.P.M. and D.S. The data was analysed by F.H.D. and S.M.S, with help from K.P.M. and D.S. on the XANES data. F.H.D. wrote the paper, with feedback from all co-authors.

III: F. H. Danmo, A. Westermoen, K. P. Marshall, D. Stoian, T. Grande, J. Glaum, and S. M. Selbach, "High entropy hexagonal manganites for fast oxygen absorption and release", *Paper manuscript, to be submitted*, 2023.

Contributions: F.H.D. and A.W. synthesised the samples, and did thermogravimetric and room temperature X-ray diffraction measurements. A.W. took SEM images. F.H.D. conducted in-house high temperature X-ray diffraction measurements, and prepared figures. Synchrotron measurements were carried out by F.H.D., A.W. and S.M.S., with technical support by K.P.M. and D.S. The data was analysed by F.H.D. and S.M.S, with help from K.P.M. and D.S. on analysis of the XANES data. F.H.D. wrote the paper, with feedback from all co-authors.

The following scientific presentations and posters were a part of the PhD work

I: F. H. Danmo, I.-E. Nylund, A. Westermoen, K. P. Marshall, D. Stoian, T. Grande, J. Glaum, and S. M. Selbach, "Kinetics of oxidation in h-$R\mathrm{Mn}_{1\text{-}x}\mathrm{Ti}_x\mathrm{O}_3$ (R = Ho, Dy)", NKS-FUM 2023 (13.02.2023-14.02.2023)

II: F. H. Danmo, T. Grande, J. Glaum, and S. M. Selbach, "Oxygen absorption in nanocrystalline hexagonal $R\mathrm{MnO}_3$ (R = Y, Ho, Dy) and the effect of Ti donor doping.", NKS-FUM 2021 (01.11.2021-02.11.2021)

III: F. H. Danmo, T. Grande, J. Glaum, and S. M. Selbach, "Oxygen absorption in donor doped $R\mathrm{MnO}_3$", E-MRS Spring meeting 2021, (31.05.2021-03.06.2021)

IV: F. H. Danmo, D. R. Småbråten, N. H. Gaukås, B. A. D. Williamson, S. H. Skjærvø, S. P. Singh, K. Wiik, T. Grande, J. Glaum, S. M. Selbach, "Oxygen absorption in donor-doped nanocrystalline $R\mathrm{MnO}_{3+\delta}$", NKS-FUM (13.02.2020-14.02.2020)

V: F. H. Danmo, D. R. Småbråten, S. H. Skjærvø, S. P. Singh, K. Wiik, T. Grande, J. Glaum, S. M. Selbach, "Oxygen absorption in donor doped nanocrystalline h-$R\mathrm{MnO}_{3+\delta}$", Joint ISAF-ICE-EMF-IWPM-PFM conference 2019, (14.07.2019-19.07.2019)

VI: F. H. Danmo, D. R. Småbråten, S. H. Skjærvø, S. P. Singh, K. Wiik, D. Meier, S. M. Selbach, "The effect of crystallite size and donor doping on the conductivity and oxygen absorption of hexagonal $R\mathrm{MnO}_{3+\delta}$", Landsmøte i kjemi, NKS-FUM, (16.10.2018-17.10.2018)

The following popular science presentations were a part of the PhD work

I: Popular science presentation titled *Oksygen-revolusjon med keramiske membraner* presented for three high school classes all over Norway (2021)

II: Popular science presentation titled *Ceramic membranes - an oxygen revolution* held at the "Pint of Science - Hot news from Nanoworld" research festival in Trondheim (20.05.2021)

III: Popular science presentation titled *New solutions for the oxygen industry* presented as a part of TEDx Trondheim Leading Lights (15.11.2020)

IV: Presentation of the research and how a researcher works, held for a 6th grade school class in Trondheim (25.11.2020)

V: Popular science presentation titled *Døra til miljøvennlig oksygen* presented as a part of the regional finale of the national research dissemination competition "Research Grand Prix" (24.09.2020)

VI: Popular science blog post for the "NTNU - TekNat" webpage of the Faculty of Natural Science titled *Oksygen-revolusjon med keramiske membranar* (2020)

VII: Popular science presentation titled *Oksygenproduksjon ved hjelp av keramiske membraner* presented as a part of the "PhD Grand Prix" research dissemination competition held by *Høiskolens Chemikerforening* (2019)

Summary

Oxygen is one of the worlds most used chemicals, with over 100 million tonnes of pure O_2 being used for industrial and medical purposes each year. The demand for O_2 is high, and expected to rise even further due to its possible application within green technologies such as oxyfuel combustion for CO_2 capture. Today, most of the industrial oxygen gas is produced through cryogenic distillation, which is an energy intensive and expensive air separation method. Alternative methods for large-scale O_2 separation from air are therefore highly desired, e.g. by oxygen permeable ceramic membranes or chemical looping air separation (CLAS). These methods can possibly reduce the energy cost of O_2 production by up to 35%, and can in addition be easily integrated into existing coal fired power plants for oxyfuel combustion. Both ceramic membranes and CLAS require a material that can transport O_2 at elevated temperatures. Perovskites have been in the spotlight for these applications in the last decades, but these materials have problems with low thermal and chemical stability, and often require operating temperatures as high as 800-1000 °C.

Hexagonal manganites ($R\mathrm{MnO}_3$, R = Sc, Y, Ho-Lu) have emerged as possible oxygen storage materials (OSMs) due to their ability to store and release large amounts of oxygen at temperatures as low as 300 °C. Due to the hexagonal $P6_3cm$ crystal structure being less dense than the perovskite structure, hexagonal manganites can incorporate oxygen as interstitials, making them fundamentally different from other OSMs which typically use oxygen vacancies for transport. As hexagonal manganites are quite new in the OSM research field, there are still

many unknowns when it comes to how the properties of the materials can be improved. In this work, we wanted to understand more of how the oxygen storage properties of hexagonal manganites can be tailored by changes in composition, both on the R^{3+} site and with aliovalent doping on the Mn^{4+} site.

In the first part of the work, the oxygen absorption properties of $R\mathrm{Mn}_{1\text{-x}}\mathrm{Ti}_{\mathrm{x}}\mathrm{O}_3$ (R = Y, Ho, Dy; x = 0, 0.15) were investigated. The materials were studied using thermogravimetric analysis (TGA) and high-temperature X-ray diffraction (HT-XRD), showing larger oxygen storage capacities for samples with smaller crystallites, larger R cations, and with added Ti. For the last two, the increased oxygen absorption was believed to be the result of the expanded ab-plane found in these materials. Ti-doping also increased the thermal stability of interstitial oxygen. Density functional theory (DFT) calculations were used to compare the trends observed experimentally. In addition, a thermodynamic model for enthalpy and entropy of oxidation was fitted to the experimental data.

In the second part of the thesis, the kinetics of oxidation of $R\mathrm{Mn}_{1\text{-x}}\mathrm{Ti}_{\mathrm{x}}\mathrm{O}_3$ (R = Ho, Dy; x = 0, 0.15) was investigated, as the Ti-doped compositions from Manuscript I showed indications of increased oxidation rates. The materials were studied using TGA with different heating and cooling rates, and time resolved X-ray absorption near edge structure (XANES) and HT-XRD with *in situ* switching of atmosphere from N_2 to O_2. It was showed that the oxidation kinetics increase with larger R, and with the addition of Ti, as the expanded ab-plane lessens the electrostatic repulsion between interstitial oxygen and the planar oxygen surrounding it.

In the third part of the thesis, the oxidation properties of high entropy hexagonal manganites with different compositions and particle sizes were examined, using the same experimental methods as in Manuscript I and II. The high compositional entropy stabilized formation of a single hexagonal phase, even for large R cations and high tolerance factors. All high entropy compositions displayed high oxygen storage capacities, with bulk materials showing increased oxygen absorption compared to single R cation bulk materials measured using fast cooling rates. The oxidation kinetics were also improved compared to low entropy hexagonal manganites, due to the high configurational entropy improving ionic conductivity, and due to the large R cations expanding the ab-plane promoting oxygen transport.

In addition to the work presented in the attached manuscripts, this thesis includes work on preparation of an asymmetric oxygen permeable membrane using $[\mathrm{Ho}_{0.98}\mathrm{In}_{0.02}]_{0.97}\mathrm{Mn}_{0.85}\mathrm{Ti}_{0.15}\mathrm{O}_3$ as the membrane material. The membrane film was deposited on top of porous $Y_{1.05}Mn_{0.85}Ti_{0.15}O_3$ substrates using spray coating, giving films with thicknesses ranging from 5 to 30 µm. All the prepared membranes showed problems with surface cracking, originating from stresses formed in the film during constrained sintering, and from the anisotropic thermal expansion of the material, which results in crack formation during cooling. The aim of the project was therefore shifted towards material development of hexagonal manganites for oxygen production methods that use OSMs in powder form, such as CLAS.

Populærvitskapleg samandrag

Oksygen er noko me ikkje klarar oss utan. Ikkje berre treng me det for å puste, me brukar det også til å lage stål, plastikk og kjemikaliar, på sjukehus, og til CO_2-fangst. Oksygen er ein ressurs me har veldig mykje av på jorda, men den er diverre vanskeleg å få tak i i rein form. Nesten alle av dei 100 millionar tonna med rein oksygengass som industrien brukar kvart år er laga ved hjelp av ein prosess kalla kryogenisk destillasjon. Der vert luft kjølt ned til nesten -200 °C slik at den vert flytande og kan bli separert til reine gassar gjennom destillasjon. Dette krev store mengder energi, og mange har difor sett etter andre metodar for å senka energiforbruket og kostnadane rundt oksygenproduksjon.

Ein moglegheit er å nytta oksid som kan lagra og sleppa ut oksygen igjen og igjen for å separera ut oksygen frå luft. Ein kan seie at dei fungerer som svampar som berre trekk til seg oksygen, medan nitrogen, argon, CO_2 og andre delar av lufta vert liggjande igjen. Desse materiala kan brukast i metodar kalla kjemisk syklisk luftseparasjon (CLAS), og luftseparasjon ved hjelp av keramiske membranar. Begge desse metodane kan spara energiforbruket til oksygenproduksjon med opptil 35 %, men det krev materialar som kjapt kan ta opp og gi frå seg oksygen, og som ikkje vert øydelagde over tid. Perovskittar (ABO_3) er ein type oksid som har vorte mykje undersøkt som oksygenlagringsmateriale, men dei fleste fungerer berre ved svært høge temperaturar, gjerne opp mot 800-1000 °C. Dette er fordi perovskittar lagrar oksygen ved at "hòl" i materialet vert flytta rundt på og fyllast opp med oksygen, og denne måten å transportera oksygen på treng mykje varme for å skje fort nok. Ved så høge temperaturar vert materiala fort øydelagde, og det trengs også mykje energi for å varma opp systema.

Heksagonale manganittar (RMnO$_3$, R = Sc, Y, Ho-Lu) er ein type oksid som nyleg har dukka opp som ein mogleg kandidat for oksygenseparasjon. Desse materiala er spesielle fordi dei kan ta opp store mengder oksygen på ein heilt annleis måte enn dei vanlege oksida; dei har ein meir open struktur enn perovskittar, som gjer at oksygen enkelt kan dytta seg inn og bevege seg mellom atoma i materialet. Dette krev mykje mindre energi enn å flytte på "hòl" i materialet, og heksagonale manganittar fungerer difor på temperaturar heilt ned mot 300 °C. Det kan spare mykje energi, det!

Denne oppgåva fokuserer på å forstå korleis oksygentransporteigenskapane til heksagonale manganittar kan forbetrast ved å endra kva grunnstoff som vert brukt i materialet. Gjennom metodar som termogravimetrisk analyse (TGA) og røntgendiffraksjon (XRD) kan me studera kor mykje oksygen materialet tar opp, og korleis strukturen endrar seg når det oksiderer. Eksperimenta viser at det å bruke større R-kation som Ho^{3+} og Dy^{3+} gjer at materiala tar opp meir oksygen på ein gong, og det oksiderer raskare for store kation enn for små. Ti^{4+} som donordopant på Mn-posisjonen aukar også både oksygenopptak og oksidasjonskinetikk. I tillegg ser me at det å bruka 5 eller 6 ulike R-kation samtidig for å danna eit såkalla høgentropimateriale forbetrar oksygentransporteigenskapane mykje, og gjer det også mogleg å bruka mindre reine og billigare råstoff for å laga materiala. Det vart også forsøkt å laga ein fungerande membranprototype av ein heksagonal manganitt, men dette vart ikkje vellykka på grunn av at materialet er svært eldfast, og fordi det lett sprekk når ein kjølar det ned.

List of abbreviations

ASU	Air separation unit
CCS	CO_2 capture and storage
CE	Chemical expansion
CIP	Cold isostatic pressing
CLAS	Chemical looping air separation
CLC	Chemical looping combustion
DFT	Density functional theory
EELS	Electron energy loss spectroscopy
ESRF	European Synchrotron Radiation Facility
HE	High entropy
HT-XRD	High temperature X-ray diffraction
IC	Ionic conductor
L_c	Characteristic thickness
MIEC	Mixed ionic-electronic conductor
$\mathbf{O_i}$	Interstitial oxygen
OSC	Oxygen storage capacity
OSM	Oxygen storage material
PSA	Pressure swing adsorption
R	Rare earth element
SEM	Scanning electron microscopy

SNBL	The Swiss-Norwegian Beamlines
STEM	Scanning transmission electron microscopy
TEC	Thermal expansion coefficient
TGA	Thermogravimetric analysis
TSA	Temperature swing adsorption
TTIP	Titanium (IV) isopropoxide
XANES	X-ray absorption near-edge structure
XRD	X-ray diffraction

Contents

1

Introduction

1.1 Background and motivation

What would we do without oxygen? This question might be a rhetorical one, and a quite trivial one as well as life as we know it would not exist without it, but many parts of our modern industrial society would not function without this vital gas. Over 100 million tons of O_2 is used for industrial purposes each year, with applications ranging from production of steel, chemicals and plastics, wastewater treatments, to medicinal use.[1–3] The demand for oxygen gas is high, and is expected to rise even further in the coming years due to its potential within CO_2 capture and storage (CCS) technologies.[4]

Even though the shift towards greener energy production methods is in progress, power plants using fossil fuels are still a large part of the total energy production across the globe, and will continue to be so for many years ahead. According to the International Energy Agency, coal power plants alone supply 38 % of the power used around the world, and is also responsible for 30 % of the CO_2 emissions globally.[5] Many have therefore looked to CCS for possible CO_2 emission reduction. For coal power plants, oxyfuel combustion has emerged as the most promising carbon capture technology, as this has a potentially lower energy consumption than other CCS processes as it can be retrofitted to existing plants.[6,7] In conventional plants, coal is burned in air, resulting in a flue gas with a CO_2 concentration of 12-16 % due to the large proportion of N_2 in air.[6] N_2 also causes formation of harmful NO_x compounds during combustion.[8] In oxyfuel combustion, on the other hand, pure

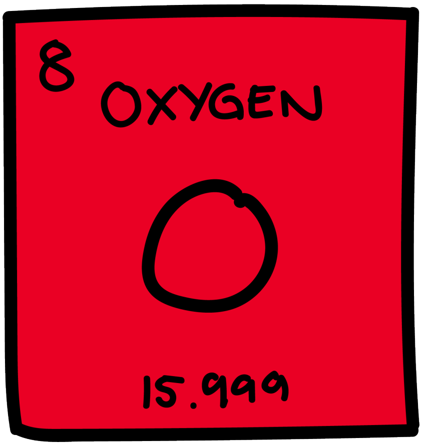

oxygen is used for combustion, which results in a flue gas containing only CO_2 and water, with CO_2 concentrations up towards 85 %.[6] The CO_2 can also be re-used as a sweep gas to control the fire temperature.[6,9]

The main challenge for oxyfuel combustion is access to cheap O_2.[9] Oxygen is often supplied through an air separation unit (ASU), producing oxygen through cryogenic distillation.[7,8] This process requires large amounts of energy for liquefaction and distillation of O_2, making the total oxyfuel CCS process energy intensive and expensive.[7,10] A more efficient oxygen production method is therefore necessary for making oxyfuel combustion more economically viable for CCS.

Two of the promising alternatives to cryogenic distillation are air separation using ceramic membranes, and chemical looping air separation (CLAS). These methods use oxides that can store and release oxygen by transport of oxygen through the crystal lattice in the form of oxygen vacancies or interstitial oxygen. Estimations show that using ceramic membranes or CLAS instead of cryogenic distillation can reduce the operating cost of the ASU by up to 35 %.[11–13] Perovskites and other similar oxides have emerged as potential oxygen storage materials (OSMs), as they have large oxygen storage capacities (OSC) and quick oxidation kinetics, but these materials require temperatures up to 1000 °C for efficient transport, at which they display low chemical and mechanical stability.[1,12,14–16] An OSM that can reversibly store and release oxygen at lower temperatures with sufficiently high kinetics for effective air separation could therefore contribute to lowering the cost of the ASU further, making oxyfuel combustion, and oxygen production in general, more cost efficient.

1.2 Aim of work

The aim of the PhD work was to explore how the oxygen storage properties of hexagonal manganites can be tailored by changes in composition, both on the R site and with aliovalent doping. The work had a particular focus on investigating the oxygen storage capacity and kinetics of oxidation, and how these change with size of the R^{3+} cation and with the addition of Ti^{4+} on the Mn site.

In the first part of the work, the aim was to investigate how the oxygen storage capacity and lattice parameter changes in hexagonal manganites varies with composition and particle sizes through thermogravimetry and high-temperature X-ray diffraction (XRD). Density functional theory (DFT) was used to substantiate the experimental work, and to compare trends in lattice parameters, chemical expansion, formation energies of O_i, and enthalpy of oxidation with different R and with Ti^{4+}. In addition, a simple thermodynamic model was developed to investigate the enthalpy and entropy of oxidation, by fitting the model to the experimental data.

The second part of the work focused on understanding the oxidation kinetics in hexagonal manganites, as the oxidation kinetics had been reported so far to be too slow for commercial applications. As Manuscript I showed indications of improved kinetics for Ti^{4+} doped materials, the effect of this dopant was studied further. The aim was to investigate the changes in oxygen storage capacity with different heating and cooling rates, and time resolved changes in lattice parameters upon exposure to O_2 atmosphere, examining how the ionic radius of R^{3+} and the addition of Ti affected the kinetics of oxidation.

The third part of the work took a different compositional approach, by exploring how a high configurational entropy would affect the oxygen transport properties of $R\mathrm{MnO}_3$. High entropy oxides have been reported to show increased ionic conductivity of e.g. Li-ions, and we wanted to investigate if this could be the case for O_i conductivity in hexagonal manganites as well. The aim was to synthesize both bulk and nanocrystalline materials of high entropy compositions, with and without Ti as a donor dopant, and to study these using the same techniques used for single R hexagonal manganites in Manuscript I and II.

In addition to the work found in Manuscripts I-III, one of the goals of the work was to develop a functional asymmetric ceramic membrane for oxygen separation from air. As hexagonal manganites are very refractory, the aim was to improve sintering of the dense film, as the film needed to be completely dense and crack free. A combination of pressing of the film, changes in sintering temperature, and two different spray coaters were used as methods to study how to improve the density and coverage of the deposited film.

2

Literature review

2.1 Oxygen production

2.1.1 Cryogenic distillation

The bulk of the worldwide supply of oxygen gas is made through the process of cryogenic distillation. This method was first developed by Carl von Linde in the beginning of the 1900s, and has continuously been improved since.[17] The concept is based on fractional distillation of liquefied air, using an air separation unit (ASU) commonly equipped with a multi-column distillation setup.[17,18] The air feed is first dried and purified through removal of water, CO_2 and other contaminants, and afterwards goes through several compression, expansion and heat exchange steps to cool it to cryogenic temperatures.[11,17] The main components of air, namely N_2, O_2 and Ar, are then separated by their differences in boiling point, and can be produced in both gaseous and liquid form.[17–19] This process is illustrated in Figure 2.1. While other methods for oxygen production are available, such as the ones described in the next sections, cryogenic distillation is the only available commercial method for large scale production of high purity O_2, with large plants supplying over 3000 tons O_2/day in a single line.[20,21] Even though this is an effective air separation method, the extensive compressing and cooling steps consumes large amounts of power, making this a very energy demanding process.[19] This is especially true for high purity products, as the separation of O_2 and Ar is challenging; when the purity of O_2 is increased from 95 % to 99.5 %, the energy requirement increases by 10 %.[17] The power input of cryogenic distillation has been more than halved since the 1970s, but as the process has matured, the decrease in power consumption over time has stagnated.[19]

2.1.2 Non-cryogenic methods

As a way to reduce the energy cost of oxygen production, many non-cryogenic air separation methods have been investigated over the years. A brief summary of a few of these methods is presented in the following sections.

Adsorption methods

Air separation through pressure swing adsorption (PSA) or temperature swing adsorption (TSA) methods are widely used processes, with 20 % of all air separation in 1997 accomplished by PSA.[22] For oxygen production, this is done in small-to-

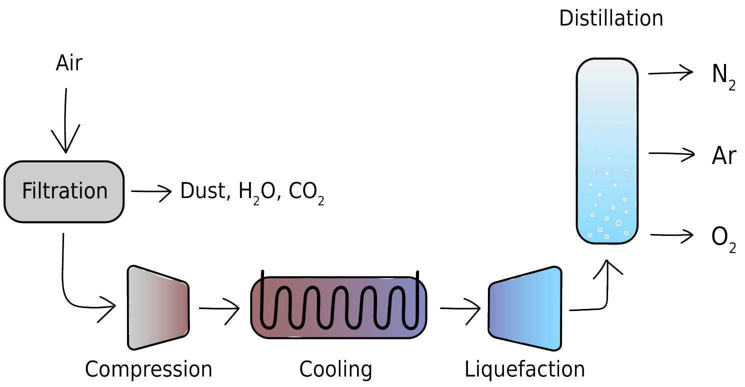

Figure 2.1: Schematic of a cryogenic air separation unit for production of O_2, Ar, and N_2.

medium scale plants producing up to 100 tons O_2/day, with on-site production of O_2 for both industrial and medical use.[8,23,24] The process is based on some materials preferentially adsorbing some molecules over others, so that the unwanted component can be removed. For production of N_2 gas, carbon molecular sieves are used for adsorbing O_2 from air, while zeolites have been used to adsorb N_2, creating oxygen gas with up to 95 % purity.[8,18,25,26] As air pass through the zeolite, N_2 is adsorbed on the material surface, and an O_2 rich stream exits the bed, as illustrated in Figure 2.2. The adsorbed N_2 can be removed by either lower pressures (PSA) or elevated temperatures (TSA), and the adsorption process can then be repeated.[27] PSA is the more common of the two, due to its faster cycle time and simpler operation.[8,18] These setups often have two to four connected adsorbers for continuous flow and production.[8,28] The largest drawback for adsorption methods is the limited selectivity of the sorbents, which restricts the purity of the product.[8,25]

Chemical looping air separation

Chemical looping air separation (CLAS) is a method that selectively separates oxygen from air, using a metal oxide with reversible absorption and release of oxygen. The concept is based on the same principle as used for chemical looping combustion (CLC), where a metal oxide supplies oxygen to a combustion reaction.[29] The metal particles are first oxidized in air (eq. 2.1), and then moved to another inter-

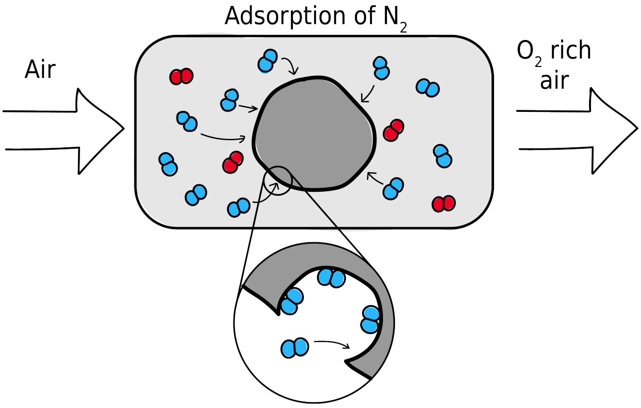

Figure 2.2: Illustration of adsorption of N_2 molecules (blue) on a zeolite surface, creating an O_2 (red) rich gas stream.

connected fluidized bed reactor where oxygen is released (eq. 2.2) using a sweep gas of either steam or CO_2.[8,24,30]

$$Me_xO_{y-2}\ (s) + O_2\ (g) \rightarrow Me_xO_y\ (s) \tag{2.1}$$

$$Me_xO_y\ (s) \rightarrow Me_xO_{y-2}\ (s) + O_2\ (g) \tag{2.2}$$

The reactions in eq. 2.1 and 2.2 are driven by changes in p_{O_2} and/or temperature, depending on if it is a temperature swing or pressure swing based setup. The CLAS method using temperature driven reduction is illustrated in Figure 2.3. If steam is used as a sweep gas, the output O_2 stream must be cooled via a condenser as to remove water, which then can be reheated and reused as sweep gas.[11,24] Binary oxide systems such as CuO/Cu_2O, Mn_2O_3/Mn_3O_4 and Co_3O_4/CoO have been studied as possible oxygen storage materials (OSMs) for CLAS,[29,30] but many have also looked to perovskites and other ternary oxides due to their large oxygen storage capacity and faster kinetics.[11,25,31,32] State of the art oxygen storage materials will be discussed further in Section 2.1.3.

Due to its lower power consumption compared to cryogenic methods,[29,33] CLAS has been studied as a promising alternative for air separation for low CO_2 emission processes, such as oxyfuel combustion or coal gasification.[8,24] A CLAS unit can

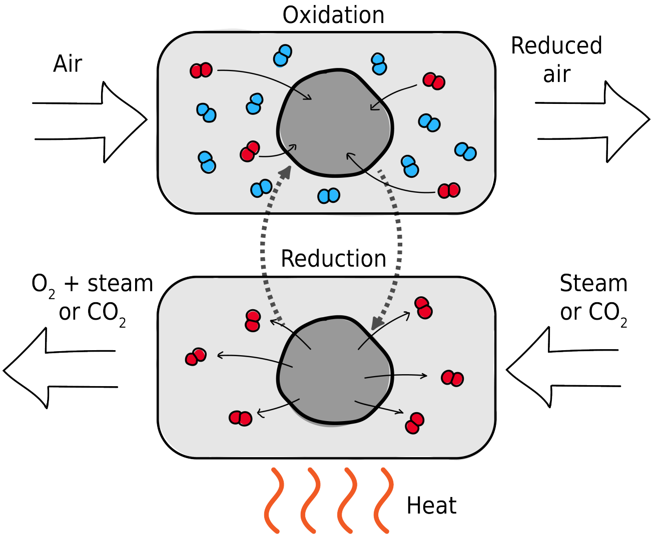

Figure 2.3: Illustration of the chemical looping air separation (CLAS) method, where an oxide is oxidized in air and then reduced to release oxygen in a cyclical process. Oxygen molecules are drawn in red, while nitrogen molecules are drawn in blue.

be retrofitted into existing industries to supply oxygen to these processes,[24,30] and models have estimated a reduction of operating cost of the ASU by 15 % when using an integrated CLAS setup instead of a cryogenic one.[11] When using waste heat from the combustion process to heat the steam needed for the sweep gas, the energy consumption is estimated to be reduced even further down to a possible 0.4 MJ/kg O_2, almost half of the 0.781 MJ/kg O_2 required for cryogenic air separation.[11]

Ceramic membranes

Air separation using oxygen conducting ceramic membranes is another promising alternative for oxygen production as it can possibly lower the cost of O_2 production by 35 % or more compared to cryogenic distillation. Ceramic membranes got a lot of attention in the late 90s and early 2000s.[12,13] These membranes utilize oxides that can selectively transport oxygen through the crystal lattice at high temperatures ($T > 600$ °C), either through oxygen vacancies or interstitial oxygen, resulting in extremely high purity O_2 gas,[1,18,34] as illustrated in Figure 2.4. The membrane material is either a pure ionic conductor (IC), or a mixed ionic-electronic conductor

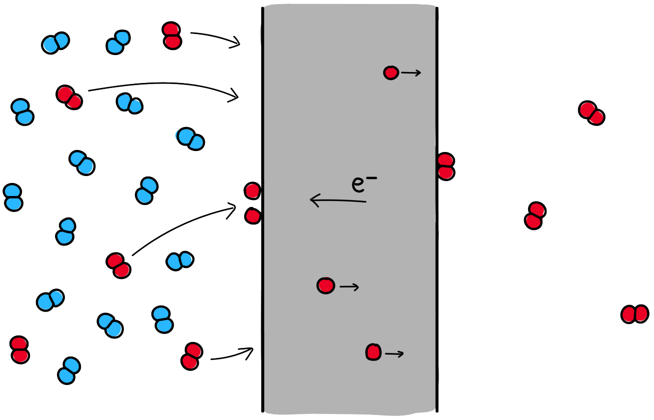

Figure 2.4: Illustration of air separation using ceramic ion transport membranes, where oxygen molecules (red) in air are decoupled into O^{2-} on the membrane surface, transported through the membrane lattice, and recombined into O_2 on the other membrane surface.

(MIEC). Perovskites are often used as membrane materials, in addition to fluorites, pyrochlore, and brownmillerites, among others.[35] IC membranes have electrodes connected on both sides to supply the electrons needed for oxygen transport.[13,34] In this case, the flow of oxygen is proportional to the current going through the membrane, resulting in good control of the amount of O_2 generated.[36] For MIEC membranes, no electrodes are needed, and oxygen is transported through the material due to a gradient in oxygen partial pressure across the membrane.[35,37] Another possibility is to use a dual-phase membrane, in which an ionic conductive material is in contact with an electronic conductor, which forms percolation networks through the membrane.[9]

Depending on the thickness of the membrane, the transport of oxygen can be limited by either the surface exchange reaction on the membrane sides, or the bulk diffusion of oxygen through the material, as shown in Figure 2.5. If the membrane is thick, bulk diffusion will be the rate limiting step, while for samples with a thickness lower than a characteristic thickness (L_c) surface exchange kinetics will be dominating.[37] As bulk diffusion is slow, the flux of oxygen through the material is inversely proportional to the membrane thickness down to L_c.[1,35,38] L_c is a material dependent property, and can vary between 0.01 to 10 mm.[9,37] Hollow fibre membranes with wall thicknesses of 200-300 µm have been successfully made, but these are often fragile and break easily.[16] As the mechanical strength

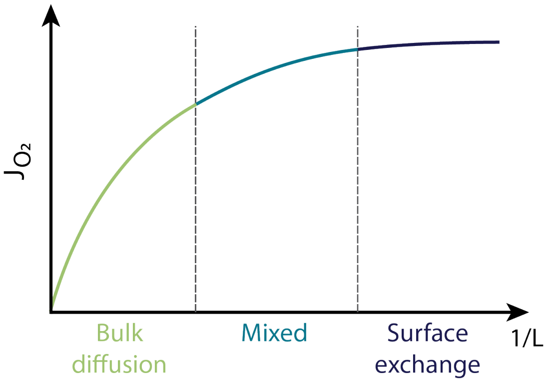

Figure 2.5: Flux of oxygen, J_{O_2}, through a ceramic membrane as a function of the reciprocal of the thickness of the membrane, $1/L$, indicating the different regions where bulk diffusion of oxygen, surface exchange of oxygen, or a mixture of the two, are the rate limiting steps of oxygen transport.

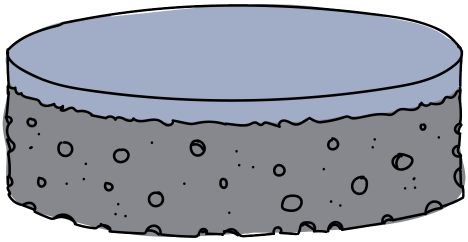

Figure 2.6: Illustration of a porous asymmetrical membrane, with the dense film deposited on top of the porous substrate. The film thickness is exaggerated.

of ceramic membranes becomes very poor when the membrane thickness is decreased, it is common to deposit the membrane as a dense film on top of a porous substrate, creating an asymmetric membrane as shown in Figure 2.6. It is advantageous to use the same material for both the membrane film and the support, as that minimizes problems with delamination due to differences in chemical and thermal expansion.[12] Such films can be made with a thickness of tens to hundreds of micrometers, with improved oxygen fluxes compared to thicker symmetric membranes.[39]

The largest issue for ceramic membranes is limited long term chemical and mechanical stability.[12] Perovskite-based membranes have shown great potential due to their high oxygen fluxes, but degrade due to reactions with CO_2, SO_2 or water vapor.[9,35] Fluorite materials such as yttria- and calcia-stabilized zirconia are more stable, but show lower oxygen fluxes than the perovskite materials at comparable conditions and thicknesses.[35] Most ionic conductive membranes also need operating temperatures as high as 800-1000 °C,[23] at which point the cations in the structure can be mobile. The gradient in the chemical potential of O_2 that causes the flux of oxygen can induce a gradient in chemical potential of the other species in the membrane, which can result in cation migration and phase separation due to kinetic demixing.[40,41] The high operating temperature also requires large amounts of electricity for heating, which is unfortunate both in an environmental perspective, and for the production cost of O_2.[16,23]

2.1.3 State of the art materials

Perovskites, fluorites and other similar oxides have dominated the CLAS and ceramic membrane research field in the last decades due to their wide flexibility in chemical composition, making it possible to fine tune the oxygen storage properties of the materials.[11,42–45] We will therefore focus on this class of materials in this section. Even though both sets of applications require materials with great oxygen storage and release capacities with quick kinetics, research on CLAS materials and membrane materials has focused on improving different properties; for CLAS, an economic improvement by increase in oxygen transport and lower operating temperatures have driven the material research in recent years, while for ceramic membranes, improvement in the chemical and mechanical stability of the materials while still maintaining a high oxygen flux has been the overarching goal.[8,9,15,16,30,35]

For CLAS applications, $La_xSr_{1\text{-}x}Co_yFe_{1\text{-}y}O_{3\text{-}\delta}$ (LSCF) was one of the first suggested perovskite materials as it shows good oxygen storage and release properties.[25] Similarly, substituting La with Ba to form perovskite $Ba_xSr_{1\text{-}x}Co_{0.8}Fe_{0.2}O_{3\text{-}\delta}$ (BSCF) has resulted in great oxygen transport properties, with oxygen desorption amounts just below 40 mg O_2 per gram perovskite after 20 cycles, twice the amount reported for LSCF.[46] Undoped $BaCoO_3$ has even greater oxygen desorption properties than the complex BSCF,[47] with maximum oxygen desorption amounts up to 50 $\mathrm{mg\,g^{-1}}$ at 850 °C[48] and good stability after 50 cycles of oxygen absorption and release. Unfortunately, full oxygen desorption takes over 30 minutes to achieve.[49] LSCF and BSCF have also been widely studied for ceramic membranes and have successfully been made as both asymmetric and hollow fibre membranes,[50–54] with hollow fibre $Ba_{0.5}Sr_{0.5}Co_{0.8}Fe_{0.2}O_{3-\delta}$ displaying oxygen fluxes up to 8 $mL\,cm^{-2}\,min^{-1}$ at 950 °C.[55] Perovskites based on alkaline earth elements have in general very high oxygen permeation fluxes, but the heightened oxygen flux unfortunately comes with a price, as BSCF is less chemically stable than LSCF, which can cause membrane failure.[1,16] Doping BSCF with Y^{3+} or higher valency cations such as W^{6+} have shown improvements in the chemical and thermal stability of the material, but this also decreases the flux down to just above 1 $mL\,cm^{-2}\,min^{-1}$.[56,57] Adding F^{-} in addition to Y^{3+} has been shown to improve the oxygen flux while maintaining great stability, with a $Ba_{0.5}Sr_{0.5}Co_{0.8}Fe_{0.17}Y_{0.03}O_{3-\delta}F_{0.09}$ disc membrane operating at 900 °C for 1300 h with a stable flux of 3 $mL\,cm^{-2}\,min^{-1}$.[58] Even with improved stability and oxygen fluxes, perovskite-based ceramic membranes still suffer from their high operating temperatures, increasing the cost needed for oxygen separation.

$SrFeO_3$ is another alkaline earth based perovskite system that is promising as OSMs for CLAS, especially as they absorb oxygen quickly at much lower temperatures than LSCF and BSCF.[15] $SrFeO_3$ doped with Ca on the A-site has shown an improved oxygen storage capacity (OSC) of up to 2.15 wt% at 500 °C and good stability after 30 cycles, but has slow reduction kinetics as full desorption takes 40 minutes.[59,60] B-site dopants, such as Co, Mn or Cu, have been found to improve the oxygen storage capacity,[44] and the use of Co enables release of O_2 down to 300 °C, making even lower operating temperatures a possibility.[61] When both Ca and Co are used as dopants, forming $Sr_{1-x}Ca_xFe_{1-y}Co_yO_{3-\delta}$ (SCFC), the oxidation kinetics are enhanced while the stability of the oxygen release properties of the material are maintained even after 10.000 cycles, but the reduction kinetics are still limited at $T < 400$ °C.[11,31,62].

Ceria- and perovskite-based dual phase membranes have also emerged as promising membrane systems, as the high thermal and chemical stability of fluorites under CO_2 make these membranes relevant for oxyfuel combustion applications.[63–65] As ceria-based materials have poor electronic conductivity, MIEC perovskite materials such as $SrFeO_3$ based materials are mixed in to act as electron conductors in addition to transport oxygen.[65] These membranes have an overweight of the ionic conducting phase, with 25-30% of the electronic conducting phase in order to have a continuous network throughout the membrane.[63] Unfortunately, these membranes still display low oxygen fluxes, often below 1 $mL\,cm^{-2}\,min^{-1}$ at $T > 900$ °C.[66,67]

2.2 Hexagonal manganites $R\mathrm{MnO}_3$

2.2.1 Crystal structure

Hexagonal manganites, $R\mathrm{MnO}_3$ (R = Sc, Y, Ho-lu), are considered as possible oxygen storage materials due to their ability to reversibly store and release large amounts of oxygen at lower temperatures.[68–72] This is discussed further in Section 2.2.2. The incorporation of oxygen as interstitials makes hexagonal manganites fundamentally different from the perovskite OSMs (see Section 2.1.3), where oxygen vacancies are the dominating point defects involved in oxygen storage and release. $R\mathrm{MnO}_3$ oxides crystallize in one of two crystal structures, depending on the ionic size of the R^{3+} cation; for large R ($r_{R^{3+}} \geq r_{\mathrm{Dy}^{3+}}$), the orthorhombic perovskite structure with space group *Pnma* is favoured, while for smaller R ($r_{R^{3+}} \leq r_{\mathrm{Ho}^{3+}}$), the hexagonal $P6_3cm$ structure is preferred.[73–75] The hexagonal crystal structure is composed of alternating layers of seven-coordinated R^{3+} and corner-sharing MnO_5 trigonal bipyramids,[76] illustrated in Figure 2.7(a),(b). Each MnO_5 polyhedron is slightly tilted with respect to the c axis, forming a pattern of trimers. This is also accompanied by a displacement of R^{3+}, with 1/3 of the R cations displaced in one direction along the c axis and 2/3 displaced in the opposite direction. The structural parameters for the $P6_3cm$ phase are given in Table 2.1. Due to an anharmonic coupling between the K_3 mode, which causes the tilting of MnO_5 and displacement of R, and the polar Γ_2^- mode, the material becomes ferroelectric below the Curie temperature of $T_C \approx 1250$ K, with a polarization of $\sim 6\ \mu\mathrm{C\,cm}^{-2}$.[77,78] The primary order parameter K_3 is described by the amplitude of the MnO_5 tilting, Q, and angle of the tilt and the displacement pattern of R, Φ, which causes a sixfold domain pattern with characteristic vortex cores.[79,80] Hexagonal manganites have been widely studied for their multiferroic properties, especially as their charged domain walls have possible applications in nanoelectronics.[81–83]

At temperatures above T $\approx$ 1250 K, hexagonal manganites undergo a phase transition to the nonpolar $P6_3/mmc$ structure with untilted MnO_5 bipyramids and uncorrugated R layers (Figure 2.7(c),(d)).[74,76] In the transition between this high temperature phase and the low temperature $P6_3cm$ phase, the trimerization of MnO_5 tilts and displacement of R causes a tripling in the unit cell volume, as $a_{P6_3cm} = \sqrt{3}a_{P6_3/mmc}$. Structural parameters of the $P6_3/mmc$ phase are given in Table 2.2. At room temperature, the energy landscape of hexagonal manganites found through Landau theory resembles a Mexican hat with six wells along the

Table 2.1: Atomic positions for YMnO_3 within the $P6_3cm$ (No. 185) space group. The lattice parameters are a = 6.2583(4) Å and c = 11.34918(12) Å.[76]

Atom	Position	x	y	z
$R1$	2a	0	0	0.2639(5)
$R2$	4b	1/3	2/3	0.2399(4)
Mn	6c	0.3094(6)	0	0
O1	6c	0.3297(7)	0	0.1656(4)
O2	6c	0.6621(7)	0	0.3394(4)
O3	2a	0	0	0.5083(7)
O4	4b	1/3	2/3	0.0153(5)

Table 2.2: Atomic positions for YMnO_3 within the $P6_3/mmc$ (No. 194) space group. The lattice parameters are a = 3.618961(15) Å and c = 11.34090(9) Å.[76]

Atom	Position	x	y	z
$R1$	2a	0	0	0
Mn	2c	1/3	2/3	1/4
O1	2b	0	0	1/4
O2	4f	1/3	2/3	0.08557(7)

brim, related to the six degenerate states and angles Φ that give rise to the sixfold domain pattern found in these materials.[84] As the material is heated to above 800 °C, the energy landscape flattens and the values of Φ start to fluctuate, and, finally, above T_C the system disorders with a continuum of all structures and possible angles Φ.[79]

When absorbing large amounts of excess oxygen ($\delta \geq 0.28$), hexagonal manganites have been shown to adapt to the $R3c$ space group.[70,72] In the $R3c$ superstructure, Mn are found as 8 coordinated instead of 5 coordinated due to interstitial oxygen as illustrated in Figure 2.8. The 3 additional oxygen positions surrounding Mn are the partially occupied O_i sites, which become more and more filled as δ increases. Structural parameters for this highly oxidized phase are listed in Table 2.3.

2.2.2 Defect chemistry

Point defects are imperative to understand and tailor the functional properties of oxide materials, which are used for a large variety of applications such as batteries, fuel cells, sensors and optics.[85,86] By understanding the defect chemistry

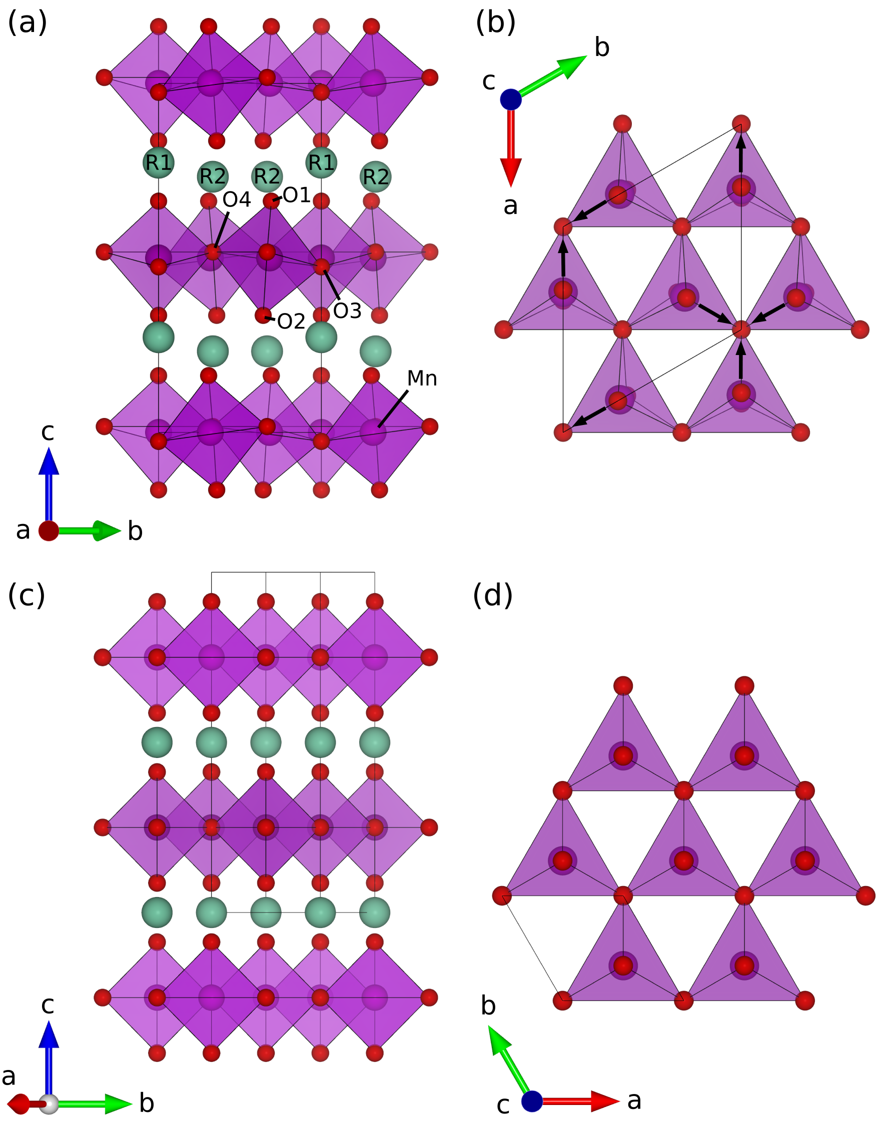

Figure 2.7: The low and high temperature crystal structures of hexagonal manganites, with turquoise R^{3+} cations and purple MnO_5 trigonal bipyramids. (a) The polar $P6_3cm$ structure, with emphasis on the atomic sites, and O3 as the trimerization centers (b) The trimerization of MnO_5 seen along the c axis, with arrows indicating the tilting direction. (c) The high temperature $P6_3/mmc$ structure, with no tilting of MnO_5 or displacements of R^{3+}. (d) The Mn-O layer in the $P6_3/mmc$ phase seen along the c axis.

Table 2.3: Atomic positions and site occupancy for $\mathrm{Dy}_{0.7}\mathrm{Y}_{0.3}\mathrm{MnO}_{3.29}$ within the $R3c$ (No. 161) space group. The lattice parameters are a = 6.2253(6) Å and c = 33.2426(9) Å.[72]

Atom	Position	x	y	z	n
$R1$	6a	0	0	-0.0819(4)	1
$R2$	6a	0	0	0.0944(3)	1
$R3$	6a	0	0	0.2345(7)	1
Mn	18b	0.2749(9)	-0.0477(6)	0	1
O1	6a	0	0	0.1669(3)	0.578
O2	6a	0	0	0.9931(2)	1
O3	6a	0	0	0.3380(9)	1
O4	18b	0.2943(3)	-0.0295(7)	0.0481(9)	1
O5	18b	0.0051(8)	0.3159(5)	0.2757(2)	1
O6	18b	0.2787(2)	0.3972(7)	0.3281(1)	0.483

of the materials, and how the type and concentration of a point defect found in the material can be controlled by e.g. dopants and thermal and atmospheric history, the properties of the materials can be improved, or entire new properties can emerge.[87] Oxygen vacancies are the dominating point defects in perovskite ABO_3 oxygen storage materials, and many of these oxides use aliovalent dopants to change the oxygen vacancy concentration and transport properties, as discussed in Section 2.1.3. Interstitial defects, with a cation or an anion positioned in an interstitial site, are less likely in such close-packed structures.[85] Some perovskites, such as $\mathrm{LaMnO}_{3+\delta}$ are known to accommodate excess oxygen, but this is charge balanced by cation vacancies instead in the form of $\mathrm{La}_{1\text{-}\delta/3}\mathrm{Mn}_{1\text{-}\delta/3}\mathrm{O}_{2+\delta}$, which requires cation diffusion.[88] As the layered $P6_3cm$ structure is ~11 % less dense than the perovskite structure,[88–90] hexagonal manganites can accommodate both oxygen vacancies, V_O, and oxygen interstitials, O_i. These two defects can also occur as anti-Frenkel defect pairs, where they coexist in the material.[91] The formations of both intrinsic defects are shown in Kröger-Vink notation in eq. 2.3 and 2.4.

$$\mathrm{O}_\mathrm{O}^\times + 2\,\mathrm{Mn}_\mathrm{Mn}^\times \xrightleftharpoons{\mathrm{RMnO_3}} \mathrm{V}_\mathrm{O}^{\bullet\bullet} + 2\,\mathrm{Mn}_\mathrm{Mn}' + \frac{1}{2}\,\mathrm{O}_2(\mathrm{g}) \tag{2.3}$$

$$\frac{1}{2}\,\mathrm{O}_2(\mathrm{g}) + 2\,\mathrm{Mn}_\mathrm{Mn}^\times \xrightleftharpoons{\mathrm{RMnO_3}} \mathrm{O}_\mathrm{i}'' + 2\,\mathrm{Mn}_\mathrm{Mn}^\bullet \tag{2.4}$$

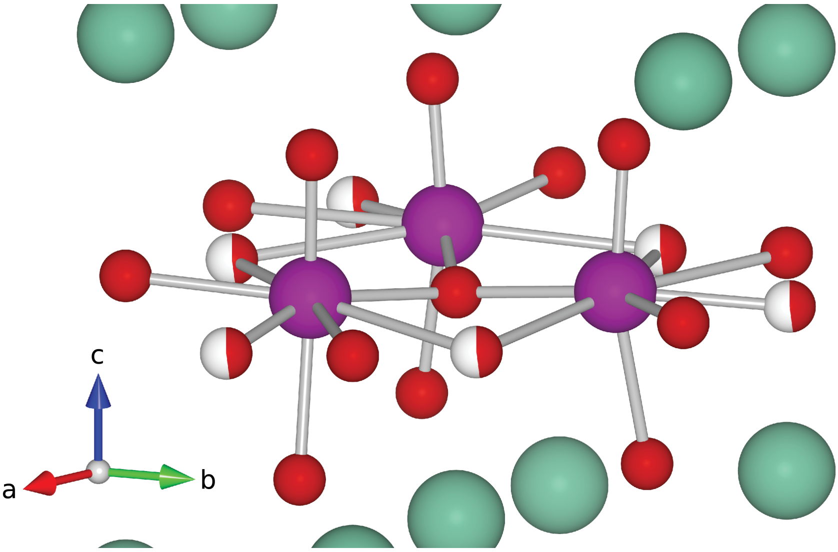

Figure 2.8: Illustration of the $R3c$ superstructure, with the 8-coordinated Mn (purple) surrounded by planar and apical oxygen (red), and oxygen on partially occupied interstitial sites.

Here, O_O^x is O^{2-} in the oxygen lattice site; Mn_{Mn}^x, Mn_{Mn}' and $Mn_{Mn}^{\bullet}$ depicts Mn^{3+}, Mn^{2+} and Mn^{4+} in Mn-sites, respectively; and $V_O^{\bullet\bullet}$ and O_i" are oxygen vacancies and interstitials, respectively. At higher temperatures and in atmospheres with low p_{O_2}, the formation of oxygen vacancies is charge balanced by reduction of Mn^{3+} to Mn^{2+} (eq. 2.3), which gives n-type conductivity.[89] At higher partial pressures of oxygen, the formation of interstitial oxygen will be dominating, with Mn^{3+} oxidizing to Mn^{4+}.[71,92] This results in p-type conductivity in RMnO$_3$, which increases with increasing amounts of O_i.[89] The interstitial oxygen is positioned in between Mn in the triangular Mn-O lattice, as illustrated in Figure 2.10.[89] The theoretical maximum oxygen content is equal to $\delta = 0.33$, when there is one O_i in each of the Mn−O layers within a 30 atom unit cell, resulting in 2/3 of Mn^{3+} being oxidized to Mn^{4+}. Higher δ than the theoretical maximum would cause oxidation of Mn across layers, or further oxidation of Mn into Mn^{5+}, which is unlikely. Upon oxidation, excess oxygen proliferates in the crystal lattice through an interstitialcy mechanism, where the interstitially positioned oxygen nudges a planar O3 oxygen into the neighbouring interstitial site.[89] This mechanism has a lower activation energy barrier than that reported for migration of vacancies in most perovskites, enabling transport of oxygen at lower temperatures.[89,93–95]

Remsen and Dabrowsky[68] were the first to report the large oxygen absorption properties of hexagonal manganites. Bulk powders of $\mathrm{Dy_{1\text{-}x}Y_xMnO_3}$ showed large oxygen absorption at temperatures below 300 °C, with a maximum δ = 0.3 for $\mathrm{Dy_{0.7}Y_{0.3}MnO_3}$ when slowly cooling the sample in oxygen atmosphere. In the years since, oxygen absorption in hexagonal manganites have received more attention, and much research has gone into understanding and improving the oxygen storage capacity of these materials. As the maximum OSC of hexagonal manganites increases with the size of the R^{3+} cation, as illustrated for R = Er, Ho, Dy in Figure 2.9, most studies have focused on using either larger R^{3+} cations such as $\mathrm{Ho^{3+}}$ and $\mathrm{Dy^{3+}}$ on the R site, or partial substitution of Y in $\mathrm{YMnO_3}$ with larger rare earth cations.[70,71,92,96–100] The latter has received more attention in the recent years, as this enables the use of larger R (R = Ce-Tb) cations without destabilizing the hexagonal phase due to a too large increase in tolerance factor, as is explained in Section 2.2.3. The increase in OSC due to larger R^{3+} cations is believed to be caused by the expanded ab-plane,[92,101] which lessens the repulsion between oxygen. Reducing the particle size from bulk powders made through solid state synthesis to nanocrystalline powders from wet-chemical synthesis methods has also been shown to improve the oxygen absorption in these materials due to shorter diffusion distances within the particle.[100,102,103]

Another way to tailor the defect chemistry of these materials, is by aliovalent doping. By adding dopants with higher valency than $\mathrm{Mn^{3+}}$, donor doping, the material can be either ionically compensated through the formation of oxygen interstitials, or electronically compensated by reduction of Mn. For the case of addition of $\mathrm{Ti^{4+}}$ on the Mn site (Figure 2.10), this is shown in Kröger-Vink notation in eq. 2.5 and 2.6 for ionic and electronic compensation, respectively.

$$2\,\mathrm{TiO_2} \xrightarrow{R\mathrm{MnO_3}} 2\,\mathrm{Ti_{Mn}^{\bullet}} + 3\,\mathrm{O_O^{\times}} + \mathrm{O_i''} \tag{2.5}$$

$$\mathrm{TiO_2} + \frac{1}{2}\,\mathrm{Mn_2O_3} \xrightarrow{R\mathrm{MnO_3}} \mathrm{Ti_{Mn}^{\bullet}} + 3\,\mathrm{O_O^{\times}} + \mathrm{Mn_{Mn}'} + \frac{1}{4}\,\mathrm{O_2(g)} \tag{2.6}$$

Here, $\mathrm{Ti_{Mn}^{\bullet}}$ is $\mathrm{Ti^{4+}}$ on the Mn site, $\mathrm{O_O^{x}}$ is $\mathrm{O^{2-}}$ in the oxygen lattice site, $\mathrm{O_i}$” is oxygen interstitials, and $\mathrm{Mn_{Mn}}$’ depicts $\mathrm{Mn^{2+}}$. At higher partial pressures of oxygen and low temperatures, the ionic compensation and formation of interstitial oxygen will be favourable, increasing the amount of $\mathrm{O_i}$ in $R\mathrm{Mn_{1\text{-}x}Ti_xO_{3+\delta}}$ by $\Delta\delta = x/2$.

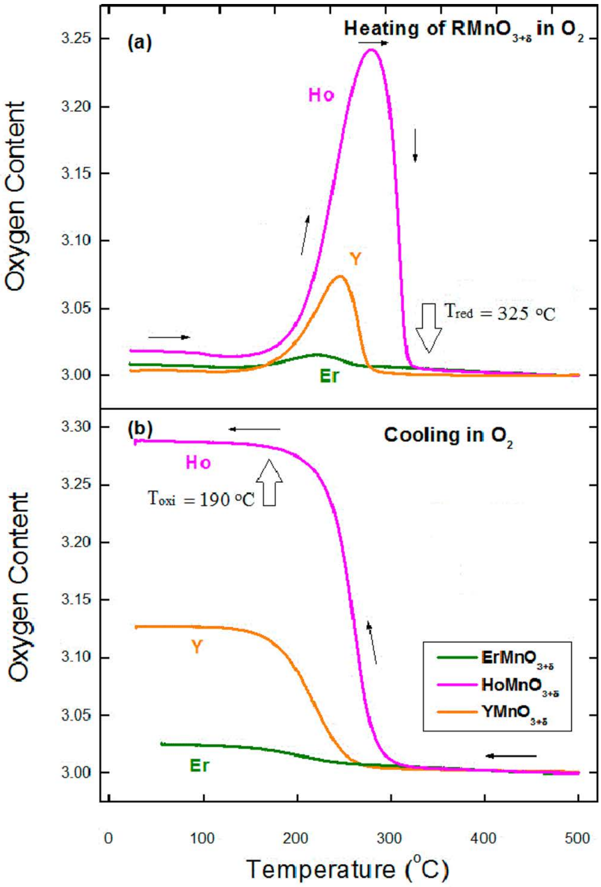

Figure 2.9: Oxygen content in $R\mathrm{MnO}_{3+\delta}$ (R = Er, Y, Ho) during heating and cooling in O_2 atmosphere, showing the increase in oxygen storage capacity with increasing size of the R cation. Reprinted with permission from Abughayada *et al.* [70] Copyright 2015 American Chemical Society.

At higher temperatures (T > 300 °C), O_i becomes entropy destabilized as entropy favours the formation of O_2 gas, but the temperature for which this destabilization occurs can also be affected by doping. Zr^{4+} and Ti^{4+} donor doping have been shown to increase both the OSC and the thermal stability of O_i in $YMnO_3$ [104,105] when used as dopants on the Y or Mn site, respectively. When adding dopants, the Mn trimerization is suppressed, reducing both the tilting angle of the MnO_5 bipyramids and the corrugation of the R^{3+} layers. [105–107] At higher concentrations

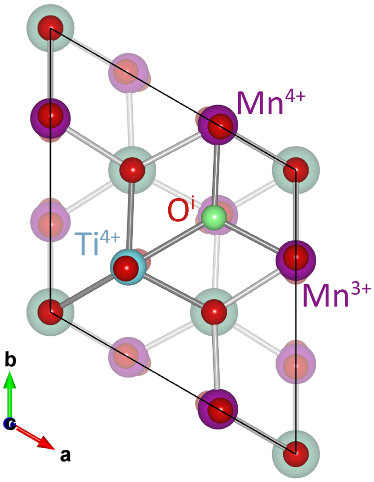

Figure 2.10: The position of interstitial oxygen (O_i) in the Mn-O lattice, with Ti^{4+} added on the Mn site. Reprinted from Danmo *et al.*[101]

of dopants ($x \geq 0.125$ for Ti^{4+}, $x \geq 0.10$ for Mo^{6+}), the polyhedra become fully rectified, stabilizing the high symmetry $P6_3/mmc$ structure at room temperature after cooling the materials in air or O_2 atmospheres.[104,108] The corrugation of the R^{3+} layers is inseparable from the MnO_5 tilting.[79]

2.2.3 Phase stability

As briefly stated in Section 2.2.1, the crystal structure of $R\mathrm{MnO}_3$ oxides is strongly governed by the size of the R cation. The stability of either the orthorhombic perovskite $Pnma$ structure or the hexagonal $P6_3cm$ can be determined from the value of the Goldschmidt tolerance factor, given in eq. 2.7, which explains the distortion from the perfect cubic perovskite.

$$t = \frac{r_R + r_O}{\sqrt{2}(r_{Mn} + r_O)} \tag{2.7}$$

Small rare earth cations ($r_{R^{3+}} \leq r_{Ho^{3+}}$), giving a tolerance factor $t < 0.855$, stabilizes the hexagonal structure at ambient conditions.[73] The ionic radii for a selection of cations are given in Table 2.4.

Table 2.4: Shannon radii of selected cations.[109] The values marked with an asterisk (*) are interpolated between the ionic radii of CN = 6 and CN = 8, while the radius for Mn^{4+} marked with an apostrophe (') is an interpolation between the ionic radii of CN = 4 and CN = 6.

Cation	Coordination number	Shannon radius (Å)
Gd^{3+}	7	1.00
Tb^{3+}	7	0.98
Tb^{4+}	7	0.82*
Dy^{3+}	7	0.97
Ho^{3+}	7	0.96*
Er^{3+}	7	0.95
Y^{3+}	7	0.96
Mn^{2+}	5	0.75
Mn^{3+}	5	0.58
Mn^{4+}	5	0.46'
Ti^{4+}	5	0.51

Using the right synthesis conditions is imperative when maneuvering the phase stability landscape of hexagonal manganites, as this can enable the use of larger rare earth cations with tolerance factors outside of the stability window for the $P6_3cm$ space group. In the case of oxygen absorption properties, larger R^{3+} cations show the greatest oxygen storage capacities, but these cations are both on, and on the wrong side of, the knife's edge when it comes to preferring the hexagonal structure. The calculated phase diagram for $YMnO_3$ is presented in Figure 2.11. Hexagonal $YMnO_3$, noted as h-$YMnO_3$ in the figure, is entropy stabilized for temperatures above 1062 K, and becomes metastable with respect to YMn_2O_5 and Y_2O_3 at temperatures below. This temperature stabilization has also been confirmed experimentally, as heating $YMnO_3$ to temperatures above 1000 °C has been shown to favour the hexagonal structure.[110,111] Pressure can also be used to affect the resulting structure, as high-pressure annealing of hexagonal $RMnO_3$ (R = Sc, Y, Ho-Lu) can cause it to convert into the orthorhombic perovskite structure.[112,113] Rare earth cations larger than Dy can be stabilized within the hexagonal structure by epitaxial stabilization of thin films grown on substrates with an in-plane hexagonal lattice,[114,115] and the same principle can be used for stabilizing the orthorhombic structure for $r_R \leq r_Y$ on perovskite substrates.[116,117] The choice of atmosphere for heat treatment is also essential; when heat treated to above 1400 °C in inert atmospheres, orthorhombic $HoMnO_3$ and $DyMnO_3$ goes through a reconstructive phase

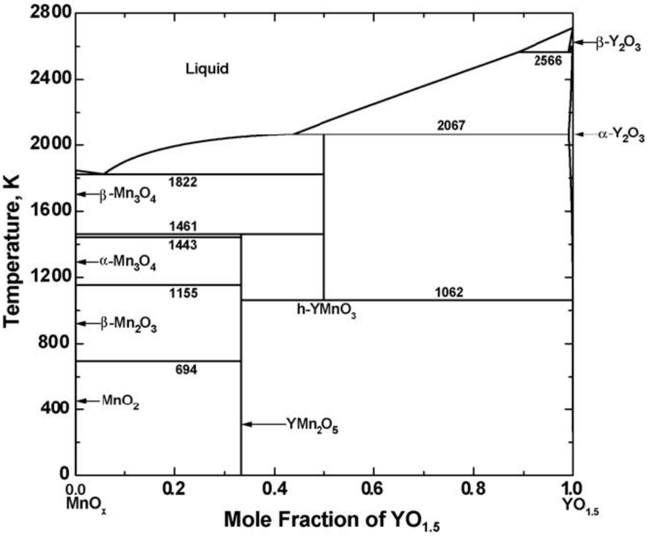

Figure 2.11: Phase diagram of the MnO_x–$\mathrm{YO}_{1.5}$ system in air. Reprinted from Journal of Alloys and Compounds, Volume 393, Chen *et al.*, Thermodynamic assessment of the Mn–Y–O system, Copyright 2005, with permission from Elsevier.[119]

transition to the hexagonal phase.[69,74] Similarly, hexagonal YMnO_3 will form in reducing conditions, while orthorhombic YMnO_3 is favoured when synthesized in oxidizing conditions.[111] When Mn^{3+} is oxidized to Mn^{4+}, the ionic radius decreases (Table 2.4), which also increases the tolerance factor (eq. 2.7), shifting it into the orthorhombic regime. This oxidation reaction is exothermic, which can also explain the temperature stabilization of the hexagonal phase.[111,118]

Another way to explore the stability window of the hexagonal structure is by isovalent substitution of YMnO_3 with larger R^{3+} on the Y-site. Rare earth elements as large as Pr^{3+} (1.06 Å) and Ce^{3+} (1.07 Å)[109] have been successfully used as R-site dopants while still achieving phase pure hexagonal materials.[98,99,120] If the proportion of the added dopant is too high, the perovskite structure can start to form, resulting in a mixed hexagonal-perovskite material. The formed material is, however, not necessarily chemically segregated; in $\mathrm{Y}_{1\text{-}x}\mathrm{Gd}_x\mathrm{MnO}_3$ with $0.19 \leq x \leq 0.38$, found to contain both the orthorhombic and the hexagonal structure, the hexagonal phase showed perfect mixing of cations with no segregation of Y and Gd.[73] For undoped $R\mathrm{MnO}_3$ with R cations larger than Ho^{3+}, or when lower crystallization temperatures are needed (e.q. when synthesizing nanocrystalline powders), a reduction of some Mn^{3+} to Mn^{2+} can be utilized to lower the tolerance factor and stabilize the hexagonal structure.[101] The hexagonal system has been shown to withstand reduction as low as $RMnO_{2.80}$, but further reduction can cause decomposition into binary oxides R_2O_3 and MnO.[68,121]

2.3 High entropy oxides

High entropy alloys and ceramics are materials with high configurational entropy due to a large number of different elements in the composition. The high entropy can cause a single phase solid solution to form, even if the different components do not show complete solubility with each other. This complex structure often results in new material properties. This was first discovered for metal alloys in 2004, where a combination of 5 or more metals in equimolar amounts resulted in stabilization of a single phase solid solution, and an increase in strength and corrosion resistance.[122,123] The high entropy concept was in 2015 adapted to oxides and ceramics as well, with the formation of single phase rock salt structure for (Mg,Ni,Co,Cu,Zn)O.[124] This has later been used to synthesize a vast number of different compositions and structures,[125–130] including perovskites,[131,132], diborides,[133], oxyfluorides[134], and carbides.[14] High entropy systems forming a single phase solid solution are usually defined as having configuration entropy larger than $S_{\text{config}} \geq 1.5\text{R}$, where R is the universal gas constant.[135] For oxides with a general structure of $\text{A}_\text{x}\text{B}_\text{y}\text{O}_\text{z}$, S_{config} can be calculated from eq. 2.8.[129]

$$S_{\text{config}} = -\text{R}\left[x\left(\sum_{a=1}^{\text{M}} x_a \ln x_a\right)_{\text{A-site}} + y\left(\sum_{b=1}^{\text{N}} y_b \ln y_b\right)_{\text{B-site}} + z\left(\sum_{o=1}^{\text{P}} z_o \ln z_o\right)_{\text{O-site}}\right] \tag{2.8}$$

Here, x_a, y_b and z_o are the mole fractions of each element on the A, B and O^{2-} sites, respectively, and M, N and P are the number of cations on the A and B sites, and anions on the O^{2-} sites, respectively. If we assume that a system only have disorder on the A sublattice, disregarding compositional changes in the B sublattice or possible oxygen defects, eq. 2.8 can be simplified to eq. 2.9.[129]

$$S_{\text{config}} = -\text{R}\left[x\left(\sum_{a=1}^{\text{M}} x_a \ln x_a\right)_{\text{A-site}}\right] \tag{2.9}$$

When 5 or more cations are added to the A-site in equimolar amounts, the configurational entropy for an ideal solid solution will then be $S_{\text{config}} \geq 1.5\text{R}$ according to eq. 2.9. The complex structure is homogeneous, with the cations uniformly distributed throughout the lattice.[124,131] The high entropy phase is usually stabilized at higher temperatures, which can lead to challenges when synthesizing samples with small particle sizes, as these synthesis methods often require lower temperatures.[124,129]

The high configurational entropy can induce promising and interesting material properties in high entropy oxides, such as colossal dielectric constants,[128], proton conductivity,[136] and high ionic conductivity.[127] Li-substituted high entropy oxides have displayed extraordinarily high Li^+ conductivity at room temperature, making them promising for reversible energy storage.[126,127] Site disorder within a lattice have been shown to improve the Li-ion conductivity of solid electrolytes,[137] which may explain how the increased ionic conductivity is connected to the high configurational entropy in high entropy oxides. It has also recently been shown that the site disorder in high entropy oxides causes an overlap in site-energy distributions, promoting ionic conductivity.[138]

3

Methods

3.1 Synthesis

A list of all chemicals used for citric acid synthesis of nanocrystalline powders and solid state synthesis of the porous membrane support is presented in Table 3.1. The compositions of the samples prepared for each of the three manuscripts included in the thesis are listed in Table 3.2.

3.1.1 Citric acid synthesis

Nanocrystalline powders were prepared using a modified citric acid synthesis method based on the one developed by Bergum *et al.*[111], illustrated in Figure 3.1. For the precursor solutions, metal acetates $Er(CH_3CO_2)_3 \cdot xH_2O$, $Y(CH_3CO_2)_3 \cdot xH_2O$, $Ho(CH_3CO_2)_3 \cdot xH_2O$, $Dy(CH_3CO_2)_3 \cdot xH_2O$, $Gd(CH_3CO_2)_3 \cdot xH_2O$, $Tb(CH_3CO_2)_3 \cdot xH_2O$, $In(CH_3CO_3)_3 \cdot xH_2O$, and $Mn(CH_3CO_2)_3 \cdot xH_2O$ were each dissolved in a mixture of citric acid and deionized water, and stirred on a hot plate set to 150 °C for 3h, or until clear. For the Ti^{4+} solution, Titanium (IV) isopropoxide (TTIP) was measured out using a syringe flushed with Ar to prevent hydrolysis of TTIP, added to a mixture of deionized water and citric acid, and stirred at 400 rpm on a hot plate set to 60 °C until clear. The molar ratio between cation and citric acid was 1:20 for Er^{3+}, Y^{3+} and Ho^{3+}; 1:35 for Dy^{3+}, Tb^{3+} and Gd^{3+}; 1:5 for In^{3+} and Mn^{3+}; and 1:6.3 for Ti^{4+}. The concentration of each solution was determined by thermogravimetric standardization at 1100 °C for R^{3+} cations, 600 °C for Mn^{3+}, and 1000 °C for Ti^{4+}. The In^{3+} precursor solution was not standardized due to the volatility of In.

The precursor solutions were mixed stoichiometrically and ethylene glycol was added as a polymerization agent, with a molar ratio of 1:1 between ethylene glycol and the citric acid in the solution. The solution was stirred on a hot plate set to 150 °C for 24-48 h, until a viscous gel had formed. The gel was transferred to a crystallization beaker and dried in a heating cabinet set to 120 °C for 72 h. The dried gel was calcined at 400 °C for 3 h and then subsequently at 600 °C for 6 h to remove all organics. The resulting amorphous powder was crystallized in N_2 at temperatures ranging from 850 to 1000 °C for 1 h, depending on the desired crystallite size. Some samples were also pre-annealed in 5 % H_2 in N_2 at temperatures between 250 and 300 °C for 10 h prior to crystallization to slightly reduce Mn^{3+} to Mn^{2+}, lowering the tolerance factor and favoring formation of the hexagonal phase.

Table 3.1: List of chemicals used for synthesis of nanocrystalline powders, bulk powders, and the porous membrane support.

Chemical	**Formula**	**Purity (wt%)**	**Supplier**
Erbium (III) acetate hydrate	$Er(CH_3CO_3)_3 \cdot xH_2O$	99.9%	Aldrich
Yttrium (III) acetate hydrate	$Y(CH_3CO_3)_3 \cdot xH_2O$	99.9%	Aldrich
Holmium (III) acetate hydrate	$Ho(CH_3CO_3)_3 \cdot xH_2O$	99.9%	AlfaAesar
Dysprosium (III) acetate hydrate	$Dy(CH_3CO_3)_3 \cdot xH_2O$	99.9%	AlfaAesar
Terbium (III) acetate hydrate	$Tb(CH_3CO_3)_3 \cdot xH_2O$	99.9%	Aldrich
Gadolinium (III) acetate hydrate	$Gd(CH_3CO_3)_3 \cdot xH_2O$	99.9%	Aldrich
Indium (III) acetate hydrate	$In(CH_3CO_3)_3 \cdot xH_2O$	99.9%	Aldrich
Manganese (II) acetate tetrahydrate	$Mn(CH_3COO)_3 \cdot 2H_2O$	99.5%	Riedel-de-Haën
Titanium (IV) isopropoxide (TTIP)	$Ti[OCH(CH_3)_2]_4$	97%	Sigma-Aldrich
Yttrium (III) oxide	Y_2O_3	99.99%	Aldrich
Gadolinium (III) oxide	Gd_2O_3	99.9%	Aldrich
Terbium (III,IV) oxide	Tb_4O_7	99.998%	Alfa Aesar
Dysprosium (III) oxide	Dy_2O_3	99.9%	Aldrich
Holmium (III) oxide	Ho_2O_3	99.99%	TermoFisher
Erbium (III) oxide	Er_2O_3	99.9%	Aldrich
Manganese (III) oxide	Mn_2O_3	99%	Aldrich
Titanium (IV) oxide	TiO_2 (anatase)	99.9%	Aldrich
Rice starch	$(C_6H_{10}O_5)_n$		Carl-Roth GmbH & Co. KG
Ethylene glycol	$C_2H_6O_2$		Merck
Dolacol D 1003			Zschimmer & Schwarz

Table 3.2: Overview of the compositions, size and naming of the samples prepared for each of the three manuscripts included in the thesis.

Work	Composition	Size	Naming
Manuscript I	$YMnO_3$	25 / 39 ± 1 nm	YMO25 / YMO39
	$YMn_{0.85}Ti_{0.15}O_3$	21 ± 1 nm	YMTO21
	$HoMnO_3$	25 / 38 ± 1 nm	HMO25 / HMO38
	$HoMn_{0.85}Ti_{0.15}O_3$	28 ± 1 nm	HMTO28
	$DyMnO_3$	30 ± 1 nm	DMO30
	$DyMn_{0.85}Ti_{0.15}O_3$	30 ± 1 nm	DMTO30
Manuscript II	$HoMnO_3$	25 ± 1 nm	-
	$HoMn_{0.85}Ti_{0.15}O_3$	28 ± 1 nm	-
	$DyMnO_3$	30 ± 1 nm	-
	$DyMn_{0.85}Ti_{0.15}O_3$	30 ± 1 nm	-
Manuscript III	$Y_{0.167}Gd_{0.167}Tb_{0.167}Dy_{0.167}Ho_{0.167}Er_{0.167}MnO_3$	28 ± 1 nm / bulk	HEO1-n / HEO1-b
	$Y_{0.167}Gd_{0.167}Tb_{0.167}Dy_{0.167}Ho_{0.167}Er_{0.167}Mn_{0.85}Ti_{0.15}O_3$	23 ± 1 nm / bulk	HEO2-n / HEO2-b
	$Y_{0.167}Gd_{0.233}Tb_{0.167}Dy_{0.167}Ho_{0.167}Er_{0.1}Mn_{0.85}Ti_{0.15}O_3$	31 ± 1 nm	HEO3-n
	$Y_{0.145}Gd_{0.210}Tb_{0.190}Dy_{0.165}Ho_{0.155}Er_{0.135}Mn_{0.85}Ti_{0.15}O_3$	24 ± 1 nm	HEO4-n
	$Y_{0.2}Gd_{0.2}Dy_{0.2}Ho_{0.2}Er_{0.2}Mn_{0.85}Ti_{0.15}O_3$	30 ± 1 nm / bulk	HEO5-n / HEO5-b

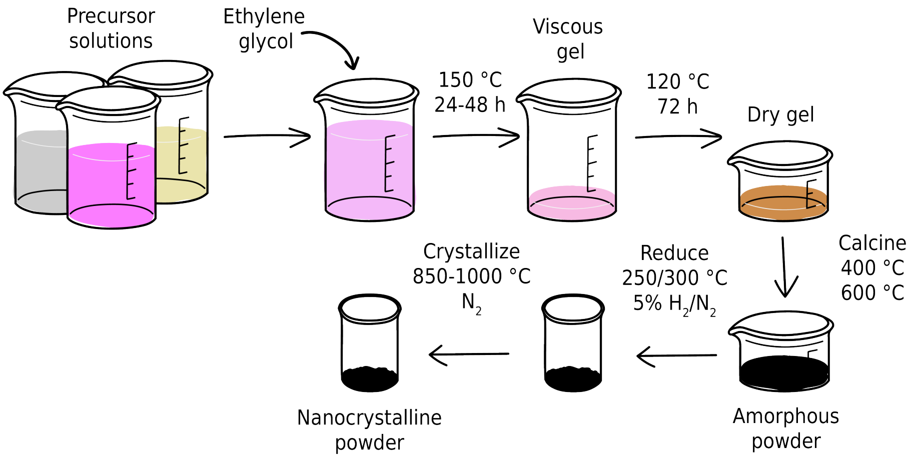

Figure 3.1: Schematic of the citric acid synthesis method used for making nanocrystalline powders, including the reduction step that was used for some of the samples.

3.1.2 Solid state synthesis

Bulk high entropy hexagonal manganites samples were made through solid state synthesis. Binary oxides of Y_2O_3, Gd_2O_3, Tb_4O_7, Dy_2O_3, Ho_2O_3, Er_2O_3, Mn_2O_3 and TiO_2 were stoichiometrically added to a 500 mL polyethylene bottle together with yttrium-stabilized zirconia milling balls (Ø 5 mm) and ethanol. The mixture was then ball mixed for 12 hours, using a ball mill with a rotation speed of 205 rpm. Afterwards, the ethanol was removed using a rotary evaporator. The powder was uniaxially pressed into pellets, which were fired in air at 1450 °C for 1 hour. Afterwards, the pellets were crushed into powders using a mortar and pestle.

3.1.3 Porous membrane supports

The porous $Y_{1.05}Mn_{0.85}Ti_{0.15}O_3$ supports used for thin film deposition were made through solid state synthesis. The slight excess of Y was chosen to impede densification of the ceramics, to keep the porosity high enough for gas percolation. Binary oxides of Y_2O_3, Mn_2O_3 and TiO_2 were added stoichiometrically to a 50 mL polyethylene bottle containing yttrium-stabilized zirconia milling balls (Ø 5 mm). 30 wt% corn starch was added as a pore former. The bottle was 60 % filled with 96 % ethanol, and mixed by ball milling at a speed of 205 rpm for 2 hours. Afterwards, the ethanol was removed using a rotary evaporator. The resulting powder was pressed into 10 to 20 mm disks, and placed on top of sacrificial powder on alumina disks. The pellets were calcined at 600 °C for 6 h in air to burn off the pore former, and then fired at 1450 °C for 1 hour. The porosity of the supports was determined using Archimedes' method. To prepare the supports for film deposition, each support was polished using a Struers LaboPol-21 with #800, #1200 and #2000 grade SiC paper, and, for some samples, polished further with a Struers Tegramin-20 using 9, 3 and 1 µm diamonds on polishing disks. Ultrasonification in ethanol was done in between each round of polishing. The supports were then dried over night in a heating cabinet set to 120 °C.

3.2 Characterization

3.2.1 X-ray diffraction (XRD)

Phase purity

The phase purity of the samples was investigated by X-ray diffraction (XRD) using a Bruker D8 Focus with Cu Kα radiation. Nanocrystalline samples were prepared in 10 mm Si cavity holders covered with a protective Kapton polyimide film, or mixed with ethanol and deposited on top of a flat Si holder. For the porous supports, the pellets were ground to powders and prepared in normal XRD powder holders. Pawley refinement of lattice parameters and crystallite size was done using the Bruker AXS TOPAS 5 software.[139]

High temperature XRD

For the two high temperature X-ray diffraction (HT-XRD) experiments where the lattice parameters of hexagonal manganites as a function of temperature and atmosphere was investigated, a Bruker D8 Advance with Cu Kα was used. For the experiments in Manuscript I,[101] the powders were prepared in alumina sample holders, and for Manuscript III the high entropy powders were dispersed in ethanol and deposited on top of a Pt strip. The samples were measured with 25 °C intervals, during heating to 550/700/725 °C for undoped, Ti-doped, and high entropy samples, respectively, then during cooling to 50 °C, and finally during re-heating to 550/700/725 °C, respectively. The measurement program is illustrated in Figure 3.2. The measurements were first performed in O_2 atmosphere, and then afterwards repeated in N_2 atmosphere for all samples. Pawley refinement of lattice parameters was done using the Bruker AXS TOPAS 5 software,[139] and by running TOPAS 5 in launch mode using Python with Jupyter Notebook.

3.2.2 *In situ* high temperature XRD (HT-XRD)

The kinetics of oxidation was studied using HT-XRD with *in situ* switching of atmosphere at the BM31 beamline of the Swiss-Norwegian Beamlines (SNBL) at the European Synchrotron Radiation Facility (ESRF) in Grenoble, France. A few milligrams of nanocrystalline powder were placed in a capillary, with quartz wool plugs on each side to keep the powder in place. The full setup is shown in Figure 3.3. Each measurement was done using a gas flow of 10 $\mathrm{mL\,min^{-1}}$, confirmed

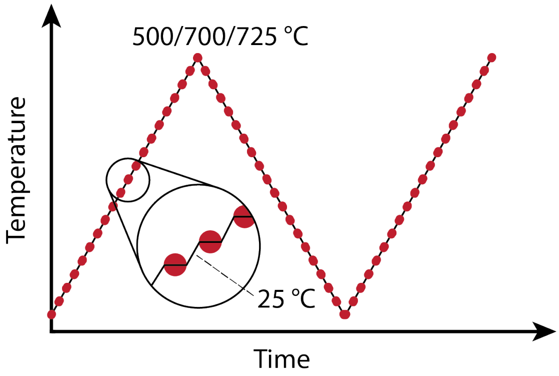

Figure 3.2: The measurement program used for the high temperature X-ray diffraction study of lattice parameter changes in O_2 and N_2 atmospheres. This program was repeated for each atmosphere.

by a Pfeiffer Vacuum Omnistar spectrometer. The diffraction measurements were performed with a wavelength of 0.338591 Å, using a Dexela 2923 area detector. The samples were first heated to 500 °C in N_2 to remove as much excess oxygen from the sample as possible, before lowering the temperature to the experiment temperature. Measurements were started in N_2 atmosphere before switching to O_2 to investigate the structural changes as the materials oxidized. The scans were continued until the samples equilibrated in the oxidized state, or after a maximum of 30 min. The measurement program for one such measurement is illustrated in Figure 3.4. This was repeated for all measurement temperatures, which were determined on a sample-to-sample basis. The samples were re-heated to 500 °C in N_2 atmosphere in between each measurement. Pawley refinement of lattice parameters was done using the Bruker AXS TOPAS 5 software in launch mode.

3.2.3 Thermogravimetric analysis (TGA)

The changes in oxygen stoichiometry with temperature in O_2 atmosphere was measured using thermogravimetric analysis (TGA). 30-60 mg of each sample was added to an alumina DSC or TG sample holder, and measured using a Netzsch STA 449 Jupiter instrument with 30 $\mathrm{mL\,min^{-1}}$ gas flow. To determine the amount of excess oxygen, δ, present in the materials, a reference point where all Mn was assumed to be found as Mn^{3+} was chosen at $T > 700$ °C. This corresponds to $\delta = 0$ and $\delta = 0.075$ for undoped and Ti-doped samples, respectively.

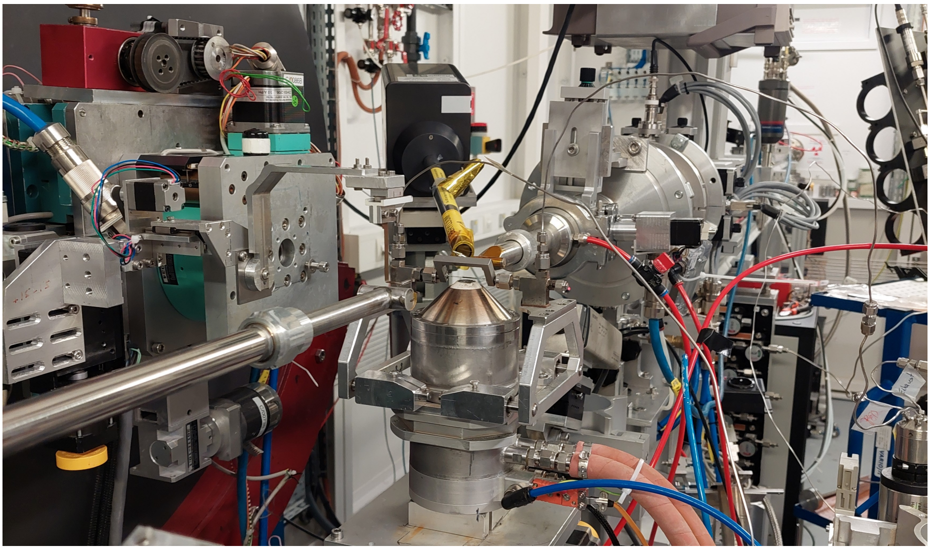

Figure 3.3: HT-XRD setup at the SNBL-ESRF synchrotron, with the capillary containing the sample being in the middle of the image.

For the measurements in Manuscript I, the samples were first quickly heated to 800 °C and subsequently cooled to 50 °C using heating and cooling rates of 20 °C/min to remove any excess oxygen, and then slowly heated to 800 °C using heating and cooling rates of 1 $°\mathrm{C\,min^{-1}}$. The $DyMn_{0.85}Ti_{0.15}O_3$ (DMTO30) sample was heat treated at 600 °C in N_2 atmosphere for 10 h prior to the measurement to remove excess oxygen, and then measured with TGA in O_2 using a heating and cooling rate of 10 $°\mathrm{C\,min^{-1}}$, due to its quick oxidation rate. For the measurements in Manuscript II, where the kinetics of oxidation was investigated, the samples were first heat treated at 600 °C in N_2 atmosphere for 10 h to remove excess oxygen. Afterwards, the samples were measured with TGA in O_2 by heating to 800 °C using heating and cooling rates of 5, 10, and 20 $°\mathrm{C\,min^{-1}}$. In Manuscript III, the bulk high entropy samples and nanocrystalline high entropy samples HEO3-HEO5 were quickly heated and cooled in O_2 prior to measurements, while nanocrystalline high entropy HEO1-n and HEO2-n samples were heat treated in N_2 before each measurement. The different measurements are summarized in Table 3.3.

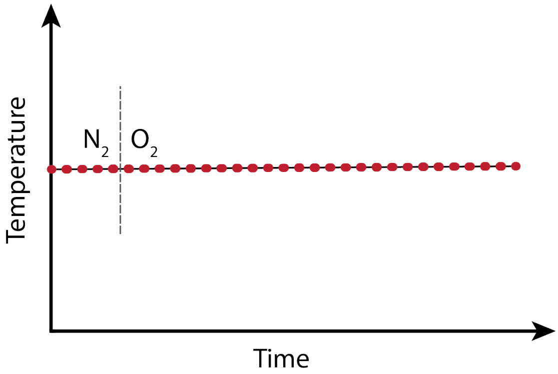

Figure 3.4: The measurement program used for one of the high temperature X-ray diffraction studies of the kinetics of oxidation, with *in situ* changes of atmosphere from N_2 to O_2. This program was repeated for each measurement temperature.

3.2.4 Scanning electron microscopy (SEM)

Scanning electron microscopy (SEM) was used to investigate the density and morphology of the samples, using a Hitachi S-3400 N scanning electron microscope, with a secondary electron detector, 5-15 kV voltage, and 40 nA probe current. Powder samples were placed on top of carbon tape, while dense samples were mounted on a sample holder. To determine the film thickness of the asymmetric membranes, the membranes were broken in half by hand, and the fracture surface was examined.

3.2.5 Transmission electron microscopy (TEM)

Transmission electron microscopy (TEM) was used to investigate the morphology of the powders, using an aberration-corrected Jeol JEM ARM220F equipped with a cold field emission gun (FEG) operated at 200 kV. Bright-field (BF) TEM and scanning TEM (STEM) images were acquired, with the latter using a beam semi-convergence angle of 27 mrad and collection angles of 67-155 mrads.

3.2.6 Determination of oxidation state of Mn

Oxygen stoichiometry found through TGA is estimated by assuming that all Mn is found as Mn^{3+} at higher temperatures, resulting in $\delta = 0$ and $\delta = 0.075$ for un-

Table 3.3: Overview of the thermogravimetric measurements performed in each of the works included in this thesis.

Manuscript	Sample	Rate (°C min^{-1})	Removal of oxygen: Quick heating/ cooling in O_2	Removal of oxygen: Heated in N_2
I	YMO29	1	x	
	YMO39	1	x	
	YMTO21	1	x	
	HMO25	1	x	
	HMO38	1	x	
	HMTO28	1	x	
	DMO30	1	x	
	DMTO30	10		x
II	$HoMnO_3$	5/10/20		x
	$DyMnO_3$	5/10/20		x
	$HoMn_{0.85}Ti_{0.15}O_3$	5/10/20		x
	$DyMn_{0.85}Ti_{0.15}O_3$	5/10/20		x
III	HEO2-b	5	x	
	HEO5-b	5	x	
	HEO1-n	5/10/20		x
	HEO2-n	5/10/20		x
	HEO3-n	5/10/20	x	
	HEO4-n	5/10/20	x	
	HEO5-n	5/10/20	x	

doped and Ti^{4+} doped samples respectively. As the Ti^{4+} doped samples did not reach equilibrium in oxygen content at the maximum measurement temperature, there is some uncertainty in the estimated values. One way to determine the oxygen stoichiometry is by determining the oxidation state of Mn, as these two are closely linked. Fully oxidized nanocrystalline powders were therefore examined using X-ray absorption near-edge structure (XANES), electron energy loss spectroscopy (EELS), and by permanganate back titration.

X-ray absorption near-edge structure (XANES)

X-ray absorption near-edge structure (XANES) measurements were performed at the BM31 beamline of the Swiss-Norwegian Beamlines (SNBL) at the European

Synchrotron Radiation Fascility (ESRF) in Grenoble, France. Samples were prepared in capillaries using the same method as for the *in situ* HT-XRD measurements described in Section 3.2.2. The absorption measurements were performed using a wavelength of 0.338591 Å and a Hitaxi Vortex single-element silicon drift detector. Due to the heavy rare earth elements attenuating the signal, causing transmission for Mn to be weak, the measurements were done in fluorescence mode. XANES measurements were performed on samples before and after oxidation, and during oxidation of the sample after *in situ* switching of atmosphere from N_2 to O_2. The measurements were normalized using Larch,[140] and the absorption edges were fitted to Mn_2O_3 and MnO_2 references using SciPy.[141]

The calculated oxidation states of manganese before and after oxidation determined from absorption edge fitting are listed in Table 3.4. Most of the calculated Mn oxidation states after oxidation do not correspond to the oxygen contents found through TGA, and exceed the theoretical maximum oxidation value of $\delta = 0.33$, corresponding to an oxidation state of 3.67. The calculated values were therefore not used further due to XANES being less reliable and robust compared to TGA. These high values may be a result of the Mn_2O_3 and MnO_2 references having Mn in an octahedral environment[142] while Mn is found in 5 coordinated trigonal bipyramids in RMnO$_3$, which can affect the position of the Mn K-edge. In addition, the rare earth cations might have an inductive effect on the structure which can cause changes in the Mn-O bond lengths, and shift the position of the Mn K-edge of the RMnO$_3$ samples compared to the Mn references.[143–145]

Electron energy loss spectroscopy (EELS)

STEM electron energy loss spectroscopy (STEM-EELS) was performed using a Quantum GIF with DualEELS with a beam current of about 400 pA. The beam semi-convergence angle was 27 mrad, while the semi-collected angle into the GIF was 67 mrad. To obtain EEL spectra from thin regions of the specimens, areas between 65 and 630 nm^2 were scanned with varying step size, but the same pixel time of 0.1 s (0.09999 s for high-loss and 9.999 e-6 s for low-loss), to obtain maps which had a total scan time of about 3.5 min. The energy dispersion was 0.25 eV/ch. Data analysis was performed with HyperSpy,[146] which was used to fit and remove the background of the Mn $L_{2,3}$ edges before plotting.

The position of the Mn$L_{2,3}$ edges are shown in Figure 3.5 for $HoMnO_3$, $HoMn_{0.85}Ti_{0.15}O_3$, $DyMnO_3$ and $DyMn_{0.85}Ti_{0.15}O_3$, with the peak maximum

Table 3.4: Oxidation states of Mn in $HoMnO_3$, $HoMn_{0.85}Ti_{0.15}O_3$, $DyMnO_3$, and $DyMn_{0.85}Ti_{0.15}O_3$ in N_2 and O_2 atmospheres at a given temperature, calculated from fitting XANES absorption edges to Mn_2O_3 and MnO_2 references.

T (°C)	Gas	$HoMnO_3$	$HoMn_{0.85}Ti_{0.15}O_3$	$DyMnO_3$	$DyMn_{0.85}Ti_{0.15}O_3$
200	N_2				3.55
	O_2				3.99
225	N_2				3.47
	O_2				4.03
250	N_2	3.28	3.26		3.43
	O_2	3.87	3.92		4.06
275	N_2	3.27			3.45
	O_2	3.68			4.00
300	N_2	3.24	3.03	2.72	3.15
	O_2	3.45	3.83	3.17	4.00
312	N_2			3.01	
	O_2			3.36	
325	N_2			2.98	3.46
	O_2			3.37	3.94
337	N_2			2.98	
	O_2			3.32	
350	N_2		3.25	2.96	3.39
	O_2		3.67	3.19	3.85

of the Mn L_3 edge found at 640 eV or lower for all samples, and that of Mn L_2 found at just above 650 eV. When comparing the measured energy position of the Mn $L_{2,3}$ edges with literature data for different oxidation states of Mn (Figure 3.6), it is clear that the Mn $L_{2,3}$ energy positions are similar to those reported for Mn^{2+}, indicating that the originally oxidized samples become reduced in the TEM due to the electron beam used for STEM-EELS, combined with the sample being under vacuum. The method was therefore deemed unfit for determining the oxidation state of oxidized samples.

Titration

The permanganate back titration method was based on that reported by Žužić and Macan[148] for manganese perovskites. In this method, Fe^{2+} in the Mohr's salt ($Fe(NH_4)_2(SO_4)_2$) solution is oxidized when mixing with Mn^{3+} and Mn^{4+} in the

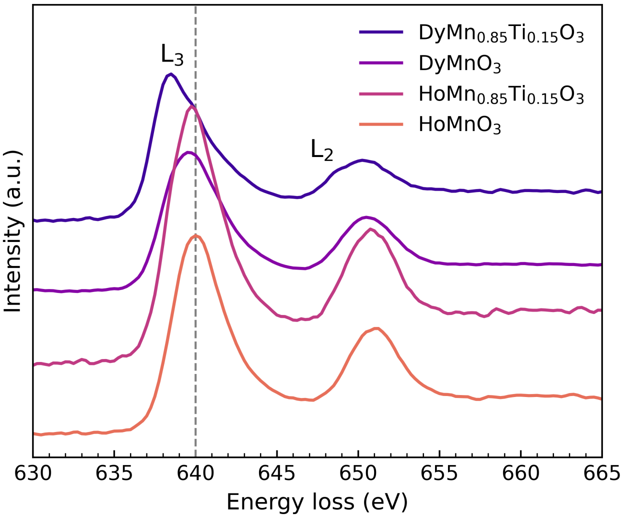

Figure 3.5: Comparison of the EELS Mn $L_{2,3}$ peaks of $HoMnO_3$, $HoMn_{0.85}Ti_{0.15}O_3$, $DyMnO_3$ and $DyMn_{0.85}Ti_{0.15}O_3$.

dissolved sample, in accordance with eq. 3.1 and 3.2, respectively.

$$Mn^{4+} + 2Fe^{2+} \rightarrow Mn^{2+} + 2Fe^{3+} \tag{3.1}$$

$$Mn^{3+} + Fe^{2+} \rightarrow Mn^{2+} + Fe^{3+} \tag{3.2}$$

The amount of unreacted Fe^{2+} in the solution can then be determined by titration with $KMnO_4$, as MnO^{4-} will oxidize Fe^{2+} to Fe^{3+}, shown in eq. 3.3.

$$MnO^{4-} + 5Fe^{2+} + 8H^{+} \rightarrow Mn^{2+} + 3Fe^{3+} + 4H_2O \tag{3.3}$$

For the undoped samples, 15 mg of powder was added to a 50 mL Erlenmeyer flask, together with 15 mL 0.5 M H_2SO_4, 10 mL 0.1 M H_3PO_4, and 10 mL 0.05 M Mohr's salt solution. The Erlenmeyer flask was covered with parafilm to avoid evaporation. The mixture was stirred on a magnetic stirring plate until it was completely dissolved. The undoped samples dissolved within 48 hours, which is twice as long

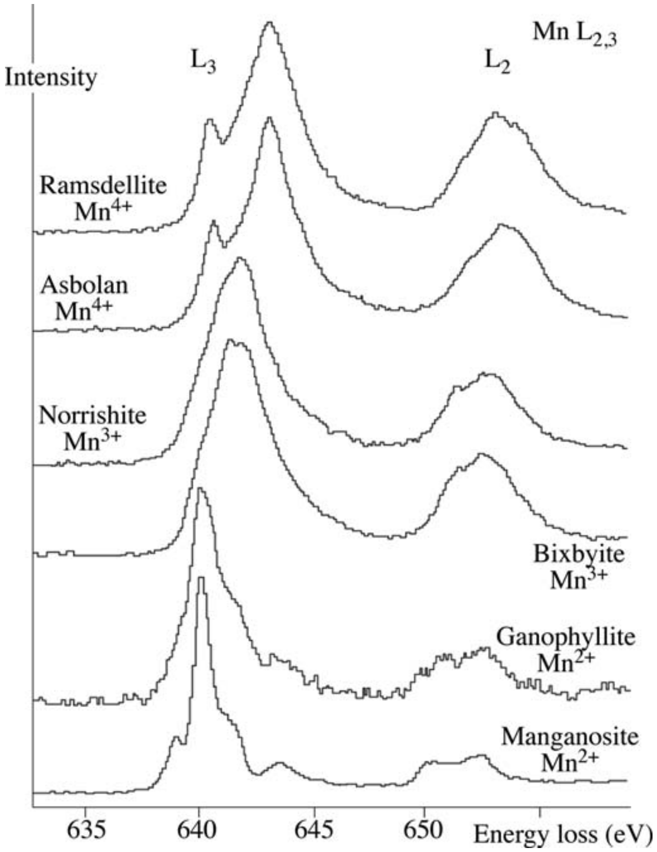

Figure 3.6: Comparison of the EELS Mn $L_{2,3}$ peaks for different minerals and Mn oxidation states. Reprinted from Williams and Carter[147] with permission from Springer Nature.

as what was reported by Žužić and Macan for perovskites. The samples containing Ti^{4+} did not dissolve within 48 hours, and later parallels were therefore stirred on a heating pad set to 80 °C over night, which sped up the dissolution process. This was also done for the later parallels of the undoped samples, which then dissolved within 1-2 hours, as the original dissolution time of 48 hours was believed to affect the accuracy of the measurement. The solution containing the dissolved sample was then titrated using a 0.02 M $KMnO_4$ solution until the titrand changed color permanently. The method is illustrated in Figure 3.7. Prior to titration, the concentration of the potassium permanganate solution was determined by titration

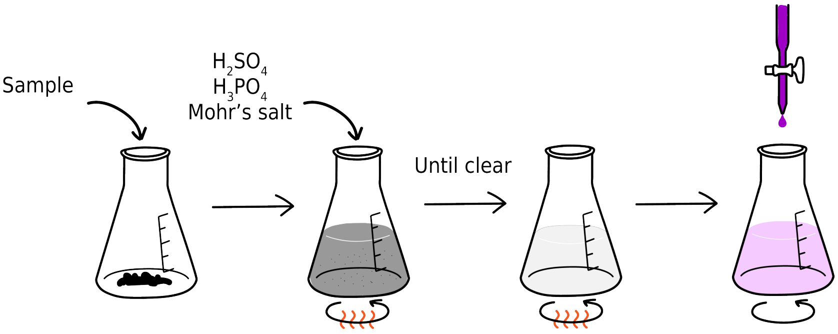

Figure 3.7: Schematic of the permanganate back titration method.

using the Mohr's salt solution. For increased accuracy, the measurement was performed on three parallels of each sample, and, for some samples, repeated for new sets of parallels. For Ti containing samples, the determined oxygen content δ was calculated using a modified eq. 3.3 with the added Ti^{4+} taken into account.

The oxygen stoichiometries found from the average manganese oxidation states determined by titration are presented in Figure 3.8. As the measurements showed low accuracy, with large variations both between parallels within the same measurement round and between measurement rounds, and large deviations from the oxygen stoichiometry found from TGA, titration was deemed unsuitable for these samples. We believe that the long dissolution time for hexagonal manganites cause some of the excess Fe^{2+} in the solutions to oxidize to Fe^{3+}, resulting in the determined oxidation state of Mn being too high, giving unreliable results.

As none of the methods described here could accurately determine the oxidation state of Mn^{3+}, the calculations of δ from TGA results were therefore still based on assumptions of the oxidation state of Mn at higher temperatures. This means that the oxygen stoichiometries from TGA presented in this work are not perfectly accurate, especially for samples containing Ti^{4+} and Tb, but should still give a good indication of the oxygen storage capacity, and the differences and trends between the different samples.

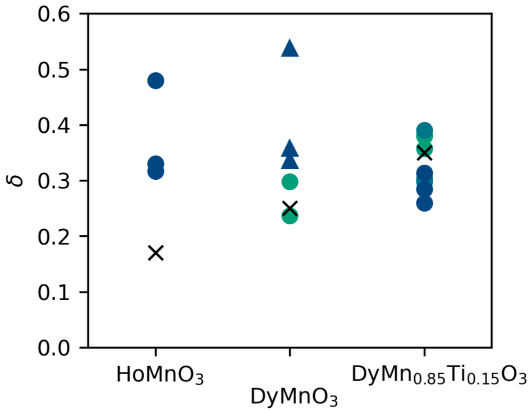

Figure 3.8: Summary of the oxygen stoichiometries determined through permanganate back titration. Triangles (△) indicate measurements done on samples that were dissolved without heating, round markers (o) are measurements done on samples dissolved using heating, the different colors of markers indicate different sets of measurements on the same sample, and crossed markers (x) indicate oxygen stoichiometry determined from TGA.

3.3 Asymmetric membrane

3.3.1 Suspension

The suspension used for spray coating was a mixture of ethanol, and nanocrystalline $[Ho_{0.98}In_{0.02}]_{0.97}Mn_{0.85}Ti_{0.15}O_3$ powder made through the citric acid synthesis method described in Section 3.1.1. The addition of In and the slight deficit on the R site was used to improve the density of the final thin film, as both promote sintering of the ceramic. The nanocrystalline powder was added to a small plastic bottle together with 96% ethanol, with solid loads ranging from 0.3 to 0.6 vol%. 40 % of the bottle was then filled with yttrium-stabilized zirconia milling balls (Ø 5 mm). The suspension was ball milled for 24 hours at a speed of 205 rpm in order to break up any agglomerates in the powder. The suspension was transferred to a tall glass sample bottle together with Dolacol D 1003 acting as a surfactant, and was sonicated using an ultrasonic needle for 15 minutes at 30 % amplitude to improve the stability of the slurry by further breaking up any soft agglomerates. The top of the bottle was covered with aluminium foil to reduce evaporation of ethanol during sonication.

3.3.2 Spray coating

Spray coating the film on the porous $Y_{1.05}Mn_{0.85}Ti_{0.15}O_3$ substrates, made through the method described in Section 3.1.3, was done using a Cocraft Airbrush on the first set of samples, and later with an Aztec spray coater with a 0.7 µm nozzle, both with an air pressure of 0.5 bar. Spray coating was chosen as the deposition method, as previous work on other methods such as dip coating and drop casting resulted in poor films.[149–152] Before coating, the substrates were heated on a heating plate set to 200 °C. 0.5 mL of the suspension was added with a pipette to the ink container on the spray coater at the time. Only the supernatant of the suspension was used, as the larger particles in the suspensions settled at the bottom of the glass bottle. When spray coating, the substrates were put on aluminium foil on top of a heating plate set to 60 °C. For each deposited layer, spraying was started off the side of the substrate, before spraying over the substrate and off on the other side. Each layer was left to dry before a new one was deposited. This process was repeated until a specific volume (2-18 mL) was deposited on each substrate, or, for later samples, for 70-100 layers, depending on the desired film thickness. For each 10th layer, the samples were rotated 90° to ensure full coverage of the film. The spray coating process is shown in Figure 3.9. To make sure the film was sufficiently dry, the samples were placed in a drying cabinet overnight. To investigate the effect of pressure on the density of the films, some samples were pressed using either a uniaxial pressing tool using 1 kN pressure, or by using a cold isostatic press with 10 kpsi pressure. The samples were calcined at 600 °C for 6 hours to remove the surfactant, and then sintered for 1 hour at 1300 or 1400 °C in air.

Figure 3.9: Spray coating of the suspension containing nanocrystalline $[Ho_{0.98}In_{0.02}]_{0.97}Mn_{0.85}Ti_{0.15}O_3$ powder on top of $Y_{1.05}Mn_{0.85}Ti_{0.15}O_3$ porous substrates.

4

Summary of results

Foreword

This chapter summarizes the main findings of the PhD work. The first three sections are dedicated to the main results from the manuscripts included in the thesis, while the last section contains a summary of the work on preparing a functioning asymmetric membrane prototype for oxygen separation. The full manuscripts can be found in the Appendix, and readers are encouraged to look to these for more information on the work summarized here.

All the separate works included in the thesis focus on improving the oxygen storage and release properties of hexagonal manganites, and evaluating them as possible new materials for air separation through CLAS or ceramic membranes. The three manuscripts investigate oxygen absorption in hexagonal manganites with different compositions and particle sizes, with the first manuscript looking at OSC and thermodynamics of oxidation of different compositions, the second investigating the kinetics of oxidation in similar materials, and the third looking at both OSC and kinetics of oxidation in high entropy compositions of hexagonal manganites.

4.1 Oxygen absorption and the effect of Ti^{4+} donor doping

The first manuscript focuses on oxygen absorption and thermodynamics of oxidation for undoped and Ti-doped $R\text{MnO}_{3+\delta}$, addressing R^{3+} cation size, the effect of aliovalent doping, and crystallite size. Ti^{4+} was chosen as a donor dopant on the Mn sublattice as it had been shown to increase the oxygen storage properties of $YMnO_3$.[104] Density functional theory (DTF) calculations and an ideal solid solution model were included to investigate the thermodynamic driving forces for oxidation.

Nanocrystalline $R\text{Mn}_{1\text{-x}}\text{Ti}_\text{x}\text{O}_{3+\delta}$ (R = Y, Ho, Dy; x = 0, 0.15) powders were prepared using the wet chemical synthesis method described in Section 3.1.1, with composition, naming, crystallite sizes and lattice parameters shown in Table 4.1. All compositions were found to be nanocrystalline, with crystallite sizes ranging from 25 to 39 nm. The oxygen storage capacity (OSC) from TGA (Figure 4.1) was found to increase with increasing ionic size of the R cation, from Y (0.96 Å, CN = 7)[109] through Ho (1.015 Å) to Dy (1.027 Å), as the larger R expands the lattice and impedes the electrostatic repulsion between O_i and planar oxygen, favoring oxygen absorption. We found that samples with smaller crystallites showed larger oxygen absorption capacity than those with larger crystallites, as the smaller size reduces the diffusion distance through the bulk of the sample. The addition of Ti^{4+} on the

Table 4.1: Composition, naming, and Pawley refined crystallite sizes and lattice parameters of as-prepared $R\text{Mn}_{1\text{-x}}\text{Ti}_\text{x}\text{O}_{3+\delta}$ compositions. All materials were refined within the $P6_3cm$ space group.

Composition	Sample name	Crystallite size (nm)	a (Å)	c (Å)
$YMnO_3$	YMO25	25 ± 1	6.141(4)	11.365(4)
$YMnO_3$	YMO39	39 ± 1	6.132(5)	11.351(5)
$YMn_{0.85}Ti_{0.15}O_3$	YMTO21	21 ± 1	6.194(4)	11.383(8)
$HoMnO_3$	HMO25	25 ± 1	6.131(0)	11.371(0)
$HoMnO_3$	HMO38	38 ± 1	6.130(1)	11.361(6)
$HoMn_{0.85}Ti_{0.15}O_3$	HMTO28	28 ± 1	6.141(8)	11.400(0)
$DyMnO_3$	DMO30	30 ± 1	6.162(3)	11.368(8)
$DyMn_{0.85}Ti_{0.15}O_3$	DMTO30	30 ± 1	6.199(3)	11.433(3)

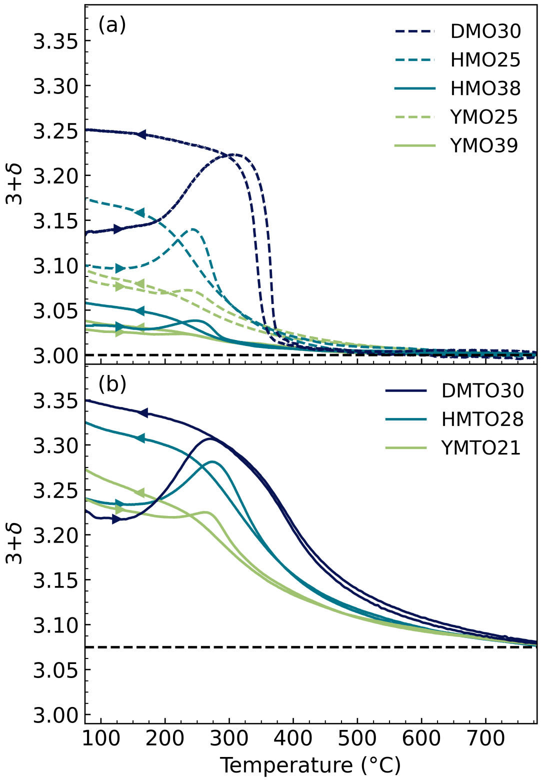

Figure 4.1: Changes in oxygen stoichiometry measured using thermogravimetric analysis (TGA) during heating and cooling in O_2 for hexagonal RMnO$_{3+\delta}$ (R = Y, Ho, Dy) with different crystallite sizes, and with (a) 0 % and (b) 15 % Ti donor doping.

Mn site increased the overall oxygen absorption, as Ti^{4+} is charge compensated by additional O_i in oxygen rich atmospheres, following eq. 2.5, and due to expansion of the *ab* plane. In addition, Ti^{4+} increased the thermal stability of interstitial oxygen, enabling oxygen absorption at higher temperatures where the oxidation kinetics are faster.

The materials were studied using high temperature X-ray diffraction at different temperatures in both O_2 and N_2 atmospheres (Figure 4.2) to investigate the changes in the crystal lattice during oxidation. All samples showed large changes in both the a and c parameters at T < 300 °C in O_2 due to chemical expansion in the

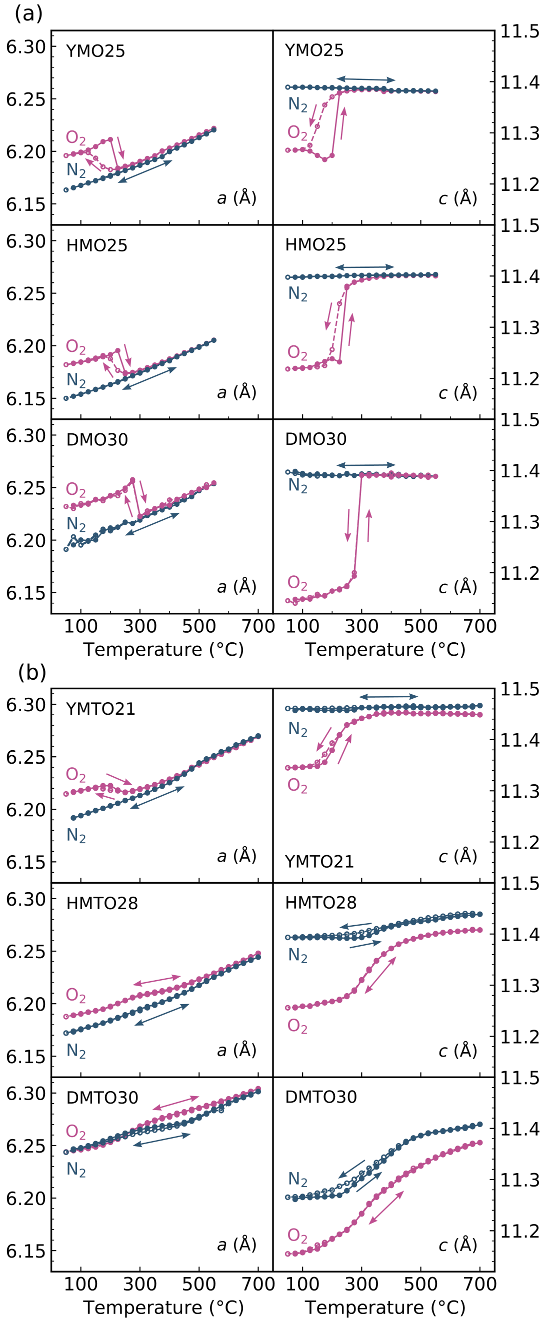

Figure 4.2: Refined lattice parameters as a function of temperature for (a) undoped and (b) Ti-doped $R\mathrm{MnO}_{3+\delta}$ (R = Y, Ho, Dy) in O_2 and N_2 atmosphere.

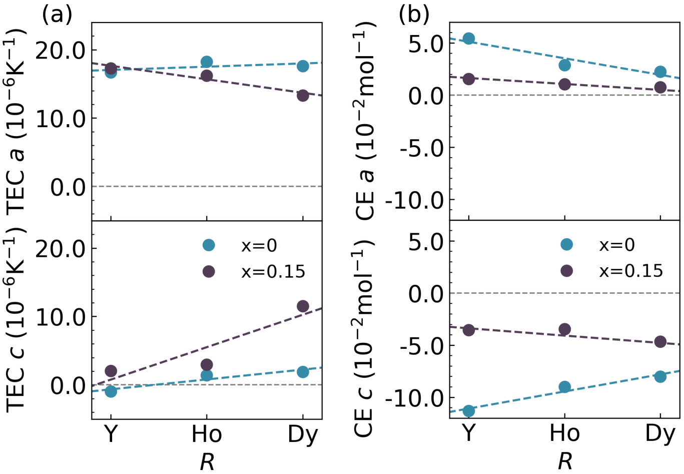

Figure 4.3: Thermal expansion coefficients (TEC) and chemical expansion (CE) for $R\mathrm{Mn}_{1\text{-}x}\mathrm{Ti}_x\mathrm{O}_3$ compositions, inferred from lattice parameter changes.

ab-plane and contraction along the *c* axis as O_i enters the Mn-O triangular lattice. As interstitial oxygen is stabilized towards higher temperatures for Ti-doped materials, the temperature interval of oxygen release during heating is broader than for undoped materials. The thermal and chemical expansion inferred from the lattice parameters in Figure 4.2 is summarized in Figure 4.3, showing a decrease in anisotropy in chemical expansion with larger *R* and added Ti^{4+}. For larger R^{3+}, this is caused by the *ab*-plane already being expanded prior to oxidation by the increase in ionic radii. In the case of the added dopant, the *ab*-plane is expanded due to Ti^{4+} causing a partial rectification of the tilted MnO_5 bipyramids.[76,104] For $DyMn_{0.85}Ti_{0.15}O_3$, which has the largest *a* parameter pre-oxidation due to both *R* cation size and the added dopant, there was close to no chemical expansion occurring during oxidation at lower temperatures (Figure 4.2). This may be due to the smaller radius of Mn^{4+} (0.46 Å, CN = 5, interpolated from CN = 4, 6)[109] compared to Mn^{3+} (0.58 Å) countering the expansion that occurs when adding O^{2-} to the lattice.

Density Functional Theory (DFT) calculated lattice parameters, chemical expansion, formation energy of interstitial oxygen, and enthalpy of oxidation for *R* = Y, Dy-Er are shown in Figure 4.4. These calculations support the trends in lattice parameters and chemical expansion during oxidation observed experimentally for

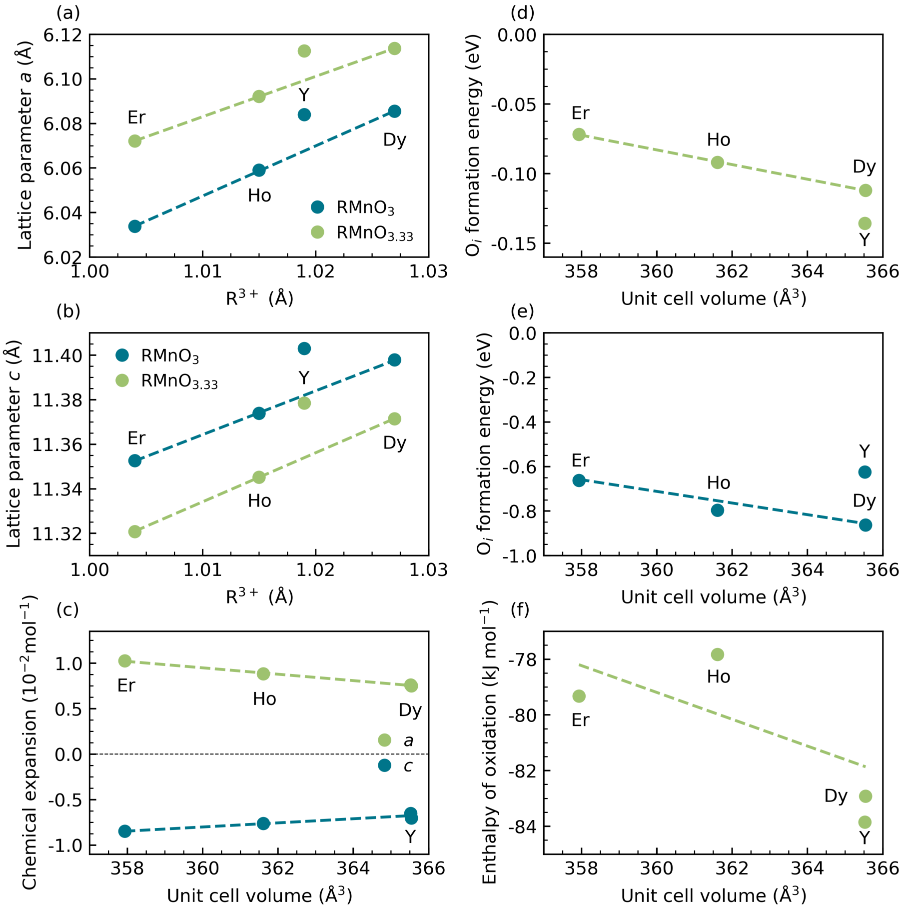

Figure 4.4: (a-b) Lattice parameters of $R\mathrm{MnO}_3$ and $R\mathrm{MnO}_{3.33}$ ($R_6\mathrm{Mn}_6\mathrm{O}_{20}$) as a function of R^{3+} Shannon radius calculated from Density Functional Theory (DFT). (c) Chemical expansion as a function of DFT relaxed stoichiometric unit cell volume. Formation enthalpy for a single O_i point defect in a charge neutral 120-atom supercell for (d) undoped and (e) Ti-doped materials. (f) Enthalpy of oxidation per O_2 molecule for the undoped $R\mathrm{MnO}_3$ from the reaction $R_6\mathrm{Mn}_6\mathrm{O}_{18} + \mathrm{O}_2\ (\mathrm{g}) = R_6\mathrm{Mn}_6\mathrm{O}_{20}$. Dashed lines are guides to the eye connecting Er, Ho and Dy data points.

R = Dy and Ho. There was also a correlation between the thermodynamic driving force for oxidation and R and Ti doping, as the formation energy for O_i became more negative with increasing R cation size, and, especially, for Ti-doped materials. As Y is a 4*d* element instead of 4*f*, it does not follow the same trends as the DFT calculated values for other R.

To discuss the thermodynamics of initial oxidation in hexagonal manganites, we used an ideal solid solution model, based on the model developed by Bakken *et al.*[153], for formation of vacancies in a perovskite. By assuming a maximum oxidation state of $\delta = 0.33$, the oxidation from $R\mathrm{MnO}_3$ to $R\mathrm{MnO}_{3.33}$ can be described by eq. 4.1:

$$2R_3\mathrm{Mn}_3{}^{3+}\mathrm{O}_9 + \mathrm{O}_2(g) \rightleftharpoons 2R_3\mathrm{Mn}^{3+}\mathrm{Mn}_2{}^{4+}\mathrm{O}_{10} \tag{4.1}$$

This oxidation reaction can be regarded as analogous to the oxidation of brownmillerite ($\mathrm{ABO}_{2.5}$) to perovskite ($\mathrm{ABO}_{3.0}$). By assuming an ideal solution with no defect-defect interaction, the partial pressure of oxygen can be described as a function of δ, $\Delta_{ox}H^0$, and $\Delta_{ox}S^0$. The ideal solid solution model is plotted for variable enthalpies and entropies of oxidation (Figure 4.5), with the ranges of values chosen from experimental work on perovskites.[45,118,153]. The model show that increasingly negative $\Delta_{ox}H^0$ increase the thermal stability of interstitial oxygen, while increasingly negative $\Delta_{ox}S^0$ narrow the temperature interval where oxygen absorption/desorption occurs. This model was fitted to the TG data measured during cooling in O_2 atmosphere (Figure 4.1), with the fitted entropy and enthalpy of oxidation for each sample given in Table 4.2. The model fit the data well at higher temperatures, where all materials are in equilibrium, but show deviations at lower temperatures ($T < 350$ °C), were ergodicity is broken. As the model assumes that full oxidation ($\delta = 0.33$) is reached at lower temperatures, the deviation is larger for the undoped materials which all display less oxygen absorption (Figure 4.1). The enthalpy and entropy values increase with increasing R cation size, following the same trends as the DFT calculations in Figure 4.4. The fitted values of $\Delta_{ox}H^0$ and $\Delta_{ox}S^0$ for undoped and Ti-doped YMnO_3 and HoMnO_3 were comparable to reported thermodynamic data for perovskites[45,118,154,155]. For DyMnO_3, the fitted values are unphysically large, showing that an ideal solution model cannot describe the narrow temperature interval for oxygen absorption/release in DyMnO_3 (Figure 4.1). We hypothesize that this can be explained by the model not accounting for defect-defect interactions, the changes in diffusion kinetics with temperature, and possibly also collective ionic motion. As an initial oxidation will expand the ab-plane due to the addition of O_i, which then can facilitate further oxidation, it can be argued that $\Delta_{ox}H^0$ is dependent on δ. At higher concentrations of O_i, the inter-

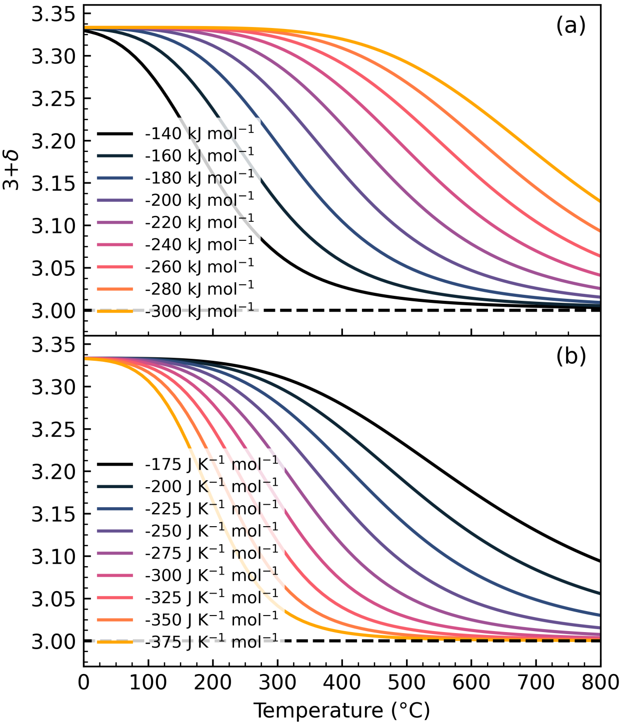

Figure 4.5: Temperature dependent oxygen stoichiometry in $R\mathrm{MnO}_{3+\delta}$ in pure O_2 atmosphere from the ideal solid solution model with (a) variable $\Delta_{ox}H^0$ with $\Delta_{ox}S^0$ fixed to -250 $\mathrm{J\,K^{-1}\,mol^{-1}}$ and (b) variable $\Delta_{ox}S^0$ with $\Delta_{ox}H^0$ fixed to -200 $\mathrm{kJ\,mol^{-1}}$.

actions between defects may also affect the enthalpy of oxidation.

Table 4.2: Entropy ($\Delta_{ox}S^0$) and enthalpy ($\Delta_{ox}H^0$) of oxidation of $R\mathrm{Mn}_{1\text{-x}}\mathrm{Ti}_{\mathrm{x}}\mathrm{O}_{3+\delta}$ (R = Y, Ho, Dy) used for fitting the ideal solid solution model to the experimental TG data (Figure 4.1).

Composition	Sample name	$\Delta_{ox}S^0$ ($\mathrm{J\,K^{-1}\,mol^{-1}}$)	$\Delta_{ox}H^0$ ($\mathrm{kJ\,mol^{-1}}$)
$YMnO_3$	YMO25	-200	-97.5
$HoMnO_3$	HMO25	-290	-160
$DyMnO_3$	DMO30	-2400	-1485
$YMn_{0.85}Ti_{0.15}O_3$	YMTO21	-195	-135
$HoMn_{0.85}Ti_{0.15}O_3$	HMTO28	-315	-225
$DyMn_{0.85}Ti_{0.15}O_3$	DMTO30	-400	-310

4.2 Kinetics of oxidation in h-$R\mathrm{Mn}_{1\text{-x}}\mathrm{Ti}_{\mathrm{x}}\mathrm{O}_3$ (R = Ho, Dy)

The main focus of the second manuscript was the kinetics of oxidation in $R\mathrm{MnO}_3$ (R = Ho, Dy). Hexagonal manganites have been reported to display slow oxidation kinetics,[99] which limits the OSC that can be utilized in cyclic oxidation and reduction processes. As the reduction kinetics are faster due to the reduction process occurring at higher temperatures than oxidation, improvement of the oxidation kinetics was the focus of this work. Results from previous work (Manuscript I,[101] summarized in Section 4.1) indicated that donor doping with Ti^{4+} had a positive impact on the oxidation kinetics, and this was further examined here. Thermogravimetric analysis (TGA) and high temperature X-ray diffraction (HT-XRD) with *in situ* changes in atmosphere was used to study the oxidation rate of the material, and the changes in lattice parameters where used to calculate surface exchange rates and activation energies of oxidation.

Nanocrystalline $R\mathrm{Mn}_{1\text{-x}}\mathrm{Ti}_{\mathrm{x}}\mathrm{O}_{3+\delta}$ (R = Ho, Dy; x = 0, 0.15) powders were synthesized using the citric acid synthesis method described in Section 3.1.1. For undoped comopsitions, the oxygen storage capacity (OSC) (Figure 4.6) was found to decrease with increasing heating and cooling rates, and a thermal hysteresis in oxygen content during heating and cooling was observed. Ti^{4+}-doped materials showed greatly enhanced kinetics compared to the undoped materials, with no thermal hysteresis in oxygen content, no loss of OSC during cooling with faster rates, and only a small decrease in OSC with faster heating rates. The same increase in oxidation kinetics for compositions containing Ti^{4+} was observed through HT-XRD measurements (Figure 4.7 and 4.8), where Ti-doped materials equilibrated significantly quicker in the oxidized state than undoped materials; $\mathrm{HoMn}_{0.85}\mathrm{Ti}_{0.15}\mathrm{O}_3$ and $\mathrm{DyMn}_{0.85}\mathrm{Ti}_{0.15}\mathrm{O}_3$ stabilized within 2 minutes at 300 °C, while DyMnO_3 needed over 15 minutes to oxidize at the same temperature. The oxidation rates were also quicker for R = Dy than R = Ho in the Ti-doped materials, indicating a relationship between kinetics and size of the rare earth element, corresponding well with what has been reported previously.[92]

As interstitial oxygen enters the Mn-O lattice, there is an expansion in the *ab*-plane and a contraction along the *c* axis, as can be observed from Figure 4.8. We hypothesize that the larger R^{3+} cations expand the *ab*-plane prior to oxidation, reducing the electrostatic repulsion between the interstitial oxygen entering the structure and planar oxygen atoms, promoting oxidation and improving the kinetics. As Ti^{4+} also expands the *ab*-plane by causing partial untilting of the MnO$_5$ trigonal bipyramids, Ti-doping will have similar effects on the kinetics as larger rare earths. The average *c*/*a* ratios of oxidized HoMnO$_3$, HoMn$_{0.85}$Ti$_{0.15}$O$_3$ and DyMn$_{0.85}$Ti$_{0.15}$O$_3$, shown in Figure 4.9, show that the trend in expansion of the *ab*-plane with larger R and the added Ti^{4+}, with the following decrease in *c*/*a*, follows the same trends as the observed oxidation kinetics. The untilting of the polyhedra, and the gradual transition towards the high symmetry $P6_3/mmc$, is also causing a partial melting of the K_3 mode. We argue that this may also affect the kinetics of the material positively, as the local ionic displacements are qualitatively similar to those occurring during the interstitial migration mechanism for interstitial oxygen.

The changes in lattice parameters during oxidation, specifically the contraction along the c axis, was used to to estimate the surface exchange rate k (Figure 4.10) through a model developed by Moreno *et al.*[156] The surface exchange rates

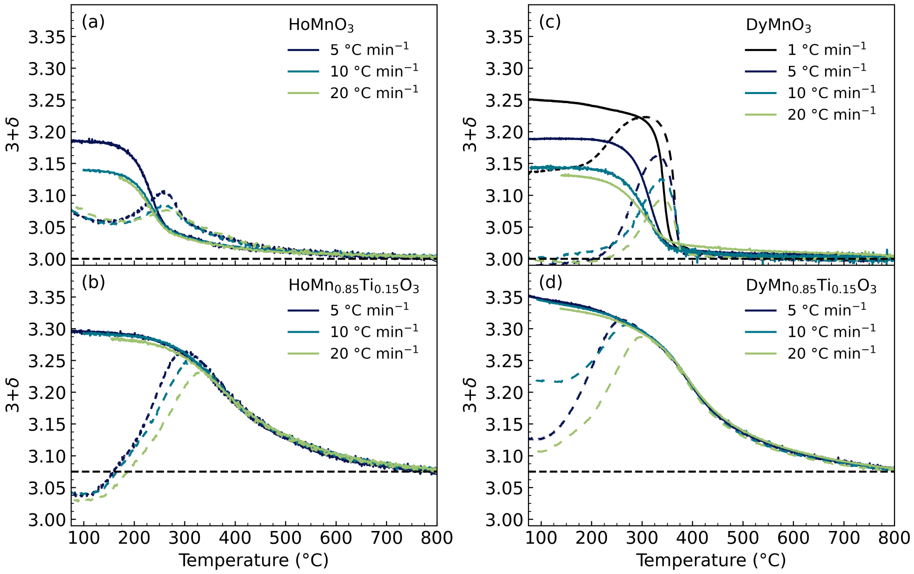

Figure 4.6: Changes in oxygen stoichiometry from thermogravimetry for (a) HoMnO$_3$, (b) HoMn$_{0.85}$Ti$_{0.15}$O$_3$, (c) DyMnO$_3$, and (d) DyMn$_{0.85}$Ti$_{0.15}$O$_3$, as a function of temperature measured during heating (dashed lines) and cooling (solid lines) in O$_2$ atmospheres, using different heating and cooling rates.

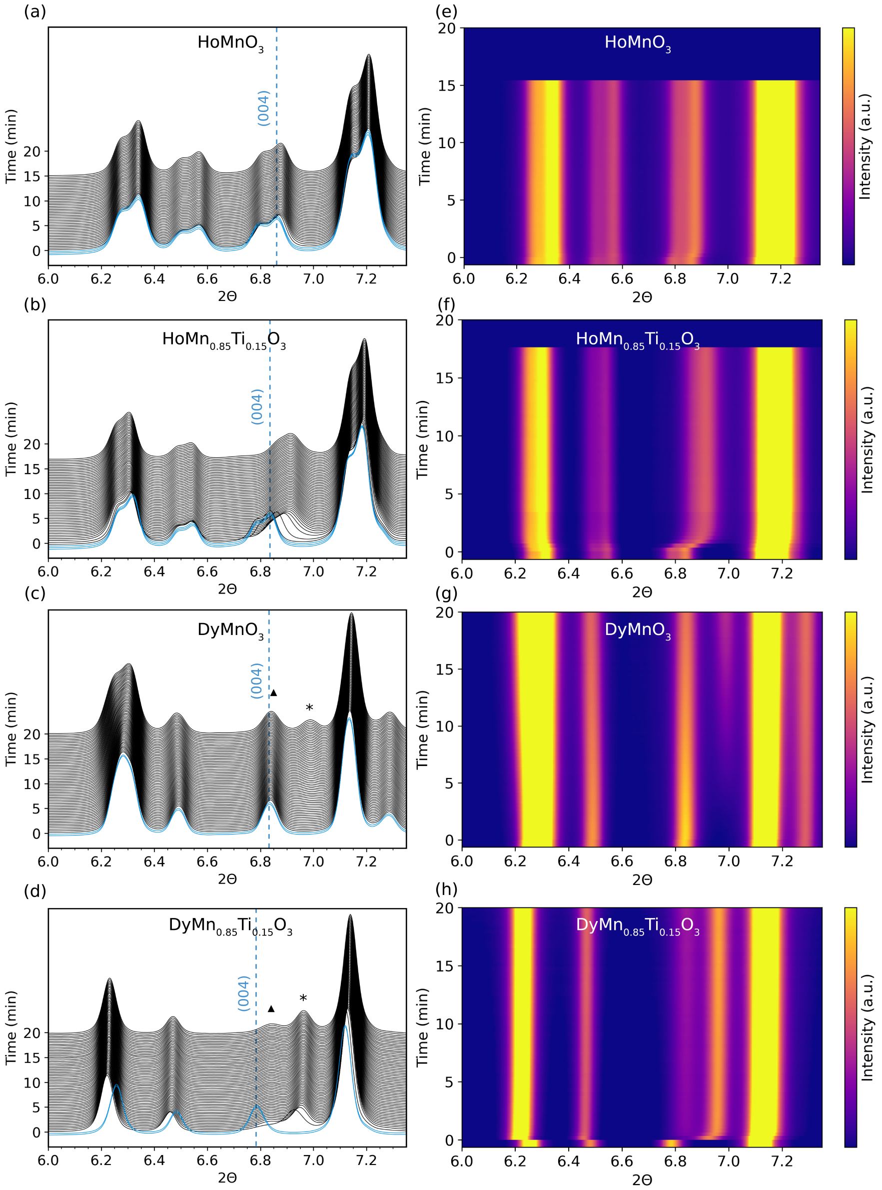

Figure 4.7: Time resolved high temperature X-ray diffractograms and 2D contour plots measured at 300 °C with *in situ* switching of atmosphere from N_2 to O_2 for (a),(e) $HoMnO_3$, (b),(f) $HoMn_{0.85}Ti_{0.15}O_3$, (c),(g) $DyMnO_3$, and (d),(h) $DyMn_{0.85}Ti_{0.15}O_3$. In (a)-(d), the blue diffractograms are measured in N_2 atmosphere, the vertical dashed lines indicate the position of the (0 0 4) reflection of $P6_3cm$ in N_2, and the baseline intensity at 6.0° 2θ indicate the time in min. after switching to O_2. Triangles (△) indicate the (1 0 10) reflection, and the asterisks (*) indicates the (0 0 12) reflection of $R3c$.

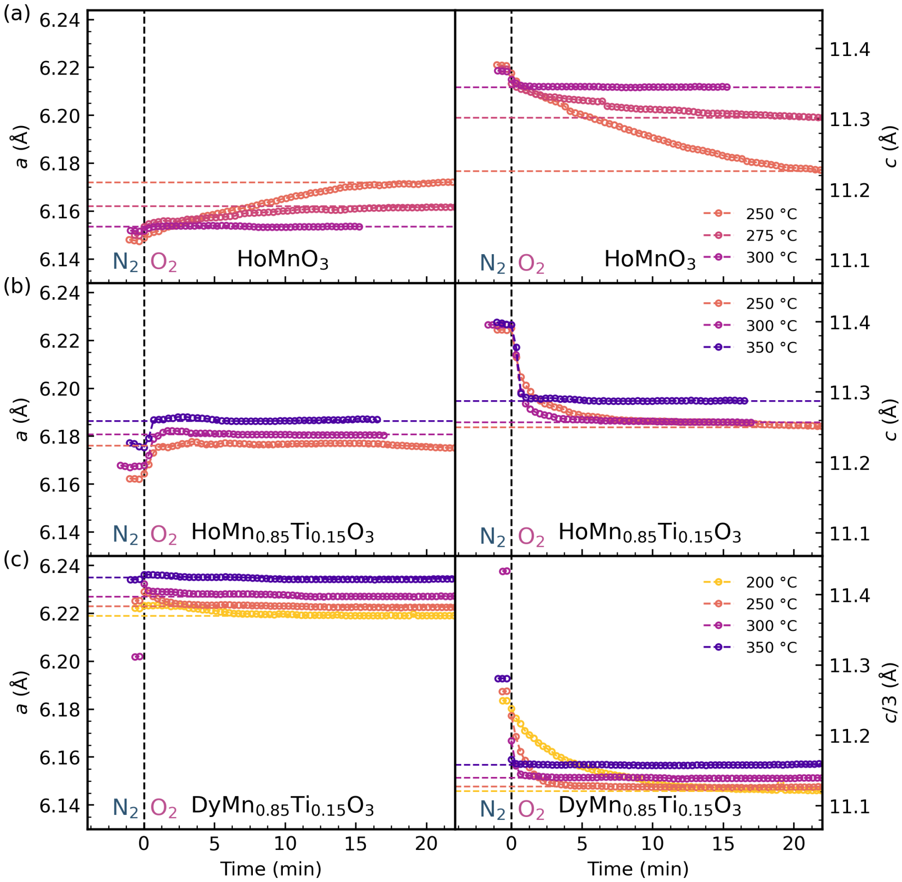

Figure 4.8: Refined lattice parameters for (a) HoMnO$_3$, (b) HoMn$_{0.85}$Ti$_{0.15}$O$_3$, and (c) DyMn$_{0.85}$Ti$_{0.15}$O$_3$ as a function of time after switching from N$_2$ to O$_2$ atmosphere at different temperatures. As the DyMn$_{0.85}$Ti$_{0.15}$O$_3$ sample was refined within the $R3c$ space group, the c parameter was divided by 3 for easier comparison.

were found to increase with increasing size of the rare earth cation, and with Ti^{4+} doping, with values comparable to those reported at significantly higher temperature in literature for perovskites and other oxides.[31,156–158] The activation energies calculated from the surface exchange rates were found to be 0.54 eV for HoMn$_{0.85}$Ti$_{0.15}$O$_3$ and 0.68 eV for DyMn$_{0.85}$Ti$_{0.15}$O$_3$. The activation energy for HoMnO$_3$ was not calculated, as using only two data points would result in a high

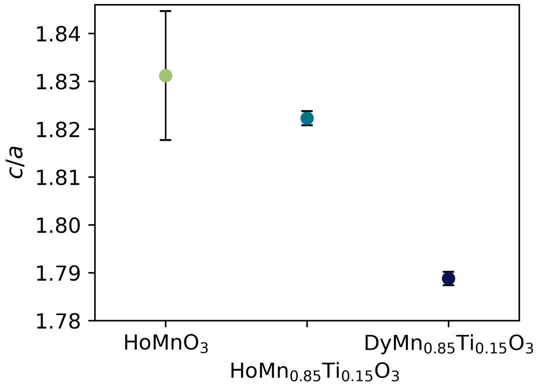

Figure 4.9: The average *c*/*a* ratios of oxidized $HoMnO_3$, $HoMn_{0.85}Ti_{0.15}O_3$ and $DyMn_{0.85}Ti_{0.15}O_3$.

uncertainty in the calculated value. The slightly higher activation energies for both Ti-doped materials compared to that of $HoMnO_3$ can be connected to the defect affinity between the dopant and interstitial oxygen. The electrostatic attraction between Ti^{4+} and the negatively charged O_i is significant enough to cause contraction in the *ab*-plane at higher concentrations of interstitial oxygen, which was observed for $DyMn_{0.85}Ti_{0.15}O_3$ during oxidation (Figure 4.8).

Finally, we argue that further work on hexagonal manganites for oxygen separation applications should focus on increasing the kinetics of oxidation in order to take advantage of the high OSC that has been reported for these materials so far.

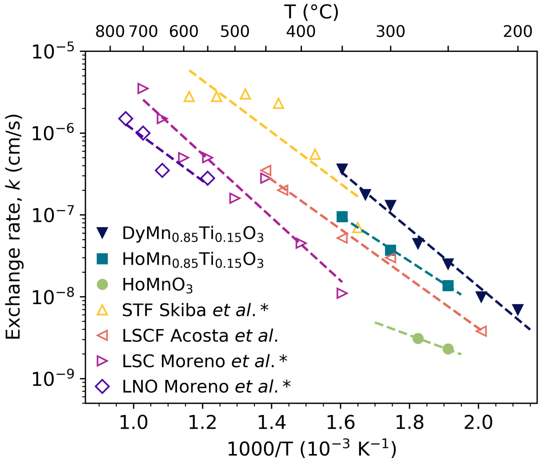

Figure 4.10: Surface exchange rates estimated from changes in lattice parameters during oxidation at different temperatures. Surface exchange rates for SrTi$_{0.65}$Fe$_{0.35}$O$_{2.825+\delta}$ from Skiba et al.,[159] (La$_{0.60}$Sr$_{0.40}$)$_{0.95}$(Co$_{0.20}$Fe$_{0.80}$)O$_{3\text{-}\delta}$ from Acosta et al.,[160] and La$_{0.6}$Sr$_{0.4}$CoO$_{3\text{-}\delta}$ and LaNiO$_{3\text{-}\delta}$ from Moreno et al.[158] are included for comparison purposes. Exchange rates marked with an asterisk (*) were measured using pO$_2$ = 0.21.

4.3 High entropy hexagonal manganites for fast oxygen absorption and release

The main focus of the third manuscript was to investigate the effects high entropy (HE) compositions have on the oxygen transport properties of hexagonal manganites. High entropy Li-ion conductive oxides have shown increased ionic conductivity compared to their low entropy counterparts, and this could possibly be true for other ionic conductors as well. In addition, high configurational entropy has been shown to promote formation of a single phase, even when including compounds that are not normally stable in that phase, which could help stabilize the hexagonal phase for larger rare earths and higher tolerance factors. Thermogravimetric analysis (TGA), X-ray absorption near-edge structure (XANES), and high temperature X-ray diffraction (HT-XRD) measured at constant temperature in both O_2 and N_2 atmosphere, and with *in situ* switching of atmospheres was used to study both the oxygen storage properties and the oxidation kinetics of several bulk and nanocrystalline high entropy hexagonal manganites, with compositions shown in Table 4.3.

Table 4.3: Overview of composition and naming of high entropy compositions used in this work.

Composition	Nano-crystalline	Bulk
$Y_{0.167}Gd_{0.167}Tb_{0.167}Dy_{0.167}Ho_{0.167}Er_{0.167}MnO_3$	HEO1-n	HEO1-b
$Y_{0.167}Gd_{0.167}Tb_{0.167}Dy_{0.167}Ho_{0.167}Er_{0.167}Mn_{0.85}Ti_{0.15}O_3$	HEO2-n	HEO2-b
$Y_{0.167}Gd_{0.233}Tb_{0.167}Dy_{0.167}Ho_{0.167}Er_{0.1}Mn_{0.85}Ti_{0.15}O_3$	HEO3-n	-
$Y_{0.145}Gd_{0.210}Tb_{0.190}Dy_{0.165}Ho_{0.155}Er_{0.135}Mn_{0.85}Ti_{0.15}O_3$	HEO4-n	-
$Y_{0.2}Gd_{0.2}Dy_{0.2}Ho_{0.2}Er_{0.2}Mn_{0.85}Ti_{0.15}O_3$	HEO5-n	HEO5-b

All nanocrystalline materials were synthesized as nanocrystalline powders through the citric acid synthesis method described in Section 3.1.1, and found to be phase pure within the $P6_3cm$ space group. This indicated that the high configurational entropy promotes stabilization of the hexagonal phase, as the tolerance factors for all of these materials ($0.859 \leq t_{HE} \leq 0.865$) are higher than the typically reported stability limit for the hexagonal $P6_3cm$ structure ($t \leq 0.855$). The bulk

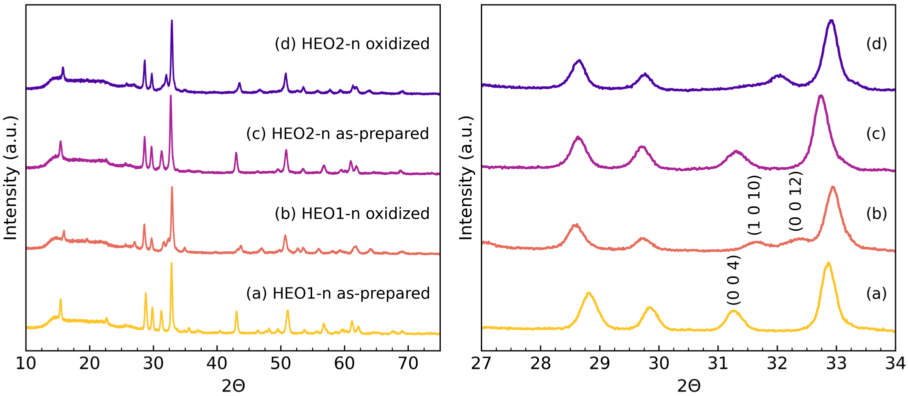

Figure 4.11: X-ray diffractograms of as-prepared and oxidized HEO1-n and HEO2-n.

powders were synthesized using the solid state synthesis method described in Section 3.1.2. The HEO2-b and HEO5-b compositions were phase pure within the hexagonal manganite structure, while the HEO1-b sample was found to contain approximately equal amounts of the hexagonal structure, and the orthorhombic perovskite $Pnma$ structure. As the other bulk samples contained Ti^{4+}, it is likely this dopant reduced Mn to Mn^{2+} at the high synthesis temperatures (1450 °C), lowering the tolerance factor of the materials into values favouring the hexagonal structure, while the undoped HEO1-b sample did not benefit from this effect.

X-ray diffractograms of the HEO1-n and HEO2-n materials (Figure 4.11) showed that the materials adapted the $R3c$ space group during oxidation, which has a tripled c axis compared to the $P6_3cm$ space group, visible by the appearance of the characteristic (1 0 10) and (0 0 12) reflections. The (1 0 10) reflection is less pronounced for HEO2-n than for HEO1-n, as the presence of Ti disrupts the $R3c$ structure.[101]

All nanocrystalline samples showed outstanding oxygen absorption properties and no decrease in OSC with increasing heating and cooling rates (Figure 4.12), with the nanocrystalline materials containing both Ti and Tb showing the highest OSC, as these elements are known to improve the oxygen absorption of hexagonal manganites.[92,97,101,161] The oxidation of Tb^{3+} to Tb^{4+} was also confirmed by XANES measurements. The compositions containing Tb had oxygen stoichiometries above the theoretical maximum of 3.33, which could imply that the interstitial oxygen

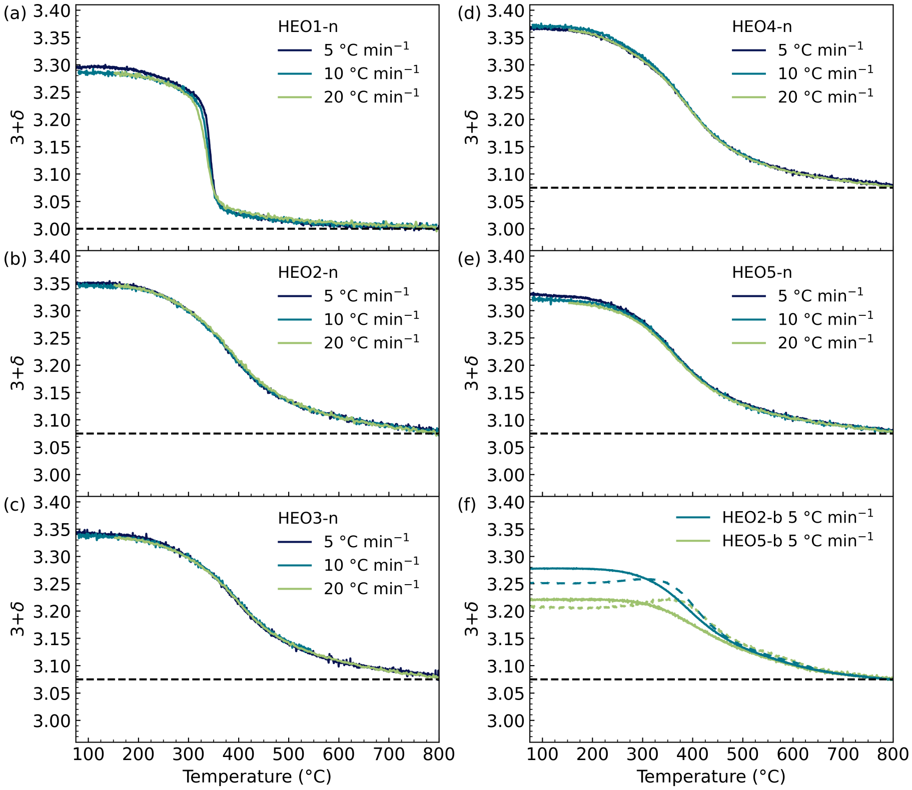

Figure 4.12: Changes in oxygen stoichiometry as a function of temperature during heating (dashed lines) of bulk powders, and cooling (solid lines) for all compositions, measured using different rates in O_2 atmosphere.

that enters the lattice due to charge compensation of Tb^{4+} are positioned in other sites than the regular interstitial sites in the Mn-O layers. The bulk HEO2-b and HEO5-b compositions absorbed less oxygen than their nanocrystalline counterparts, likely due to the large difference in particle size (~30 nm for nanocrystalline powders, tens of micrometer for bulk powders). Nevertheless, the bulk materials displayed increased oxygen absorption compared to other reported bulk hexagonal manganites measured using equally fast rates, indicating significant improvement in oxidation kinetics and ionic transport for high entropy compositions.

To investigate the changes in properties with equimolar high entropy compositions with and without Ti donor doping, the HEO1-n and HEO-2 compositions were chosen for further experiments. Refined lattice parameters found through HT-XRD at different temperatures during heating and cooling in O_2 (Figure 4.13) showed that both compositions displayed a significant contraction along the *c* axis at $T < 400$ °C, related to the incorporation of interstitial oxygen that occurs at lower temperatures found through TGA (Figure 4.12). The undoped HEO1-n sample showed expansion in the *ab*-plane during oxidation, which is typical for hexagonal manganites. The HEO2-n sample, on the other hand, showed a slight contraction along *a* at lower temperatures in O_2, similarly to what was reported for $DyMn_{0.85}Ti_{0.15}O_3$ in Manuscript II;[161] the combination of large *R* cations and Ti-doping cause an expansion of the *ab*-plane in the structure, which further expands during oxidation until a point were the negatively charged interstitial oxygen cause electrostatic contraction between cations, reducing size of the *ab*-plane.

The kinetics of oxidation of HEO1-n and HEO2-n were studied using synchrotron HT-XRD with *in situ* switching of atmosphere from N_2 to O_2 at different temperatures, with X-ray diffractograms and 2D contour plots shown in Figure 4.14. The contraction along the *c* axis that occurs during oxidation can be seen by the shift in the $(0\ 0\ 12)_{161}$ reflection for HEO1-n (Figure 4.14 (a)-(d)), and the $(0\ 0\ 4)_{185}$ reflection for HEO2-n (Figure 4.14 (e)-(h)), towards higher angles. We found that the oxidation time decreased with increasing temperature, and with the addition of Ti^{4+}. As the (1 0 10) (~6.8° 2θ) and (0 0 12) (~6.9° 2θ) reflections are visible for the HEO1-n sample before switching to O_2 atmosphere, this sample was likely partially oxidized prior to the measurements.

Time resolved lattice parameters showed that both compositions displayed a net contraction in both parameters during oxidation, with decreasing oxidation times with increasing temperatures, and with Ti-doping (Figure 4.15). The oxidation times were substantially shorter than what was reported for undoped hexagonal manganites previously,[99,161] indicating a large improvement in kinetics due to the high configurational entropy. High entropy compositions have been shown to have increased ionic transport properties of Li due to overlapping site energies,[138] and we hypothesize that similar effects are occurring for O_i here. In addition, the use of large *R* cations are also known to improve the kinetics of oxidation in hexagonal manganites, due to their larger ionic radii expanding the *ab*-plane, promoting ionic transport.[161] Figure 4.13 also showed that the *a* parameter of HEO1-n found at 200 °C in N_2 ($a \approx 6.20$ Å) was much smaller than the starting parameter in Figure 4.15 at the same temperature ($a \approx 6.25$ Å). This, combined with the observed presence of

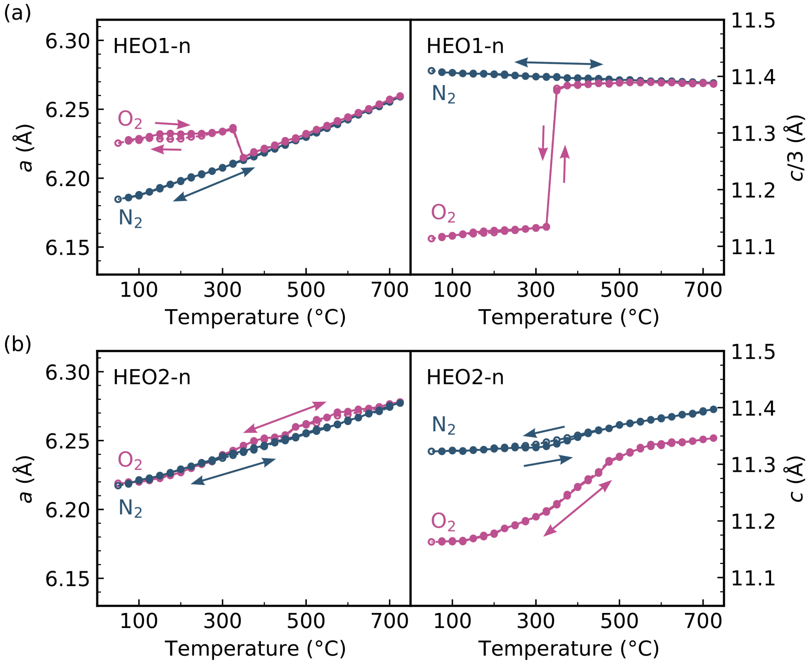

Figure 4.13: Refined lattice parameters a and c as a function of temperature and atmosphere for (a) HEO1-n and (b) HEO2-n, found from HT-XRD during heating and cooling. As the HEO1-n sample was refined within the $R3c$ space group, $c/3$ is shown for easier comparison with the values of HEO2-n refined within the $P6_3cm$ space group.

the oxidized $R3c$ structure in Figure 4.14 prior to *in situ* switching of atmosphere to O_2, indicated that the HEO1-n sample undergoes a large expansion during the first stage of oxidation, followed by a contraction in the ab-plane during the later stages of oxidation. The same was observed for HEO2-n in Figure 4.15, although the expansion and contraction was less significant in value.

The surface exchange rates of oxygen were estimated from the time resolved contraction in the c parameters in Figure 4.15 using the model developed by Moreno *et al.*[156] (Figure 4.16), and showed improved rates for high entropy compositions compared to the single R undoped and doped counterparts studied in Manuscript II.[161] The rates calculated for HEO1-n are likely an underestimation, as this sample was partially oxidized prior to switching to O_2 atmosphere, and the rates are therefore only calculated for the last, and slower, part of the full oxidation.

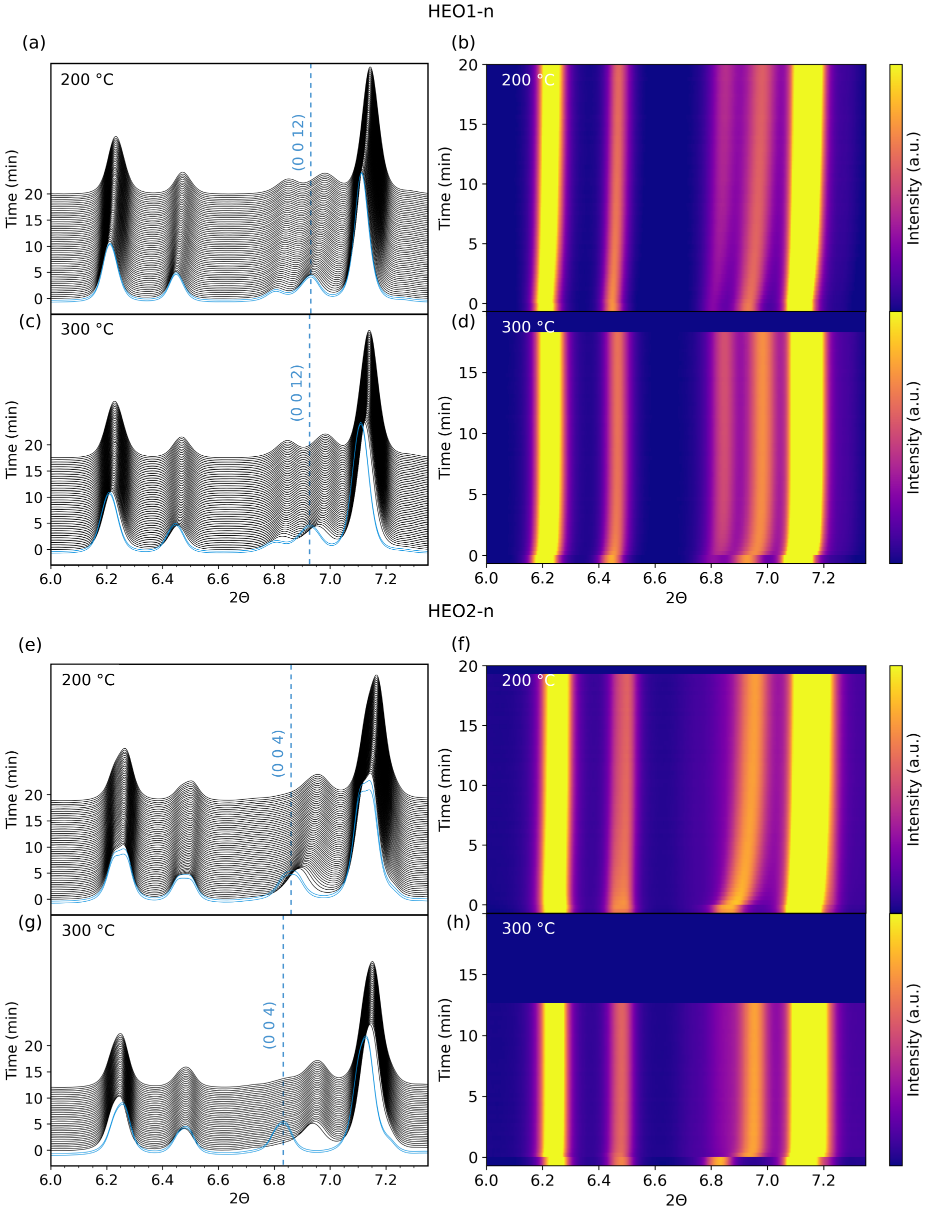

Figure 4.14: Time resolved high temperature X-ray diffractograms and 2D contour plots of (a)-(d) HEO1-n and (e)-(h) HEO2-n measured with *in situ* switching of atmospheres from N_2 (blue) to O_2 (black) at 200 °C and 300 °C. The diffractograms shown in blue are measured in N_2, with the baseline intensity at 6.0° 2θ indicating the time in minutes after switching to O_2 atmosphere. Vertical dashed blue lines indicate the initial position of the $(0\ 0\ 4)_{185}$/ $(0\ 0\ 12)_{161}$ reflections measured in N_2.

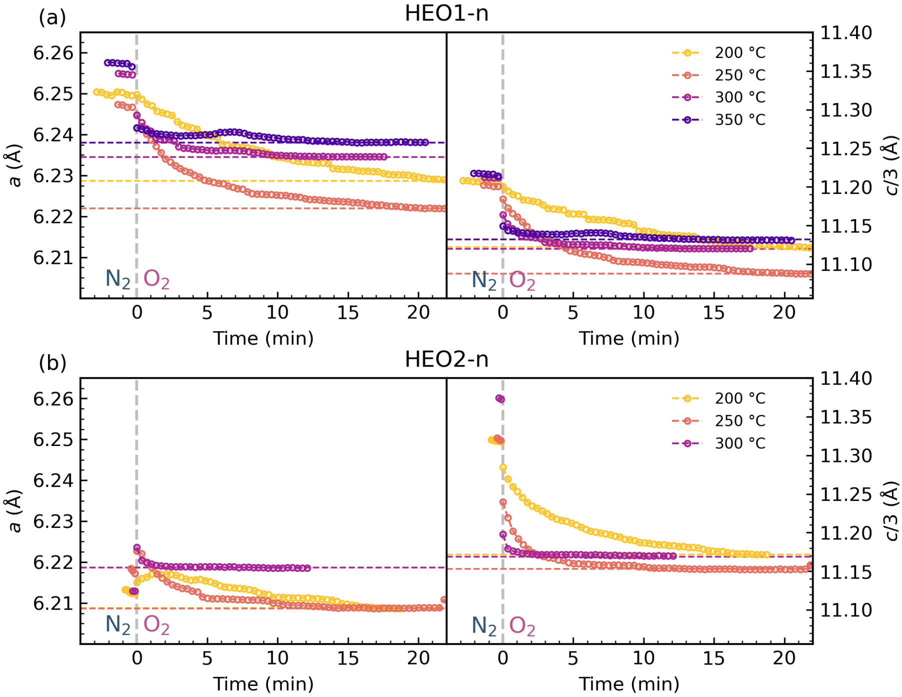

Figure 4.15: Refined lattice parameters for (a) HEO1-n and (b) HEO2-n as a function of time after *in situ* switching of atmosphere from N_2 to O_2. Both samples were refined within the $R3c$ space group, and $c/3$ is therefore shown for easier comparison with the $P6_3cm$ space group. The dashed horizontal lines indicate the value of the lattice parameters in the fully oxidized state at different temperatures.

All the high entropy materials studied here showed outstanding oxygen absorption properties insensitive to the exact rare earth composition, indicating that these materials have good compositional flexibility. This could enable the use of less refined and cheaper raw materials which are composed of multiple rare earths, lowering the material cost of hexagonal manganites significantly.

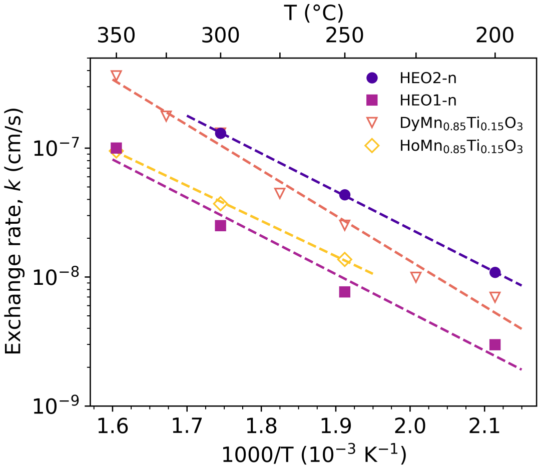

Figure 4.16: Surface exchange rates of oxygen for HEO1-n and HEO2-n. The surface exchange rates for $HoMnO_3$, $HoMn_{0.85}Ti_{0.15}O_3$ and $DyMn_{0.85}Ti_{0.15}O_3$ are included from Danmo *et al.*[161] for comparison.

4.4 Asymmetric membrane

In the early stages of this PhD work, significant time and effort went into attempting to prepare a prototype of a hexagonal manganite asymmetric membrane for oxygen separation, using $[Ho_{0.98}In_{0.02}]_{0.97}Mn_{0.85}Ti_{0.15}O_3$ as the membrane film on top of $Y_{1.05}Mn_{0.85}Ti_{0.15}O_3$ porous substrates. A short summary, highlighting a handful of the prepared membranes, is presented in this section. As hexagonal manganites are quite refractory materials with an anisotropic thermal expansion coefficient, they are difficult to sinter into dense ceramics, and nanocrystalline powders were therefore used for the thin film to promote sintering. The membranes were made as explained in Section 3.3.1 and 3.3.2. The first set of membranes were deposited using the Cocraft Airbrush with 9 mL of suspension per membrane with 0.3 vol% solid load, with one membrane being pressed using a uniaxial pressing tool and 1 kN pressure. Both membranes were then sintered at 1400 °C for 1 hour.

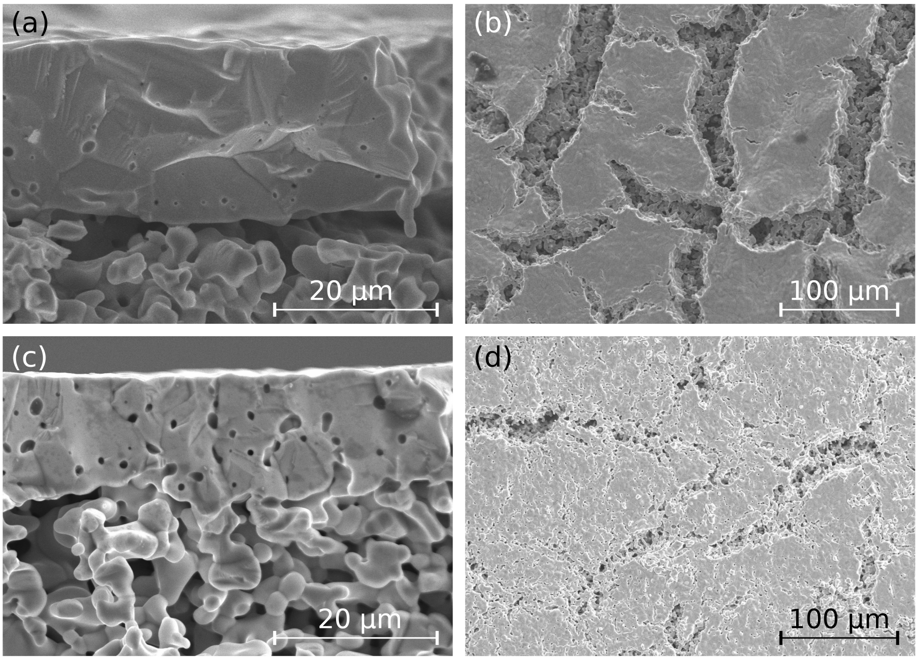

Figure 4.17: SEM images showing cross section and top view of the (a),(b) unpressed and (c),(d) pressed $[Ho_{0.98}In_{0.02}]_{0.97}Mn_{0.85}Ti_{0.15}O_3$ films.

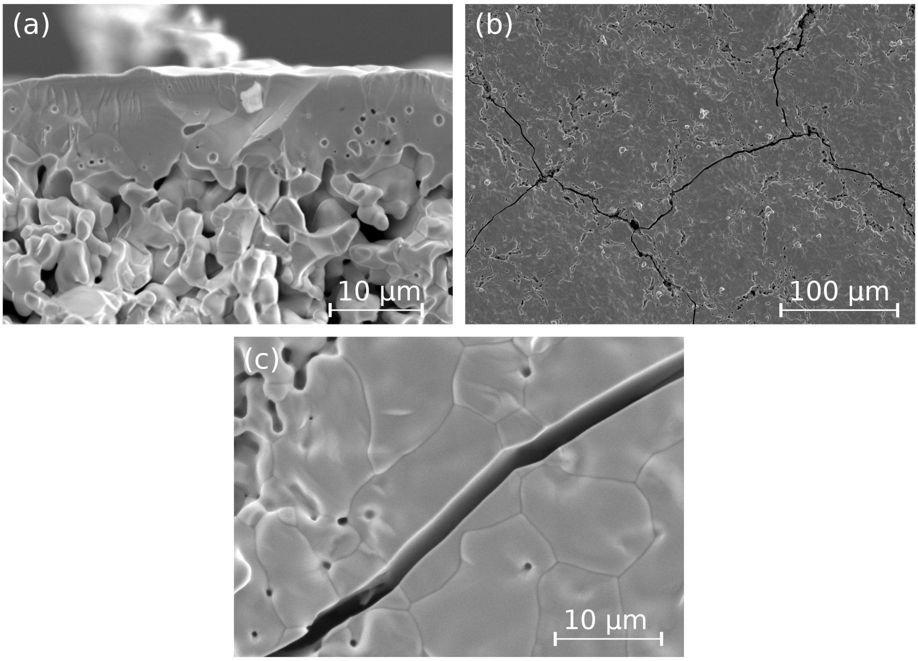

Figure 4.18: SEM images of the (a) cross section and (b),(c) top view of the membrane pressed using CIP and sintered at 1400 °C.

Both films were observed to be quite dense, but the unpressed film (Figure 4.17 (a),(b)) showed a large degree of cracking in the film, reaching through to the substrate causing some delamination. This cracking was also present in the pressed film (Figure 4.17 (c),(d)), but to a lesser extent.

As the density of the sintered uniaxially pressed film was deemed insufficient, cold isostatic pressing (CIP) using pressures of 10 kpsi was tested on films deposited using 9 mL suspension with 0.6 vol % solid load, with one of the resulting membranes shown in Figure 4.18. This film showed improved overall density, with fewer large cracks on the surface. What was observed instead was significant transgranular cracking, propagating through the whole film surface. As the cracks go through the grains, we hypothesize that these cracks form during cooling of the sintered film. Hexagonal manganites display anisotropic thermal expansion, with an expansion in the a parameter and a contraction along the c axis upon heating.[74,162] In addition, the material undergoes a phase transition from the nonponar $P6_3/mmc$ structure to the polar $P6_3cm$ structure during cooling, causing a non-linear change in the unit cell volume, as explained in Section 2.2.1. These two effects combined can cause large stresses within the material during cooling from the sintering temperatures, which can cause crack formation when the stresses become large enough.[163] Ti-doping is known to reduce the anisotropy of the crystal structure, and also stabilize the high temperature $P6_3/mmc$ structure at room temperature, reducing the degree of microcracking in $R\mathrm{MnO_3}$.[162] As the membrane film is doped with Ti, it is believed that the anisotropic thermal expansion therefore is the largest contributor to the cracking. Other materials with anisotropic thermal expansion also display microcracking when the grain sizes become large enough, with $\mathrm{MgTi_2O_5}$ showing crack formation when grains become larger than 3 µm.[164] The film sintered at 1400 °C (Figure 4.18) had grains up towards 25 µm in size, which could increase the amounts of stresses within the film significantly. The sintering temperature was therefore kept at 1300 °C for the subsequent films to keep the grain size as small as possible.

To investigate if the large surface cracking of the film was occuring during drying of the deposited film or during sintering, SEM was used to investigate the film after drying the deposited film, after pressing (CIP), after calcining the films to remove the surfactant used for the suspension and powders from the CIP sample containers, and after sintering at 1300 °C. The resulting SEM images (Figure 4.19) show that the cracks appear after sintering, with no visible cracks after drying, pressing, or calcination of the film. These cracks were therefore believed to have been formed during densification of the thin film, as the film experiences constrained sintering; as the film sinters, it shrinks in all directions, but as the bottom of the film is constrained by the substrate, tensile stresses will form within the film. When these stresses become large enough, the film cracks.[165] For the unpressed film, the shrinkage needed for full densification, and therefore also the resulting tensile stresses, are higher than for the pressed film, where the particles have already been pressed together. The film also showed large degrees of agglomerates on the film surface, which may be a result of sedimentation of agglomerated solids in the suspension due to poor suspension stability.

The Cocraft Airbrush was used for several more film depositions, but many of these had large agglomerates like those shown in Figure 4.19, and varying film thicknesses ranging from 5 to 30 µm even when using identical deposition volumes and solid loads. An Aztec spray coater was therefore tested out for later films. One of the membranes made with the new spray coater is shown in Figure 4.20. These

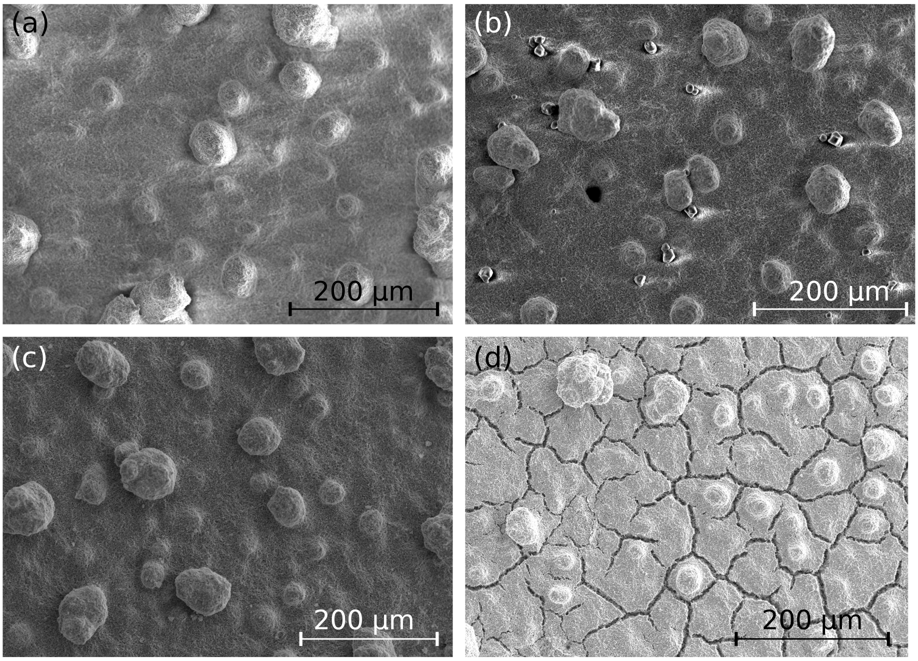

Figure 4.19: SEM images of the (a) dried film, (b) pressed film, (c) calcined film, and (d) sintered film. The extra particles in (b) are powders originating from the CIP sample containers.

membranes showed no large agglomerates, and gave more consistent film thicknesses ranging from 10 to 20 µm. The Aztec spray coater used a separate ink container with a connected hose on the top, resulting in the supernatant of the suspension being used instead of sucking out the suspension (and therefore also agglomerated sediments) from the bottom of the container, as the first spray coater did. These films still had significant sintering and transgranular cracking, with the sintering cracks going down through the film, exposing the substrate. The transgranular cracking was observed to propagate from one sintering crack to the next, indicating that the already formed sintering cracks act as instigation points for crack formation. The film also contained significant porosity.

As none of the prepared films showed good coverage or density, making a ceramic membrane of hexagonal manganites using deposition methods such as spray coating was deemed an improbable, if not impossible, task. Due to the refractory nature

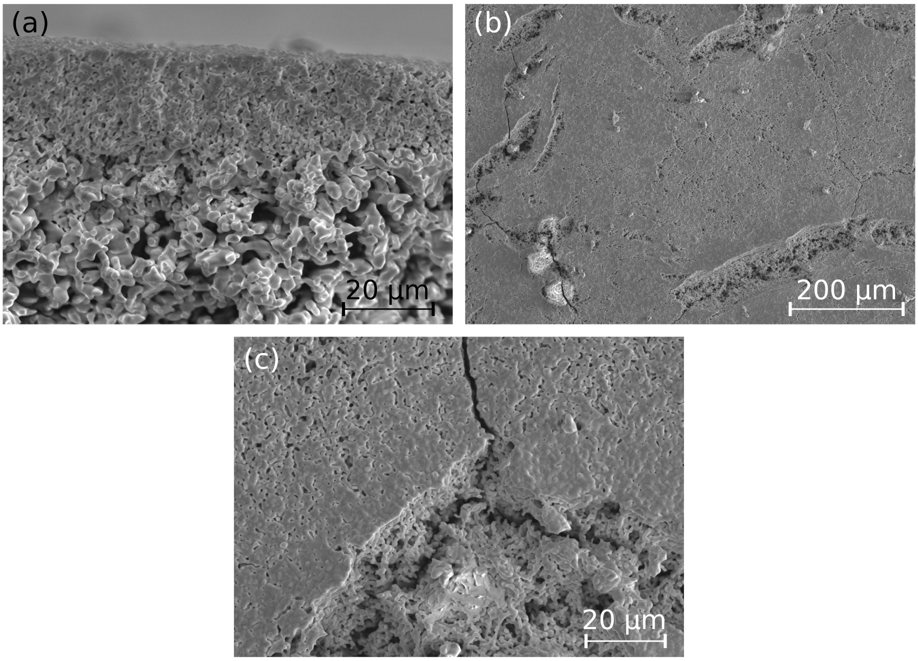

Figure 4.20: SEM images of the (a) cross section and (b),(c) top view of the membrane made using the Aztec spray coater.

of hexagonal manganites, they are more thermally stable at higher temperatures than e.g. perovskites are, but this, combined with the strongly anisotropic thermal expansion coefficient, make the materials much more difficult to sinter into dense ceramics. Increased sintering temperatures promotes sintering, but this results in larger grains which increases cracking due to stresses in the film caused by the anisotropic thermal expansion of hexagonal manganites. Other preparation methods, such as co-sintering of substrate and film and top-down approaches were considered, but were not tested as they would likely be unsuccessful; the pressed porous substrates were very delicate and fragile before firing and would likely not hold its shape during the film deposition, and the thermal anisotropy and refractory nature of hexagonal manganites make sintering a dense and crack-free polycrystalline sample that can be polished down to desired thicknesses practically impossible. We therefore believe that hexagonal manganites are more promising in applications where powder materials are needed, and shifted the focus of the PhD project to optimizing the oxygen absorption and release properties of the material.

5

Overview and outlook

The aim of this project was to investigate the oxygen absorption and release properties of hexagonal manganites with different compositions on both the *R*- and the Mn-sites. The oxygen storage capacity was found to increase with increasing size of the *R* cation, either by using larger ions such as Dy as the sole *R* cation, or by using multiple cations with both small and large ionic radii in high entropy compositions. The latter also stabilized the hexagonal phase for high tolerance factors, enabling the use of larger average ionic radii in the compositions without forming the orthorhombic perovskite phase. The addition of Ti^{4+} was found to improve both the OSC, the thermal stability of interstitial oxygen, O_i, and the kinetics of oxidation of both single *R* and high entropy compositions. The increased size of the *ab*-plane caused by larger *R* and Ti, which also changes the structure towards the high temperature $P6_3/mmc$ structure, promotes transport of interstitial oxygen due to reduced electrostatic repulsion between O_i and planar oxygen, improving both the OSC and the kinetics. Improved kinetics were also found for high entropy compositions, with both nanocrystalline and bulk materials showing improved oxygen storage and transport properties, with the properties being insensitive towards the exact rare earth cation composition. The high compositional flexibility of high entropy materials could enable synthesis from cheaper raw materials containing multiple different rare earth cations, while still resulting in materials with outstanding oxygen transport properties.

While the properties of hexagonal manganites have been continuously improved, there are still a few stones that are left unturned. There is good consensus on the effects of using differently sized *R* cations, with larger *R* cations giving the most desired properties for air separation methods such as CLAS, but these cations are often more expensive than e.g. Y, with Nd, Pr and Dy being listed as critical elements as they are vital for e.g. magnets in wind turbine generators.[166–168] One of the larger drawbacks of hexagonal manganites is precisely the increased material cost due to the price and high demand of rare earths, compared to the more abundant elements that can be used for different perovskite structures. Further focus on optimization of the chemical composition of hexagonal manganites should therefore take the cost of the materials into account. A high entropy composition using an unrefined mixture of "left over" rare earth cations could drastically lower the material cost, and could therefore be explored as a possible synthesis route.

Materials based on $YMnO_3$ substituted with larger *R* show high OSC[92,97–100] and are fairly cheap compared to $HoMnO_3$ and $DyMnO_3$, but their slow oxidation rates leaves much to be desired. One possible route for further material improvement is through the use of aliovalent dopants. We have shown that using 15 % Ti^{4+} on the Mn site improves the oxygen storage and release properties of hexagonal manganites, and other dopants could have similar, or better, effects on the material as well. Using Zr^{4+} as a dopant on the Y-site is known to increase both the OSC and the thermal stability of O_i in $YMnO_3$,[169] similarly to how Ti^{4+} affects the material. It is therefore likely that added Zr can influence the kinetics of oxidation of hexagonal manganites as well. Co-doping with aliovalent dopants on both the R- and the Mn-site is also a possibility.

Our study on high entropy hexagonal manganites investigated only a handful of different compositions, and many other combinations of rare earth elements could possibly lead to even greater oxygen transport properties. In addition, very little is known about the oxidation mechanism of R^{3+} to R^{4+}, and the excess oxygen that can charge balance this reaction. These interstitial oxygen could possibly be located in other sites than the common interstitial sites found in the Mn-O planes. The thermodynamics of this reaction are also possibly quite different from the typical oxidation of Mn, and should be studied further.

The ideal thermodynamic model developed for Manuscript I could describe some trends in oxidation thermodynamics of hexagonal manganites. This work also showed that an ideal model had a poor fit to some of the studied compositions, especially for large R cations with narrow temperature ranges for oxidation. As the model assumed ideal solution, with no defect-defect interactions, the calculated enthalpies and entropies of oxidation were independent on oxygen content. Further investigations of the thermodynamics of hexagonal manganites could be an interesting pathway to follow, either by development of more advanced models which take interactions between interstitial oxygen into account, or by investigating oxygen absorption with different p_{O_2} using thermogravimetric analysis.

With some of the compositions studied in this work showing superior oxygen absorption rates compared to what has been reported in literature, testing the absorption and release properties of the materials in similar conditions as those used for air separation should be the next step. Rapid cyclic oxidation and reduction steps, with determination of the amount of absorbed and released oxygen, could determine if these materials are indeed viable for air separation applications.

Bibliography

[1] S. M. Hashim, A. R. Mohamed, and S. Bhatia, “Current status of ceramic-based membranes for oxygen separation from air,” *Advances in colloid and interface science*, vol. 160, no. 1-2, pp. 88–100, 2010.

[2] M. J. Kirschner, A. Alekseev, S. Dowy, M. Grahl, L. Jansson, P. Keil, G. Lauermann, M. Meilinger, W. Schmehl, H. Weckler, and C. Windmeier, “Oxygen,” in *Ullmann’s Encyclopedia of Industrial Chemistry*, pp. 1–32, Weinheim, Germany: Wiley-VCH Verlag GmbH Co. KGaA, 2017.

[3] World Health Organization, “Oxygen.” `https://www.who.int/health-topics/oxygen`, 2023. Accessed: 15. February 2023.

[4] N. Prosser and M. Shah, “Current and future oxygen (O_2) supply technologies for oxy-fuel combustion,” in *Oxy-Fuel Combustion for Power Generation and Carbon Dioxide (*CO_2*) Capture*, pp. 195–227, Elsevier, 2011.

[5] I.E.A. Global, “Global Energy & CO_2 Status Report 2019.” `https://www.iea.org/reports/global-energy-co2-status-report-2019`, 2019.

[6] R. Stanger, T. Wall, R. Spörl, M. Paneru, S. Grathwohl, M. Weidmann, G. Scheffknecht, D. McDonald, K. Myöhänen, J. Ritvanen, S. Rahiala, T. Hyppänen, J. Mletzko, A. Kather, and S. Santos, “Oxyfuel combustion for CO_2 capture in power plants,” *International Journal of Greenhouse Gas Control*, vol. 40, pp. 55–125, 2015.

[7] S. Yadav and S. S. Mondal, “A review on the progress and prospects of oxy-fuel carbon capture and sequestration (CCS) technology,” *Fuel*, vol. 308, no. September 2021, p. 122057, 2022.

[8] F. Wu, M. D. Argyle, P. A. Dellenback, and M. Fan, “Progress in O_2 separation for oxy-fuel combustion–A promising way for cost-effective CO_2 capture: A review,” *Progress in Energy and Combustion Science*, vol. 67, pp. 188–205, 2018.

[9] Y. Wei, W. Yang, J. Caro, and H. Wang, “Dense ceramic oxygen permeable membranes and catalytic membrane reactors,” *Chemical Engineering Journal*, vol. 220, pp. 185–203, 2013.

[10] T. Wilberforce, A. Baroutaji, B. Soudan, A. H. Al-Alami, and A. G. Olabi, “Outlook of carbon capture technology and challenges,” *Science of the Total Environment*, vol. 657, pp. 56–72, 2019.

[11] E. Krzystowczyk, V. Haribal, J. Dou, and F. Li, “Chemical Looping Air Separation Using a Perovskite-Based Oxygen Sorbent: System Design and Process Analysis,” *ACS Sustainable Chemistry and Engineering*, vol. 9, no. 36, pp. 12185–12195, 2021.

[12] P. Dyer, “Ion transport membrane technology for oxygen separation and syngas production,” *Solid State Ionics*, vol. 134, no. 1-2, pp. 21–33, 2000.

[13] K. Zhang, J. Sunarso, Z. Shao, W. Zhou, C. Sun, S. Wang, and S. Liu, “Research progress and materials selection guidelines on mixed conducting perovskite-type ceramic membranes for oxygen production,” *RSC Advances*, vol. 1, no. 9, p. 1661, 2011.

[14] J. Zhou, J. Zhang, F. Zhang, B. Niu, L. Lei, and W. Wang, “High-entropy carbide: A novel class of multicomponent ceramics,” *Ceramics International*, vol. 44, no. 17, pp. 22014–22018, 2018.

[15] B. Bulfin, J. Lapp, S. Richter, D. Gubàn, J. Vieten, S. Brendelberger, M. Roeb, and C. Sattler, “Air separation and selective oxygen pumping via temperature and pressure swing oxygen adsorption using a redox cycle of $SrFeO_3$ perovskite,” *Chemical Engineering Science*, vol. 203, pp. 68–75, 2019.

[16] D. D. Athayde, D. F. Souza, A. M. A. Silva, D. Vasconcelos, E. H. M. Nunes, J. C. Diniz da Costa, and W. L. Vasconcelos, “Review of perovskite ceramic synthesis and membrane preparation methods,” *Ceramics International*, vol. 42, no. 6, pp. 6555–6571, 2016.

[17] F. G. Kerry, *Industrial Gas Handbook*. CRC Press, 2007.

[18] A. R. Smith and J. Klosek, “A review of air separation technologies and their integration with energy conversion processes,” *Fuel Processing Technology*, vol. 70, no. 2, pp. 115–134, 2001.

[19] W. F. Castle, “Air sepration and liquefaction: Recent developments and prospects for the beginning of the new millennium,” *International Journal of Refrigeration*, vol. 25, no. 1, pp. 158–172, 2002.

[20] R. J. Allam, “Improved oxygen production technologies,” *Energy Procedia*, vol. 1, no. 1, pp. 461–470, 2009.

[21] A. Ebrahimi, M. Meratizaman, H. A. Reyhani, O. Pourali, and M. Amidpour, “Energetic, exergetic and economic assessment of oxygen production from two columns cryogenic air separation unit,” *Energy*, vol. 90, pp. 1298–1316, 2015.

[22] S. U. Rege and R. T. Yang, “Limits for Air Separation by Adsorption with LiX Zeolite,” *Industrial and Engineering Chemistry Research*, vol. 36, no. 12, pp. 5358–5365, 1997.

[23] S. S. Hashim, A. R. Mohamed, and S. Bhatia, “Oxygen separation from air using ceramic-based membrane technology for sustainable fuel production and power generation,” *Renewable and Sustainable Energy Reviews*, vol. 15, no. 2, pp. 1284–1293, 2011.

[24] C. Zhou, K. Shah, and B. Moghtaderi, "Techno-economic assessment of integrated chemical looping air separation for oxy-fuel combustion: An Australian case study," *Energy and Fuels*, vol. 29, no. 4, pp. 2074–2088, 2015.

[25] Z. Yang, Y. S. Lin, and Y. Zeng, "High-temperature sorption process for air separation and oxygen removal," *Industrial and Engineering Chemistry Research*, vol. 41, no. 11, pp. 2775–2784, 2002.

[26] A. Jayaraman, R. T. Yang, S. H. Cho, T. S. Bhat, and V. N. Choudary, "Adsorption of nitrogen, oxygen and argon on Na-CeX zeolites," *Adsorption*, vol. 8, no. 4, pp. 271–278, 2002.

[27] C. A. Grande, "Advances in Pressure Swing Adsorption for Gas Separation," *ISRN Chemical Engineering*, vol. 2012, pp. 1–13, 2012.

[28] R. T. Yang, *Gas Separation By Adsorption Processes*. Series On Chemical Engineering, World Scientific Publishing Company, 1997.

[29] B. Moghtaderi, "Application of chemical looping concept for air separation at high temperatures," *Energy and Fuels*, vol. 24, no. 1, pp. 190–198, 2010.

[30] K. Shah, B. Moghtaderi, and T. Wall, "Selection of suitable oxygen carriers for chemical looping air separation: A thermodynamic approach," *Energy and Fuels*, vol. 26, no. 4, pp. 2038–2045, 2012.

[31] J. Dou, E. Krzystowczyk, X. Wang, T. Robbins, L. Ma, X. Liu, and F. Li, "A- and B-site Codoped $SrFeO_3$ Oxygen Sorbents for Enhanced Chemical Looping Air Separation," *ChemSusChem*, vol. 13, no. 2, pp. 385–393, 2020.

[32] J. Vieten, B. Bulfin, F. Call, M. Lange, M. Schmücker, A. Francke, M. Roeb, and C. Sattler, "Perovskite oxides for application in thermochemical air separation and oxygen storage," *Journal of Materials Chemistry A*, vol. 4, no. 35, pp. 13652–13659, 2016.

[33] C. Zhou, K. Shah, H. Song, J. Zanganeh, E. Doroodchi, and B. Moghtaderi, "Integration Options and Economic Analysis of an Integrated Chemical Looping Air Separation Process for Oxy-fuel Combustion," *Energy and Fuels*, vol. 30, no. 3, pp. 1741–1755, 2016.

[34] P. V. Hendriksen, P. H. Larsen, M. Mogensen, F. W. Poulsen, and K. Wiik, "Prospects and problems of dense oxygen permeable membranes," *Catalysis Today*, vol. 56, no. 1-3, pp. 283–295, 2000.

[35] J. Sunarso, S. Baumann, J. M. Serra, W. A. Meulenberg, S. Liu, Y. S. Lin, and J. C. Diniz da Costa, "Mixed ionic–electronic conducting (MIEC) ceramic-based membranes for oxygen separation," *Journal of Membrane Science*, vol. 320, no. 1-2, pp. 13–41, 2008.

[36] S. P. S. Badwal and F. T. Ciacchi, "Ceramic Membrane Technologies for Oxygen Separation," *Advanced Materials*, vol. 13, no. 12–13, pp. 993–996, 2001.

[37] H. J. M. Bouwmeester, H. Kruidhof, and A. Burggraaf, "Importance of the surface exchange kinetics as rate limiting step in oxygen permeation through mixed-conducting oxides," *Solid State Ionics*, vol. 72, pp. 185–194, 1994.

[38] X. Zhu and W. Yang, *Mixed Conducting Ceramic Membranes*. Berlin, Heidelberg: Springer Berlin Heidelberg, 2017.

[39] X. Chang, C. Zhang, Y. He, X. Dong, W. Jin, and N. Xu, "A Comparative Study of the Performance of Symmetric and Asymmetric Mixed-conducting Membranes," *Chinese Journal of Chemical Engineering*, vol. 17, no. 4, pp. 562–570, 2009.

[40] M. Martin, "Materials in thermodynamic potential gradients," *The Journal of Chemical Thermodynamics*, vol. 35, no. 8, pp. 1291–1308, 2003.

[41] H. Lein, K. Wiik, and T. Grande, "Kinetic demixing and decomposition of oxygen permeable membranes," *Solid State Ionics*, vol. 177, no. 19-25, pp. 1587–1590, 2006.

[42] X. Zhu, K. Li, L. Neal, and F. Li, "Perovskites as Geo-inspired Oxygen Storage Materials for Chemical Looping and Three-Way Catalysis: A Perspective," *ACS Catalysis*, vol. 8, no. 9, pp. 8213–8236, 2018.

[43] A. Demont, S. Abanades, and E. Beche, "Investigation of perovskite structures as oxygen-exchange redox materials for hydrogen production from thermochemical two-step water-splitting cycles," *Journal of Physical Chemistry C*, vol. 118, no. 24, pp. 12682–12692, 2014.

[44] E. Krzystowczyk, X. Wang, J. Dou, V. Haribal, and F. Li, "Substituted $SrFeO_3$ as robust oxygen sorbents for thermochemical air separation: correlating redox performance with compositional and structural properties," *Physical Chemistry Chemical Physics*, vol. 22, no. 16, pp. 8924–8932, 2020.

[45] J. Vieten, B. Bulfin, M. Senholdt, M. Roeb, C. Sattler, and M. Schmücker, "Redox thermodynamics and phase composition in the system $SrFeO_{3\text{-}\delta}$ — $SrMnO_{3\text{-}\delta}$," *Solid State Ionics*, vol. 308, no. April, pp. 149–155, 2017.

[46] Q. Shen, Y. Zheng, C. Luo, and C. Zheng, "Development and characterization of $Ba_{1\text{-}x}Sr_xCo_{0.8}Fe_{0.2}O_{3\text{-}\delta}$ perovskite for oxygen production in oxyfuel combustion system," *Chemical Engineering Journal*, vol. 255, pp. 462–470, 2014.

[47] H. Ding, Y. Xu, C. Luo, Q. Wang, S. Li, G. Cai, L. Zhang, Y. Zheng, and Q. Shen, "Oxygen desorption behavior of sol-gel derived perovskite-type oxides in a pressurized fixed bed reactor," *Chemical Engineering Journal*, vol. 323, pp. 340–346, 2017.

[48] Q. Shen, Y. Zhang, H. Ding, L. Wu, Y. Xu, B. Shi, Y. Zheng, and J. Yuan, "Performance and stability enhancement of perovskite-type nanomaterials applied for carbon capture utilizing oxyfuel combustion," *Energies*, vol. 10, no. 2, 2017.

[49] G. Cai, C. Luo, Y. Zheng, D. Cao, T. Luo, X. Li, F. Wu, and L. Zhang, "$BaCoO_{3\text{-}\delta}$ perovskite-type oxygen carrier for chemical looping air separation, part I: Determination of oxygen non-stoichiometry and cyclic stability of oxygen carrier," *Separation and Purification Technology*, vol. 302, no. August, p. 121972, 2022.

[50] F. Schulze-Küppers, S. Baumann, F. Tietz, H. J. Bouwmeester, and W. A. Meulenberg, "Towards the fabrication of $La_{0.98\text{-}x}Sr_xCo_{0.2}Fe_{0.8}O_{3\text{-}\delta}$ perovskite-type oxygen transport membranes," *Journal of the European Ceramic Society*, vol. 34, no. 15, pp. 3741–3748, 2014.

[51] F. Schulze-Küppers, S. Baumann, W. A. Meulenberg, D. Stöver, and H. P. Buchkremer, "Manufacturing and performance of advanced supported $Ba_{0.5}Sr_{0.5}Co_{0.8}Fe_{0.2}O_{3-\delta}$ (BSCF) oxygen transport membranes," *Journal of Membrane Science*, vol. 433, pp. 121–125, 2013.

[52] S. Baumann, J. M. Serra, M. P. Lobera, S. Escolástico, F. Schulze-Küppers, and W. A. Meulenberg, "Ultrahigh oxygen permeation flux through supported $Ba_{0.5}Sr_{0.5}Co_{0.8}Fe_{0.2}O_{3-\delta}$ membranes," *Journal of Membrane Science*, vol. 377, no. 1-2, pp. 198–205, 2011.

[53] N. Han, W. Zhang, W. Guo, S. Xie, C. Zhang, X. Zhang, J. Fransaer, and S. Liu, "Novel oxygen permeable hollow fiber perovskite membrane with surface wrinkles," *Separation and Purification Technology*, vol. 261, no. January, p. 118295, 2021.

[54] S. Liu and G. R. Gavalas, "Oxygen selective ceramic hollow fiber membranes," *Journal of Membrane Science*, vol. 246, no. 1, pp. 103–108, 2005.

[55] J. W. Chae, Y. K. Park, E. Magnone, and J. H. Park, "Oxygen permeation properties of Sm/Sr co-doped ceria decorated $Ba_{0.5}Sr_{0.5}Co_{0.8}Fe_{0.2}O_{3-\delta}$ hollow fiber membrane," *Journal of Industrial and Engineering Chemistry*, vol. 76, pp. 508–514, 2019.

[56] Q. Zhang, G. Hu, V. Starchenko, G. Wan, E. M. Dufresne, Y. Dong, H. Liu, H. Zhou, H. Jeen, K. Saritas, J. T. Krogel, F. A. Reboredo, H. N. Lee, A. R. Sandy, I. C. Almazan, P. Ganesh, and D. D. Fong, "Phase Transition Dynamics in a Complex Oxide Heterostructure," *Physical Review Letters*, vol. 129, no. 23, p. 235701, 2022.

[57] J. Zhang, Z. Zhang, Y. Chen, X. Xu, C. Zhou, G. Yang, W. Zhou, and Z. Shao, "Materials design for ceramic oxygen permeation membranes: Single perovskite vs. single/double perovskite composite, a case study of tungsten-doped barium strontium cobalt ferrite," *Journal of Membrane Science*, vol. 566, no. September, pp. 278–287, 2018.

[58] K. Qiu, Y. Liu, J. Tan, T. Wang, G. Zhang, Z. Liu, and W. Jin, "Fluorine-doped barium cobaltite perovskite membrane for oxygen separation and syngas production," *Ceramics International*, vol. 46, no. 17, pp. 27469–27475, 2020.

[59] N. Miura, H. Ikeda, and A. Tsuchida, "$Sr_{1-x}Ca_xFeO_{3-\delta}$ as a New Oxygen Sorbent for the High-Temperature Pressure-Swing Adsorption Process," *Industrial and Engineering Chemistry Research*, vol. 55, no. 11, pp. 3091–3096, 2016.

[60] G. Luongo, F. Donat, and C. R. Müller, "Structural and thermodynamic study of Ca A- or Co B-site substituted $SrFeO_{3-\delta}$ perovskites for low temperature chemical looping applications," *Physical Chemistry Chemical Physics*, vol. 22, no. 17, pp. 9272–9282, 2020.

[61] H. Ikeda, A. Tsuchida, J. Morita, and N. Miura, "$SrCo_xFe_{1-x}O_{3-\delta}$ Oxygen Sorbent Usable for High-Temperature Pressure-Swing Adsorption Process Operating at Approximately 300 °C," *Industrial and Engineering Chemistry Research*, vol. 55, no. 22, pp. 6501–6505, 2016.

[62] B. Bulfin, J. Vieten, S. Richter, J. M. Naik, G. R. Patzke, M. Roeb, C. Sattler, and A. Steinfeld, "Isothermal relaxation kinetics for the reduction and oxidation of $SrFeO_3$ based perovskites," *Physical Chemistry Chemical Physics*, vol. 22, no. 4, pp. 2466–2474, 2020.

[63] X. Zhu and W. Yang, “Microstructural and Interfacial Designs of Oxygen-Permeable Membranes for Oxygen Separation and Reaction–Separation Coupling,” *Advanced Materials*, vol. 31, no. 50, p. 1902547, 2019.

[64] S. Huang, W. Li, Z. Cao, H. Li, H. Ma, X. Zhu, and W. Yang, “Effect of Bi doping on the performance of dual-phase oxygen-permeable membranes,” *Journal of Membrane Science*, vol. 579, no. January, pp. 342–350, 2019.

[65] J. Wang, Q. Jiang, D. Liu, L. Zhang, L. Cai, Y. Zhu, Z. Cao, W. Li, X. Zhu, and W. Yang, “Effect of inner strain on the performance of dual-phase oxygen permeable membranes,” *Journal of Membrane Science*, vol. 644, no. October 2021, p. 120142, 2022.

[66] X. Wang, L. Shi, Y. Huang, L. Zeng, M. Boubeche, D. Li, and H. Luo, “CO_2-Tolerant Oxygen Permeation Membranes Containing Transition Metals as Sintering Aids with High Oxygen Permeability,” *Processes*, vol. 9, no. 3, p. 528, 2021.

[67] A. A. Plazaola, A. C. Labella, Y. Liu, N. B. Porras, D. A. P. Tanaka, M. V. S. Annaland, and F. Gallucci, “Mixed ionic-electronic conducting membranes (MIEC) for their application in membrane reactors: A review,” *Processes*, vol. 7, no. 3, 2019.

[68] S. Remsen and B. Dabrowski, “Synthesis and oxygen storage capacities of hexagonal $Dy_{1-x}Y_xMnO_{3+\delta}$,” *Chemistry of Materials*, vol. 23, no. 17, pp. 3818–3827, 2011.

[69] S. Remsen, B. Dabrowski, O. Chmaissem, J. Mais, and A. Szewczyk, “Synthesis and oxygen content dependent properties of hexagonal $DyMnO_{3+\delta}$,” *Journal of Solid State Chemistry*, vol. 184, no. 8, pp. 2306–2314, 2011.

[70] C. Abughayada, B. Dabrowski, S. Kolesnik, D. E. Brown, and O. Chmaissem, “Characterization of Oxygen Storage and Structural Properties of Oxygen-Loaded Hexagonal $RMnO_{3+\delta}$ (R = Ho, Er, and Y),” *Chemistry of Materials*, vol. 27, no. 18, pp. 6259–6267, 2015.

[71] K. Świerczek, A. Klimkowicz, K. Nishihara, S. Kobayashi, A. Takasaki, M. Alanizy, S. Kolesnik, B. Dabrowski, S. Seong, and J. Kang, “Oxygen storage properties of hexagonal $HoMnO_{3+\delta}$,” *Physical Chemistry Chemical Physics*, vol. 19, no. 29, pp. 19243–19251, 2017.

[72] C. Abughayada, B. Dabrowski, M. Avdeev, S. Kolesnik, S. Remsen, and O. Chmaissem, “Structural, magnetic, and oxygen storage properties of hexagonal $Dy_{1-x}Y_xMnO_{3+\delta}$,” *Journal of Solid State Chemistry*, vol. 217, pp. 127–135, 2014.

[73] J.-W. Bos, B. B. van Aken, and T. T. M. Palstra, “Site Disorder Induced Hexagonal-Orthorhombic Transition in $Y^{3+}_{1-x}Gd^{3+}_{x}MnO_3$,” *Chemistry of Materials*, vol. 13, no. 12, pp. 4804–4807, 2001.

[74] S. M. Selbach, A. N. Løvik, K. Bergum, J. R. Tolchard, M. A. Einarsrud, and T. Grande, “Crystal structure, chemical expansion and phase stability of $HoMnO_3$ at high temperature,” *Journal of Solid State Chemistry*, vol. 196, pp. 528–535, 2012.

[75] H. W. Brinks, J. Rodríguez-Carvajal, H. Fjellvåg, A. Kjekshus, and B. C. Hauback, “Crystal and magnetic structure of orthorhombic $HoMnO_3$,” *Physical Review B - Condensed Matter and Materials Physics*, vol. 63, no. 9, pp. 944111–9441112, 2001.

[76] A. S. Gibbs, K. S. Knight, and P. Lightfoot, “High-temperature phase transitions of hexagonal $YMnO_3$,” *Physical Review B*, vol. 83, no. 9, p. 1958, 2011.

[77] B. B. Van Aken, T. T. Palstra, A. Filippetti, and N. A. Spaldin, “The origin of ferroelectricity in magnetoelectric $YMnO_3$,” *Nature Materials*, vol. 3, no. 3, pp. 164–170, 2004.

[78] C. J. Fennie and K. M. Rabe, “Ferroelectric transition in $YMnO_3$ from first principles,” *Physical Review B - Condensed Matter and Materials Physics*, vol. 72, no. 10, pp. 1–4, 2005.

[79] S. H. Skjærvø, Q. N. Meier, M. Feygenson, N. A. Spaldin, S. J. Billinge, E. S. Bozin, and S. M. Selbach, “Unconventional Continuous Structural Disorder at the Order-Disorder Phase Transition in the Hexagonal Manganites,” *Physical Review X*, vol. 9, no. 3, p. 31001, 2019.

[80] M. Šafránková, J. Fousek, and S. A. Kižaev, “Domains in ferroelectric in $YMnO_3$,” *Czechoslovak Journal of Physics*, vol. 17, no. 6, pp. 559–560, 1967.

[81] D. Meier, J. Seidel, A. Cano, K. Delaney, Y. Kumagai, M. Mostovoy, N. A. Spaldin, R. Ramesh, and M. Fiebig, “Anisotropic conductance at improper ferroelectric domain walls,” *Nature Materials*, vol. 11, no. 4, pp. 284–288, 2012.

[82] J. A. Mundy, J. Schaab, Y. Kumagai, A. Cano, M. Stengel, I. P. Krug, D. M. Gottlob, H. Doğanay, M. E. Holtz, R. Held, Z. Yan, E. Bourret, C. M. Schneider, D. G. Schlom, D. A. Muller, R. Ramesh, N. A. Spaldin, and D. Meier, “Functional electronic inversion layers at ferroelectric domain walls,” *Nature Materials*, vol. 16, no. 6, pp. 622–627, 2017.

[83] D. R. Småbråten, Q. N. Meier, S. H. Skjærvø, K. Inzani, D. Meier, and S. M. Selbach, “Charged domain walls in improper ferroelectric hexagonal manganites and gallates,” *Physical Review Materials*, vol. 2, no. 11, p. 114405, 2018.

[84] S. Artyukhin, K. T. Delaney, N. A. Spaldin, and M. Mostovoy, “Landau theory of topological defects in multiferroic hexagonal manganites,” *Nature Materials*, vol. 13, no. 1, pp. 42–49, 2014.

[85] H. L. Tuller and S. R. Bishop, “Point defects in oxides: Tailoring materials through defect engineering,” *Annual Review of Materials Research*, vol. 41, pp. 369–398, 2011.

[86] S. Aggarwal and R. Ramesh, “Point defect chemistry of metal oxide heterostructures,” *Annual Review of Materials Science*, vol. 28, no. 1, pp. 463–499, 1998.

[87] S. V. Kalinin and N. A. Spaldin, “Functional Ion Defects in Transition Metal Oxides,” *Science*, vol. 341, no. 6148, pp. 858–859, 2013.

[88] J. A. van Roosmalen and E. H. Cordfunke, “The defect chemistry of $LaMnO_{3\pm\delta}$. 4. defect model for $LaMnO_{3+\delta}$,” *Journal of Solid State Chemistry*, vol. 110, no. 1, pp. 109–112, 1994.

[89] S. H. Skjærvø, E. T. Wefring, S. K. Nesdal, N. H. Gaukås, G. H. Olsen, J. Glaum, T. Tybell, and S. M. Selbach, “Interstitial oxygen as a source of p-type conductivity in hexagonal manganites,” *Nature Communications*, vol. 7, no. 7491, 2016.

[90] S. M. Griffin, M. Reidulff, S. M. Selbach, and N. A. Spaldin, “Defect Chemistry as a Crystal Structure Design Parameter: Intrinsic Point Defects and Ga Substitution in $InMnO_3$,” *Chemistry of Materials*, vol. 29, no. 6, pp. 2425–2434, 2016.

[91] D. M. Evans, T. S. Holstad, A. B. Mosberg, D. R. Småbråten, P. E. Vullum, A. L. Dadlani, K. Shapovalov, Z. Yan, E. Bourret, D. Gao, J. Akola, J. Torgersen, A. T. van Helvoort, S. M. Selbach, and D. Meier, "Conductivity control via minimally invasive anti-Frenkel defects in a functional oxide," *Nature Materials*, vol. 19, no. 11, pp. 1195–1200, 2020.

[92] M. Otomo, T. Hasegawa, Y. Asakura, and S. Yin, "Remarkable Effects of Lanthanide Substitution for the Y-Site on the Oxygen Storage/Release Performance of $YMnO_{3+\delta}$," *ACS Applied Materials and Interfaces*, vol. 13, no. 27, pp. 31691–31698, 2021.

[93] E. A. Kotomin, Y. A. Mastrikov, E. Heifets, and J. Maier, "Adsorption of atomic and molecular oxygen on the $LaMnO_3$ (001) surface: Ab initio supercell calculations and thermodynamics," *Physical Chemistry Chemical Physics*, vol. 10, no. 31, pp. 4644–4649, 2008.

[94] J. M. Polfus, B. Yildiz, and H. L. Tuller, "Origin of fast oxide ion diffusion along grain boundaries in Sr-doped $LaMnO_3$," *Physical Chemistry Chemical Physics*, vol. 20, no. 28, pp. 19142–19150, 2018.

[95] J. Carrasco, F. Illas, N. Lopez, E. A. Kotomin, Y. F. Zhukovskii, R. A. Evarestov, Y. A. Mastrikov, S. Piskunov, and J. Maier, "First-principles calculations of the atomic and electronic structure of F centers in the bulk and on the (001) surface of $SrTiO_3$," *Physical Review B - Condensed Matter and Materials Physics*, vol. 73, no. 6, 2006.

[96] O. Parkkima, S. Malo, M. Hervieu, E. L. Rautama, and M. Karppinen, "New $R\mathrm{MnO}_{3+\delta}$ (R=Y, Ho; $\delta\approx0.35$) phases with modulated structure," *Journal of Solid State Chemistry*, vol. 221, pp. 109–115, 2015.

[97] A. Klimkowicz, K. Cichy, O. Chmaissem, B. Dabrowski, B. Poudel, K. Świerczek, K. M. Taddei, and A. Takasaki, "Reversible oxygen intercalation in hexagonal $Y_{0.7}Tb_{0.3}MnO_{3+\delta}$: toward oxygen production by temperature-swing absorption in air," *Journal of Materials Chemistry A*, vol. 7, no. 6, pp. 2608–2618, 2019.

[98] A. Klimkowicz, T. Hashizume, K. Cichy, S. Tamura, K. Świerczek, A. Takasaki, T. Motohashi, and B. Dabrowski, "Oxygen separation from air by the combined temperature swing and pressure swing processes using oxygen storage materials $Y_{1x}(Tb/Ce)_xMnO_{3+\delta}$," *Journal of Materials Science*, vol. 55, no. 33, pp. 15653–15666, 2020.

[99] K. Cichy, K. Świerczek, K. Jarosz, A. Klimkowicz, M. Marzec, M. Gajewska, and B. Dabrowski, "Towards efficient oxygen separation from air: Influence of the mean rare-earth radius on thermodynamics and kinetics of reactivity with oxygen in hexagonal $Y_{1\text{-}x}R_xMnO_{3+\delta}$," *Acta Materialia*, vol. 205, 2021.

[100] K. Cichy, M. Zając, and K. Świerczek, "Evaluation of applicability of Nd- and Sm-substituted $Y_{1\text{-}x}R_xMnO_{3+\delta}$ in temperature swing absorption for energy-related technologies," *Energy*, vol. 239, pp. 1–9, 2022.

[101] F. H. Danmo, B. A. Williamson, D. R. Småbråten, N. H. Gaukås, E. R. Østli, T. Grande, J. Glaum, and S. M. Selbach, "Oxygen absorption in nanocrystalline h-$R\mathrm{MnO}_3$ (R = Y, Ho, Dy) and the effect of Ti donor doping," *Chemistry of Materials, under review*.

[102] A. Klimkowicz, K. Świerczek, S. Kobayashi, A. Takasaki, W. Allahyani, and B. Dabrowski, "Improvement of oxygen storage properties of hexagonal $YMnO_{3+\delta}$ by microstructural modifications," *Journal of Solid State Chemistry*, vol. 258, no. August 2017, pp. 471–476, 2018.

[103] Y. Asakura, A. Miyake, M. Otomo, and S. Yin, "Improvement of the O_2 storage/release rate of $YMnO_3$ nanoparticles synthesized by the polymerized complex method," *Dalton Transactions*, vol. 49, no. 4, pp. 966–971, 2020.

[104] I. Levin, V. Krayzman, T. A. Vanderah, M. Tomczyk, H. Wu, M. G. Tucker, H. Y. Playford, J. C. Woicik, C. L. Dennis, and P. M. Vilarinho, "Oxygen-storage behavior and local structure in Ti-substituted YMnO₃," *Journal of Solid State Chemistry*, vol. 246, no. November 2016, pp. 29–41, 2017.

[105] Z. L. Moreno Botello, A. Caneiro, P. Roussel, and G. Gauthier, "Synthesis and preliminary study of pure and Zr-doped $YMnO_3$ compounds as Solid Oxide Fuel Cells electrode," *Journal of Alloys and Compounds*, vol. 690, pp. 348–355, 2017.

[106] T. Katsufuji, M. Masaki, A. Machida, M. Moritomo, K. Kato, E. Nishibori, M. Takata, M. Sakata, K. Ohoyama, K. Kitazawa, and H. Takagi, "Crystal structure and magnetic properties of hexagonal RMnO$_3$ (R=Lu, and Sc) and the effect of doping," *Physical Review B - Condensed Matter and Materials Physics*, vol. 66, no. 13, pp. 1–8, 2002.

[107] Y. Aikawa, T. Katsufuji, T. Arima, and K. Kato, "Effect of Mn trimerization on the magnetic and dielectric properties of hexagonal $YMnO_3$," *Physical Review B - Condensed Matter and Materials Physics*, vol. 71, no. 18, pp. 1–5, 2005.

[108] A. Durán, C. Herbert, M. García-Guaderrama, J. Mata, and G. Tavizón, "Zr and Mo doped $YMnO_3$: The role of dopants on the structural, microstructural, chemical state, and dielectric properties," *Ceramics International*, vol. 48, no. 12, pp. 17009–17019, 2022.

[109] R. D. Shannon, "Revised effective ionic radii and systematic studies of interatomic distances in halides and chalcogenides," *Acta Crystallographica Section A*, vol. 32, no. 5, pp. 751–767, 1976.

[110] H. W. Brinks, H. Fjellvåg, and A. Kjekshus, "Synthesis of Metastable Perovskite-type $YMnO_3$ and $HoMnO_3$," *Journal of Solid State Chemistry*, vol. 129, no. 2, pp. 334–340, 1997.

[111] K. Bergum, H. Okamoto, H. Fjellvåg, T. Grande, M. A. Einarsrud, and S. M. Selbach, "Synthesis, structure and magnetic properties of nanocrystalline $YMnO_3$," *Dalton Transactions*, vol. 40, no. 29, pp. 7583–7589, 2011.

[112] K. Uusi-Esko, J. Malm, N. Imamura, H. Yamauchi, and M. Karppinen, "Characterization of RMnO$_3$ (R = Sc, Y, Dy-Lu): High-pressure synthesized metastable perovskites and their hexagonal precursor phases," *Materials Chemistry and Physics*, vol. 112, no. 3, pp. 1029–1034, 2008.

[113] Y. H. Huang, H. Fjellvåg, M. Karppinen, B. C. Hauback, H. Yamauchi, and J. B. Goodenough, "Crystal and magnetic structure of the orthorhombic perovskite YbMnO 3," *Chemistry of Materials*, vol. 18, no. 8, pp. 2130–2134, 2006.

[114] J. H. Lee, P. Murugavel, H. Ryu, D. Lee, J. Y. Jo, J. W. Kim, H. J. Kim, K. H. Kim, Y. Jo, M. H. Jung, Y. H. Oh, Y. W. Kim, J. G. Yoon, J. S. Chung, and T. W. Noh, "Epitaxial stabilization of a new multiferroic hexagonal phase of $TbMnO_3$ thin films," *Advanced Materials*, vol. 18, no. 23, pp. 3125–3129, 2006.

[115] A. A. Bosak, C. Dubourdieu, J. P. Sénateur, O. Y. Gorbenko, and A. R. Kaul, "Epitaxial stabilization of hexagonal $R\mathrm{MnO}_3$ (R = Eu-Dy) manganites," *Journal of Materials Chemistry*, vol. 12, no. 4, pp. 800–801, 2002.

[116] K. Uusi-Esko, J. Malm, and M. Karppinen, "Atomic layer deposition of hexagonal and orthorhombic $YMnO_3$ thin films," *Chemistry of Materials*, vol. 21, no. 23, pp. 5691–5694, 2009.

[117] K. Uusi-Esko and M. Karppinen, "Extensive series of hexagonal and orthorhombic $R\mathrm{MnO}_3$ (R = Y, La, Sm, Tb, Yb, Lu) thin films by atomic layer deposition," *Chemistry of Materials*, vol. 23, no. 7, pp. 1835–1840, 2011.

[118] L. Rørmark, A. B. Mørch, K. Wiik, S. Stølen, and T. Grande, "Enthalpies of Oxidation of $CaMnO_{3\text{-}\delta}$, $Ca_2MnO_{4\text{-}\delta}$ and $SrMnO_{3\text{-}\delta}$ Deduced Redox Properties," *Chemistry of Materials*, vol. 13, no. 11, pp. 4005–4013, 2001.

[119] M. Chen, B. Hallstedt, and L. J. Gauckler, "Thermodynamic assessment of the Mn–Y–O system," *Journal of Alloys and Compounds*, vol. 393, no. 1-2, pp. 114–121, 2005.

[120] K. Cichy and K. Świerczek, "Influence of doping on the transport properties of $Y_{1\text{-x}}Ln_xMnO_{3+\delta}$ (Ln: Pr, Nd)," *Crystals*, vol. 11, no. 5, pp. 1–13, 2021.

[121] A. J. Overton, J. L. Best, I. Saratovsky, and M. A. Hayward, "Influence of Topotactic Reduction on the Structure and Magnetism of the Multiferroic $YMnO_3$," *Chemistry of Materials*, vol. 21, no. 20, pp. 4940–4948, 2009.

[122] J. W. Yeh, S. K. Chen, S. J. Lin, J. Y. Gan, T. S. Chin, T. T. Shun, C. H. Tsau, and S. Y. Chang, "Nanostructured high-entropy alloys with multiple principal elements: Novel alloy design concepts and outcomes," *Advanced Engineering Materials*, vol. 6, no. 5, 2004.

[123] B. Cantor, I. T. Chang, P. Knight, and A. J. Vincent, "Microstructural development in equiatomic multicomponent alloys," *Materials Science and Engineering A*, vol. 375-377, no. 1-2 SPEC. ISS., pp. 213–218, 2004.

[124] C. M. Rost, E. Sachet, T. Borman, A. Moballegh, E. C. Dickey, D. Hou, J. L. Jones, S. Curtarolo, and J. P. Maria, "Entropy-stabilized oxides," *Nature Communications*, vol. 6, 2015.

[125] B. L. Musicó, D. Gilbert, T. Z. Ward, K. Page, E. George, J. Yan, D. Mandrus, and V. Keppens, "The emergent field of high entropy oxides: Design, prospects, challenges, and opportunities for tailoring material properties," *APL Materials*, vol. 8, no. 4, 2020.

[126] A. Sarkar, L. Velasco, D. Wang, Q. Wang, G. Talasila, L. de Biasi, C. Kübel, T. Brezesinski, S. S. Bhattacharya, H. Hahn, and B. Breitung, "High entropy oxides for reversible energy storage," *Nature Communications*, vol. 9, no. 1, 2018.

[127] D. Bérardan, S. Franger, A. K. Meena, and N. Dragoe, “Room temperature lithium superionic conductivity in high entropy oxides,” *Journal of Materials Chemistry A*, vol. 4, no. 24, pp. 9536–9541, 2016.

[128] D. Bérardan, S. Franger, D. Dragoe, A. K. Meena, and N. Dragoe, “Colossal dielectric constant in high entropy oxides,” *Physica Status Solidi - Rapid Research Letters*, vol. 10, no. 4, pp. 328–333, 2016.

[129] A. Sarkar, B. Breitung, and H. Hahn, “High entropy oxides: The role of entropy, enthalpy and synergy,” *Scripta Materialia*, vol. 187, pp. 43–48, 2020.

[130] C. Oses, C. Toher, and S. Curtarolo, “High-entropy ceramics,” *Nature Reviews Materials*, vol. 5, no. 4, pp. 295–309, 2020.

[131] S. Jiang, T. Hu, J. Gild, N. Zhou, J. Nie, M. Qin, T. Harrington, K. Vecchio, and J. Luo, “A new class of high-entropy perovskite oxides,” *Scripta Materialia*, vol. 142, pp. 116–120, 2018.

[132] D. A. Vinnik, V. E. Zhivulin, E. A. Trofimov, S. A. Gudkova, A. Y. Punda, A. N. Valiulina, M. Gavrilyak, O. V. Zaitseva, S. V. Taskaev, M. U. Khandaker, A. Alqahtani, D. A. Bradley, M. I. Sayyed, V. A. Turchenko, A. V. Trukhanov, and S. V. Trukhanov, “A-site cation size effect on structure and magnetic properties of $Sm(Eu,Gd)Cr_{0.2}Mn_{0.2}Fe_{0.2}CO_{0.2}Ni_{0.2}O_3$ high-entropy solid solutions,” *Nanomaterials*, vol. 12, no. 1, 2022.

[133] J. Gild, Y. Zhang, T. Harrington, S. Jiang, T. Hu, M. C. Quinn, W. M. Mellor, N. Zhou, K. Vecchio, and J. Luo, “High-Entropy Metal Diborides: A New Class of High-Entropy Materials and a New Type of Ultrahigh Temperature Ceramics,” *Scientific Reports*, vol. 6, no. November, pp. 2–11, 2016.

[134] Q. Wang, A. Sarkar, D. Wang, L. Velasco, R. Azmi, S. S. Bhattacharya, T. Bergfeldt, A. Düvel, P. Heitjans, T. Brezesinski, H. Hahn, and B. Breitung, “Multi-anionic and -cationic compounds: New high entropy materials for advanced Li-ion batteries,” *Energy and Environmental Science*, vol. 12, no. 8, pp. 2433–2442, 2019.

[135] D. B. Miracle, J. D. Miller, O. N. Senkov, C. Woodward, M. D. Uchic, and J. Tiley, “Exploration and development of high entropy alloys for structural applications,” *Entropy*, vol. 16, no. 1, pp. 494–525, 2014.

[136] M. Gazda, T. Miruszewski, D. Jaworski, A. Mielewczyk-Gryń, W. Skubida, S. Wachowski, P. Winiarz, K. Dzierzgowski, M. Łapiński, I. Szpunar, and E. Dzik, “Novel Class of Proton Conducting Materials - High Entropy Oxides,” *ACS Materials Letters*, vol. 2, no. 10, pp. 1315–1321, 2020.

[137] G. K. Phani Dathar, J. Balachandran, P. R. Kent, A. J. Rondinone, and P. Ganesh, “Li-ion site disorder driven superionic conductivity in solid electrolytes: a first-principles investigation of β-Li_3PS_4,” *Journal of Materials Chemistry A*, vol. 5, no. 3, pp. 1153–1159, 2017.

[138] Y. Zeng, B. Ouyang, J. Liu, Y. W. Byeon, Z. Cai, L. J. Miara, Y. Wang, and G. Ceder, “High-entropy mechanism to boost ionic conductivity,” *Science*, vol. 378, no. 6626, pp. 1320–1324, 2022.

[139] A. A. Coelho, “Topas Academic: General profile and structure analysis software for powder diffraction data,” *Bruker AXS, Karlsruhe, Germany*, 2007.

[140] M. Newville, “Larch: An analysis package for XAFS and related spectroscopies,” *Journal of Physics: Conference Series*, vol. 430, no. 1, 2013.

[141] P. Virtanen, R. Gommers, T. E. Oliphant, M. Haberland, T. Reddy, D. Cournapeau, E. Burovski, P. Peterson, W. Weckesser, J. Bright, S. J. van der Walt, M. Brett, J. Wilson, K. J. Millman, N. Mayorov, A. R. Nelson, E. Jones, R. Kern, E. Larson, C. J. Carey, Polat, Y. Feng, E. W. Moore, J. VanderPlas, D. Laxalde, J. Perktold, R. Cimrman, I. Henriksen, E. A. Quintero, C. R. Harris, A. M. Archibald, A. H. Ribeiro, F. Pedregosa, P. van Mulbregt, and and SciPy 1.0 Contributors, “SciPy 1.0: fundamental algorithms for scientific computing in Python,” *Nature Methods*, vol. 17, no. 3, pp. 261–272, 2020.

[142] J. E. Post, “Manganese oxide minerals: Crystal structures and economic and environmental significance,” *Proceedings of the National Academy of Sciences of the United States of America*, vol. 96, no. 7, pp. 3447–3454, 1999.

[143] A. K. Padhi, K. S. Nanjundaswamy, and J. B. Goodenough, “Phospho-olivines as Positive-Electrode Materials for Rechargeable Lithium Batteries,” *Journal of The Electrochemical Society*, vol. 144, no. 4, pp. 1188–1194, 1997.

[144] A. K. Padhi, K. S. Nanjundaswamy, C. Masquelier, S. Okada, and J. B. Goodenough, “Effect of Structure on the Fe^{3+} / Fe^{2+} Redox Couple in Iron Phosphates,” *Journal of The Electrochemical Society*, vol. 144, no. 5, pp. 1609–1613, 1997.

[145] R. Sarangi, “X-ray absorption near-edge spectroscopy in bioinorganic chemistry: Application to M-O$_2$ systems,” *Coordination Chemistry Reviews*, vol. 257, no. 2, pp. 459–472, 2013.

[146] F. de la Peña, E. Prestat, V. T. Fauske, P. Burdet, J. Lähnemann, P. Jokubauskas, T. Furnival, M. Nord, T. Ostasevicius, K. E. MacArthur, D. N. Johnstone, M. Sarahan, J. Taillon, T. Aarholt, Pquinn-dls, V. Migunov, A. Eljarrat, J. Caron, C. Francis, T. Nemoto, T. Poon, S. Mazzucco, Actions-user, N. Tappy, N. Cautaerts, S. Somnath, T. Slater, M. Walls, F. Winkler, and H. W. Ånes, “hyperspy/hyperspy: Release v1.7.3,” 2022.

[147] D. B. Williams and C. B. Carter, *Transmission Electron Microscopy*, vol. 16. Boston, MA: Springer US, 2009.

[148] A. Žužić and J. Macan, “Permanganometric determination of oxygen nonstoichiometry in manganites,” *Open Ceramics*, vol. 5, no. October 2020, 2021.

[149] S. M. Hoggen, *Development of an asymmetrical oxygen permeable membrane based on hexagonal manganites*. Master’s thesis, Norwegian University of Science and Technology, 2016.

[150] M. M. Adnan, *A new material for oxygen-permeable membranes*. Master’s thesis, Norwegian University of Science and Technology, 2017.

[151] F. P. Danmo, *Development of a mixed-conducting layered oxide for asymmetric oxygen permeable membranes*. Master’s thesis, Norwegian University of Science and Technology, 2018.

[152] S. S. Kielland, *Development of An Asymmetrical Membrane for Oxygen Exchange and Production*. Master's thesis, Norwegian University of Science and Technology, 2019.

[153] E. Bakken, T. Norby, and S. Stølen, "Redox energetics of perovskite-related oxides," *Journal of Materials Chemistry*, vol. 12, no. 2, pp. 317–323, 2002.

[154] E. Bakken, J. Boerio-Goates, T. Grande, B. Hovde, T. Norby, L. Rørmark, R. Stevens, and S. Stølen, "Entropy of oxidation and redox energetics of $CaMnO_{3-\delta}$," *Solid State Ionics*, vol. 176, no. 29-30, pp. 2261–2267, 2005.

[155] E. Bakken, T. Norby, and S. Stølen, "Nonstoichiometry and reductive decomposition of $CaMnO_{3-\delta}$," *Solid State Ionics*, vol. 176, no. 1-2, pp. 217–223, 2005.

[156] R. Moreno, P. García, J. Zapata, J. Roqueta, J. Chaigneau, and J. Santiso, "Chemical Strain Kinetics Induced by Oxygen Surface Exchange in Epitaxial Films Explored by Time-Resolved X-ray Diffraction," *Chemistry of Materials*, vol. 25, no. 18, pp. 3640–3647, 2013.

[157] Q. Yang, T. E. Burye, R. R. Lunt, and J. D. Nicholas, "In situ oxygen surface exchange coefficient measurements on lanthanum strontium ferrite thin films via the curvature relaxation method," *Solid State Ionics*, vol. 249-250, pp. 123–128, 2013.

[158] R. Moreno, J. Zapata, J. Roqueta, N. Bagués, and J. Santiso, "Chemical Strain and Oxidation-Reduction Kinetics of Epitaxial Thin Films of Mixed Ionic-Electronic Conducting Oxides Determined by X-Ray Diffraction," *Journal of The Electrochemical Society*, vol. 161, no. 11, pp. F3046–F3051, 2014.

[159] E. J. Skiba, T. Chen, and N. H. Perry, "Simultaneous Electrical, Electrochemical, and Optical Relaxation Measurements of Oxygen Surface Exchange Coefficients: $Sr(Ti,Fe)O_{3-\delta}$ Film Crystallization Case Study," *ACS Applied Materials and Interfaces*, vol. 12, no. 43, pp. 48614–48630, 2020.

[160] M. Acosta, F. Baiutti, X. Wang, A. Cavallaro, J. Wu, W. Li, S. C. Parker, A. Aguadero, H. Wang, A. Tarancón, and J. L. MacManus-Driscoll, "Surface chemistry and porosity engineering through etching reveal ultrafast oxygen reduction kinetics below 400 °C in B-site exposed $(La,Sr)(Co,Fe)O_3$ thin-films," *Journal of Power Sources*, vol. 523, 2022.

[161] F. H. Danmo, I.-E. Nylund, A. Westermoen, K. P. Marshall, D. Stoian, T. Grande, J. Glaum, and S. M. Selbach, "Oxidation kinetics of nanocrystalline h-$RMn_{1-x}Ti_xO_{3+\delta}$ (R = Ho, Dy)," *Submitted*, 2023.

[162] M. Tomczyk, A. M. Senos, I. M. Reaney, and P. M. Vilarinho, "Reduction of microcracking in $YMnO_3$ ceramics by Ti substitution," *Scripta Materialia*, vol. 67, no. 5, pp. 427–430, 2012.

[163] M. Tomczyk, A. M. Senos, P. M. Vilarinho, and I. M. Reaney, "Origin of microcracking in $YMnO_3$ ceramics," *Scripta Materialia*, vol. 66, no. 5, pp. 288–291, 2012.

[164] J. A. Kuszyk and R. C. Bradt, "Influence of Grain Size of Effects of Thermal Expansion Anisotropy in $MgTi_2O_5$," *Journal of the American Ceramic Society*, vol. 56, pp. 420–423, 1973.

[165] R. K. Bordia and R. Raj, “Sintering Behavior of Ceramic Films Constrained by a Rigid Substrate,” *Journal of the American Ceramic Society*, vol. 68, no. 6, pp. 287–292, 1985.

[166] European Commission, “Study on the Critical Raw Materials for the EU,” tech. rep., 2023.

[167] M. Li, C. Wang, Z. Chen, K. Xu, and J. Lu, “New Concepts in Electrolytes,” *Chemical Reviews*, vol. 120, no. 14, pp. 6783–6819, 2020.

[168] D. T. Blagoeva, P. Alves Dias, A. Marmier, and C. C. Pavel, “Assessment of potential bottlenecks along the materials supply chain for the future deployment of low-carbon energy and transport technologies in the EU.,” *Wind power, photovoltaic and electric vehicles technologies, time frame*, vol. 2030, 2015.

[169] Z. L. Moreno Botello, A. Montenegro, N. Grimaldos Osorio, M. Huvé, C. Pirovano, D. R. Småbråten, S. M. Selbach, A. Caneiro, P. Roussel, and G. H. Gauthier, “Pure and Zr-doped $YMnO_{3+\delta}$ as a YSZ-compatible SOFC cathode: A combined computational and experimental approach,” *Journal of Materials Chemistry A*, vol. 7, no. 31, pp. 18589–18602, 2019.

Index

Appended papers

Manuscript I

Manuscript II

Manuscript III

Manuscript I

Oxygen absorption in nanocrystalline h-RMnO$_3$ (R=Y, Ho, Dy) and the effect of Ti donor doping

F. H. Danmo, B. A. D. Williamson, D. R. Småbråten, N. H. Gaukås, E. R. Østli, T. Grande, J. Glaum, and S. M. Selbach, *Manuscript submitted to Chemistry of Materials, under review*

Oxygen absorption in nanocrystalline h-RMnO$_3$ (R=Y, Ho, Dy) and the effect of Ti donor doping

Frida Hemstad Danmo, Benjamin A. D. Williamson, Didrik R. Småbråten, Nikolai H. Gaukås, Elise R. Østli, Tor Grande, Julia Glaum, and Sverre M. Selbach*

Department of Materials Science and Engineering, NTNU Norwegian University of Science and Technology, NO-7491 Trondheim, Norway.

**E-mail: selbach@ntnu.no*

Abstract

Hexagonal manganites, RMnO$_3$ (R = Sc, Y, Ho-Lu), can reversibly store and release large quantities of oxygen at temperatures in the range of 150-400 °C. The oxygen storage properties can be tuned by combining different R^{3+} cations, aliovalent dopants and crystallite sizes in the nanometer range. Here we study oxygen absorption of nanocrystalline RMn$_{1-x}$Ti$_x$O$_3$ (R = Y, Ho, Dy; x = 0, 0.15) using thermogravimetric analysis (TGA), and high-temperature X-ray diffraction (HT-XRD) in O$_2$ and N$_2$ atmospheres. The maximum oxygen storage capacity increases from R = Y through Ho and Dy, and even further with Ti^{4+} as a donor dopant. Density functional theory (DFT) calculations show that the observed trends in oxygen absorption capacity are correlated with the enthalpy of oxidation and the lattice parameters. Ti^{4+} also increases the thermal stability of absorbed oxygen and thereby extends the operation range to higher temperatures where the absorption and desorption kinetics are faster. Reducing the size of the crystallites improves the oxygen storage capacity as well as the absorption kinetics due to shorter diffusion distances. Finally, a thermodynamic model for oxidation of RMnO$_3$ is presented and fitted to TGA data and the implications for the microscopic understanding of the oxidation process are discussed.

INTRODUCTION

Oxides that can reversibly store and release oxygen at elevated temperatures find a broad range of applications, such as chemical looping combustion (CLC) for production of hydrogen and syngas, separation of oxygen from air using pressure swing adsorption (PSA), as automotive exhaust catalysts, and as electrodes in solid oxide fuel cells (SOFC).[1–5] CeO_2 and CeO_2-ZrO_2 solid solutions are among the most studied oxygen carriers and have been widely used for the treatment of exhaust gas, but are prone to a decrease in surface area due to particle coarsening at higher temperatures, causing an efficiency loss at lower temperatures and an increase in exhaust fumes.[6,7] For high temperature applications like pressure swing adsorption, sorbents such as those based on the $La_{1-x}Sr_xCo_{1-y}Fe_yO_{3-\delta}$ (LSCF) perovskite system,[5,8–10] and double perovskites such as $BaYMn_2O_{5+\delta}$[11] have been widely studied. Common to these material systems is that oxygen vacancies are the main point defects involved in oxygen storage and transport, and the concentration of vacancies can be tuned by aliovalent dopants.[6] The limited diffusivity of oxygen vacancies limit the lower temperature range of operation for these materials, and cation mobility at the necessary operating temperatures can lead to degradation in the form of coarsening, kinetic demixing[12] and surface segregation.[13]

Hexagonal manganites with composition RMnO$_3$ (R=Sc, Y, Ho-Lu) can store large amounts of oxygen at low temperatures[14,15] and are also more refractory than perovskites, indicated by the crystallization temperature from amorphous gel of at least 800 °C.[16] The layered hexagonal manganites are prone to anti-Frenkel defect formation[17] and can also incorporate excess oxygen on interstitial sites, which is possible due to the structure being less close-packed than the perovskite structure.[18–20] Oxygen interstitials move through an interstitialcy mechanism with a low energy barrier compared to those reported for vacancy migration in perovskites,[18,21–23] enabling oxygen transport and exchange at lower temperatures. Remsen and Dabrowski[14] first reported this reversible absorption and release of oxygen for $Dy_{1-x}Y_xMnO_{3+\delta}$ ($0 \leq \delta \leq 0.35$), and similar large excess oxygen values have later been reported for other RMnO$_3$ compositions.[15,24–30]

RMnO$_3$ oxides can crystallize in one of two crystal structures, depending on the ionic radius of the R^{3+} cation; larger cations ($r_{R^{3+}} \geq r_{Dy^{3+}}$) and a Goldschmidt tolerance factor of $t > 0.855$ favor orthorhombic perovskite structure with space group *Pnma*, while the hexagonal $P6_3cm$ structure is preferred for smaller rare earth ions ($r_{R^{3+}} \leq r_{Ho^{3+}}$) and $t < 0.855$.[31–35] The hexagonal phase is stabilized with respect to the orthorhombic phase both by high temperature and in inert or reducing conditions.[16,31] Crystallizing these materials in inert atmosphere at high temperatures can thus favor the hexagonal phase for R^{3+} larger than Ho^{3+}, and conversely high pressure,[36,37] low temperature,[38] and oxidizing atmosphere favors the orthorhombic phase even for smaller R^{3+}. The $P6_3cm$ structure is composed of alternating layers of seven-coordinated R^{3+} and five-coordinated Mn^{3+} in corner-sharing trigonal bipyramids, shown in Figure 1. Interstitial oxygen sites are located between three Mn^{3+} ions in the triangular lattice of MnO_5 bipyramids,[18] and are charge compensated by oxidation of two out of three nearest-neighbor Mn^{3+} to Mn^{4+}, as described by eq. (1) in Kröger-Vink notation:

$$\frac{1}{2}\mathrm{O_2(g)} + 2\,\mathrm{Mn_{Mn}^{x}} \rightarrow \mathrm{O_i''} + 2\,\mathrm{Mn_{Mn}^{\bullet}} \qquad (1)$$

For high oxygen contents, interstitial oxygen in the MnO_5 layers give rise to new hexagonal superstructures depending on the value of δ.[15,24,28] Partial substitution of Y^{3+} in $YMnO_3$ with larger R^{3+} such as Tb, Ce, Nd, and Sm improves the oxygen storage and transport properties of these materials, as oxygen absorption and ionic radius of R^{3+} are strongly correlated.[28–30,39–41] Donor dopants like Ti^{4+} on the Mn sublattice can also further increase the maximum storage capacity,[42,43] as oxygen interstitials (eq. 2) are energetically favored as a charge compensation mechanism for Ti^{4+} compared to reduction of Mn^{3+} to Mn^{2+} (eq. 3).[27]

$$2\,\mathrm{TiO_2} \rightarrow 2\mathrm{Ti_{Mn}^{\bullet}} + 3\,\mathrm{O_O^{x}} + \mathrm{O_i''} \qquad (2)$$

$$\mathrm{TiO_2} + \frac{1}{2}\,\mathrm{Mn_2O_3} \rightarrow \mathrm{Ti_{Mn}^{\bullet}} + 3\,\mathrm{O_O^{x}} + \mathrm{Mn_{Mn}'} + \frac{1}{4}\mathrm{O_2(g)} \qquad (3)$$

For Ti^{4+}-doped samples, the value of δ therefore depends on both the Ti^{4+} concentration and on the fraction of Mn present as Mn^{4+} in the system, as all oxidation of Mn is caused by excess oxygen.[43] The addition of Ti^{4+} also stabilizes the high temperature $P6_3/mmc$ structure from above the ferroelectric T_C of ~980 °C[44] to room temperature when cooling down the material in air or oxygen atmosphere.[43] This can be understood as Ti^{4+} and O_i softening the K_3 distortion mode driving the ferroelectric transition,[35,45,46] resulting in an expansion of the *ab*-plane, a contraction of the *c*-axis and a net unit cell expansion. The oxygen absorption of hexagonal manganites can also be tuned by particle size and morphology.[40,47] In general, catalytic activity for the splitting or recombination of O_2 molecules increases with decreasing particle size and increasing surface area.[48,49] Furthermore, the diffusion distance in smaller particles will be shorter and oxygen saturation will occur faster.[50] Asakura *et al.*[47] and Klimkowicz *et al.*[51] have both showed that the oxygen storage and release rate in $YMnO_3$ was enhanced for nanoparticles synthesized using a wet chemical synthesis method, compared to $YMnO_3$ bulk samples.

While the oxygen absorption of prototypical $YMnO_3$ has been studied with respect to aliovalent doping,[27,43] *R*-site substitution,[28–30,39,40] and particle size,[40,47,51] we hypothesize that these effects can be further enhanced by replacing Y^{3+} with Ho^{3+} or Dy^{3+}, as bulk undoped $HoMnO_3$ and $DyMnO_3$

both show larger oxygen storage capacity than $YMnO_3$.[14,15,24] Nanocrystalline and donor doped $HoMnO_3$ and $DyMnO_3$ are hence expected to show improved oxygen storage capacity compared to corresponding $YMnO_3$-based materials.

Here we study oxygen absorption and desorption in nanocrystalline hexagonal RMnO$_3$ (R = Y, Ho, Dy), with and without 15% Ti donor doping. The oxygen storage capacity increases with smaller crystallite size and larger R^{3+} cation from Y through Ho to Dy. Donor doping with Ti^{4+} on the Mn sublattice further increases the oxygen storage capacity and increases the thermal stability of excess oxygen, thereby extending the range of possible operating temperatures. We corroborate the experimental findings with DFT calculations which show a correlation between the enthalpy of oxidation and the enthalpy of formation for oxygen interstitials for different R^{3+}, as well as with lattice parameters. Unit cell expansion is suggested as an explanation for enhanced oxygen storage capacity, regardless of whether it is caused by chemical expansion from larger R^{3+}, softening of the ferroelectric mode by Ti^{4+} doping, or by finite size-induced lattice expansion.[16]

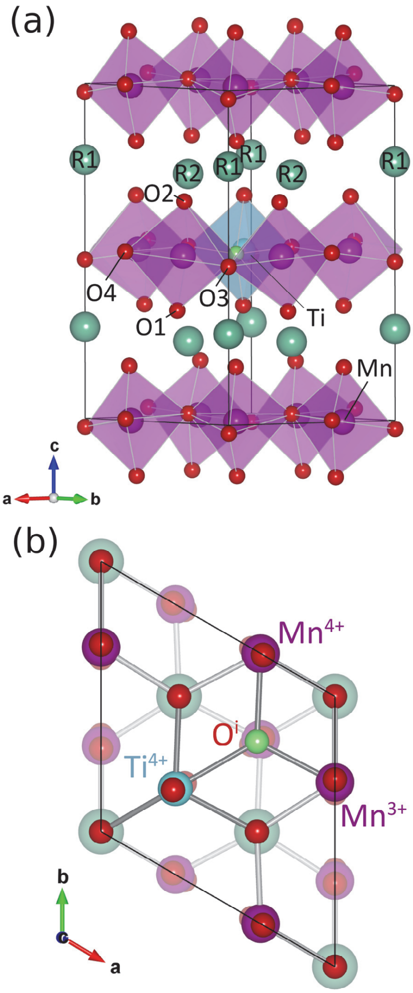

Figure 1. (a) The hexagonal crystal structure with space group $P6_3cm$ of $R\mathrm{MnO}_3$ with purple MnO_5 bipyramids, blue Ti^{4+} on the Mn-lattice, turquoise R atoms, and green spheres indicating interstitial oxygen. (b) Position of interstitial oxygen in the Mn-O triangular lattice, with the added Ti on the Mn site.

METHODS

Synthesis. Undoped and Ti-doped nanocrystalline *R*MnO$_3$ samples were prepared using a modified citric acid synthesis method previously reported by Bergum *et al.*[16] For the precursor solutions, Y(CH$_3$CO$_2$)$_3$·xH$_2$O (Aldrich), Ho(CH$_3$CO$_2$)$_3$·xH$_2$O (AlfaAesar), Dy(CH$_3$CO$_2$)$_3$·xH$_2$O (AlfaAesar), and Mn(CH$_3$CO$_2$)$_3$·xH$_2$O (Riedel-de-Haën) were each dissolved in a mixture of citric acid (99%, Sigma-Aldrich) and deionized water while stirring at 400 rpm on a hot plate set to 150 °C, resulting in a molar ratio of cation to citric acid of 1:15 for Y^{3+}, 1:20 for Ho^{3+}, 1:35 for Dy^{3+}, and 1:5 for Mn^{3+}. For the Ti^{4+} precursor solution, titanium (IV) isopropoxide (TTIP) (Sigma-Aldrich) was added to a mixture of citric acid and deionized water kept at 60 °C under stirring in a molar ratio of 1:6.3. Stoichiometric amounts of cation precursors were mixed with ethylene glycol (EG) (Merck), with a 1:1 molar ratio between EG and citric acid. The final solutions were kept on a hot plate at 150 °C until a viscous gel was formed. This gel was heated to 400 °C and kept for 3 h, before heating to 600 °C at a rate of 200 °C h^{-1} and calcined for 6 h. The resulting amorphous powders were crystallized in N$_2$ atmosphere at temperatures ranging from 850 to 1000 °C to obtain different crystallite sizes. Ho- and Dy-containing samples were pre-annealed in 5% H$_2$ in N$_2$ to reduce a fraction of Mn^{3+} to Mn^{2+} prior to crystallization to reduce the effective tolerance factor and favor crystallization of the hexagonal phase.

Characterization. X-ray diffraction (XRD) was performed with a Bruker D8 Focus with Cu Kα radiation. Lattice parameters and average crystallite size of the powders were determined by Pawley refinement using TOPAS 5.[52] Oxygen stoichiometry was determined by thermogravimetric analysis (TGA) with a Netzsch STA 449C Jupiter with flowing O$_2$. The samples were first heated to 800 °C at 200 °C h^{-1} in O$_2$ atmosphere and subsequently cooled using rates of 20 °C min^{-1} inside the TGA to purge excess oxygen before measurements. Ti-doped DyMnO$_3$ was annealed for 10 h at 600 °C in N$_2$ to avoid rapid oxidation of this material during cooling. TGA was carried out from ambient to 800 °C in O$_2$ atmosphere with heating and cooling rates of 1 °C min^{-1}, except for the Ti-doped DyMnO$_3$ sample, which could be measured at 10 °C min^{-1} due to very fast oxidation kinetics. High temperature X-ray diffraction (HT-XRD) was performed with a Bruker D8 Advance with Cu Kα radiation to investigate the changes in lattice parameters for the samples in O$_2$ and N$_2$ atmospheres. The samples were measured with 25 °C intervals, first during heating to 550 °C and 700 °C for undoped and Ti-doped samples, respectively, then during cooling to 50 °C, and thereafter during re-heating to 550 or 700 °C, respectively. The samples were finally cooled to room temperature, and the measurements were repeated in N$_2$ atmosphere. All samples were heated to 500 °C in N$_2$ atmosphere for 10 h prior to the HT-XRD measurements to purge excess oxygen. The lattice parameters were determined by Pawley refinements using TOPAS 5.[53,54] Diffractograms of all samples were refined with the $P6_3cm$ space group, except for $DyMnO_3$ where the $Ia\overline{3}$ space group was included to account for the presence of Dy_2O_3. The $R3c$ structure[15,24] was used instead of the $P6_3cm$ for the highly oxidized h-$DyMnO_3$ phase in O_2 atmosphere to account for superstructure peaks. The c lattice parameter of the $R3c$ structure (Z=18) was divided by 3 for direct comparison with the $P6_3cm$ (Z=6) structure.

Computational details. All calculations were performed using plane-wave periodic density functional theory (DFT) within the Vienna *ab-initio* Simulation Package (VASP)[55–58] and the PBEsol[59] functional. The projector-augmented wave (PAW) method[60] was employed to describe the interactions between the core and the valence electrons using the Y_sv, Dy_3, Ho_3, Er_3, Mn_pv, Ti_sv and O pseudopotentials supplied with VASP, where all *f*-electrons are kept in the pseudopotential core. A Hubbard U[61] value of 3 eV on Mn 3d was used to account for self-interactions and a frustrated collinear antiferromagnetic (F-AFM) order was set to approximate the true non-collinear magnetic structure.[18]

Structural optimizations of bulk $RMnO_3$ were performed using a plane-wave energy cut-off of 550 eV and a Γ-centred k-point mesh of 4×4×2 allowing atomic positions, lattice vector and cell angle and volume to relax until forces on all atoms were less than 0.01 eV $Å^{-1}$. To simulate the effects of oxygen absorption, the formation enthalpy of an oxygen interstitial (O_i), corresponding to a very low δ, was calculated using 2x2x1 supercells (120+1 atoms) created from relaxed bulk structures. To simulate a very high δ value, two O_i were inserted into the 30-atom unit cell, one in each Mn-O layer, giving a stoichiometry of $R_6Mn_6O_{20}$ or $RMnO_{3.33}$ and the cells were fully relaxed. To simulate Ti-doping, 1 out of 24 Mn in a 120-atom supercell was replaced by Ti. This lower concentration (~4%) compared to the experimental (15%) was chosen instead of 1 out of 6 Mn in a 30 atom unit cell (~17%) to avoid artificial Ti-ordering due to periodic boundary conditions.

The enthalpy of formation of a defect (D) in a charge neutral cell was calculated from:

$$\Delta H_f(D) = (E^{D,q} - E^H) + \sum_i (E_i + \mu_i)\,, \tag{4}$$

where E^H and $E^{D,q}$ are the total energies of the undoped host and defect supercells respectively, and E_i and μ_i correspond to the elemental reference energy of species 'i' and the associated chemical potential, respectively. Charged supercells were not calculated due to the large non-stoichiometry found in these materials. The enthalpy of oxidation was calculated per mole O_2 (g) using equation (5)[62]

$$R_6\mathrm{Mn}_6\mathrm{O}_{18}\ (\mathrm{s}) + \mathrm{O}_2\ (\mathrm{g}) = R_6\mathrm{Mn}_6\mathrm{O}_{20}. \tag{5}$$

RESULTS

The hexagonal $P6_3cm$ structure is the main phase in all investigated samples, as indicated by the X-ray diffractograms of the as-synthesized materials shown in Figure 2. Traces of the orthorhombic *Pnma* phase are found in the Ho-containing samples, indicated with asterisks. The $DyMnO_3$ sample contains ~14% Dy_2O_3 as a secondary phase as determined from Rietveld (Supplementary Note 1). Pre-annealing in 5% H_2 atmosphere followed by high-temperature crystallization in N_2 favors the hexagonal phase, while a one-step crystallization of samples with R = Dy in N_2 gave mainly the competing orthorhombic perovskite phase. The increased background in Ti-doped $YMnO_3$ is caused by the Kapton polyimide film protecting the sample. The (012) and (014) reflections, characteristic for the $P6_3cm$ space group, are less pronounced for the samples containing Ti compared to undoped materials.

Refined lattice parameters from Pawley refinement show that the unit cell dimensions increase with R cation size, with Ti doping, and with smaller crystallite size, in agreement with previous work.[16,63] All samples are nanocrystalline with average crystallite sizes ranging from 21 to 39 nm. The composition, sample labelling, refined lattice parameters a and c, and refined crystallite size for all as-synthesized samples are summarized in Table 1. All samples are labelled based on composition and crystallite size. The a and c parameters are similar in value for all the undoped $R\mathrm{MnO}_3$ samples, with $DyMnO_3$ having a subtly larger a parameter, expected from the larger Shannon radius of 7-coordinated Dy (1.027 Å) compared to that of Y (0.96 Å) and Ho (1.015 Å).[64] The samples with the largest refined crystallite sizes are also the same samples that were crystallized at the highest temperatures. Thermal and atmospheric history of all samples is summarized in Table S1. While Ti^{4+} (0.51 Å) is smaller than Mn^{3+} (0.58 Å), the expansion of the unit cell with addition of Ti^{4+} can be rationalized from charge-compensating reduction of Mn^{3+} (0.58 Å) to the larger Mn^{2+} (0.75 Å) in N_2 atmosphere.

Table 1: Composition, naming, and Pawley refined lattice parameters and crystallite sizes of as-synthesized $R\text{Mn}_{1-x}\text{Ti}_x\text{O}_3$ samples. All samples were refined within the $P6_3cm$ space group.

Composition	Crystallite size (nm)	Sample name	*a* (Å)	*c* (Å)	Volume (Å^3)	*c*/*a*
$YMnO_3$	25 ± 1	YMO25	6.141(4)	11.365(4)	371.2	1.850
$YMnO_3$	39 ± 1	YMO39	6.132(5)	11.351(5)	369.7	1.851
$YMn_{0.85}Ti_{0.15}O_3$	21 ± 1	YMTO21	6.194(4)	11.383(8)	378.3	1.837
$HoMnO_3$	25 ± 1	HMO25	6.131(0)	11.371(0)	370.2	1.854
$HoMnO_3$	38 ± 1	HMO38	6.130(1)	11.361(6)	369.7	1.853
$HoMn_{0.85}Ti_{0.15}O_3$	28 ± 1	HMTO28	6.141(8)	11.400(0)	372.4	1.856
$DyMnO_3$	30 ± 1	DMO30	6.162(3)	11.368(8)	373.9	1.844
$DyMn_{0.85}Ti_{0.15}O_3$	30 ± 1	DMTO30	6.199(3)	11.433(3)	380.5	1.844

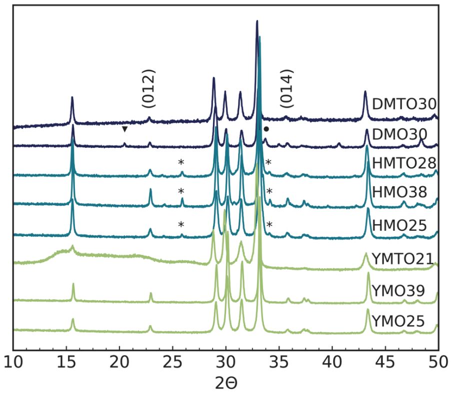

Figure 2. X-ray diffractograms of as-synthesized materials with compositions and labels explained in Table 1. The asterisks (*) indicate reflections originating from the competing orthorhombic perovskite phase, the circle (●) indicates the presence of Dy_2O_3, while the triangle (▼) mark an unidentified reflection.

An essential property of oxygen carriers is the amount of oxygen that can be stored within the material. The maximum oxygen storage capacity of all investigated samples increases with increasing *R* cation size, decreasing crystallite size, and with the addition of Ti. The changes in oxygen stoichiometry as a function of temperature, measured using thermogravimetry, are shown in Figure

3. All undoped samples (Figure 3a) absorb oxygen during heating starting from about 200 °C, with the absorbed oxygen being stabilized towards increasingly higher temperatures from Y through Ho to Dy. The maximum δ values also follow the same trend, with Dy having a maximum of $\delta = 0.25$ during cooling (the Dy_2O_3 phase in this sample is assumed not to oxidize). The value of δ compares well with those reported for measurements done at 1 °C min^{-1} in previous studies.[29,51,65] The smaller crystallite samples, YMO25 and HMO25, display a greater oxygen absorption than the larger crystallite samples, YMO39 and HMO38. The temperature interval where oxygen desorption occurs also becomes increasingly narrower from Y to Ho and, especially Dy. A hysteresis in the oxygen content, with a width of up to 100 °C, is observed during cooling and heating, as also reported for other $RMnO_3$.[29,40]

For the Ti-doped samples in Figure 3b, the same trend in maximum value of δ as a function of R can be seen as for the undoped samples in Figure 3a. The temperature intervals for which oxygen absorption and release occurs are also significantly expanded for all the Ti-doped samples compared to the undoped materials. An anticipated plateau at $\delta = 0.075$, corresponding to all Mn present as Mn^{3+} is not reached even at 800 °C, which is the highest temperature measured. Donor doping with Ti^{4+} thus strongly stabilizes O_i to higher temperatures. Compared to the undoped samples displayed in Figure 3a, the maximum excess oxygen for each $RMnO_{3+\delta}$ is also greatly enhanced with Ti substitution, with an increase from $\delta = 0.10$ in YMO25 to 0.27 in YMTO21, from $\delta = 0.17$ in HMO25 to 0.33 in HMTO28, and from $\delta = 0.25$ in DMO30 to 0.35 in DMTO30. The point of maximum excess oxygen during heating is also shifted towards higher temperatures for R = Y, Ho. Some thermal hysteresis in the oxygen content can be seen for the R =Y, Ho samples, while DMTO30 shows little to no hysteresis, suggesting significantly faster oxygen transport kinetics for the latter sample. For calculating δ, a reference point where all Mn is assumed to be Mn^{3+} was chosen at the minimum mass from TGA above 500 °C for each measurement. This point was set to $\delta = 0$ and $\delta = 0.075$ for undoped and Ti-doped samples, respectively, although the Ti-doped samples do not reach a stable plateau even at 800 °C.

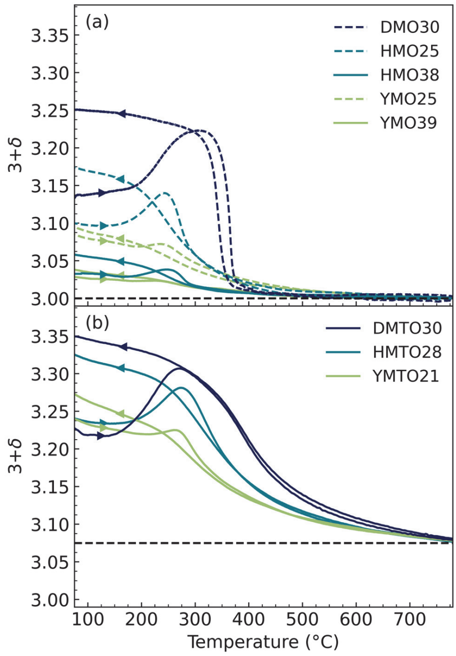

Figure 3. Oxygen stoichiometry during heating and cooling in O_2 for hexagonal $R\text{MnO}_{3+\delta}$ (R=Y, Ho, Dy) for different rare earth cations and crystallite sizes with (a) 0% and (b) 15% Ti donor doping.

X-ray diffractograms for all investigated samples measured with 25 °C increments during *cooling* in oxygen atmosphere are displayed in Figure 4. Incorporation of interstitial oxygen causes a unit cell expansion in the *ab*-plane and a unit cell contraction along the *c*-axis, with the latter easily seen from the position of the (004) reflection. For both undoped and Ti-doped Y and Ho containing samples, the (004) reflection is shifted towards higher 2θ values, while an additional reflection adjacent to the (004) appears for the DMO30 and DMTO30 samples, as discussed further below.

The (004) reflection at approximately 2θ = 31.4° in all diffractograms is shifted towards higher 2θ angles during oxidation, signifying a contraction of the *c* lattice parameter. This shift in (004) position becomes more pronounced from *R* = Y through Ho to Dy for both undoped and Ti-doped samples. The onset temperature for the shift occurs between 150 and 250 °C for undoped samples, and at increasingly higher temperatures for the Ti-doped samples from *R* = Y through Ho and Dy. Ti-doped samples display this (004) position shift over a wider temperature range compared to undoped $R\text{MnO}_3$

samples. Both the relative magnitude and the temperature ranges of (004) shifts agree with the oxygen storage capacities and oxidation onset temperatures observed from the TGA data in Figure 3. Along with the shift of (004), the (110) and (111) reflections are shifted towards lower 2θ angles for all samples. For all *R* = Y and Ho undoped samples, broadening of the (004) reflections is observed upon oxidation, most prominently for HMO25, and this is attributed to inhomogeneous lattice strain caused by oxygen interstitials. For the DMO30 sample, the shift of the (004) reflection is accompanied by a new reflection at approximately 2θ = 31.5°. A similar reflection is also observed for the DMTO30 sample in Figure 4 (f), with this new reflection gradually appearing at 2θ = 31.5° while the original reflection is shifted towards 2θ = 32° during cooling. For the DMO30 sample, the reflection appearing at ~29° 2θ is due to Dy_2O_3 secondary phase.

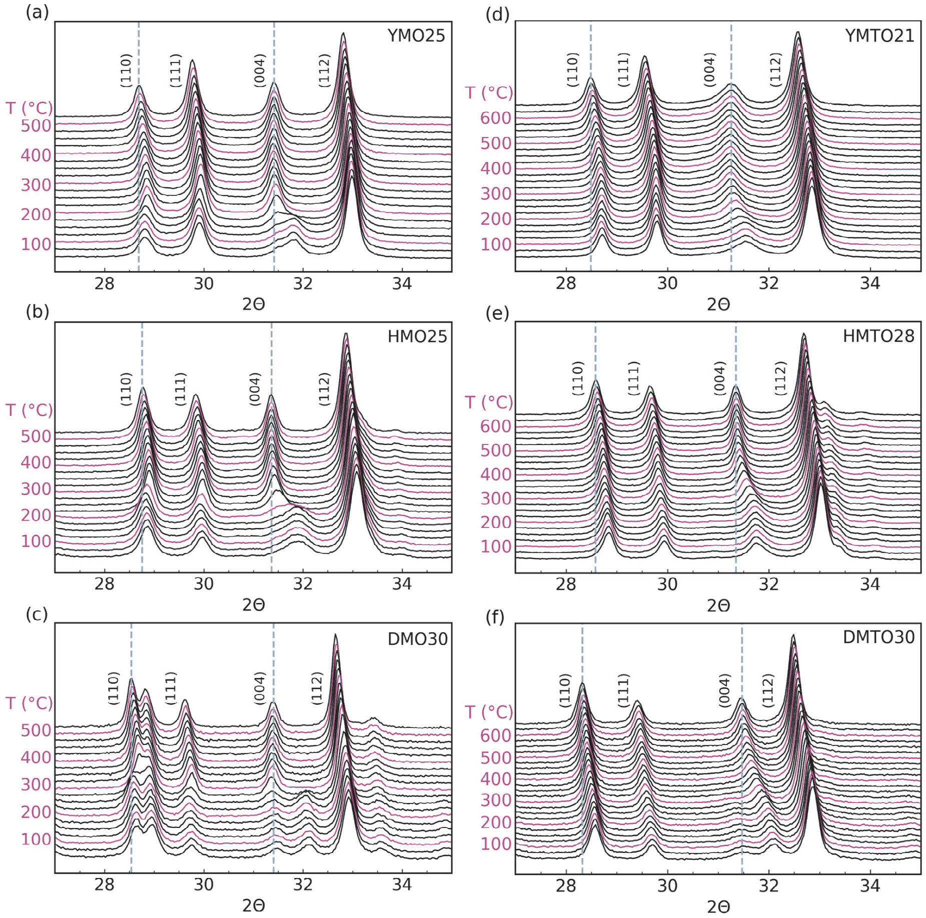

Figure 4. X-ray diffractograms of (a) $YMnO_3$, (b) $HoMnO_3$, (c) $DyMnO_3$, (d) $YMn_{0.85}Ti_{0.15}O_3$, (e) $HoMn_{0.85}Ti_{0.15}O_3$, and (f) $DyMn_{0.85}Ti_{0.15}O_3$ measured every 25 °C during cooling in O_2 atmosphere.

The lattice parameters reflect the oxidation of the materials as the incorporation of interstitial oxygen into the MnO_5 layers cause significant anisotropic chemical expansion, as already evident from the X-ray diffractograms presented in Figure 4. All samples show shifts in refined lattice parameters (Figure 5) during heating and cooling in O_2 atmosphere, but not in N_2 atmosphere, confirming that the structural changes are caused by the reversible absorption and release of oxygen. The thermal evolution of lattice parameters *a* and *c* in O_2 and N_2 atmosphere are shown for undoped samples in

Figure 5a and Ti-doped samples in Figure 5b. For the undoped $R\mathrm{MnO_3}$ (R = Y, Ho, Dy) samples, there is an abrupt and large change in both lattice parameters during cooling in O_2 from high temperatures as oxygen is absorbed at temperatures between 150 °C and 300 °C, depending on R. The c axis contracts and the ab plane expands over a temperature interval of approximately 100 °C for R = Y, Ho, while for R = Dy the temperature interval is only ~25 °C. During heating, the reverse changes take place as oxygen is released, but this occurs over a smaller temperature interval of only ~25 °C, and at slightly higher temperatures than the absorption during cooling for R = Y, Ho, constituting a small hysteresis. For R = Dy, no hysteresis can be seen, which is in accordance with the small thermal hysteresis found from TGA results presented in Figure 3. The temperature ranges of abrupt anisotropic changes in lattice parameters agree with the TGA results presented in Figure 3, confirming oxygen absorption and release as the origin of the anisotropic lattice contraction and expansion, respectively. The magnitude of change of the c parameter in Figure 5a reflects the increasing amount of incorporated O_i from Y to Ho and Dy as shown in Figure 3. As expected, during heating and cooling in N_2, no abrupt changes in lattice parameters are observed.

The increased oxygen storage capacity and thermal stability of O_i caused by Ti doping of $R\mathrm{MnO_3}$, evident from the TGA data in Figure 3, is also reflected by the changes in lattice parameters upon heating and cooling in O_2 and N_2. Both lattice parameters are subtly larger for Ti-doped YMTO21 than for undoped YMO25, indicating a net expansion of the unit cell upon Ti-doping. Lattice parameters a and c for the Ti-doped YMTO21 show qualitatively similar changes in O_2 as for the undoped YMO25, but the chemical expansion and contraction is spread out over a wider temperature interval, as expected from the TGA data in Figure 3. YMTO21 also differ from YMO25 by displaying little to no hysteresis upon heating and cooling, and a plateau at T = 350 °C is reached during heating in O_2, after which only thermal and no chemical expansion is observed as the sample is heated further. Even at higher temperatures there is a gap between the c parameter measured in O_2 and in N_2, indicating that a significant content of absorbed oxygen is stabilized towards higher temperatures by Ti doping. In N_2 atmosphere, no significant change in lattice parameters can be seen beyond thermal expansion in the ab-plane.

In O_2 atmosphere, the HMTO28 and DMTO30 samples behave similarly to the YMTO21 sample. For HMTO28, the sample does not seem to reach a definitive plateau where only thermal expansion is observed during heating, indicating that chemical expansion from interstitial oxygen vacating the structure occurs up to at least T = 700 °C. There is also a visible shift in the c parameter during heating and cooling in N_2 atmosphere, suggesting that some incorporation of O_i takes place even in a low pO_2 atmosphere (nominally 5.0 purity, $\sim 10^{-4}$–10^{-6} atm). The gap between the high temperature values of the *c* parameter in O_2 and N_2 atmosphere indicates that O_i is stabilized to higher temperatures to a greater extent than in YMTO21. No hysteresis in the lattice parameters can be seen for neither the HMTO28 nor the DMTO30 samples in O_2, but there is a visible hysteresis in N_2 for the *c* parameter for the former, and for both parameters for the latter. For DMTO30, transition from the highly oxidized state at low temperatures to the low oxidized state at higher temperatures in O_2 is gradual and occurs over a broad temperature interval, as can be seen from the *c* parameters in Figure 5b for DMTO30. The *c* parameter differs significantly between N_2 and O_2 atmospheres even at 700 °C, indicating a significant concentration of O_i in O_2 atmosphere at high temperatures.

For all samples, the expansion and contraction in the *ab* plane during absorption and desorption of O_i is less significant for the Ti-doped samples, with almost no change in values for HMTO28. For DMTO30 the expansion/contraction in the *a* parameter is reversed during absorption/release in O_2 compared to the other samples, as discussed further below. For the latter sample, expansion and contraction is also seen for the *a* parameter in N_2 atmosphere.

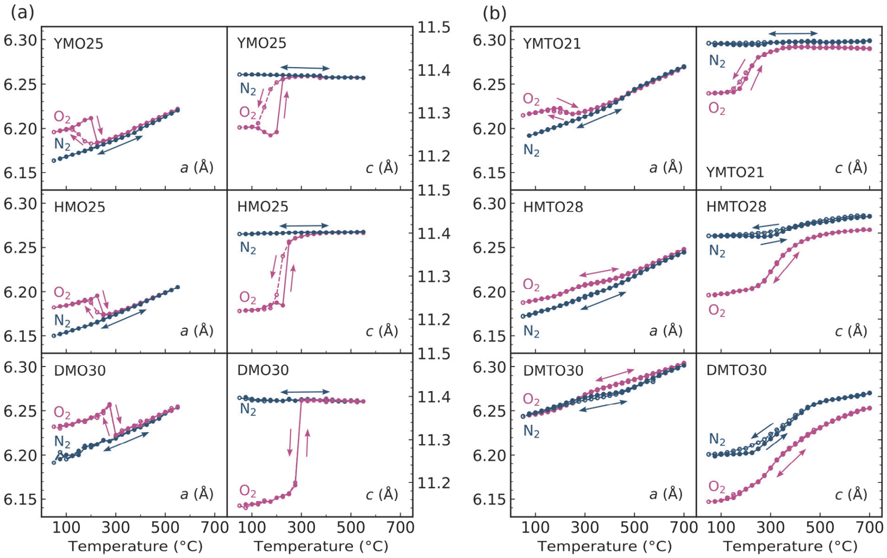

Figure 5. Refined lattice parameters *a* and *c* as a function of temperature for (a) undoped and (b) Ti-doped $RMnO_{3+\delta}$ (*R* = Y, Ho, Dy) in O_2 and N_2 atmosphere.

The DFT calculated lattice parameters of $R\mathrm{MnO_3}$ and the ‘maximally oxidized’ model case of $R\mathrm{MnO_{3.33}}$ are strongly correlated with the size of the R^{3+} cation, as shown in Figure 6a. The lattice parameters for R = Dy, Ho and Er scale close to linearly with cation size, while R = Y has somewhat larger than expected lattice parameters compared to the other R, which are 4f rather than 4d elements. The trends in lattice parameters reflect the experimentally observed in Table 1 and Figure 5. Er is included to the computational study as a reference to illustrate the trends with R^{3+} radius as isostructural $\mathrm{ErMnO_3}$ is known to oxidize less readily than the materials studied here.[15] The DFT calculated 0 K chemical expansion (calculated using eq. (S2)) resulting from incorporating two $\mathrm{O_i}$ per 30-atom unit cell is presented in Figure 6c. While the qualitative trends between different R are reproduced, the chemical expansion from DFT is smaller than what was experimentally measured using HT-XRD, shown in Figure 5. This quantitative difference is attributed to the calculations being done for a 0 K situation and with artificially ordered $\mathrm{O_i}$ because of periodic boundary conditions. The highly anisotropic chemical expansion, with expansion of the *ab* plane and contraction of the *c* axis upon oxidation, becomes smaller for larger R. The potential for chemical expansion of the *ab* plane is smaller for larger R where the lattice parameters are already expanded by the chemical pressure exerted by larger R cations. This trend is supported by the lattice parameters inferred from HT-XRD in $\mathrm{N_2}$ and $\mathrm{O_2}$ in Figure 5. The contraction of the *c* axis follows a reduction of the amplitude of the K_3 distortion mode[45] driving the ferroelectric transition. Inclusion of $\mathrm{O_i}$ leads to a reduction of the $\mathrm{MnO_5}$ tilting angle[18] and the corrugation of the R layer is strongly coupled to this polyhedral tilting through the short and strong R2-O4 ionic bond[46].

The thermodynamic driving force for oxidation is now computationally addressed. For low contents of absorbed oxygen, supercells with stoichiometry ~$R\mathrm{MnO_{3.04}}$ are used to calculate the enthalpy of formation for a single $\mathrm{O_i}$. A clear trend is observed that incorporation of an $\mathrm{O_i}$ defect becomes more energetically favorable for larger R (Figure 6d), although the formation enthalpies are of very similar magnitude. The formation enthalpies are plotted as a function of DFT relaxed unit cell volume for stoichiometric materials. Compared to the undoped compounds, Ti-doping strongly stabilizes $\mathrm{O_i}$ formation by 0.49 to 0.75 eV, and more for larger than smaller R. (Figure 6e). A negative enthalpy of formation for a point defect is uncommon and depends strongly on the choice of oxygen chemical potential (here: oxidizing limit, μ_O = -5.14 eV) and on the choice of Hubbard U as a larger U will favor occupation of transition metal d-states and thus energetically disfavor oxidation. However, a negative enthalpy of oxidation is necessary to give a negative Gibbs free energy of oxidation, as experimentally observed, as the oxidation reaction where $\mathrm{O_2}$ molecules are consumed must have a large negative entropy of reaction.

To assess the thermodynamic driving force for ‘full’ oxidation, the enthalpy of oxidation is calculated per O_2 molecule, as shown in Figure 6f. Following the arguments above, the enthalpies of oxidation are negative as expected and this is the driving force for the oxidation reaction. The calculated values for different R show the same spread as the O_i formation enthalpies in Figure 6d with values corresponding to -78 to -84 kJ mol^{-1}, but do not follow the same simple trend with R^{3+} radius. This suggest that thermodynamics alone cannot explain the experimentally observed differences in oxygen storage capacity for different R, as discussed further below.

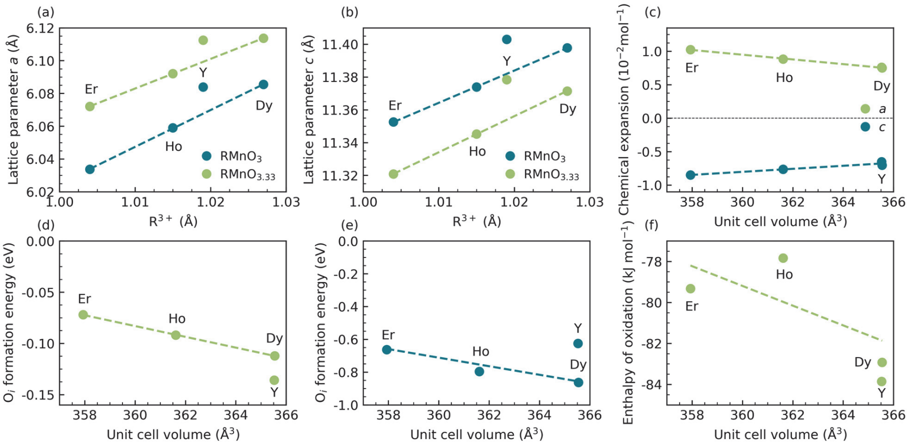

Figure 6. (a-b) DFT calculated lattice parameters of $R\mathrm{MnO}_3$ and $R\mathrm{MnO}_{3.33}$ ($R_6\mathrm{Mn}_6\mathrm{O}_{20}$) as a function of R^{3+} Shannon radius.[64] (c) Chemical expansion as a function of DFT relaxed stoichiometric unit cell volume. Formation enthalpy for a single O_i point defect in a charge neutral 120-atom supercell for (d) undoped and (e) Ti-doped materials. (f) Enthalpy of oxidation per O_2 molecule for the undoped materials from the reaction $R_6\mathrm{Mn}_6\mathrm{O}_{18}$ + O_2 (g) = $R_6\mathrm{Mn}_6\mathrm{O}_{20}$. Dashed lines are guides to the eye connecting Er, Ho and Dy data points (similar pseudopotentials, see text for explanation).

DISCUSSION

Nanocrystalline samples show greater oxygen storage capacity than bulk material cooled at the same rate. As reducing the crystallite size does not increase the thermal stability of absorbed oxygen, the observed increase in capacity is mainly attributed to shorter diffusion distances which allow exchange of oxygen with the atmosphere down to lower temperatures.[50] A larger surface area will also improve the oxygen surface exchange kinetics, but it is not known whether bulk diffusion or surface exchange is the rate-limiting factor for oxygen absorption and desorption in these materials.

Ti-doping and application potential. As evident from TGA (Figure 3) and HT-XRD (Figures 4 and 5), Ti-doping raises both the measured maximum oxygen absorption capacity and the thermal stability of absorbed oxygen compared to undoped materials, following eq. (2). As a donor dopant, Ti^{4+} on Mn^{3+} sites, increases the electrostatic attraction for O_i in the position illustrated in Figure 1 and only one Mn^{3+} needs to be oxidized instead of two for charge compensation in the vicinity of Ti^{4+}. Furthermore, as eq. (3) describes, a Ti^{4+} donor dopant that is not charge compensated by an O_i leads to a reduction of d^4 Mn^{3+} to d^5 Mn^{2+}. In the trigonal bipyramidal crystal field splitting this implies occupation of the higher energy Mn $3d_{z^2}$ orbital,[66] creating a strong thermodynamic driving force for absorption of O_i (eq. (2)) to avoid reduction of Mn^{3+} to Mn^{2+} (eq. (3)). This interpretation is supported by the present and previous[67] DFT calculations. Increasing the stability of absorbed oxygen to higher temperatures may raise the kinetics of pressure-swing separation of oxygen from air, but the broad temperature interval of oxygen absorption for Ti-doped samples is less ideal for temperature-swing separation. Ti-doping also reduces thermal hysteresis in oxygen absorption (Figure 3) and further studies are needed to understand the kinetics of bulk mass transport and oxygen surface exchange to identify possible rate-limiting steps. In contrast, for undoped materials, R = Dy gives both the highest oxygen storage capacity and thermal stability as well as a narrow temperature interval of oxidation, which is preferable for temperature-swing separation of oxygen from air.

Chemical and thermal expansion. The large differences in oxygen absorption for the different R cations agree with literature reports[14,15,24–26] on undoped materials. Y-containing samples display the smallest absorption and Dy-samples the largest, following a trend in Shannon radii where larger R^{3+} cations give larger oxygen absorption, although no significant difference in lattice parameters was observed experimentally between $YMnO_3$ and $HoMnO_3$ with similar crystallite sizes (Table 1). The change in the c lattice parameter upon oxygen absorption and release is correlated with the amount of oxygen absorbed, while a corresponding trend is not seen for the *ab*-plane. The larger R^{3+} cations are believed to expand the ab-plane and thus reduce the electrostatic repulsion between O_i and regular planar O3 and O4 and therefore thermodynamically favor oxygen absorption. For initial oxygen absorption for low δ values, this hypothesis is supported by the DFT calculated O_i formation enthalpies in Figure 6d, while the situation is likely to become more complex upon gradual filling of vacant O_i sites as no simple trend is observed for the enthalpy of oxidation in Figure 6f. Following the unit cell expansion hypothesis, Ti-doping also expands the *ab*-plane (Table 1) despite the smaller

Shannon radius of Ti^{4+} compared to Mn^{3+}, and this expansion is attributed to partial rectification of tilted corner-sharing MnO_5 bipyramids.[35]

Anisotropic chemical expansion (CE) and thermal expansion (TE) are summarized in Figure 7 where the thermal expansion (Figure 7a) is inferred from HT-XRD data collected upon cooling in N_2 atmosphere. Details on how CE and TEC were calculated are given in the Supporting Information. Any 'excess' expansion or contraction of the lattice parameter i in O_2 atmosphere upon cooling is attributed to chemical expansion (Figure 7b) and calculated from $CE = \frac{1}{i_o}\left(\frac{\Delta i}{\delta}\right)$ with $\Delta\delta$ taken from the TGA measurements presented in Figure 3. Estimated error bars are smaller than the symbol size.

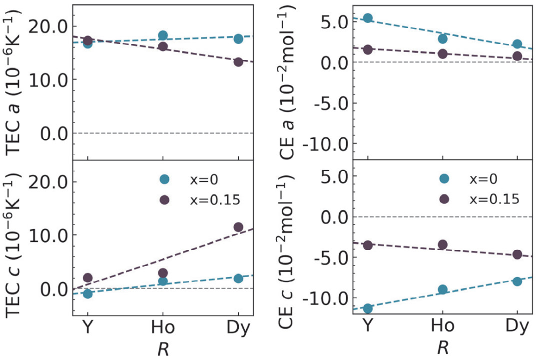

Figure 7. Thermal expansion coefficients (TEC) and chemical expansion (CE) for $RMn_{1-x}Ti_xO_3$ samples.

Thermal expansion is more anisotropic for larger R and more isotropic for Ti-doped than undoped samples. In contrast, chemical expansion is more anisotropic for smaller R and generally much smaller for Ti-doped samples. Smaller CE for larger R is qualitatively in agreement with the DFT results in Figure 6b, but with larger values than the calculated. A quantitative comparison between 0 K calculation and finite temperature measurements is difficult, also because chemical expansion of transition metal oxides is sensitive to computational parameters.[68] As Ti-doping already expands the *ab*-plane by partly rectifying the MnO_5 tilting,[43] the smaller CE observed for Ti-doped samples may be rationalized from the *ab*-plane already being more expanded prior to oxygen absorption compared to undoped samples. Correspondingly, chemical contraction of the *c*-axis is much smaller for Ti-doped samples, and of similar magnitude for all *R*. A possible reason for the smaller chemical expansion of Ti-doped samples is that the *ab*-plane is already expanded before oxygen absorption occurs because of the mentioned un-tilting of the MnO_5 bipyramids, which both Ti-doping and O_i[18] incorporation both induce. With already partly rectified bipyramids, the expansion caused by incorporation of O_i may then be counteracted and even dominated by the considerably smaller radius of Mn^{4+} (0.46 Å, CN = 5, interpolated from CN=4,6) compared to Mn^{3+} (0.58 Å).[64] Ti-doped $HoMnO_3$ (HMTO30) and particularly Ti-doped $DyMnO_3$ (DMTO30) display non-linearity in lattice parameters also in N_2 atmosphere (Figure 5), in contrast with the other samples, which is likely an effect of trace amounts of oxygen in 5.0 N_2 gas.

Chemical expansion is most easily visualized from the (004) reflection (Figure 4). Pronounced broadening of the (004) reflection upon oxidation for the Y- and Ho-containing samples indicate structural disorder and inhomogeneous lattice strain caused by the incorporation of O_i. This reflection broadening is not as prominent in the DMO30 sample, but here a new reflection appears adjacent to the (004) reflection. This apparent splitting of the (004) reflection has been attributed to a new hexagonal phase named Hex1 with space group *R*3*c*, which has been reported at higher oxygen content ($\delta > 0.28$).[15,24] In this superstructure, the *c*-axis of the original unit cell is tripled, with the appearing two reflections at ~31.5° 2θ and ~32° 2θ having Miller indices (1010) and (0012), respectively. Even if the DMO30 sample has a maximum oxygen content of $\delta = 0.25$ from TGA (Figure 3), the appearance of this reflection could stem from a Hex1 phase, even though this structure is usually observed for higher δ. The absence of a distinct extra reflection for the other samples with $\delta > 0.28$, HMTO28 and DMTO30, implies a more disordered structure or distribution of O_i.

Thermodynamic model. We now address the thermodynamics of oxidation of hexagonal manganites. While a variation in the maximum δ of 0.33-0.35 in $RMnO_{3+\delta}$ has been reported for cooling in O_2 atmosphere[14,24,69] (even larger values of up to 0.45 have also been reported for $Y_{0.7}Tb_{0.3}MnO_{3+\delta}$[28]), we here use $\delta = 0.33$ to approximate the maximally oxidized phase as the stoichiometry $R_3Mn_3O_{10}$. We note that only the HMTO and DMTO materials reached comparable values for δ from TGA with a cooling rate of 1 °C min^{-1} (Figure 3). Following these assumptions, complete oxidation of $RMnO_3$ to $RMnO_{3+\delta}$ can be described by eq. (6):

$$2\ R_3Mn_3^{3+}O_9 + O_2(g) \rightleftarrows 2\ R_3Mn^{3+}Mn_2^{4+}O_{10} \quad (6)$$

To discuss the thermodynamics of the oxidation reaction, the solid solution model by Bakken *et al.*[70] for formation of oxygen vacancies in a perovskite, $ABO_{3-\delta}$ is adapted, utilizing that oxidation of $RMnO_{3+\delta}$ from $RMnO_{3.00}$ with $\delta = 0.00$ to $RMnO_{3.33}$ with $\delta = 0.33$ is analogous to oxidation of $ABO_{2.50}$

brownmillerite to perovskite $ABO_{3.00}$. Equivalent to RMnO$_3$ incorporating 'excess' O$_i$, unfilled interstitial sites in $R_3Mn_3O_{10-\delta}$ can be regarded as oxygen vacancies where stoichiometric RMnO$_3$ is written as $R_3Mn_3O_9$. The formation of oxygen vacancies, $\mathrm{V}_\mathrm{O}^{\bullet\bullet}$, in $R_3Mn_3O_{10}$ is shown in Kroger-Vink notation in eq. (7):

$$2\mathrm{O}_\mathrm{O}^\mathrm{x} + 4\mathrm{Mn}_\mathrm{Mn}^\mathrm{x} \leftrightarrow 2\mathrm{V}_\mathrm{O}^{\bullet\bullet} + 4\mathrm{Mn}_\mathrm{Mn}' + \mathrm{O}_2(\mathrm{g})\ (7)$$

The equilibrium constant, K, for the defect formation in eq. (7) is given by

$$K = \frac{[\mathrm{V}_\mathrm{O}^{\bullet\bullet}]^2[\mathrm{Mn}_\mathrm{Mn}']^4}{[\mathrm{O}_\mathrm{O}^\mathrm{x}]^2[\mathrm{Mn}_\mathrm{Mn}^\mathrm{x}]^4} \cdot p_{\mathrm{O}_2}\ (8)$$

The Gibbs energy of formation for any given configuration of RMnO$_{3+\delta}$ can now be expressed from a reaction between $R_3Mn_3O_9$ and $R_3Mn_3O_{10}$:

$$\Delta_\mathrm{f} G_{c(R_3\mathrm{Mn}_3\mathrm{O}_{10-\delta})} = (2-2\delta)\Delta_f G_m^0(R_3\mathrm{Mn}_3\mathrm{O}_{10}) + 2\delta\Delta_f G_m^0(R_3\mathrm{Mn}_3\mathrm{O}_9) \qquad (9)$$

Ideal solution is assumed in eq. (9), implying no interactions between oxygen interstitials. By expressing the site fractions [i] in eq. (8) as a function of oxygen vacancies, δ, the partial pressure of oxygen can be described by eq. (10):

$$\log p\mathrm{O}_2 = \left(\frac{1}{RTln10}\right)\left[2\Delta_f G^0(R_3\mathrm{Mn}_3\mathrm{O}_{10}) - 2\Delta_f G^0(R_3\mathrm{Mn}_3\mathrm{O}_9)\right] + 4[\log(2-2\delta) - \log(2\delta)] - 2\log\left(\frac{\delta}{10-\delta}\right)\ (10)$$

To model the oxygen stoichiometry of RMnO$_{3+\delta}$ measured by TGA as a function of temperature in pure O$_2$ atmosphere, pO$_2$ in eq. (10) is set to 1.0 and eq. (11) expresses the Gibbs energy of oxidation:

$$\Delta_\mathrm{ox} G^0 = 2\Delta_f G^0(R_3\mathrm{Mn}_3\mathrm{O}_{10}) - 2\Delta_f G^0(R_3\mathrm{Mn}_3\mathrm{O}_9) = \Delta_\mathrm{ox} H^0 - T\Delta_{ox} S^0, \qquad (11)$$

for the oxidation reaction in eq. (6). Before fitting the experimental TGA data we first illustrate how the enthalpy and entropy of oxidation influences the temperature-dependent δ in Figure 8 with a range of values chosen from experimental work on related ternary transition metal perovskites.[70–72]

The plots of the thermodynamic model show that an increasingly negative $\Delta_\mathrm{ox} H^0$ (Figure 8a) stabilizes absorbed interstitial oxygen to higher temperatures, counteracting the positive $T\Delta_\mathrm{ox} S^0$ contribution to $\Delta_\mathrm{ox} G^0$. This implies that $\Delta_\mathrm{ox} H^0$ should become increasingly negative for larger R,[14,15,24] e.g. by substituting Y in YMnO$_3$ with larger R^{3+} cations like Tb^{3+},[28,30] Ho^{3+} and Dy^{3+}, and upon donor doping with Ti^{4+} (this study) and Zr^{4+},[27] in qualitative agreement with the present and previous experimental observations. The effect of increasingly negative $\Delta_\mathrm{ox} S^0$ (Figure 8b) is to make the temperature interval of complete oxidation narrower, simultaneously shifting both the onset and completion of oxidation to lower temperatures. We note that the DFT calculated $\Delta_{\mathrm{ox}}H^0$ cannot quantitatively explain the experimental observations as the calculated values are too small and would predict oxidation at lower temperatures than experimentally observed, unless a correspondingly small $\Delta_{\mathrm{ox}}S^0$ is used to compensate. Furthermore, attempts to fit the TGA data to the thermodynamic model with DFT calculated $\Delta_{\mathrm{ox}}H^0$ and $\Delta_{\mathrm{ox}}S^0$ values below 150 J $K^{-1}mol^{-1}$ give a much broader temperature interval of oxidation than that observed experimentally. The trends between the different materials studied were, however, reproduced by the DFT results in Figure 6 (d-f).

As this is a thermodynamic model, kinetics and ergodicity[50] is ignored, and in real h-RMnO$_3$ materials oxygen becomes immobile and effectively frozen in the lattice below ~150-200 °C.[14,15,24,65] While the thermodynamic model implicitly assumes that a maximum oxygen content of $\delta = 0.33$ is always reached, δ measured by TGA deviates from the thermodynamic model at lower temperatures where the available thermal energy is insufficient for thermodynamic equilibrium to be reached. For this reason, we also only fit TGA data upon cooling as the material starts in equilibrium at higher temperatures, and because it is difficult to quantify at what temperature ergodicity is broken.

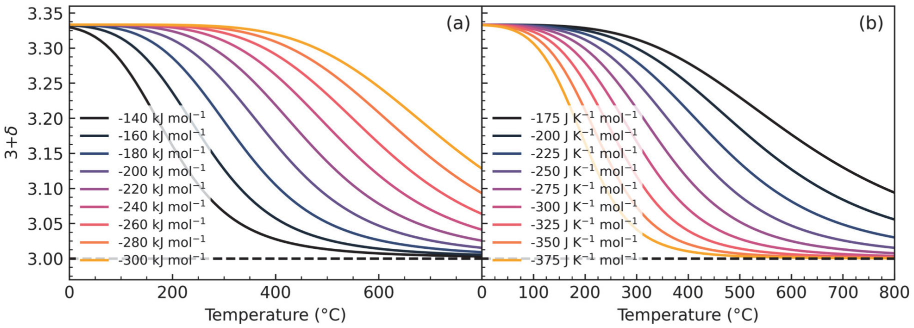

Figure 8. Temperature dependent oxygen stoichiometry in RMnO$_{3+\delta}$ in pure O$_2$ atmosphere from eq. (10) with (a) variable $\Delta_{\mathrm{ox}}H^0$ with $\Delta_{\mathrm{ox}}S^0$ fixed to -250 J $K^{-1}mol^{-1}$ and (b) variable $\Delta_{\mathrm{ox}}S^0$ with $\Delta_{\mathrm{ox}}H^0$ fixed to -200 kJ mol^{-1}.

Fits of the thermodynamic model to experimental data from TGA are presented in Figure 9 where $\Delta_{\mathrm{ox}}H^0$ and $\Delta_{\mathrm{ox}}S^0$ were used as fitting parameters. For fitting the data of Ti-containing samples, the minimum value of δ in eq. (10) was adjusted to 0.075. At higher temperatures, where the materials are in equilibrium, the model fits the experimental data for all undoped samples well. The deviation between the model and measured data starts at progressively higher values of δ for R = Y, Ho and Dy, reflecting the difference in oxygen storage capacity for different R. The temperature onset of deviation can be regarded as the temperature where ergodicity is broken, and this occurs at ~250 °C for R = Y and Ho, and at ~325 °C for R = Dy. For Ti-doped samples, shown in panels (d), (e) and (f) in Figure 9, the deviation between model and data at lower temperatures is less significant due to the larger maximum δ measured for these samples. At temperatures over ~450 °C, the model predicts a lower δ for R = Ho, Dy than what has been measured. Possible reasons for this deviation are that in the present model with a maximum δ of 3.33, neither surface adsorption nor possible oxidation of Dy^{3+} to Dy^{4+} [73] is considered. Given that the thermodynamic model assumes ideal solution with no interactions between absorbed O_i and thus a δ-independent $\Delta_{ox}H^0$ and $\Delta_{ox}S^0$, the fitted values of these thermodynamic quantities must be examined further and are summarized in Table 2. Fitted values for $\Delta_{ox}H^0$ and $\Delta_{ox}S^0$ are of similar magnitude for both undoped and Ti-doped R = Y and Ho, and are comparable to previously reported values for related perovskite materials[71,72,74,75]. The DFT calculated $\Delta_{ox}H^0$values only give a reasonable match for undoped $YMnO_3$ and apparently underestimates the $\Delta_{ox}H^0$ values for the other materials studied here. The fitted values for $\Delta_{ox}S^0$ for the Ti-doped for R = Y, Ho samples are slightly larger compared to those of the undoped samples. The values for the Ho-sample are somewhat larger than for that based on Y, reflecting the higher temperature of oxidation for the Ho-sample (trends are illustrated in Figure 8). The same trend can be seen for all Ti-doped samples, where the fitted values increase for increasing R-cation size. The fitted values for $DyMnO_{3+\delta}$ are, in contrast, unphysically large, but necessary to fit the measured data to the applied model which is based on ideal solution. Clearly, an ideal solution model with δ-independent $\Delta_{ox}H^0$ and $\Delta_{ox}S^0$ cannot describe the oxidation of $DyMnO_{3+\delta}$ as it occurs over a too narrow temperature interval. Following the preceding discussion of the role of *ab*-plane expansion, it is possible that partial oxidation strongly facilitates further oxidation of $DyMnO_{3+\delta}$ as O_i causes chemical expansion of the *ab*-plane, possibly reducing O-O_i repulsion and thus make $\Delta_{ox}H^0$ more negative, up to a value of δ where O_i-O_i repulsion is expected to dominate and make $\Delta_{ox}H^0$ less negative. This anticipated δ-dependent variation of $\Delta_{ox}H^0$ is not captured by an ideal solution model where defect-defect interactions are ignored. Different diffusion kinetics at different oxidation temperatures is also not accounted for in a purely thermodynamic model, and this is expected to affect the temperature interval of oxidation measured upon a finite cooling rate (here 1 °C min^{-1}). Finally, collective ionic motion[76] may also contribute to the narrow temperature interval of oxidation observed for $DyMnO_{3+\delta}$, especially given the inherently cooperative nature of the interstitialcy mechanism established for migration oxygen ions[17,18], but longer-range cooperative ionic motion has not yet been studied for finite oxygen hyperstoichiometry in hexagonal manganites.

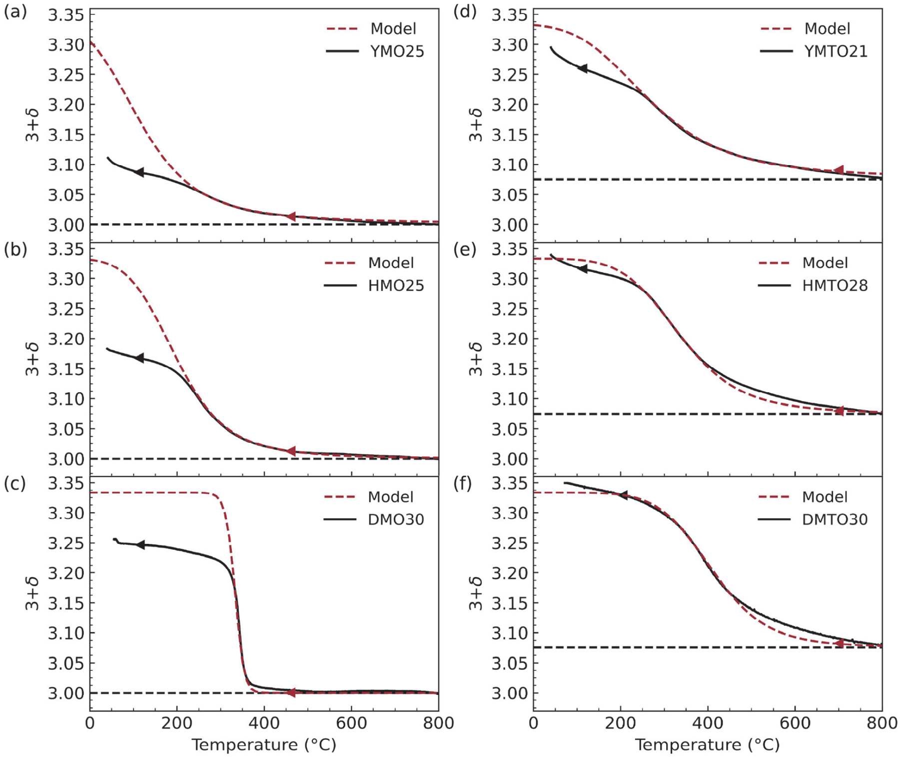

Figure 9: Fitted oxygen stoichiometry as a function of temperature with p_{O2} set to 1.0 is shown as solid lines, experimental data are shown as dashed lines for nanocrystalline (a) $YMnO_{3+\delta}$, (b) $HoMnO_{3+\delta}$, (c) $DyMnO_{3+\delta}$, (d) $YMn_{0.85}Ti_{0.15}O_{3+\delta}$, (e) $HoMn_{0.85}Ti_{0.15}O_{3+\delta}$ and (f) $DyMn_{0.85}Ti_{0.15}O_{3+\delta}$. Horizontal dashed lines correspond to all Mn present as Mn^{3+} and thus $\delta = 0$ for (a-c) and $\delta = 0.075$ for (d-f).

Table 2. Entropy and enthalpy of oxidation of $R\text{Mn}_{1\text{-x}}\text{Ti}_\text{x}\text{O}_{3+\delta}$ (R = Y, Ho, Dy) used for fitting the ideal solid solution model to the experimental data from TGA measurements.

Composition	Sample name	$\Delta_{\text{ox}}S^0$ (J K^{-1}mol^{-1})	$\Delta_{\text{ox}}H^0$ (kJ mol^{-1})
$\text{YMnO}_{3+\delta}$	YMO25	-200	-97.5
$\text{HoMnO}_{3+\delta}$	HMO25	-290	-160
$\text{DyMnO}_{3+\delta}$	DMO30	-2400	-1485
$\text{YMn}_{0.85}\text{Ti}_{0.15}\text{O}_{3+\delta}$	YMTO21	-195	-135
$\text{HoMn}_{0.85}\text{Ti}_{0.15}\text{O}_{3+\delta}$	HMTO28	-315	-225
$\text{DyMn}_{0.85}\text{Ti}_{0.15}\text{O}_{3+\delta}$	DMTO30	-400	-310

CONCLUSIONS

The oxygen storage capacity of nanocrystalline hexagonal $R\text{MnO}_{3+\delta}$ has been observed by thermogravimetric analysis (TGA) to increase with increasing size of the R^{3+} cation and with 15% Ti-doping of the Mn-sublattice. The thermal stability of absorbed oxygen, signified by the onset temperature for absorption upon cooling, was found to be ~75 °C higher for R = Dy than for R = Y and Ho, in agreement with previous studies of bulk materials. Ti-doping stabilizes absorbed oxygen to higher temperatures and Ti-doped samples oxidize over a wider temperature range than undoped samples. High-temperature X-ray diffraction in O_2 and N_2 showed that the chemical expansion from oxygen absorption is smaller for larger R in undoped samples, and significantly smaller for Ti-doped samples than for undoped. Super-reflections emerge upon oxidation of DyMnO_3 and $\text{DyMn}_{0.85}\text{Ti}_{0.15}\text{O}_3$, signifying the appearance of a new ordered phase, while only shifts in the Bragg reflections were observed for the other samples studied by HT-XRD. Density functional theory (DFT) calculations support the experimental observations of chemical expansion, predict a correlation between initial thermodynamic driving force for oxidation at low values of δ and the size of R^{3+}, and show that Ti-doping strongly stabilizes absorbed interstitial oxygen. A trend in the enthalpy of oxidation from $\delta = 0$ to $\delta = 0.33$ with R could not be inferred from the DFT calculations, suggesting that the process in real materials is complex and involves both thermodynamic and kinetic factors. A thermodynamic model for oxidation was derived assuming ideal solution and this model could be fitted to TGA data for R = Y and Ho with reasonable values for the enthalpy and entropy of reduction, but not for R = Dy, where the narrow temperature interval of oxidation yields unphysically large values for these thermodynamic quantities. The limitations of the ideal solution thermodynamic model are discussed with respect to the microscopic mechanisms involved in oxygen absorption in hexagonal manganites.

ACKNOWLEDGEMENTS

We thank Kristin Høydalsvik Wells for help with the HT-XRD measurements, and MSc Tormod Østmoe for preparing the $DyMnO_3$ amorphous powder. Financial support from the Research Council of Norway for BADW and DRS through projects 275810 and 275139, respectively, is acknowledged. Computational resources were provided by Sigma2 – The National Infrastructure for High-Performance Computing and Data Storage in Norway - through project NN9264K. Financial support from NTNU Norwegian University of Science and Technology is acknowledged.

REFERENCES

(1) Rydén, M.; Lyngfelt, A.; Mattisson, T.; Chen, D.; Holmen, A.; Bjørgum, E. Novel Oxygen-Carrier Materials for Chemical-Looping Combustion and Chemical-Looping Reforming; $La_xSr_{1-x}Fe_yCo_{1-y}O_{3-d}$ Perovskites and Mixed-Metal Oxides of NiO, Fe_2O_3 and Mn_3O_4. *Int. J. Greenh. Gas Control* **2008**, *2* (1), 21–36.

(2) Yao, H. C.; Yao, Y. F. Y. Ceria in Automotive Exhaust Catalysts. I. Oxygen Storage. *J. Catal.* **1984**, *86* (2), 254–265.

(3) Kim, C. H.; Qi, G.; Dahlberg, K.; Li, W. Strontium-Doped Perovskites Rival Platinum Catalysts for Treating NO_x in Simulated Diesel Exhaust. *Science (80-.).* **2010**, *327* (5973), 1624–1627.

(4) Protasova, L.; Snijkers, F. Recent Developments in Oxygen Carrier Materials for Hydrogen Production via Chemical Looping Processes. *Fuel* **2016**, *181*, 75–93.

(5) Yang, Z.; Lin, Y. S.; Zeng, Y. High-Temperature Sorption Process for Air Separation and Oxygen Removal. *Ind. Eng. Chem. Res.* **2002**, *41* (11), 2775–2784.

(6) Fornasiero, P.; Graziani, M.; Kaspar, J. Use of CeO_2-Based Oxides in the Three-Way Catalysis. *Catal. Today* **1999**, *50*, 285–298.

(7) Chen, H. Y.; Chang, H. L. R. Development of Low Temperature Three-Way Catalysts for Future Fuelefficient Vehicles. *Johnson Matthey Technol. Rev.* **2015**, *59* (1), 64–67.

(8) Guntuka, S.; Banerjee, S.; Farooq, S.; Srinivasan, M. P. A- and B-Site Substituted Lanthanum Cobaltite Perovskite as High Temperature Oxygen Sorbent. 1. Thermogravimetric Analysis of Equilibrium and Kinetics. *Ind. Eng. Chem. Res.* **2008**, *47* (1), 154–162.

(9) Miura, N.; Ikeda, H.; Tsuchida, A. $Sr_{1-x}Ca_xFeO_{3-\delta}$ as a New Oxygen Sorbent for the High-Temperature Pressure-Swing Adsorption Process. *Ind. Eng. Chem. Res.* **2016**, *55* (11), 3091–3096.

(10) Magnone, E.; Kim, J. R.; Park, J. H. Effect of Synthesis Method on Oxygen Adsorption/Desorption Properties of La-Sr-Co-Fe-O Perovskite-Type Oxide. *J. Therm. Anal. Calorim.* **2014**, *117* (3), 1221–1229.

(11) Motohashi, T.; Ueda, T.; Masubuchi, Y.; Takiguchi, M.; Setoyama, T.; Oshima, K.; Kikkawa, S. Remarkable Oxygen Intake/Release Capability of $BaYMn_2O_{5+\delta}$: Applications to Oxygen Storage Technologies. *Chem. Mater.* **2010**, *22* (10), 3192–3196.

(12) Lein, H.; Wiik, K.; Grande, T. Kinetic Demixing and Decomposition of Oxygen Permeable Membranes. *Solid State Ionics* **2006**, *177* (19–25), 1587–1590.

(13) Jalili, H.; Chen, Y.; Yildiz, B. Structural, Chemical, and Electronic State on $La_{0.7}Sr_{0.3}MnO_3$ Dense Thin-Film

Surfaces at High Temperature: Surface Segregation. *ECS Trans.* **2010**, *28* (11), 235–240.

(14) Remsen, S.; Dabrowski, B. Synthesis and Oxygen Storage Capacities of Hexagonal $Dy_{1-x}Y_xMnO_{3+\delta}$. *Chem. Mater.* **2011**, *23* (17), 3818–3827.

(15) Abughayada, C.; Dabrowski, B.; Kolesnik, S.; Brown, D. E.; Chmaissem, O. Characterization of Oxygen Storage and Structural Properties of Oxygen-Loaded Hexagonal $RMnO_{3+\delta}$ (R = Ho, Er, and Y). *Chem. Mater.* **2015**, *27* (18), 6259–6267.

(16) Bergum, K.; Okamoto, H.; Fjellvåg, H.; Grande, T.; Einarsrud, M. A.; Selbach, S. M. Synthesis, Structure and Magnetic Properties of Nanocrystalline $YMnO_3$. *Dalt. Trans.* **2011**, *40* (29), 7583–7589.

(17) Evans, D. M.; Holstad, T. S.; Mosberg, A. B.; Småbråten, D. R.; Vullum, P. E.; Dadlani, A. L.; Shapovalov, K.; Yan, Z.; Bourret, E.; Gao, D.; Akola, J.; Torgersen, J.; van Helvoort, A. T. J.; Selbach, S. M.; Meier, D. Conductivity Control via Minimally Invasive Anti-Frenkel Defects in a Functional Oxide. *Nat. Mater.* **2020**, *19* (11), 1195–1200.

(18) Skjærvø, S. H.; Wefring, E. T.; Nesdal, S. K.; Gaukås, N. H.; Olsen, G. H.; Glaum, J.; Tybell, T.; Selbach, S. M. Interstitial Oxygen as a Source of P-Type Conductivity in Hexagonal Manganites. *Nat. Commun.* **2016**, *7* (7491).

(19) van Roosmalen, J. A. M.; Cordfunke, E. H. P. The Defect Chemistry of $LaMnO_{3\pm\delta}$. 4. Defect Model for $LaMnO_{3+\delta}$. *Journal of Solid State Chemistry*. 1994, pp 109–112.

(20) Griffin, S. M.; Reidulff, M.; Selbach, S. M.; Spaldin, N. A. Defect Chemistry as a Crystal Structure Design Parameter: Intrinsic Point Defects and Ga Substitution in InMnO 3. *Chem. Mater.* **2016**, *29* (6), 2425–2434.

(21) Kotomin, E. A.; Mastrikov, Y. A.; Heifets, E.; Maier, J. Adsorption of Atomic and Molecular Oxygen on the $LaMnO_3$ (001) Surface: Ab Initio Supercell Calculations and Thermodynamics. *Phys. Chem. Chem. Phys.* **2008**, *10* (31), 4644–4649.

(22) Polfus, J. M.; Yildiz, B.; Tuller, H. L. Origin of Fast Oxide Ion Diffusion along Grain Boundaries in Sr-Doped $LaMnO_3$. *Phys. Chem. Chem. Phys.* **2018**, *20* (28), 19142–19150.

(23) Carrasco, J.; Illas, F.; Lopez, N.; Kotomin, E. A.; Zhukovskii, Y. F.; Evarestov, R. A.; Mastrikov, Y. A.; Piskunov, S.; Maier, J. First-Principles Calculations of the Atomic and Electronic Structure of F Centers in the Bulk and on the (001) Surface of $SrTiO_3$. *Phys. Rev. B - Condens. Matter Mater. Phys.* **2006**, *73* (6).

(24) Abughayada, C.; Dabrowski, B.; Avdeev, M.; Kolesnik, S.; Remsen, S.; Chmaissem, O. Structural, Magnetic, and Oxygen Storage Properties of Hexagonal $Dy_{1-x}Y_xMnO_{3+\delta}$. *J. Solid State Chem.* **2014**, *217*, 127–135.

(25) Parkkima, O.; Malo, S.; Hervieu, M.; Rautama, E. L.; Karppinen, M. New $RMnO_{3+\delta}$ (R=Y, Ho; Δ≈0.35) Phases with Modulated Structure. *J. Solid State Chem.* **2015**, *221*, 109–115.

(26) Świerczek, K.; Klimkowicz, A.; Nishihara, K.; Kobayashi, S.; Takasaki, A.; Alanizy, M.; Kolesnik, S.; Dabrowski, B.; Seong, S.; Kang, J. Oxygen Storage Properties of Hexagonal $HoMnO_{3+\delta}$. *Phys. Chem. Chem. Phys.* **2017**, *19* (29), 19243–19251.

(27) Moreno Botello, Z. L.; Montenegro, A.; Grimaldos Osorio, N.; Huvé, M.; Pirovano, C.; Småbråten, D. R.; Selbach, S. M.; Caneiro, A.; Roussel, P.; Gauthier, G. H. Pure and Zr-Doped $YMnO_{3+\delta}$ as a YSZ-Compatible SOFC Cathode: A Combined Computational and Experimental Approach. *J. Mater. Chem. A* **2019**, *7* (31), 18589–18602.

(28) Klimkowicz, A.; Cichy, K.; Chmaissem, O.; Dabrowski, B.; Poudel, B.; Świerczek, K.; Taddei, K. M.; Takasaki, A. Reversible Oxygen Intercalation in Hexagonal $Y_{0.7}Tb_{0.3}MnO_{3+\delta}$: Toward Oxygen Production by Temperature-Swing Absorption in Air. *J. Mater. Chem. A* **2019**, *7* (6), 2608–2618.

(29) Cichy, K.; Świerczek, K.; Jarosz, K.; Klimkowicz, A.; Marzec, M.; Gajewska, M.; Dabrowski, B. Towards Efficient Oxygen Separation from Air: Influence of the Mean Rare-Earth Radius on Thermodynamics and Kinetics of Reactivity with Oxygen in Hexagonal $Y_{1-x}R_xMnO_{3+\delta}$. *Acta Mater.* **2021**, *205*.

(30) Klimkowicz, A.; Hashizume, T.; Cichy, K.; Tamura, S.; Świerczek, K.; Takasaki, A.; Motohashi, T.; Dabrowski, B. Oxygen Separation from Air by the Combined Temperature Swing and Pressure Swing Processes Using Oxygen Storage Materials $Y_{1-x}(Tb/Ce)_xMnO_{3+\delta}$. *J. Mater. Sci.* **2020**, *55* (33), 15653–15666.

(31) Selbach, S. M.; Løvik, A. N.; Bergum, K.; Tolchard, J. R.; Einarsrud, M. A.; Grande, T. Crystal Structure,

Chemical Expansion and Phase Stability of $HoMnO_3$ at High Temperature. *J. Solid State Chem.* **2012**, *196*, 528–535.

(32) Bos, J.-W. G.; van Aken, B. B.; Palstra, T. T. M. Site Disorder Induced Hexagonal-Orthorhombic Transition in $Y^{3+}_{1-x}\,Gd^{3+}_{x}MnO_3$. *Chem. Mater.* **2001**, *13* (12), 4804–4807.

(33) Brinks, H. W.; Rodríguez-Carvajal, J.; Fjellvåg, H.; Kjekshus, A.; Hauback, B. C. Crystal and Magnetic Structure of Orthorhombic $HoMnO_3$. *Phys. Rev. B* **2001**, *63* (9), 204.

(34) Asaka, T.; Nemoto, K.; Kimoto, K.; Arima, T.; Matsui, Y. Crystallographic Superstructure of Ti-Doped Hexagonal $YMnO_3$. *Phys. Rev. B* **2005**, *71* (1), 317.

(35) Gibbs, A. S.; Knight, K. S.; Lightfoot, P. High-Temperature Phase Transitions of Hexagonal $YMnO_3$. *Phys. Rev. B* **2011**, *83* (9), 1958.

(36) Huang, Y. H.; Fjellvåg, H.; Karppinen, M.; Hauback, B. C.; Yamauchi, H.; Goodenough, J. B. Crystal and Magnetic Structure of the Orthorhombic Perovskite $YbMnO_3$. *Chem. Mater.* **2006**, *18* (8), 2130–2134.

(37) Zhou, J.-S.; Goodenough, J. B.; Gallardo-Amores, J. M.; Morán, E.; Alario-Franco, M. A.; Caudillo, R. Hexagonal versus Perovskite Phase of Manganite $RMnO_3$ (R=Y, Ho, Er, Tm, Yb, Lu). *Phys. Rev. B* **2006**, *74* (1), 725.

(38) Brinks, H. W.; Fjellvåg, H.; Kjekshus, A. Synthesis of Metastable Perovskite-Type $YMnO_3$ and $HoMnO_3$. *J. Solid State Chem.* **1997**, *129* (2), 334–340.

(39) Cichy, K.; Świerczek, K. Influence of Doping on the Transport Properties of $Y_{1-x}Ln_xMnO_{3+\delta}$ (Ln: Pr, Nd). *Crystals* **2021**, *11* (5), 1–13.

(40) Cichy, K.; Zając, M.; Świerczek, K. Evaluation of Applicability of Nd- and Sm-Substituted $Y_{1-x}R_xMnO_{3+\delta}$ in Temperature Swing Absorption for Energy-Related Technologies. *Energy* **2022**, *239*, 1–9.

(41) Otomo, M.; Hasegawa, T.; Asakura, Y.; Yin, S. Remarkable Effects of Lanthanide Substitution for the Y-Site on the Oxygen Storage/Release Performance of YMnO3+δ. *ACS Appl. Mater. Interfaces* **2021**, *13* (27), 31691–31698.

(42) Aikawa, Y.; Katsufuji, T.; Arima, T.; Kato, K. Effect of Mn Trimerization on the Magnetic and Dielectric Properties of Hexagonal $YMnO_3$. *Phys. Rev. B - Condens. Matter Mater. Phys.* **2005**, *71* (18), 1–5.

(43) Levin, I.; Krayzman, V.; Vanderah, T. A.; Tomczyk, M.; Wu, H.; Tucker, M. G.; Playford, H. Y.; Woicik, J. C.; Dennis, C. L.; Vilarinho, P. M. Oxygen-Storage Behavior and Local Structure in Ti-Substituted $YMnO_3$. *J. Solid State Chem.* **2017**, *246*, 29–41.

(44) Lilienblum, M.; Lottermoser, T.; Manz, S.; Selbach, S. M.; Cano, A.; Fiebig, M. Ferroelectricity in the Multiferroic Hexagonal Manganites. *Nat. Phys.* **2015**, *11* (12), 1070–1073.

(45) Fennie, C. J.; Rabe, K. M. Ferroelectric Transition in $YMnO_3$ from First Principles. *Phys. Rev. B - Condens. Matter Mater. Phys.* **2005**, *72* (10), 1–4.

(46) Skjærvø, S. H.; Meier, Q. N.; Feygenson, M.; Spaldin, N. A.; Billinge, S. J. L.; Bozin, E. S.; Selbach, S. M. Unconventional Continuous Structural Disorder at the Order-Disorder Phase Transition in the Hexagonal Manganites. *Phys. Rev. X* **2019**, *9* (3), 31001.

(47) Asakura, Y.; Miyake, A.; Otomo, M.; Yin, S. Improvement of the O_2 Storage/Release Rate of $YMnO_3$ Nanoparticles Synthesized by the Polymerized Complex Method. *Dalt. Trans.* **2020**, *49* (4), 966–971.

(48) Han, L.; Zhou, Z.; Bollas, G. M. Heterogeneous Modeling of Chemical-Looping Combustion. Part 2: Particle Model. *Chem. Eng. Sci.* **2014**, *113*, 116–128.

(49) Cao, S.; Tao, F. F.; Tang, Y.; Li, Y.; Yu, J. Size- and Shape-Dependent Catalytic Performances of Oxidation and Reduction Reactions on Nanocatalysts. *Chem. Soc. Rev.* **2016**, *45* (17), 4747–4765.

(50) Grande, T.; Tolchard, J. R.; Selbach, S. M. Anisotropic Thermal and Chemical Expansion in Sr-Substituted $LaMnO_{3+\delta}$: Implications for Chemical Strain Relaxation. *Chem. Mater.* **2012**, *24* (2), 338–345.

(51) Klimkowicz, A.; Świerczek, K.; Kobayashi, S.; Takasaki, A.; Allahyani, W.; Dabrowski, B. Improvement of Oxygen Storage Properties of Hexagonal $YMnO_{3+\delta}$ by Microstructural Modifications. *J. Solid State Chem.* **2018**,

258 (August 2017), 471–476.

(52) Coelho, A. A. Topas Academic: General Profile and Structure Analysis Software for Powder Diffraction Data. *Bruker AXS, Karlsruhe, Ger.* **2007**.

(53) Evans, J. S. O. Advanced Input Files & Parametric Quantitative Analysis Using Topas. *Mater. Sci. Forum* **2010**, *651*, 1–9.

(54) Kluyver, T.; Ragan-Kelley, B.; Pérez, F.; Granger, B.; Bussonnier, M.; Frederic, J.; Kelley, K.; Hamrick, J.; Grout, J.; Corlay, S.; Ivanov, P.; Avila, D.; Abdalla, S.; Willing, C. Jupyter Notebooks—a Publishing Format for Reproducible Computational Workflows. *Position. Power Acad. Publ. Play. Agents Agendas - Proc. 20th Int. Conf. Electron. Publ. ELPUB 2016* **2016**, 87–90.

(55) Kresse, G.; Hafner, J. Ab Initio Molecular Dynamics for Liquid Metals. *Phys. Rev. B* **1993**, *47* (1), 558–561.

(56) Kresse, G.; Hafner, J. Ab Initio Molecular-Dynamics Simulation of the Liquid-Metalamorphous- Semiconductor Transition in Germanium. *Phys. Rev. B* **1994**, *49* (20), 14251–14269.

(57) Kresse, G.; Furthmüller, J. Efficient Iterative Schemes for Ab Initio Total-Energy Calculations Using a Plane-Wave Basis Set. *Phys. Rev. B - Condens. Matter Mater. Phys.* **1996**, *54* (16), 11169–11186.

(58) Kresse, G.; Furthmüller, J. Efficiency of Ab-Initio Total Energy Calculations for Metals and Semiconductors Using a Plane-Wave Basis Set. *Comput. Mater. Sci.* **1996**, *6* (1), 15–50.

(59) Perdew, J. P.; Burke, K.; Ernzerhof, M. Generalized Gradient Approximation Made Simple. *Phys. Rev. Lett.* **1996**, *77* (18), 3865–3868.

(60) Blöchl, P. E. Projector Augmented-Wave Method. *Phys. Rev. B* **1994**, *50* (24), 17953–17979.

(61) Dudarev, S.; Botton, G. Electron-Energy-Loss Spectra and the Structural Stability of Nickel Oxide: An LSDA+U Study. *Phys. Rev. B - Condens. Matter Mater. Phys.* **1998**, *57* (3), 1505–1509.

(62) Wang, L.; Maxisch, T.; Ceder, G. Oxidation Energies of Transition Metal Oxides within the GGA+U Framework. *Phys. Rev. B - Condens. Matter Mater. Phys.* **2006**, *73* (19), 1–6.

(63) Tripathi, S.; Petkov, V.; Selbach, S. M.; Bergum, K.; Einarsrud, M. A.; Grande, T.; Ren, Y. Structural Coherence and Ferroelectric Order in Nanosized Multiferroic $YMnO_3$. *Phys. Rev. B - Condens. Matter Mater. Phys.* **2012**, *86* (9), 1–8.

(64) Shannon, R. D. Revised Effective Ionic Radii and Systematic Studies of Interatomic Distances in Halides and Chalcogenides. *Acta Crystallogr. Sect. A* **1976**, *32* (5), 751–767.

(65) Świerczek, K.; Klimkowicz, A.; Nishihara, K.; Kobayashi, S.; Takasaki, A.; Alanizy, M.; Kolesnik, S.; Dabrowski, B.; Seong, S.; Kang, J. Oxygen Storage Properties of Hexagonal $HoMnO_{3+\delta}$. *Phys. Chem. Chem. Phys.* **2017**, *19* (29), 19243–19251.

(66) Van Aken, B. B.; Bos, J.; de Groot, R. A.; Palstra, T. T. Asymmetry of Electron and Hole Doping in $YMnO_3$. *Phys. Rev. B - Condens. Matter Mater. Phys.* **2001**, *63* (12), 1251271–1251274.

(67) Holstad, T. S.; Evans, D. M.; Ruff, A.; Småbråten, D. R.; Schaab, J.; Tzschaschel, C.; Yan, Z.; Bourret, E.; Selbach, S. M.; Krohns, S.; Meier, D. Electronic Bulk and Domain Wall Properties in B -Site Doped Hexagonal $ErMnO_3$. *Phys. Rev. B* **2018**, *97* (8), 1–7.

(68) Marthinsen, A.; Grande, T.; Selbach, S. M. Microscopic Link between Electron Localization and Chemical Expansion in $AMnO_3$ and $ATiO_3$ Perovskites (A = Ca, Sr, Ba). *J. Phys. Chem. C* **2020**, *124* (24), 12922–12932.

(69) Remsen, S.; Dabrowski, B.; Chmaissem, O.; Mais, J.; Szewczyk, A. Synthesis and Oxygen Content Dependent Properties of Hexagonal $DyMnO_{3+\delta}$. *J. Solid State Chem.* **2011**, *184* (8), 2306–2314.

(70) Bakken, E.; Norby, T.; Stølen, S. Redox Energetics of Perovskite-Related Oxides. *J. Mater. Chem.* **2002**, *12* (2), 317–323.

(71) Vieten, J.; Bulfin, B.; Senholdt, M.; Roeb, M.; Sattler, C.; Schmücker, M. Redox Thermodynamics and Phase Composition in the System $SrFeO_{3-\delta}$ — $SrMnO_{3-\delta}$. *Solid State Ionics* **2017**, *308* (April), 149–155.

(72) Rørmark, L.; Mørch, A. B.; Wiik, K.; Stølen, S.; Grande, T. Enthalpies of Oxidation of $CaMnO_{3-\delta}$, $Ca_2MnO_{4-\delta}$

and $SrMnO_{3-\delta}$ Deduced Redox Properties. *Chem. Mater.* **2001**, *13* (11), 4005–4013.

(73) Han, D.; Uda, T.; Nose, Y.; Okajima, T.; Murata, H.; Tanaka, I.; Shinoda, K. Tetravalent Dysprosium in a Perovskite-Type Oxide. *Adv. Mater.* **2012**, *24* (15), 2051–2053.

(74) Bakken, E.; Norby, T.; Stølen, S. Nonstoichiometry and Reductive Decomposition of $CaMnO_{3-\delta}$. *Solid State Ionics* **2005**, *176* (1–2), 217–223.

(75) Bakken, E.; Boerio-Goates, J.; Grande, T.; Hovde, B.; Norby, T.; Rørmark, L.; Stevens, R.; Stølen, S. Entropy of Oxidation and Redox Energetics of $CaMnO_{3-\delta}$. *Solid State Ionics* **2005**, *176* (29–30), 2261–2267.

(76) Mohn, C. E.; Allan, N. L.; Freeman, C. L.; Ravindran, P.; Stølen, S. Collective Ionic Motion in Oxide Fast-Ion-Conductors. *Phys. Chem. Chem. Phys.* **2004**, *6* (12), 3052–3055.

Supporting Information

Oxygen absorption in nanocrystalline h-RMnO$_3$ (R=Y, Ho, Dy) and the effect of Ti donor doping.

Frida Hemstad Danmo, Benjamin A. D. Williamson, Didrik R. Småbråten, Nikolai H. Gaukås, Elise R. Østli, Tor Grande, Julia Glaum, and Sverre M. Selbach*

Department of Materials Science and Engineering, NTNU Norwegian University of Science and Technology, NO-7491 Trondheim, Norway.

**E-mail: selbach@ntnu.no*

S1. Phase purity and thermal history of samples

Table S1. Thermal history of samples after synthesis of raw amorphous powders from sol-gel synthesis.

Composition	Sample name	Calcination in air	Pre-annealing in 5% H_2	Annealing in N_2
$YMnO_3$	YMO25	600 °C, 6h	300 °C, 10h	900 °C, 1h
$YMnO_3$	YMO39	600 °C, 6h	-	1000 °C, 1h
$YMn_{0.85}Ti_{0.15}O_3$	YMTO21	600 °C, 6h	-	900 °C, 1h, 900 °C, 3h
$HoMnO_3$	HMO25	600 °C, 6h	-	850 °C, 1h
$HoMnO_3$	HMO38	600 °C, 6h	-	900 °C (air), 2h, 950 °C (N_2), 0.5h
$HoMn_{0.85}Ti_{0.15}O_3$	HMTO28	600 °C, 6h	300 °C, 10h	900 °C, 1h
$DyMnO_3$	DMO30	600 °C, 6h	300 °C, 10h	950 °C, 1h
$DyMn_{0.85}Ti_{0.15}O_3$	DMTO30	600 °C, 6h	300 °C, 10h	900 °C, 1h

All samples containing R = Y are found to be phase pure from X-ray diffraction. The increased background for YMTO21 is caused by a Kapton polyimide film protecting the sample during measurements. All samples containing R = Ho are phase pure, with a small trace of the orthorhombic *Pnma* phase. The DMO30 sample contains 14 molar% Dy_2O_3, determined from Rietveld refinement. The DMTO30 sample is found to be phase pure from X-ray diffraction.

S2. Full high temperature X-ray diffractograms

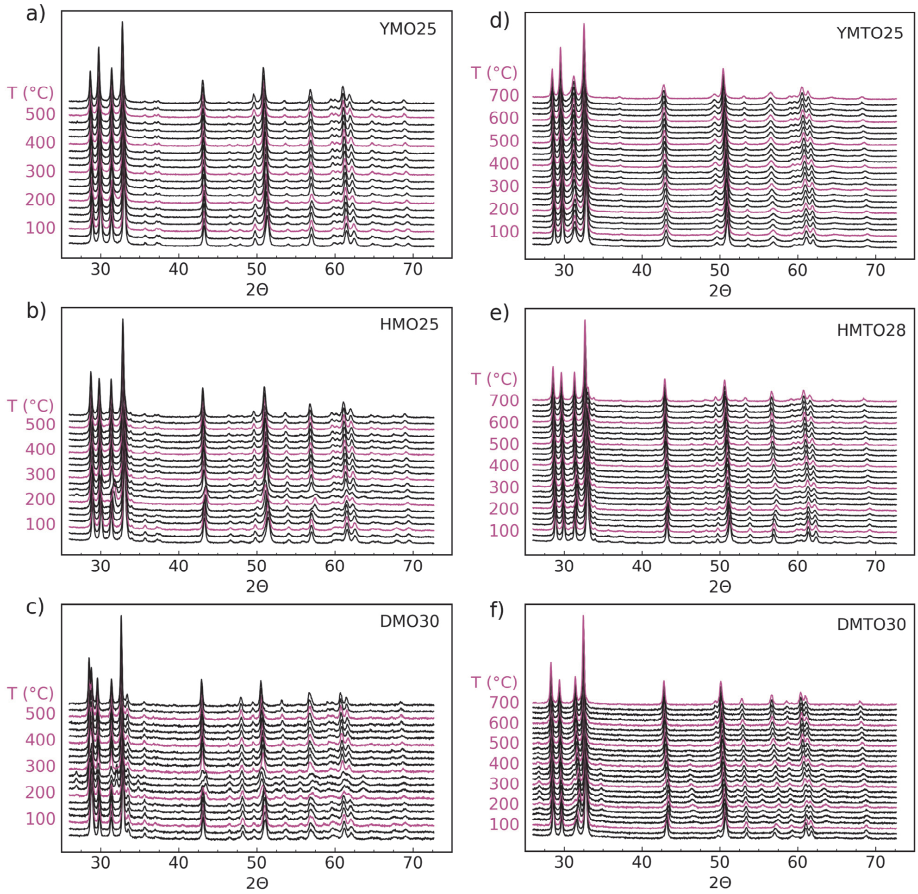

Figure S1. X-ray diffractograms for $R\mathrm{Mn}_{1-x}\mathrm{Ti}_x\mathrm{O}_3$ (R = Y, Ho, Dy) measured at constant temperatures with 25 °C intervals during first heating cycle in O_2 atmosphere.

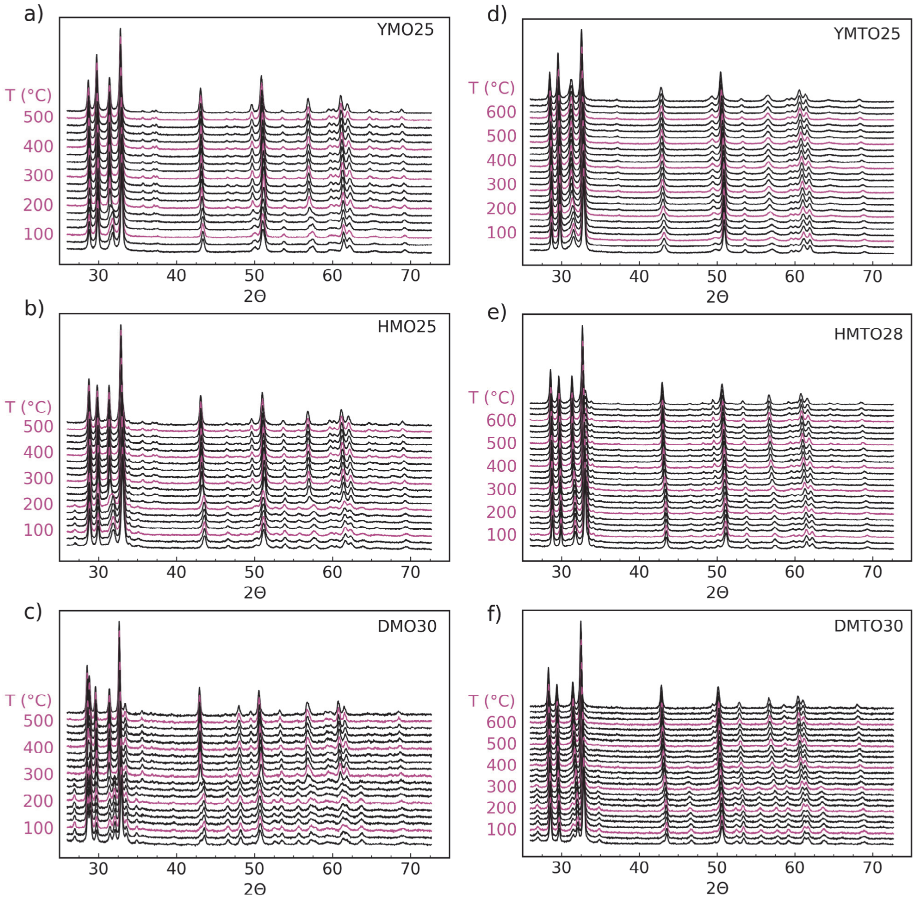

Figure S2. X-ray diffractograms for $R\mathrm{Mn}_{1-x}\mathrm{Ti}_x\mathrm{O}_3$ (R = Y, Ho, Dy) measured at constant temperatures with 25 °C intervals during first cooling cycle in O_2 atmosphere.

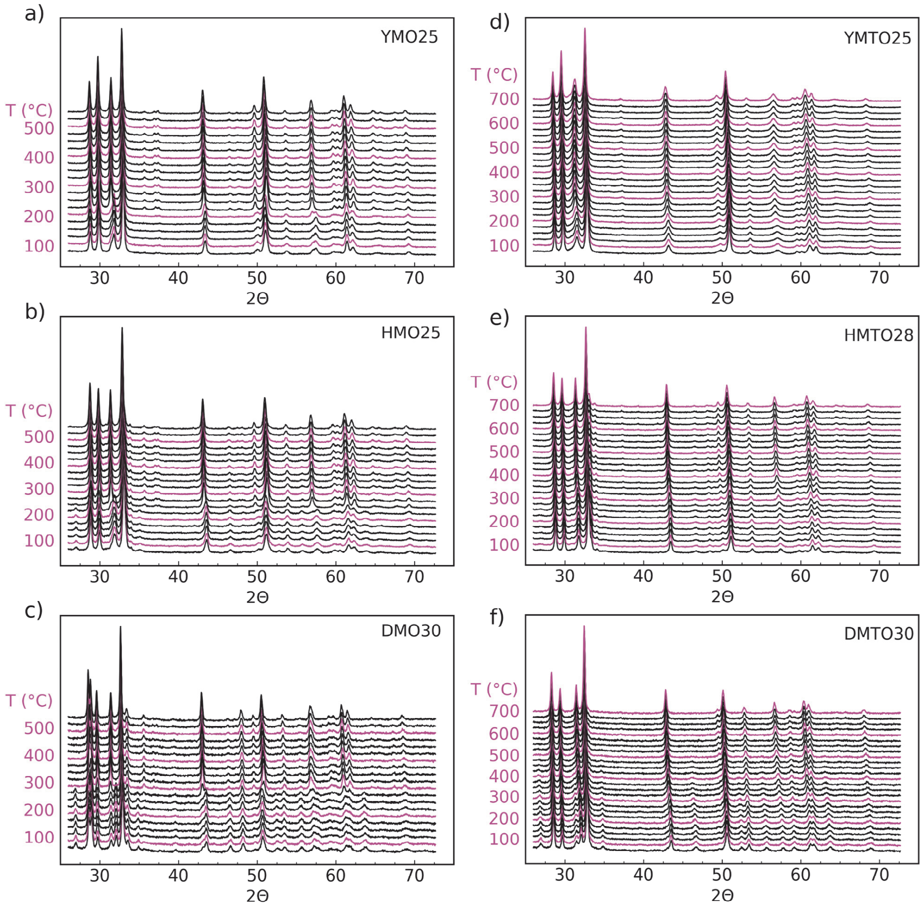

Figure S3. X-ray diffractograms for $R\text{Mn}_{1\text{-}x}\text{Ti}_x\text{O}_3$ (R = Y, Ho, Dy) measured at constant temperatures with 25 °C intervals during second heating cycle in O_2 atmosphere.

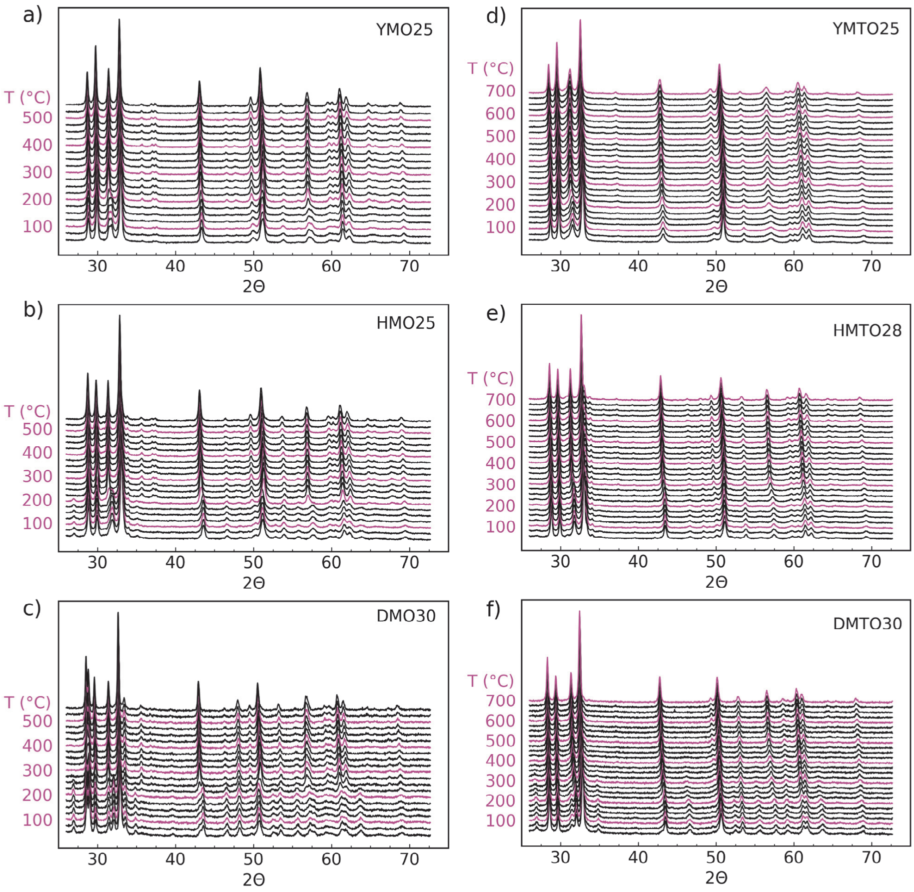

Figure S4. X-ray diffractograms for RMn$_{1-x}$Ti$_x$O$_3$ (R = Y, Ho, Dy) measured at constant temperatures with 25 °C intervals during first heating cycle in N$_2$ atmosphere.

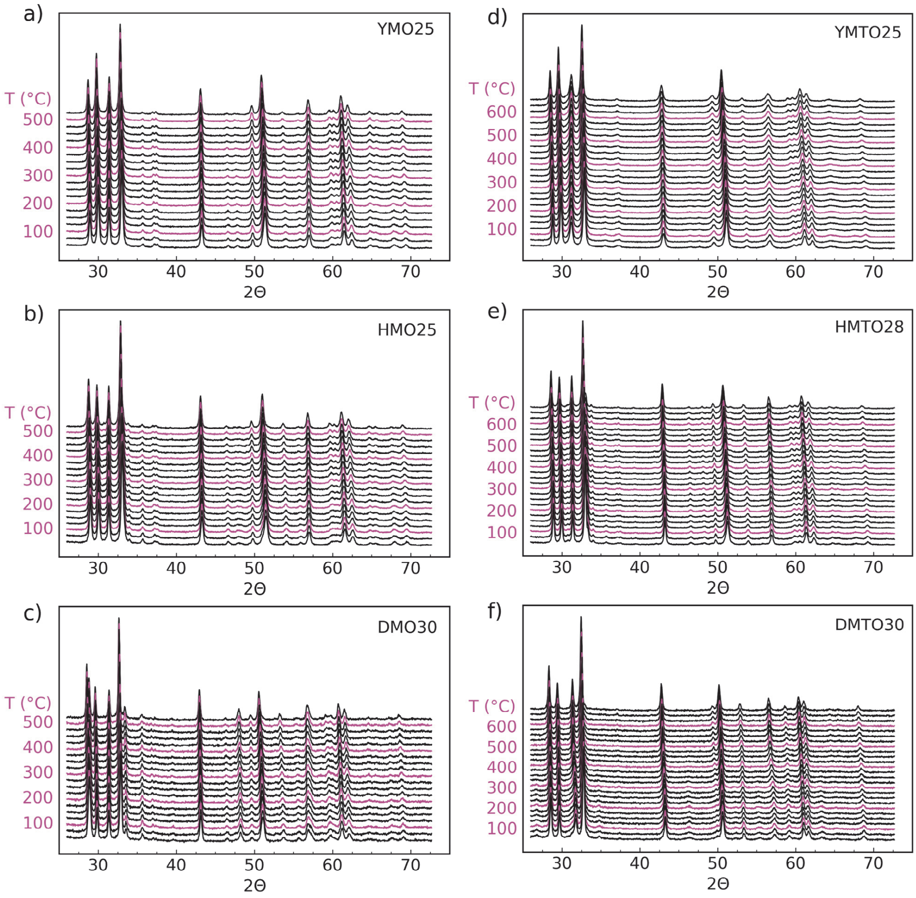

Figure S5. X-ray diffractograms for $RMn_{1-x}Ti_xO_3$ (R = Y, Ho, Dy) measured at constant temperatures with 25 °C intervals during first cooling cycle in N_2 atmosphere.

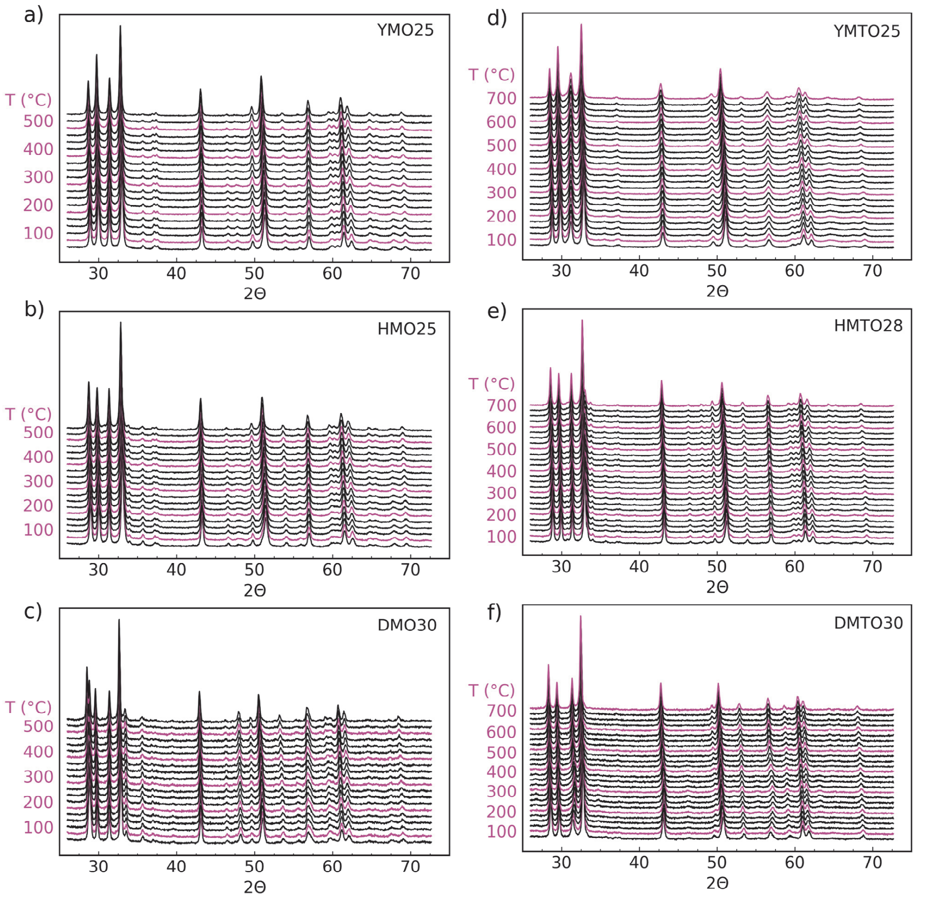

Figure S6. X-ray diffractograms for $R\mathrm{Mn}_{1-x}\mathrm{Ti}_x\mathrm{O}_3$ (R = Y, Ho, Dy) measured at constant temperatures with 25 °C intervals during second heating cycle in N_2 atmosphere.

S3. Thermal and chemical expansion calculations

The thermal expansion coefficient (TEC), found as the difference in a measured lattice parameter, i, was calculated using eq. (S1).

$$TEC_i = \frac{1}{i_0}\left(\frac{\Delta i}{\Delta T}\right) \qquad \text{(S1)}$$

As the lattice parameters used for calculating TEC must only be affected by thermal expansion, and not chemical expansion, only parameters measured in N_2 atmosphere were chosen. As some samples show signs of oxidation in N_2 atmosphere, the temperature interval for calculating TEC was chosen on a sample-to-sample basis. These are summarized in Table S2. The TEC was calculated for lattice parameters measured during both heating and cooling, and the average values for each sample are shown in Figure 7.

Table S2: Temperature interval used for calculating the thermal expansion coefficient (TEC) using lattice parameters found from HT-XRD measurements.

	T_1	T_2
$YMnO_3$	200 °C	350 °C
$HoMnO_3$	200 °C	350 °C
$DyMnO_3$	225 °C	350 °C
$YMn_{0.85}Ti_{0.15}O_3$	200 °C	350 °C
$HoMn_{0.85}Ti_{0.15}O_3$	200 °C	300 °C
$DyMn_{0.85}Ti_{0.15}O_3$	100 °C	250 °C

The chemical expansion (CE), found as the difference in a measured lattice parameter, *i*, between a non-oxidized and a fully oxidized state, was calculated using eq. (S2).

$$CE_i = \frac{1}{i_o}\left(\frac{\Delta i}{\delta}\right) \tag{S2}$$

Here, δ is the maximum oxygen storage for each sample found from TGA measurements, shown in Figure 3. As some of the samples show signs of oxidation in N_2 atmosphere (Figure 5), the lattice parameter for the non-oxidized state was found by extrapolating the lattice parameters measured temperatures above the onset temperature for oxidation, down to the temperature where the material is believed to be fully oxidized and is only affected by thermal expansion during further cooling. Due to the differences in onset temperature of oxidation during heating and cooling for each sample, the temperature where CE was calculated was chosen on a sample-to-sample basis. The temperature interval for calculating the slope for extrapolation (T_1, T_2) and the temperature for where CE was calculated for each sample (T_{ox}), is shown in Table S3. CE was calculated from lattice parameters during both heating and cooling, and the average values for each sample are shown in Figure 7.

Table S3: Temperature interval (T_1, T_2) used for extrapolation and temperature (T_{ox}) used for calculating chemical expansion using lattice parameters found from high temperature XRD measurements.

	Heating			Cooling		
	T_1	T_2	T_{ox}	T_1	T_2	T_{ox}
$YMnO_3$	200 °C	300 °C	100 °C	225 °C	325 °C	200 °C
$HoMnO_3$	250 °C	350 °C	175 °C	275 °C	375 °C	225 °C
$DyMnO_3$	275 °C	375 °C	200 °C	300 °C	400 °C	250 °C
$YMn_{0.85}Ti_{0.15}O_3$	275 °C	375 °C	125 °C	275 °C	375 °C	150 °C
$HoMn_{0.85}Ti_{0.15}O_3$	400 °C	500 °C	225 °C	450 °C	550 °C	225 °C
$DyMn_{0.85}Ti_{0.15}O_3$	500 °C	600 °C	150 °C	500 °C	600 °C	150 °C

Manuscript II

Oxidation kinetics of nanocrystalline h-RMn$_{1\text{-}x}$Ti$_x$O$_3$ (R = Ho, Dy)

F. H. Danmo, I.-E. Nylund, A. Westermoen, K. P. Marshall, D. Stoian, T. Grande, J. Glaum, and S. M. Selbach, *Submitted*

Oxidation kinetics of nanocrystalline h-RMn$_{1-x}$Ti$_x$O$_3$ (R = Ho, Dy)

Frida Hemstad Danmo,[1] Inger-Emma Nylund,[1] Aamund Westermoen, [1] Kenneth P. Marshall,[2] Dragos Stoian,[2] Tor Grande,[1] Julia Glaum,[1] and Sverre M. Selbach[1,]*

[1]Department of Materials Science and Engineering, NTNU Norwegian University of Science and Technology, NO-7491 Trondheim, Norway.

[2]The Swiss-Norwegian Beamlines (SNBL), European Synchrotron Radiation Facility, Grenoble 38043, France

**E-mail: selbach@ntnu.no*

ABSTRACT

Hexagonal manganites, RMnO$_3$ (R = Sc, Y, Ho-Lu), are potential oxygen storage materials for air separation due to their reversible oxygen storage and release properties. Their outstanding ability to absorb and release oxygen at relatively low temperatures of 250-400 °C hold promise of saving energy compared to current industrial methods. Unfortunately, the low temperature of operation also implies slow kinetics of oxygen exchange in these materials, which would make them inefficient in applications such as chemical looping air separation. Here, we show that the oxidation kinetics of RMnO$_3$ can be improved through Ti^{4+}-doping as well as by increasing the rare earth cation size. The rate of oxygen absorption of nanocrystalline RMn$_{1-x}$Ti$_x$O$_3$ (R = Ho, Dy; x = 0, 0.15) was investigated by thermogravimetric analysis, X-ray absorption near edge structure, and high temperature X-ray diffraction (HT-XRD) with *in situ* switching of atmosphere from N$_2$ to O$_2$. The kinetics of oxidation increases for larger R and even more with Ti^{4+} donor doping, as both induce expansion of the *ab*-plane which reduces the electrostatic repulsion between oxygen in the lattice upon oxygen ion migration. Surface exchange rates and activation energies of oxidation were determined from changes in lattice parameters observed through HT-XRD upon *in situ* switching of atmosphere.

INTRODUCTION

Oxygen gas is imperative to a number of diverse applications such as medical treatments, and production of steel, polymer materials and pharmaceuticals.[1] The demand for pure oxygen gas is already high and increasing every year. The emerging potential for using oxygen in oxy-combustion technology for CO_2 capture may also further increase the demand in the coming years.[2] Today, the bulk supply of oxygen is made through the highly energy-demanding process of cryogenic distillation.[3,4] In recent years, air separation by oxygen absorption has been studied as a promising energy-efficient alternative for oxygen production.[5] These methods are usually referred to as chemical looping air separation (CLAS), and utilize materials with reversible oxygen storage and release properties, known as "oxygen storage materials" (OSMs)[6], in an either pressure swing- or temperature swing-based method. A suitable material for CLAS can rapidly absorb and release large amounts of oxygen, preferably at lower temperatures to reduce energy costs, and must not degrade over time.[7]

Possible oxygen carriers include transition metal oxides, ranging from binary manganese, iron and copper oxides to complex ternary metal oxides.[8] Perovskite-type oxides ($ABO_{3-\delta}$), such as $La_xSr_{1-x}MO_3$ (M= Mn, Co, Fe), $CaMnO_3$, or $SrFeO_3$ based materials, are possible OSMs due to their high oxygen storage capacities (OSC) and as their properties can be fine-tuned due having broad cation compositional flexibility.[9–14] These materials, which are widely studied transition metal-based oxygen carriers, utilize oxygen vacancies for storage and transport of oxygen, and allow for reversible switching between a reduced $ABO_{3-\delta}$ state and an oxidized ABO_3 state depending on temperature and partial pressure of oxygen, p_{O2}. Generally, bulk transport of oxygen is rate-limiting for particles larger than ~1 µm, while the catalytic splitting or formation of the O_2 molecule on the surface is rate-limiting for smaller particles.[15] As oxygen vacancies in perovskites have limited mobility, temperatures as high 600-800 °C are generally required to achieve sufficiently rapid oxygen exchange.[9,16] At such elevated temperature these materials are prone to degradation and kinetic demixing.[17] The oxygen storage capacity and oxygen exchange kinetics can be improved by doping on the A-site, B-site, or both.[11,18] Compared to $Sr_{0.8}Ca_{0.2}FeO_3$ and $CaMnO_3$, $Sr_{0.8}Ca_{0.2}Fe_{0.4}Co_{0.6}O_{3-\delta}$ and $Ca_{0.8}Sr_{0.2}MnO_3$ show faster surface oxygen exchange kinetics, shorter times required for oxidation, and smaller activation energy for bulk oxygen diffusion.[13,18] Similar kinetics have also been found for $SrFeO_3$ based materials[19,20] making both material systems good candidates for CLAS at lower temperatures.

Hexagonal manganites, $R\text{MnO}_{3+\delta}$ (R=Sc, Y, Ho-Lu), are possible OSMs due to their large oxygen storage capacities at lower temperatures.[21–25] $R\text{MnO}_3$ oxides can crystallize in one of two crystal structures depending on the size of the R^{3+} cation, with smaller cations ($r_{R}{}^{3+} \leq r_{Ho}{}^{3+}$) favoring the layered hexagonal structure of interest here with space group $P6_3cm$ (Figure 1), while larger cations ($r_{R^{3+}} \geq r_{Dy^{3+}}$) favors the orthorhombic perovskite *Pnma* structure.[26] The hexagonal $P6_3cm$ structure is less close-packed than the *Pnma* perovskite structure, and excess oxygen is accommodated as interstitials in the hexagonal polymorph, in contrast to cation vacancies in the perovskite structure.[27–29] Calculated energy barriers for migration of interstitial oxygen through an interstitialcy mechanism are about 0.4-0.6 eV and lower compared to most oxygen vacancy migration barriers found in perovskites,[27,30–32] enabling significant transport of oxygen interstitials at temperatures even below 200 °C. Unfortunately, at such low temperatures these materials suffer from slow oxidation kinetics in bulk form. Even nanocrystalline samples, which generally show much faster oxidation kinetics than bulk materials,[33] show reduced OSC with faster cooling rates.[24,34–39] The maximum OSC of hexagonal manganites has been improved by *R*-site dopants.[34,36,37,40] However, improving the kinetics of oxygen exchange is crucial for potential industrial applications. E.g. doping $YMnO_{3+\delta}$ with larger *R* cations results in oxygen contents as high as $\delta = 0.45$ at slow cooling rates in oxygen atmosphere.[34] Unfortunately, as these compositions have relatively slow redox kinetics, only a portion of the full capacity can be utilized within the timeframes needed for efficient temperature or pressure swing CLAS. Nanocrystalline $Y_{0.95}Pr_{0.05}MnO_3$ has been shown to only need minutes to reduce from $\delta = 0.2$ to $\delta = 0.0$ in air at T > 270 °C, while re-oxidation to $\delta = 0.2$ requires several hours, as this occurs at a lower temperature where the redox kinetics are slower.[36] Similar oxidation timeframes have also been reported for undoped $YMnO_3$ and $HoMnO_3$.[24,35] Larger *R* cations do seem to affect the redox kinetics, as using *R* larger than Dy^{3+} has resulted in improved oxidation rates for $R_{0.25}Y_{0.75}MnO_3$ (R = Tb, Gd, Sm) and $Y_{0.6}Tb_{0.2}Ce_{0.2}MnO_3$,[37,40] and donor doping can increase both the OSC and the thermal stability of interstitial oxygen in hexagonal manganites.[39,41,42] There are also indications that Ti^{4+}-doping of the Mn sublattice[43] can also improve the oxygen exchange kinetics.[39] The rate limiting step for cyclic processes like CLAS is oxidation and the oxidation kinetics of hexagonal manganites must be improved to enable commercial applications.

Here, we study the oxidation kinetics of $RMn_{1-x}Ti_xO_3$ (R=Ho, Dy; x=0, 0.15) by thermogravimetry, and high temperature X-ray diffraction and X-ray absorption spectroscopy with *in situ* switching of atmosphere. The oxidation kinetics are improved with increasing size of R^{3+} and with 15% Ti^{4+} donor doping. Larger R^{3+} and particularly Ti^{4+} doping causes an expansion of the *ab*-plane and a lower ferroelectric Curie temperature, and both effects are suggested to improve the oxygen bulk transport. Surface exchange rates and activation energies were calculated from lattice parameter changes, using chemical expansion to gauge the oxygen content. The surface exchange kinetics are similar to literature reports on state-of-the-art materials measured at significantly higher temperatures. Finally, we discuss future avenues for further improving the oxidation kinetics of hexagonal manganites by aliovalent doping.

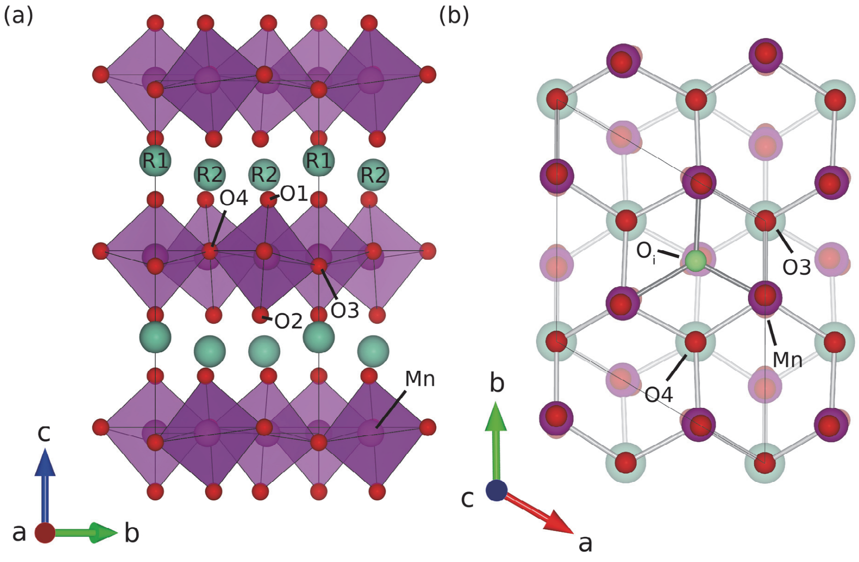

Figure 1: (a) The hexagonal *P*6$_3$*cm* crystal structure with turquoise R^{3+} cations, red oxygen atoms, and the MnO_5 trigonal bipyramids shown as purple polyhedra. (b) The Mn-O plane seen along the *c* axis, with the added O_i (green) on the interstitial site in between Mn. Figures made using VESTA.[44]

METHODS

Synthesis.

Nanocrystalline $RMn_{1-x}Ti_xO_3$ samples were prepared using a previously reported modified citric acid synthesis route.[39,45] Metal acetates $Ho(CH_3CO_2)_3 \cdot xH_2O$ (AlfaAesar), $Dy(CH_3CO_2)_3 \cdot xH_2O$ (AlfaAesar), and $Mn(CH_3CO_2)_3 \cdot xH_2O$ (Riedel-de-Haën) were each dissolved in a mixture of citric acid (99% Sigma-Aldrich) and deionized water with a molar ratio of cation to citric acid of 1:20 for Ho^{3+}, 1:35 for Dy^{3+}, and 1:5 for Mn^{3+}. The precursor solutions were stirred on a hot plate set to 150 °C until clear. For the Ti^{4+} precursor solution, titanium (IV) isopropoxide (TTIP) (Sigma-Aldrich) was added to citric acid dissolved in deionized water, with a molar ratio of cation to citric acid of 1:6.3, and stirred on a hot plate set to 60 °C until clear. The cation precursors were mixed in stoichiometric amounts, and ethylene glycol (EG) (Merck) was added with a 1:1 molar ratio between EG and citric acid. The solutions were stirred on a hot plate set to 150 °C until a viscous gel was formed, which was then dried at 120 °C for three days. The dried gels were heated to 400 °C and kept for 3 h, and subsequently calcined at 600 °C for 6 h. The calcined amorphous powders were then crystallized at temperatures ranging from 850 °C to 950 °C in N_2 atmosphere for 1 h. Some of the samples were pre-annealed in 5% H_2 in N_2 atmosphere at temperatures ranging from 250 °C to 300 °C prior to crystallization to achieve phase pure powders.[39]

Characterization.

To investigate phase purity and lattice parameters, X-ray diffraction (XRD) was performed using a Bruker D8 Focus with Cu Kα radiation. Lattice parameters and average crystallite size of the different powders (Table 1) were determined by Pawley refinement using Bruker AXS TOPAS 5.[46] All samples were refined within the $P6_3cm$ space group. The $DyMnO_3$ sample contains 14 molar% Dy_2O_3, inferred from Rietveld refinement. Oxygen stoichiometry as a function of temperature was analyzed by thermogravimetric analysis (TGA) using a Netzsch STA 449C Jupiter with 30 mL min^{-1} O_2 gas flow. The samples were heated to and subsequently cooled from 800 °C using heating rates of 5, 10 and 20 °C min^{-1}. Calculations of δ were based on a reference point chosen at the lowest mass at $T > 700$ °C where all Mn is assumed to be found as Mn^{3+}, corresponding to $\delta = 0$ and $\delta = 0.075$ for undoped and Ti-doped samples, respectively. Prior to the TGA measurements, all samples were heated to 600 °C for 10 h in N_2 atmosphere to remove excess oxygen.

The morphology of the samples was studied using transmission electron microscopy (TEM) imaging, performed on an aberration-corrected Jeol JEM ARM200F equipped with a cold field emission gun (FEG) operated at 200 kV. Bright-field (BF) TEM and scanning TEM (STEM) images were acquired and are shown in Figure 2 for $HoMnO_3$ and $HoMn_{0.85}Ti_{0.15}O_3$. For the STEM image acquisition, a beam semi-convergence angle of 27 mrad and collection angles of 67-155 mrads were used.

High temperature X-ray diffraction (HT-XRD) and X-ray absorption near edge structure (XANES) measurements with *in situ* switching of atmosphere were carried out at the BM31 beamline of the Swiss-Norwegian Beamlines (SNBL) at the European Synchrotron Radiation Facility (ESRF) in Grenoble, France. A few milligrams of each sample were each placed in a capillary with quartz wool on each side. All experiments were performed using 10 mL min^{-1} gas flow, which was verified using a Pfeiffer Vacuum Omnistar spectrometer. For diffraction measurements, a wavelength of 0.338591 Å and a Dexela 2923 area detector was used. A Hitachi Vortex single-element silicon drift detector was used to measure the XANES fluorescence signal. Absorption measurements were done in fluorescence mode, as transmission for Mn was weak due to the heavy rare earth elements attenuating the signal. XANES measurements were performed prior to, and after, each X-ray diffraction measurement. In addition, each sample was measured once using XANES with *in situ* switching of atmosphere at a temperature chosen for each sample to display reasonable kinetics. Prior to the synchrotron measurements, all samples were heated to 600 °C in N_2 atmosphere to remove any excess oxygen from the structure. The samples were heated 500 °C in N_2 atmosphere in between each measurement. TOPAS 5 operating in launch mode was used for Pawley refinement of lattice parameters. Larch[47] was used for normalization of XANES measurements.

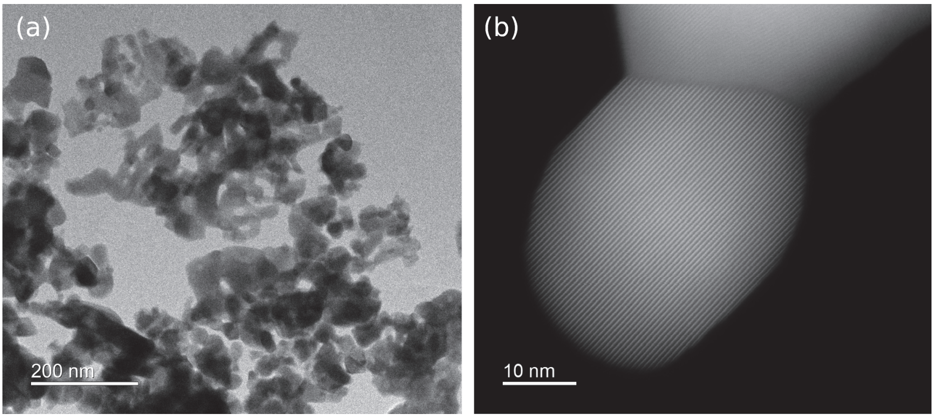

Figure 2: (a) BF TEM image of the nanocrystalline $HoMnO_3$ powder. (b) STEM image of a crystallite in the $HoMn_{0.85}Ti_{0.15}O_3$ sample.

Table 1: Composition and Pawley refined crystallite size and lattice parameters of as-prepared $RMn_{1-x}Ti_xO_3$ samples. All samples were refined within the $P6_3cm$ space group.

Composition	Crystallite size (nm)	*a* (Å)	*c* (Å)	Volume (Å^3)	*c*/*a*
$HoMnO_3$	25 ± 1	6.131(0)	11.371(0)	370.2	1.854
$HoMn_{0.85}Ti_{0.15}O_3$	28 ± 1	6.141(8)	11.400(0)	372.4	1.856
$DyMnO_3$	30 ± 1	6.162(3)	11.368(8)	373.9	1.844
$DyMn_{0.85}Ti_{0.15}O_3$	30 ± 1	6.199(3)	11.433(3)	380.5	1.844

RESULTS

The changes in oxygen stoichiometry as a function of temperature, measured by thermogravimetric analysis at different heating and cooling rates in O_2 atmosphere, are shown in Figure 3. All samples show oxygen absorption at temperatures below ~350 °C during heating and cooling, with the maximum oxygen stoichiometry during heating found at ~300 °C. The maximum oxygen stoichiometry decreases with increasing heating rates as less time is spent in the temperature region where oxidation occurs. All samples reach a plateau in oxygen stoichiometry when cooling to temperatures below 200 °C, where further oxidation is hindered by slower kinetics at low temperatures. For the undoped samples in panels (a) and (c), the oxygen stoichiometry at this plateau decreases significantly with faster cooling rates. These materials also display a significant thermal hysteresis in oxygen stoichiometry during heating and cooling, and the width of the hysteresis for $DyMnO_3$ increases from ~30 °C to ~60 °C when increasing the rate from 1 °C min^{-1} to 5 °C min^{-1}. No differences in the kinetics of oxidation between $HoMnO_3$ and $DyMnO_3$ can be inferred from the TGA measurements.

In contrast to the undoped materials, the Ti-doped materials (Figure 3(b), (d)) show no thermal hysteresis in oxygen stoichiometry upon heating and cooling, and the oxygen storage capacity is insensitive to increasing cooling rates. During heating, these samples start to oxidize at much lower temperatures than undoped samples, with temperature onsets of oxidation at ~100 °C for $HoMn_{0.85}Ti_{0.15}O_3$ and $DyMn_{0.85}Ti_{0.15}O_3$, compared to ~150 °C and ~200 °C for $HoMnO_3$ and $DyMnO_3$, respectively. This indicates that Ti^{4+} donor doping greatly improves the kinetics of oxidation as well as that it stabilizes oxygen interstitials to higher temperatures.

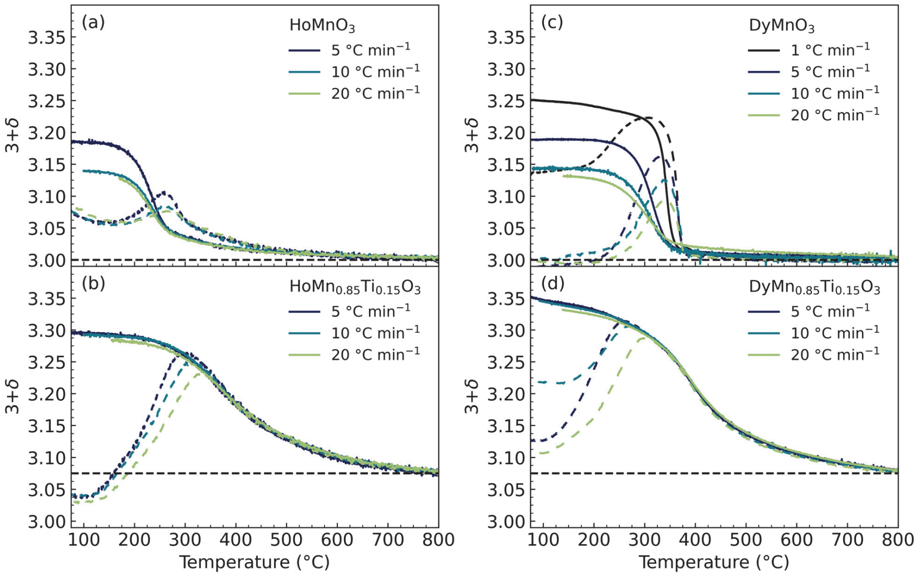

Figure 3: Oxygen stoichiometry 3+δ measured by TGA during heating (dashed lines) and cooling (solid lines) in O_2 atmosphere using different heating and cooling rates for (a) $HoMnO_3$, (b) $HoMn_{0.85}Ti_{0.15}O_3$, (c) $DyMnO_3$ and (d) $DyMn_{0.85}Ti_{0.15}O_3$. The horizontal dashed lines indicate the oxygen stoichiometry where all Mn is assumed to be Mn^{3+}, for Ti-doped samples this corresponds to $\delta = 0.075$.

All samples display a partial oxidation of Mn, from Mn^{3+} to Mn^{4+}, when exposed to O_2 atmosphere. Normalized X-ray absorption near-edge structure (XANES) spectra of the Mn *K*-edge measured before and after oxidation at 300 °C are shown in Figure 4, and at other temperatures in Supplementary Figures S2-4. The spectra collected after oxidation, noted "O_2" in Figure 4, are all shifted towards higher energies than the spectra measured in N_2. As shown by the Mn_2O_3 and MnO_2 references, with the Mn *K*-edge of MnO_2 being at higher energies than that of Mn_2O_3, this shift indicates an oxidation process from Mn^{3+} to Mn^{4+}, which is the expected charge compensation mechanism upon absorption of oxygen. The Ti-doped samples in panels (b) and (d) display a shift with greater magnitude than the undoped samples, indicating that a larger amount of Mn^{3+} has been oxidized to Mn^{4+}. This corresponds well with the larger oxygen content that Ti-doped samples possess at 300 °C (Figure 3). The spectra of $HoMnO_3$ in (a) shows the smallest change in absorption edge energies after being exposed to O_2, as this composition shows low oxygen storage capacity ($\delta \approx 0.06$) at this temperature.

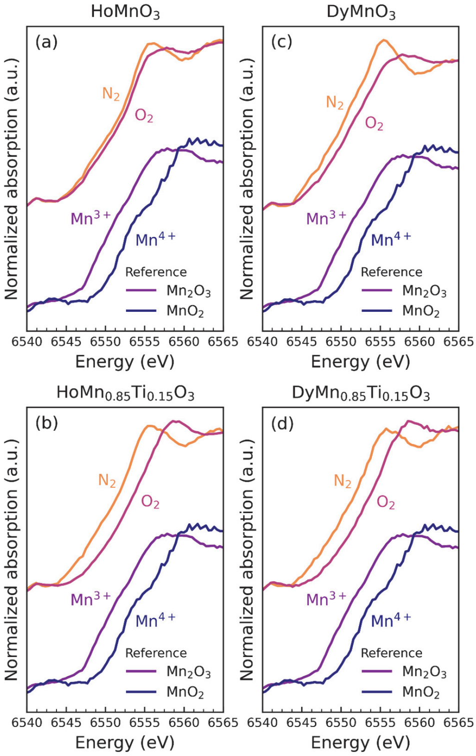

Figure 4: Normalized XANES spectra at the Mn *K*-edge of (a) $HoMnO_3$, (b) $HoMn_{0.85}Ti_{0.15}O_3$, (c) $DyMnO_3$ and (d) $DyMn_{0.85}Ti_{0.15}O_3$ before (N_2) and after oxidation (O_2) at 300 °C. The spectra of Mn_2O_3 and MnO_2 are shown as references.

XANES spectra measured during oxidation after *in situ* switching of atmosphere from N_2 to O_2 are shown in Figure 5. The Mn *K*-edge position shifts progressively to higher energies with time, with the Ti-doped samples reaching the highest oxidation state faster than the undoped samples. The largest shifts in edge position occurs during the first 10 minutes for all samples. Temperatures for each sample were chosen where the oxidation progresses at a speed allowing good quality spectra to be collected within a reasonable time.

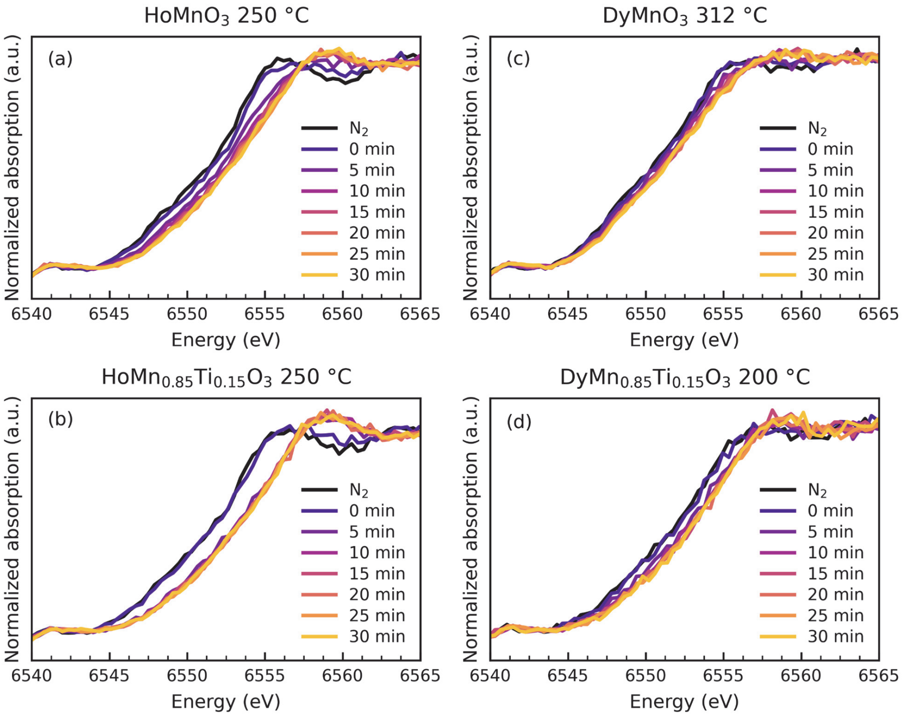

Figure 5: Normalized time-resolved XANES collected upon *in situ* switching of atmosphere from N_2 to O_2 for (a) $HoMnO_3$, (b) $HoMn_{0.85}Ti_{0.15}O_3$, (c) $DyMnO_3$ and (d) $DyMn_{0.85}Ti_{0.15}O_3$ at different temperatures. Measurements done in O_2 are labelled as the time after switching from N_2 to O_2 atmosphere.

Synchrotron X-ray diffractograms measured at 300 °C upon *in situ* switching of atmosphere from N_2 to O_2 are shown in Figure 6, depicted as waterfall plots in (a)-(d) and as 2D contour plots in (e)-(h). Measurements at other temperatures can be found in Figures S6-S11 in the Supporting Information. All samples show shifts in position of the (0 0 4) reflection at ~6.8° 2θ towards higher angles during oxidation, reflecting a contraction of the *c* axis when interstitial oxygen enters MnO-planes. This contraction is attributed to partial rectification of the tilting of the MnO_5 bipyramids and the smaller radius of Mn^{4+} which is charge compensating interstitial O^{2-}. In the Dy-containing samples, shown in panels (c,d) and (g,h), the single (0 0 4) reflection of the $P6_3cm$ structure (marked with triangles ▲) is replaced by the two (1 0 10) and (0 0 12) reflections (marked with asterisks *) of the new structure with space group *R*3*c* during oxidation, respectively. The appearance of these two reflections demonstrates the transition to the oxygen-rich structure with space group *R*3*c* ($\delta > 0.28$), where the *c*-axis is tripled compared to the stoichiometric structure with space group $P6_3cm$.[23,25,39] Another observable in Figure 6 is the faster oxidation process for the Ti-doped samples compared to the undoped samples; both $HoMn_{0.85}Ti_{0.15}O_3$ and $DyMn_{0.85}Ti_{0.15}O_3$ stabilize within 2 minutes, while $DyMnO_3$ needs over 15 minutes to fully oxidize. The $HoMnO_3$ sample does not oxidize significantly at 300 °C, as the TGA measurements in Figure 3 show.

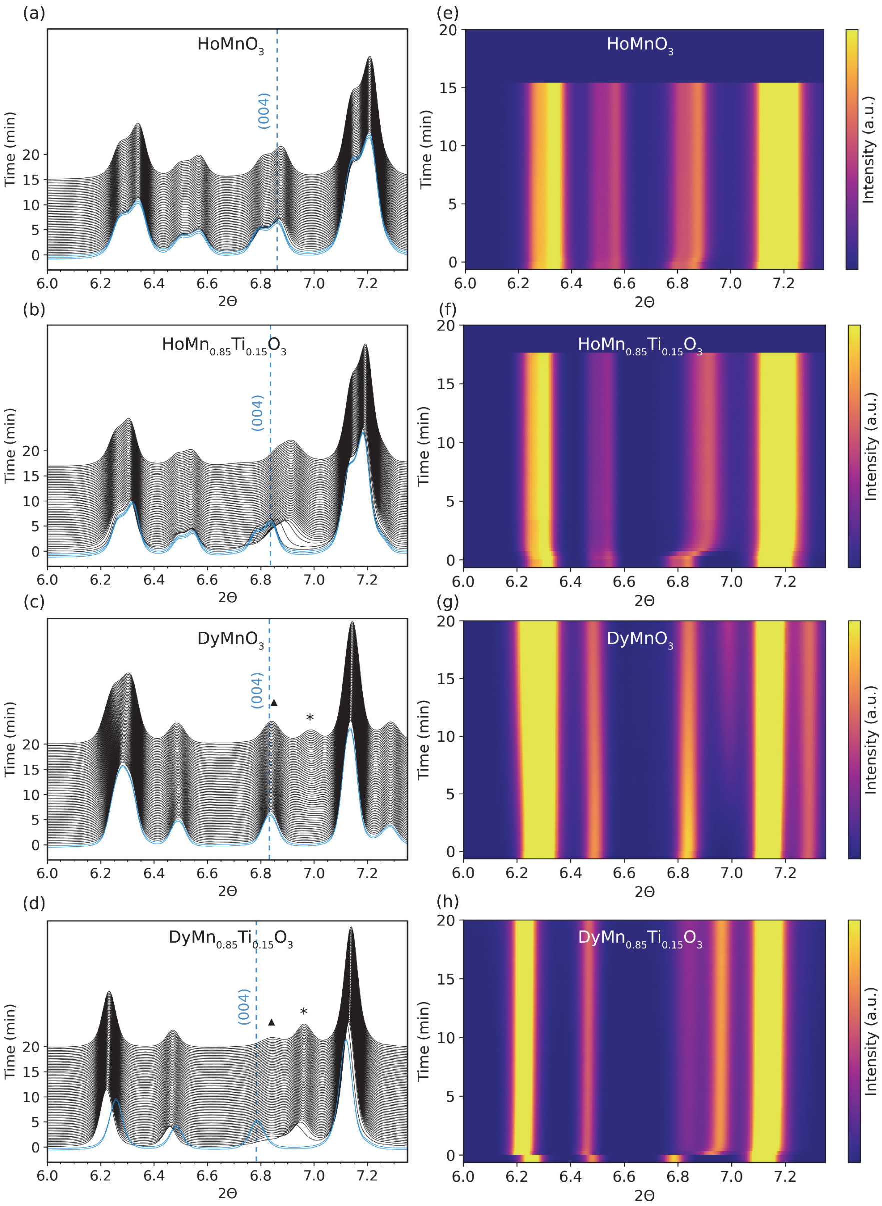

Figure 6: X-ray diffractograms and 2D contour plots of (a),(e) $HoMnO_3$, (b),(f) $HoMn_{0.85}Ti_{0.15}O_3$, (c),(g) $DyMnO_3$ and (d),(h) $DyMn_{0.85}Ti_{0.15}O_3$ measured at 300 °C as a function of time after *in situ* switching of atmosphere from N_2 (blue) to O_2 (black). The baseline intensity at 6.0° 2θ in (a)-(d)

indicates the time in min. after switching from N_2 to O_2 purge gas. Vertical dashed lines (blue) indicate the initial position of the (0 0 4) reflection measured in N_2. The triangles (▲) indicate the (1 0 10) reflection, and the asterisks (*) indicates the (0 0 12) reflection, both characteristic for the $R3c$ space group.

Changes in lattice parameters are proposed to be closely linked to the oxygen stoichiometry through chemical expansion,[48] through which the kinetics of oxidation can be investigated indirectly.[49] Lattice parameters of $HoMnO_3$, $HoMn_{0.85}Ti_{0.15}O_3$ and $DyMn_{0.85}Ti_{0.15}O_3$ as a function of time after switching from N_2 to O_2 atmosphere at different temperatures are shown in Figure 7, with measurements of $DyMn_{0.85}Ti_{0.15}O_3$ at additional temperatures included in Figure S12 in the Supporting Information. For all samples, the oxidation process is faster with increasing temperatures, as expected. The net expansion and contraction of the lattice parameters decrease with increasing temperature, as the materials oxidize less at higher temperatures. This is most significant for $HoMnO_3$ (Figure 7(a)), with almost no change in lattice parameters above 300 °C where most of the excess oxygen has already desorbed, as measured by TGA (Figure 3). Both undoped (Figure 7(a)) and Ti-doped $HoMnO_3$ (Figure 7(b)) show an expansion in the a parameter during oxidation, while Ti-doped $DyMnO_3$ (Figure 7(c)) shows initially an expansion and then a contraction as the sample oxidizes further. This is in accordance with previous work on Ti-doped $DyMnO_3$.[39] The equilibration time for the oxidation decreases with increasing R cation size and with Ti-doping; at 250 °C $HoMnO_3$ takes over 20 minutes to reach equilibrium, while Ti-doped $HoMnO_3$ and $DyMnO_3$ each take ~15 minutes and ~5 minutes, respectively. At 350 °C, both Ti-doped samples oxidize very rapidly, with Ti-doped $HoMnO_3$ reaching equilibrium in <1 minute, and Ti-doped $DyMnO_3$ in a few seconds. Lattice parameters for undoped $DyMnO_3$ are not shown due to unstable Pawley refinements of the data collected under the gradual transition between $P6_3cm$ and $R3c$ during oxidation.

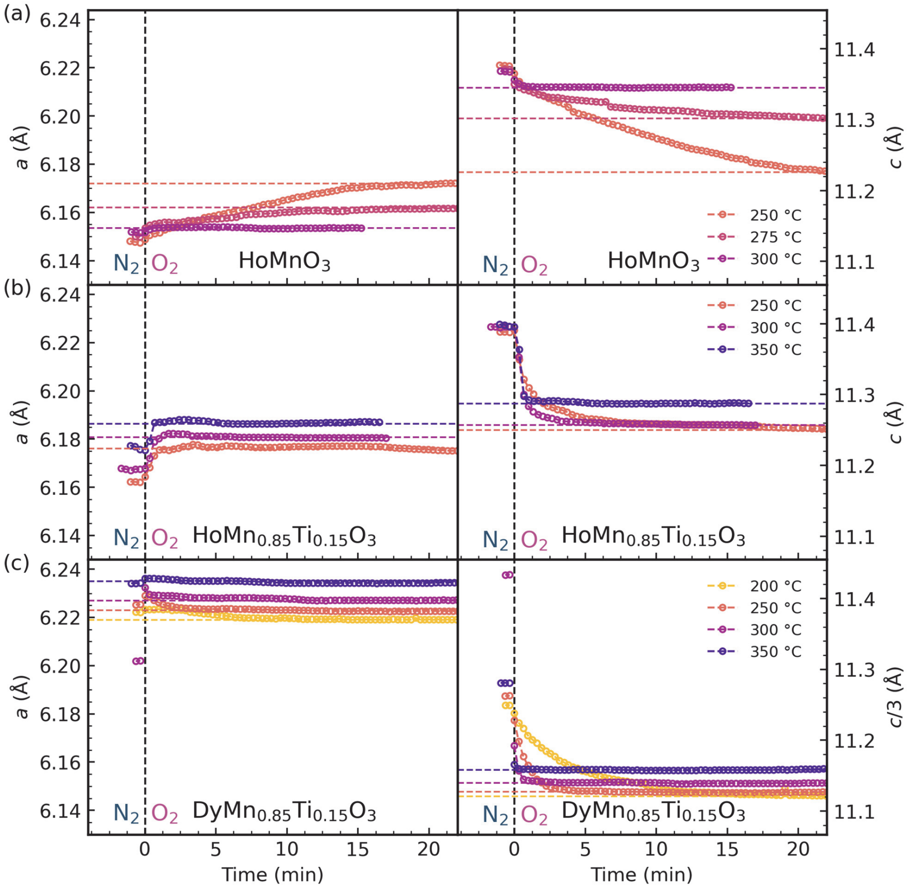

Figure 7: Refined lattice parameters *a* and *c* as a function of time after switching from N_2 to O_2 atmosphere for (a) $HoMnO_3$, (b) $HoMn_{0.85}Ti_{0.15}O_3$, and (c) $DyMn_{0.85}Ti_{0.15}O_3$. For $DyMn_{0.85}Ti_{0.15}O_3$, which were refined within the *R*3*c* space group, *c*/a is shown for easier comparison with the refinements within the $P6_3cm$ space group.

DISCUSSION

Ionic radii of *R*. The oxidation kinetics of hexagonal manganites improve from Ho^{3+} (1.015 Å, C.N=7[50]) to the larger Dy^{3+} (1.027 Å), as seen from the X-ray diffractograms (Figure 6) and lattice parameters (Figure 7). A direct comparison of the kinetics between undoped $HoMnO_3$ and $DyMnO_3$ is not straight forward as these materials oxidize at different temperatures. The relationship between unit cell volume and oxygen diffusion rate has previously been reported for $R_{0.25}Y_{0.75}MnO_3$, which showed improved oxygen absorption and release rates with larger R^{3+} cations than Dy^{3+}.[37] We hypothesize that the expansion of the unit cell caused by the larger R^{3+} cations, which necessarily increases the interatomic distances in the Mn-O sublattice, reduces the electrostatic repulsion between planar oxygen ions and the migrating O_i ion in the interstitialcy mechanism.[27] Unit cell expansion, particularly in the *ab*-plane, thus improves the kinetics of oxygen absorption and desorption.

Ti donor doping. As evident from both TGA (Figure 3) and time-resolved *in situ* measurements (Figures 5-7), there is a significant increase in the oxidation rate upon doping with 15% Ti, reducing the time for full oxidation by an order of magnitude. In the hexagonal $P6_3cm$ structure, each MnO_5 bipyramid in the *ab*-layer is slightly tilted in a pattern of trimers and the R^{3+} cations are displaced along the *c*-axis.[51] Ti^{4+} ions on the Mn^{3+} sites have been shown to stabilize the high symmetry $P6_3/mmc$ phase with untilted bipyramids and non-displaced *R* to lower temperatures.[52] We hypothesize that the less distorted structure, comparable to the high-symmetry phase, also favors faster oxidation, as higher symmetry in general promotes ionic conductivity and because of the ion migration mechanism in these materials as discussed below. $HoMn_{0.85}Ti_{0.15}O_3$ and $DyMn_{0.85}Ti_{0.15}O_3$ display larger *a* lattice parameters compared to their undoped counterparts both before (Table 1) and after oxidation (Figure 7), resulting in an expanded *ab*-plane similar to the effect of larger R^{3+}.

The average c/a ratios determined from the refined lattice parameters of oxidized samples (Figure 7) are shown in Figure 8, showing an evolution towards, and beyond, the value of 1.81 found at the T_C of $YMnO_3$.[51,53] The change of structure towards the $P6_3/mmc$ structure as induced by Ti-doping is also significant because it implies a reduction of the distortion mode amplitude of the K_3 distortion mode driving the transition to $P6_3cm$.[51,53–55] In real space, the ionic displacement vectors resulting from freezing in the K_3 mode have strong similarities to those describing the transition state of the interstitialcy migration mechanism for O_i.[27] While the connection between phonons and ionic migration is generally poorly understood,[56,57] we hypothesize that Ti doping-induced partial melting of the K_3 mode, pushing the material towards higher symmetry, also enhances the kinetics of oxygen bulk transport.

The absence of thermal hysteresis during heating and cooling, the increased maximum OSC, and the close-to-zero decrease in OSC upon increasing cooling rate found through TGA (Figure 3), show that Ti-doped *R*MnO_3 can be utilized for oxygen absorption at faster rates than undoped materials. As demonstrated both here (Figure 3) and in previous studies,[39,41] interstitial oxygen is stabilized towards higher temperatures for Ti-doped samples. Compared to undoped samples, Ti-doping enables pressure swing absorption at higher temperatures where the kinetics of oxidation and reduction will be much faster.

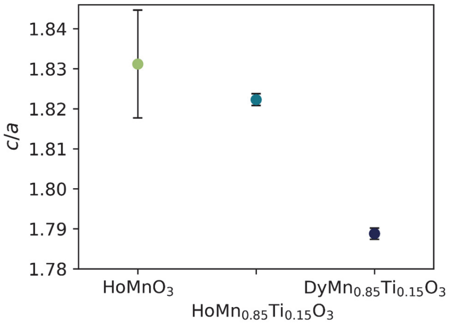

Figure 8: Average *c*/*a* of oxidized $HoMnO_3$, $HoMn_{0.85}Ti_{0.15}O_3$ and $DyMn_{0.85}Ti_{0.15}O_3$. For $DyMn_{0.85}Ti_{0.15}O_3$, *c*/3 was used instead of *c* for easier comparison between the *R*3*c* and *P*6$_3$*cm* structures.

Surface exchange rate. The significant contraction along the *c* axis induced by incorporation of interstitial oxygen can be used as a measure of the oxygen content, and thus the oxygen surface exchange rate can be inferred from the transient lattice parameters during oxidation after switching from N_2 to O_2 atmosphere. We investigated the kinetics of oxidation by fitting refined lattice parameters to the model developed by Moreno et al.[49] For sufficiently small sample dimensions, usually below a few tens of micrometers, the surface exchange reaction is the rate limiting step for oxygen incorporation.[58,59] Using the contraction of the *c* parameter as a measure of the degree of oxidation of the material, a direct correspondence between unit cell parameter and concentration of oxygen is assumed. The defect concentration at a given time, $c(t)$, will then follow an exponential equation,

$$\frac{[c_{eq} - c(t)]}{[c_{eq} - c_{t=0}]} = \exp\left(-\frac{k_{exch}}{d} \cdot t\right) \tag{1}$$

where c_{eq} is the equilibrium concentration, $c_{t=0}$ is the start concentration, k_{exch} is the surface exchange rate coefficient, and d is the average size of the material sample, e.g. film thickness, or in our case half the particle size. The surface exchange rate k can now be estimated by fitting the refined c lattice parameters presented in Figure 7 and Figure S12 to eq. (1).

The calculated oxygen surface exchange rates for $HoMnO_3$, $HoMn_{0.85}Ti_{0.15}O_3$ and $DyMn_{0.85}Ti_{0.15}O_3$ are presented in Figure 9. The surface exchange rates increase with increasing R cation size, and with Ti-doping, and the rates of the Ti-doped samples are comparable to what has been reported for perovskites and other oxides at much higher temperatures.[15,49,58,60–65] The surface exchange rate for $HoMnO_3$ at 300 °C is not included, as very little oxidation happens in this sample at higher temperatures, and the resulting calculated exchange rate is therefore unreliable.

The activation energies calculated from the surface exchange rates for each sample were found to be 0.54 eV for $HoMn_{0.85}Ti_{0.15}O_3$ and 0.68 eV for $DyMn_{0.85}Ti_{0.15}O_3$. The activation energy for $HoMnO_3$ was not calculated as this sample had only two data points, which would result in a high uncertainty in the calculated value. These activation energies are slightly lower than the typical values reported for hexagonal $Pr_{0.05}Y_{0.95}MnO_3$ (0.8-0.9 eV)[66] and for perovskites (~0.7-1.1 eV).[15,62,67,68] The activation energies for the Ti-doped samples are higher than that of the undoped $HoMnO_3$, which can be a result of defect affinity between the dopant and interstitial oxygen. From Figure 7, it can be observed that $DyMn_{0.85}Ti_{0.15}O_3$ displays an initial expansion followed by a contraction in the *ab*-plane during oxidation, which differs from the other samples that only show expansion. One possible explanation for this is that the electrostatic attraction between the Ti^{4+} present in the already expanded *ab*-plane and the negatively charged O_i entering the lattice is larger than the electrostatic repulsion between planar oxygen and O_i, causing a contraction along the a axis and an increase in stability of interstitial oxygen in the structure compared to the undoped samples. Substituting $YMnO_3$ with larger R cations such as Sm^{3+} can stabilize the oxidized phase and thus lower the oxygen release rate.[37] The TGA data in Figure 3 show no sign that the stronger bond between Ti^{4+} and O_i is lowering the rate of oxygen release, and the lack of thermal hysteresis confirms that the kinetics of reduction is still fast.

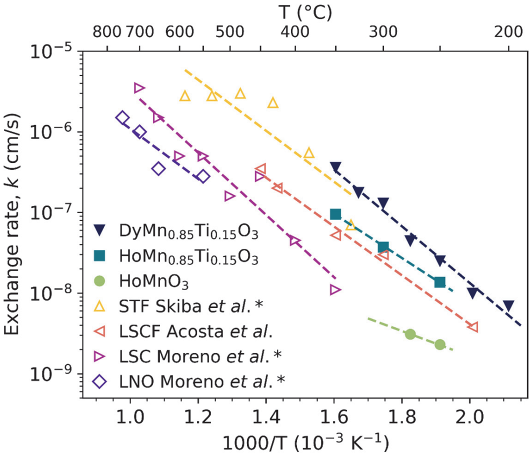

Figure 9: Temperature dependence of oxygen surface exchange rates *k* upon changing atmosphere from N_2 to O_2. Surface exchange rates for $SrTi_{0.65}Fe_{0.35}O_{2.825+\delta}$ from Skiba *et al.*,[62] $(La_{0.60}Sr_{0.40})_{0.95}(Co_{0.20}Fe_{0.80})O_{3-\delta}$ from Acosta *et al.*,[65] and $La_{0.6}Sr_{0.4}CoO_{3-\delta}$ and $LaNiO_{3-\delta}$ from Moreno *et al.*[15] are included for comparison purposes. Exchange rates marked with an asterisk (*) were measured using $p_{O2} = 0.21$.

For hexagonal manganites to be used for CLAS, both the OSC and the kinetics of oxidation and reduction must be sufficiently high. While the OSC of hexagonal manganites has become competitive compared to other material classes, future work on RMnO$_3$ for CLAS should focus on improving the oxidation kinetics. It is now established that larger R^{3+} improves both the oxidation rate and OSC, and large rare earth dopants should be included in future studies. The addition of Ti^{4+} affects both the OSC and the kinetics of oxidation positively, but it also limits these materials to pressure swing applications, as the broad temperature interval for oxidation and reduction is impractical for temperature swing processes. Other aliovalent dopants may also be beneficial, e.g. Zr^{4+} on the Y-sublattice has displayed similar effects as Ti^{4+} on the Mn-sublattice for the OSC and thermal stability of O_i,[42] but its effect on oxidation kinetics is unknown.

CONCLUSIONS

The kinetics of oxidation of nanocrystalline RMnO$_3$ has been studied by thermogravimetric analysis and high temperature X-ray diffraction upon *in situ* switching of atmosphere from N_2 to O_2. The rate of oxidation increases for larger R^{3+} cations and with 15% Ti^{4+}-doping on the Mn sublattice. The oxygen storage capacity of Ti-doped samples is insensitive to the rate of cooling in O_2 atmosphere, signifying very fast kinetics of oxidation. Changes in lattice parameters inferred from HT-XRD showed that the oxidation times decrease substantially when Ho^{3+} is replaced by the larger Dy^{3+}, and, even more when substituting 15% Ti^{4+} on the Mn sublattice. The oxidation of $DyMn_{0.85}Ti_{0.15}O_3$, which showed the fastest kinetics, was completed within only a few seconds at 350 °C in O_2 atmosphere. Faster oxidation kinetics were correlated with expansion of the *ab*-plane caused by the larger ionic radius of Dy^{3+}, and the Ti^{4+}-doping-induced partial rectification of the tilted MnO_5 trigonal bipyramids, which also results in a smaller *c*/*a* ratio. The change in structure towards the high symmetry $P6_3/mmc$ phase is also hypothesized to improve the kinetics of oxygen transport. The changes in lattice parameters were used to calculate surface exchange rates, which also showed improvement with larger rare earth cation and with Ti-doping.

ACKNOWLEDGEMENTS

We thank MSc Tormod Østmoe for preparing the $DyMnO_3$ amorphous powder. Financial support from NTNU Norwegian University of Science and Technology is acknowledged. The TEM and STEM work was performed with support from the Research Council of Norway through the Norwegian Center for Transmission Electron Microscopy, NORTEM (197405/F50) and MoZEES, a Norwegian Centre for Environment-friendly Energy Research (FME), co-sponsored by the Research Council of Norway (project number 2057653) and 40 partners from research, industry, and public sector. We would also like to thank the Swiss-Norwegian Beamlines (SNBL) BM31 at the European Synchrotron Radiation Facility (ESRF, Grenoble, France) for providing beamtime, and the staff for their assistance during the beamtime.

REFERENCES

(1) Kirschner, M. J.; Alekseev, A.; Dowy, S.; Grahl, M.; Jansson, L.; Keil, P.; Lauermann, G.; Meilinger, M.; Schmehl, W.; Weckler, H.; Windmeier, C. Oxygen. In *Ullmann's Encyclopedia of Industrial Chemistry*; Wiley-VCH Verlag GmbH & Co. KGaA: Weinheim, Germany, 2017; pp 1–32. https://doi.org/10.1002/14356007.a18_329.pub2.

(2) Wu, F.; Argyle, M. D.; Dellenback, P. A.; Fan, M. Progress in O2 Separation for Oxy-Fuel Combustion–A Promising Way for Cost-Effective CO2 Capture: A Review. *Prog. Energy Combust. Sci.* **2018**, *67*, 188–205. https://doi.org/10.1016/j.pecs.2018.01.004.

(3) Häring, H. W.; Ahner, C.; Belloni, A. *Industrial Gases Processing*; Wiley, 2008.

(4) Smith, A. .; Klosek, J. A Review of Air Separation Technologies and Their Integration with Energy Conversion Processes. *Fuel Process. Technol.* **2001**, *70* (2), 115–134. https://doi.org/10.1016/S0378-3820(01)00131-X.

(5) Zhou, C.; Shah, K.; Moghtaderi, B. Techno-Economic Assessment of Integrated Chemical Looping Air Separation for Oxy-Fuel Combustion: An Australian Case Study. *Energy and Fuels* **2015**, *29* (4), 2074–2088. https://doi.org/10.1021/ef5022076.

(6) Moghtaderi, B. Application of Chemical Looping Concept for Air Separation at High Temperatures. *Energy and Fuels* **2010**, *24* (1), 190–198. https://doi.org/10.1021/ef900553j.

(7) Wu, F.; Argyle, M. D.; Dellenback, P. A.; Fan, M. Progress in O2 Separation for Oxy-Fuel Combustion–A Promising Way for Cost-Effective CO2 Capture: A Review. *Prog. Energy Combust. Sci.* **2018**, *67*, 188–205. https://doi.org/10.1016/j.pecs.2018.01.004.

(8) Tang, M.; Xu, L.; Fan, M. Progress in Oxygen Carrier Development of Methane-Based Chemical-Looping Reforming: A Review. *Appl. Energy* **2015**, *151*, 143–156. https://doi.org/10.1016/j.apenergy.2015.04.017.

(9) Zhu, X.; Li, K.; Neal, L.; Li, F. Perovskites as Geo-Inspired Oxygen Storage Materials for Chemical Looping and Three-Way Catalysis: A Perspective. *ACS Catal.* **2018**, *8* (9), 8213–8236. https://doi.org/10.1021/acscatal.8b01973.

(10) Demont, A.; Abanades, S.; Beche, E. Investigation of Perovskite Structures as Oxygen-Exchange Redox Materials for Hydrogen Production from Thermochemical Two-Step Water-Splitting Cycles. *J. Phys. Chem. C* **2014**, *118* (24), 12682–12692. https://doi.org/10.1021/jp5034849.

(11) Krzystowczyk, E.; Wang, X.; Dou, J.; Haribal, V.; Li, F. Substituted $SrFeO_3$ as Robust Oxygen Sorbents for Thermochemical Air Separation: Correlating Redox Performance with Compositional and Structural Properties. *Phys. Chem. Chem. Phys.* **2020**, *22* (16), 8924–8932. https://doi.org/10.1039/d0cp00275e.

(12) Vieten, J.; Bulfin, B.; Senholdt, M.; Roeb, M.; Sattler, C.; Schmücker, M. Redox Thermodynamics and Phase Composition in the System $SrFeO_{3-\delta}$ — $SrMnO_{3-\delta}$. *Solid State Ionics* **2017**, *308* (April), 149–155. https://doi.org/10.1016/j.ssi.2017.06.014.

(13) Bulfin, B.; Vieten, J.; Starr, D. E.; Azarpira, A.; Zachäus, C.; Hävecker, M.; Skorupska, K.; Schmücker, M.; Roeb, M.; Sattler, C. Redox Chemistry of $CaMnO_3$ and $Ca_{0.8}Sr_{0.2}MnO_3$ Oxygen Storage Perovskites. *J. Mater. Chem. A* **2017**, *5* (17), 7912–7919. https://doi.org/10.1039/c7ta00822h.

(14) Krzystowczyk, E.; Haribal, V.; Dou, J.; Li, F. Chemical Looping Air Separation Using a Perovskite-Based Oxygen Sorbent: System Design and Process Analysis. *ACS Sustain. Chem. Eng.* **2021**, *9* (36), 12185–12195. https://doi.org/10.1021/acssuschemeng.1c03612.

(15) Moreno, R.; Zapata, J.; Roqueta, J.; Bagués, N.; Santiso, J. Chemical Strain and Oxidation-Reduction Kinetics of Epitaxial Thin Films of Mixed Ionic-Electronic Conducting Oxides Determined by X-Ray Diffraction. *J. Electrochem. Soc.* **2014**, *161* (11), F3046–F3051. https://doi.org/10.1149/2.0091411jes.

(16) Cai, G.; Luo, C.; Zheng, Y.; Cao, D.; Luo, T.; Li, X.; Wu, F.; Zhang, L. $BaCoO_{3-\delta}$ Perovskite-Type Oxygen Carrier for Chemical Looping Air Separation, Part I: Determination of Oxygen Non-Stoichiometry and Cyclic Stability of Oxygen Carrier. *Sep. Purif. Technol.* **2022**, *302* (July), 121972. https://doi.org/10.1016/j.seppur.2022.121972.

(17) Lein, H.; Wiik, K.; Grande, T. Kinetic Demixing and Decomposition of Oxygen Permeable Membranes. *Solid State Ionics* **2006**, *177* (19–25), 1587–1590. https://doi.org/10.1016/j.ssi.2006.03.001.

(18) Dou, J.; Krzystowczyk, E.; Wang, X.; Robbins, T.; Ma, L.; Liu, X.; Li, F. A- and B-site Codoped $SrFeO_3$ Oxygen Sorbents for Enhanced Chemical Looping Air Separation. *ChemSusChem* **2020**, *13* (2), 385–393. https://doi.org/10.1002/cssc.201902698.

(19) Bulfin, B.; Lapp, J.; Richter, S.; Gubàn, D.; Vieten, J.; Brendelberger, S.; Roeb, M.; Sattler, C. Air Separation and Selective Oxygen Pumping via Temperature and Pressure Swing Oxygen Adsorption Using a Redox Cycle of $SrFeO_3$ Perovskite. *Chem. Eng. Sci.* **2019**, *203*, 68–75. https://doi.org/10.1016/j.ces.2019.03.057.

(20) Vieten, J.; Bulfin, B.; Call, F.; Lange, M.; Schmücker, M.; Francke, A.; Roeb, M.; Sattler, C. Perovskite Oxides for Application in Thermochemical Air Separation and Oxygen Storage. *J. Mater. Chem. A* **2016**, *4* (35), 13652–13659. https://doi.org/10.1039/c6ta04867f.

(21) Remsen, S.; Dabrowski, B. Synthesis and Oxygen Storage Capacities of Hexagonal $Dy_{1-x}Y_xMnO_{3+\delta}$. *Chem. Mater.* **2011**, *23* (17), 3818–3827. https://doi.org/10.1021/cm2006956.

(22) Remsen, S.; Dabrowski, B.; Chmaissem, O.; Mais, J.; Szewczyk, A. Synthesis and Oxygen Content Dependent Properties of Hexagonal $DyMnO_{3+\delta}$. *J. Solid State Chem.* **2011**, *184* (8), 2306–2314. https://doi.org/10.1016/j.jssc.2011.06.037.

(23) Abughayada, C.; Dabrowski, B.; Kolesnik, S.; Brown, D. E.; Chmaissem, O. Characterization of Oxygen Storage and Structural Properties of Oxygen-Loaded Hexagonal $RMnO_{3+\delta}$ (R = Ho, Er, and Y). *Chem. Mater.*

2015, *27* (18), 6259–6267. https://doi.org/10.1021/acs.chemmater.5b01817.

(24) Świerczek, K.; Klimkowicz, A.; Nishihara, K.; Kobayashi, S.; Takasaki, A.; Alanizy, M.; Kolesnik, S.; Dabrowski, B.; Seong, S.; Kang, J. Oxygen Storage Properties of Hexagonal $HoMnO_{3+\delta}$. *Phys. Chem. Chem. Phys.* **2017**, *19* (29), 19243–19251. https://doi.org/10.1039/c7cp03556j.

(25) Abughayada, C.; Dabrowski, B.; Avdeev, M.; Kolesnik, S.; Remsen, S.; Chmaissem, O. Structural, Magnetic, and Oxygen Storage Properties of Hexagonal $Dy_{1-x}Y_xMnO_{3+\delta}$. *J. Solid State Chem.* **2014**, *217*, 127–135. https://doi.org/10.1016/j.jssc.2014.05.017.

(26) Selbach, S. M.; Løvik, A. N.; Bergum, K.; Tolchard, J. R.; Einarsrud, M. A.; Grande, T. Crystal Structure, Chemical Expansion and Phase Stability of $HoMnO_3$ at High Temperature. *J. Solid State Chem.* **2012**, *196*, 528–535. https://doi.org/10.1016/j.jssc.2012.07.024.

(27) Skjærvø, S. H.; Wefring, E. T.; Nesdal, S. K.; Gaukås, N. H.; Olsen, G. H.; Glaum, J.; Tybell, T.; Selbach, S. M. Interstitial Oxygen as a Source of P-Type Conductivity in Hexagonal Manganites. *Nat. Commun.* **2016**, *7*, 13745.

(28) van Roosmalen, J. A. M.; Cordfunke, E. H. P. The Defect Chemistry of $LaMnO_{3\pm\delta}$. 4. Defect Model for $LaMnO_{3+\delta}$. *Journal of Solid State Chemistry*. 1994, pp 109–112. https://doi.org/10.1006/jssc.1994.1143.

(29) Griffin, S. M.; Reidulff, M.; Selbach, S. M.; Spaldin, N. A. Defect Chemistry as a Crystal Structure Design Parameter: Intrinsic Point Defects and Ga Substitution in $InMnO_3$. *Chem. Mater.* **2016**, *29* (6), 2425–2434. https://doi.org/10.1021/acs.chemmater.6b04207.

(30) Kotomin, E. A.; Mastrikov, Y. A.; Heifets, E.; Maier, J. Adsorption of Atomic and Molecular Oxygen on the $LaMnO_3$ (001) Surface: Ab Initio Supercell Calculations and Thermodynamics. *Phys. Chem. Chem. Phys.* **2008**, *10* (31), 4644–4649. https://doi.org/10.1039/b804378g.

(31) Polfus, J. M.; Yildiz, B.; Tuller, H. L. Origin of Fast Oxide Ion Diffusion along Grain Boundaries in Sr-Doped $LaMnO_3$. *Phys. Chem. Chem. Phys.* **2018**, *20* (28), 19142–19150. https://doi.org/10.1039/c8cp02443j.

(32) Carrasco, J.; Illas, F.; Lopez, N.; Kotomin, E. A.; Zhukovskii, Y. F.; Evarestov, R. A.; Mastrikov, Y. A.; Piskunov, S.; Maier, J. First-Principles Calculations of the Atomic and Electronic Structure of F Centers in the Bulk and on the (001) Surface of $SrTiO_3$. *Phys. Rev. B - Condens. Matter Mater. Phys.* **2006**, *73* (6). https://doi.org/10.1103/PhysRevB.73.064106.

(33) Grande, T.; Tolchard, J. R.; Selbach, S. M. Anisotropic Thermal and Chemical Expansion in Sr-Substituted LaMnO 3+δ: Implications for Chemical Strain Relaxation. *Chem. Mater.* **2012**, *24* (2), 338–345. https://doi.org/10.1021/cm2030608.

(34) Klimkowicz, A.; Cichy, K.; Chmaissem, O.; Dabrowski, B.; Poudel, B.; Świerczek, K.; Taddei, K. M.; Takasaki, A. Reversible Oxygen Intercalation in Hexagonal $Y_{0.7}Tb_{0.3}MnO_{3+\delta}$: Toward Oxygen Production by Temperature-Swing Absorption in Air. *J. Mater. Chem. A* **2019**, *7* (6), 2608–2618. https://doi.org/10.1039/c8ta09235d.

(35) Klimkowicz, A.; Świerczek, K.; Kobayashi, S.; Takasaki, A.; Allahyani, W.; Dabrowski, B. Improvement of Oxygen Storage Properties of Hexagonal $YMnO_{3+\delta}$ by Microstructural Modifications. *J. Solid State Chem.* **2018**, *258* (August 2017), 471–476. https://doi.org/10.1016/j.jssc.2017.10.037.

(36) Cichy, K.; Świerczek, K.; Jarosz, K.; Klimkowicz, A.; Marzec, M.; Gajewska, M.; Dabrowski, B. Towards Efficient Oxygen Separation from Air: Influence of the Mean Rare-Earth Radius on Thermodynamics and Kinetics of Reactivity with Oxygen in Hexagonal $Y_{1-x}R_xMnO_{3+\delta}$. *Acta Mater.* **2021**, *205*, 116544. https://doi.org/10.1016/j.actamat.2020.116544.

(37) Otomo, M.; Hasegawa, T.; Asakura, Y.; Yin, S. Remarkable Effects of Lanthanide Substitution for the Y-Site on the Oxygen Storage/Release Performance of $YMnO_{3+\delta}$. *ACS Appl. Mater. Interfaces* **2021**, *13* (27), 31691–31698. https://doi.org/10.1021/acsami.1c06880.

(38) Cichy, K.; Zając, M.; Świerczek, K. Evaluation of Applicability of Nd- and Sm-Substituted $Y_{1-x}R_xMnO_{3+\delta}$ in Temperature Swing Absorption for Energy-Related Technologies. *Energy* **2022**, *239*, 1–9. https://doi.org/10.1016/j.energy.2021.122429.

(39) Danmo, F. H.; Williamson, B. A. D.; Småbråten, D. R.; Gaukås, N. H.; Østli, E. R.; Grande, T.; Glaum, J.; Selbach, S. M. Oxygen Absorption in Nanocrystalline H-RMnO3 (R=Y, Ho, Dy) and the Effect of Ti Donor Doping. *Under review.*

(40) Klimkowicz, A.; Hashizume, T.; Cichy, K.; Tamura, S.; Świerczek, K.; Takasaki, A.; Motohashi, T.; Dabrowski, B. Oxygen Separation from Air by the Combined Temperature Swing and Pressure Swing Processes Using Oxygen Storage Materials $Y_{1-x}(Tb/Ce)_xMnO_{3+\delta}$. *J. Mater. Sci.* **2020**, *55* (33), 15653–15666. https://doi.org/10.1007/s10853-020-05158-5.

(41) Levin, I.; Krayzman, V.; Vanderah, T. A.; Tomczyk, M.; Wu, H.; Tucker, M. G.; Playford, H. Y.; Woicik, J. C.; Dennis, C. L.; Vilarinho, P. M. Oxygen-Storage Behavior and Local Structure in Ti-Substituted $YMnO_3$. *J. Solid State Chem.* **2017**, *246* (November 2016), 29–41. https://doi.org/10.1016/j.jssc.2016.10.029.

(42) Moreno Botello, Z. L.; Montenegro, A.; Grimaldos Osorio, N.; Huvé, M.; Pirovano, C.; Småbråten, D. R.; Selbach, S. M.; Caneiro, A.; Roussel, P.; Gauthier, G. H. Pure and Zr-Doped $YMnO_{3+\delta}$ as a YSZ-Compatible SOFC Cathode: A Combined Computational and Experimental Approach. *J. Mater. Chem. A* **2019**, *7* (31), 18589–18602. https://doi.org/10.1039/c9ta04912f.

(43) Holstad, T. S.; Evans, D. M.; Ruff, A.; Småbråten, D. R.; Schaab, J.; Tzschaschel, C.; Yan, Z.; Bourret, E.; Selbach, S. M.; Krohns, S.; Meier, D. Electronic Bulk and Domain Wall Properties in B -Site Doped Hexagonal $ErMnO_3$. *Phys. Rev. B* **2018**, *97* (8), 1–7. https://doi.org/10.1103/PhysRevB.97.085143.

(44) Momma, K.; Izumi, F. VESTA 3 for Three-Dimensional Visualization of Crystal, Volumetric and Morphology Data. *J. Appl. Crystallogr.* **2011**, *44* (6), 1272–1276. https://doi.org/10.1107/S0021889811038970.

(45) Bergum, K.; Okamoto, H.; Fjellvåg, H.; Grande, T.; Einarsrud, M. A.; Selbach, S. M. Synthesis, Structure and Magnetic Properties of Nanocrystalline $YMnO_3$. *Dalt. Trans.* **2011**, *40* (29), 7583–7589. https://doi.org/10.1039/c1dt10536a.

(46) Coelho, A. A. Topas Academic: General Profile and Structure Analysis Software for Powder Diffraction Data. *Bruker AXS, Karlsruhe, Ger.* **2007**.

(47) Newville, M. Larch: An Analysis Package for XAFS and Related Spectroscopies. *J. Phys. Conf. Ser.* **2013**, *430* (1). https://doi.org/10.1088/1742-6596/430/1/012007.

(48) Adler, S. B. Chemical Expansivity of Electrochemical Ceramics. *J. Am. Ceram. Soc.* **2001**, *84* (9), 2117–2119. https://doi.org/10.1111/j.1151-2916.2001.tb00968.x.

(49) Moreno, R.; García, P.; Zapata, J.; Roqueta, J.; Chaigneau, J.; Santiso, J. Chemical Strain Kinetics Induced by Oxygen Surface Exchange in Epitaxial Films Explored by Time-Resolved X-Ray Diffraction. *Chem. Mater.* **2013**, *25* (18), 3640–3647. https://doi.org/10.1021/cm401714d.

(50) Shannon, R. D. Revised Effective Ionic Radii and Systematic Studies of Interatomic Distances in Halides and Chalcogenides. *Acta Crystallogr. Sect. A* **1976**, *32* (5), 751–767. https://doi.org/10.1107/S0567739476001551.

(51) Gibbs, A. S.; Knight, K. S.; Lightfoot, P. High-Temperature Phase Transitions of Hexagonal $YMnO_3$. *Phys. Rev. B* **2011**, *83* (9), 1958. https://doi.org/10.1103/PhysRevB.83.094111.

(52) Tomczyk, M.; Senos, A. M. O. R.; Reaney, I. M.; Vilarinho, P. M. Reduction of Microcracking in $YMnO_3$ Ceramics by Ti Substitution. *Scr. Mater.* **2012**, *67* (5), 427–430. https://doi.org/10.1016/j.scriptamat.2012.04.042.

(53) Skjærvø, S. H.; Meier, Q. N.; Feygenson, M.; Spaldin, N. A.; Billinge, S. J. L.; Bozin, E. S.; Selbach, S. M. Unconventional Continuous Structural Disorder at the Order-Disorder Phase Transition in the Hexagonal Manganites. *Phys. Rev. X* **2019**, *9* (3), 31001. https://doi.org/10.1103/PhysRevX.9.031001.

(54) Fennie, C. J.; Rabe, K. M. Ferroelectric Transition in $YMnO_3$ from First Principles. *Phys. Rev. B - Condens. Matter Mater. Phys.* **2005**, *72* (10), 1–4. https://doi.org/10.1103/PhysRevB.72.100103.

(55) Lilienblum, M.; Lottermoser, T.; Manz, S.; Selbach, S. M.; Cano, A.; Fiebig, M. Ferroelectricity in the Multiferroic Hexagonal Manganites. *Nat. Phys.* **2015**, *11* (12), 1070–1073. https://doi.org/10.1038/nphys3468.

(56) Koettgen, J.; Zacherle, T.; Grieshammer, S.; Martin, M. Ab Initio Calculation of the Attempt Frequency of Oxygen Diffusion in Pure and Samarium Doped Ceria. *Phys. Chem. Chem. Phys.* **2017**, *19* (15), 9957–9973. https://doi.org/10.1039/c6cp04802a.

(57) Krauskopf, T.; Muy, S.; Culver, S. P.; Ohno, S.; Delaire, O.; Shao-Horn, Y.; Zeier, W. G. Comparing the Descriptors for Investigating the Influence of Lattice Dynamics on Ionic Transport Using the Superionic Conductor Na3PS4-XSex. *J. Am. Chem. Soc.* **2018**, *140* (43), 14464–14473. https://doi.org/10.1021/jacs.8b09340.

(58) Bouwmeester, H. J. M.; Kruidhof, H.; Burggraaf, A. Importance of the Surface Exchange Kinetics as Rate Limiting Step in Oxygen Permeation through Mixed-Conducting Oxides. *Solid State Ionics* **1994**, *72*, 185–194. https://doi.org/10.1016/0167-2738(94)90145-7.

(59) Fischer, E.; Hertz, J. L. Measurability of the Diffusion and Surface Exchange Coefficients Using Isotope Exchange with Thin Film and Traditional Samples. *Solid State Ionics* **2012**, *218*, 18–24. https://doi.org/10.1016/j.ssi.2012.05.003.

(60) Yang, Q.; Burye, T. E.; Lunt, R. R.; Nicholas, J. D. In Situ Oxygen Surface Exchange Coefficient Measurements on Lanthanum Strontium Ferrite Thin Films via the Curvature Relaxation Method. *Solid State Ionics* **2013**, *249–250*, 123–128. https://doi.org/10.1016/j.ssi.2013.07.025.

(61) Chen, T.; Harrington, G. F.; Masood, J.; Sasaki, K.; Perry, N. H. Emergence of Rapid Oxygen Surface Exchange Kinetics during in Situ Crystallization of Mixed Conducting Thin Film Oxides. *ACS Appl. Mater. Interfaces* **2019**, *11* (9), 9102–9116. https://doi.org/10.1021/acsami.8b21285.

(62) Skiba, E. J.; Chen, T.; Perry, N. H. Simultaneous Electrical, Electrochemical, and Optical Relaxation Measurements of Oxygen Surface Exchange Coefficients: Sr(Ti,Fe)O 3−d Film Crystallization Case Study. *ACS Appl. Mater. Interfaces* **2020**, *12* (43), 48614–48630. https://doi.org/10.1021/acsami.0c14265.

(63) Stangl, A.; Riaz, A.; Rapenne, L.; Caicedo, J. M.; De Dios Sirvent, J.; Baiutti, F.; Jiménez, C.; Tarancón, A.; Mermoux, M.; Burriel, M. Tailored Nano-Columnar La2NiO4cathodes for Improved Electrode Performance. *J. Mater. Chem. A* **2022**, *10* (5), 2528–2540. https://doi.org/10.1039/d1ta09110g.

(64) Yang, G.; Kim, S. Y.; Sohn, C.; Keum, J. K.; Lee, D. Influence of Heterointerfaces on the Kinetics of Oxygen Surface Exchange on Epitaxial La1.85Sr0.15CuO4 Thin Films. *Appl. Sci.* **2021**, *11* (9), 1–9. https://doi.org/10.3390/app11093778.

(65) Acosta, M.; Baiutti, F.; Wang, X.; Cavallaro, A.; Wu, J.; Li, W.; Parker, S. C.; Aguadero, A.; Wang, H.; Tarancón, A.; MacManus-Driscoll, J. L. Surface Chemistry and Porosity Engineering through Etching Reveal Ultrafast Oxygen Reduction Kinetics below 400 °C in B-Site Exposed (La,Sr)(Co,Fe)O3 Thin-Films. *J. Power Sources* **2022**, *523* (December 2021), 230983. https://doi.org/10.1016/j.jpowsour.2022.230983.

(66) Cichy, K.; Świerczek, K. Influence of Doping on the Transport Properties of $Y_{1-x}Ln_xMnO_{3+\delta}$ (Ln: Pr, Nd). *Crystals* **2021**, *11* (5), 1–13. https://doi.org/10.3390/cryst11050510.

(67) Li, M.; Pietrowski, M. J.; De Souza, R. A.; Zhang, H.; Reaney, I. M.; Cook, S. N.; Kilner, J. A.; Sinclair, D. C. A Family of Oxide Ion Conductors Based on the Ferroelectric Perovskite $Na_{0.5}Bi_{0.5}TiO_3$. *Nat. Mater.* **2014**, *13* (1), 31–35. https://doi.org/10.1038/nmat3782.

(68) Kharton, V. V.; Marques, F. M. B.; Atkinson, A. Transport Properties of Solid Oxide Electrolyte Ceramics: A Brief Review. *Solid State Ionics* **2004**, *174* (1–4), 135–149. https://doi.org/10.1016/j.ssi.2004.06.015.

Supporting Information for:

Oxidation kinetics of nanocrystalline h-RMn$_{1-x}$Ti$_x$O$_3$ (R = Ho, Dy)

Frida Hemstad Danmo,[1] Inger-Emma Nylund,[1] Aamund Westermoen,[1] Kenneth P. Marshall,[2] Dragos Stoian,[2] Tor Grande,[1] Julia Glaum,[1] and Sverre M. Selbach[1,]*

[1]Department of Materials Science and Engineering, NTNU Norwegian University of Science and Technology, NO-7491 Trondheim, Norway.

[2]The Swiss-Norwegian Beamlines (SNBL), European Synchrotron Radiation Facility, Grenoble 38043, France

[*]E-mail: selbach@ntnu.no

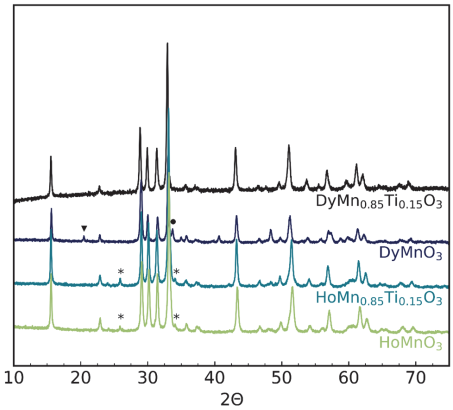

Figure S1: X-ray diffractograms of as-synthesized materials with compositions and labels explained in Table 1. The asterisks (*) indicate reflections originating from the orthorhombic perovskite *Pnma* phase, the triangle (▼) indicate reflections from an unidentified phase, and the circle (●) indicates the presence of Dy_2O_3.

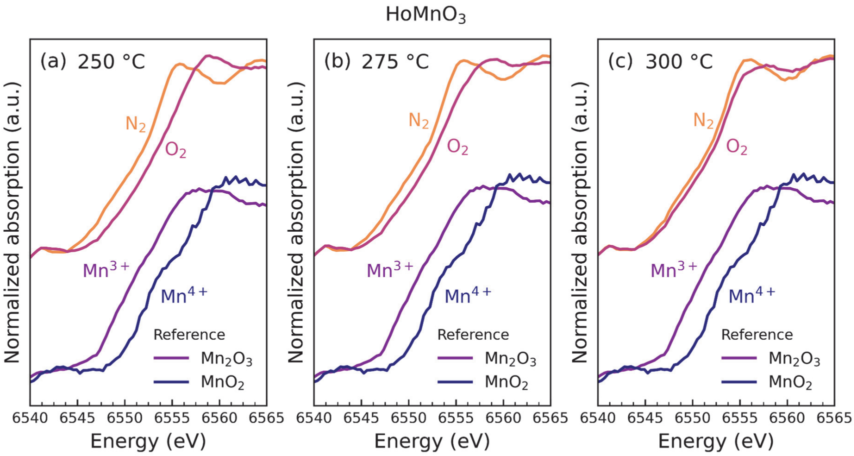

Figure S2: Normalized X-ray absorption near-edge structure (XANES) spectra at the Mn *K*-edge of $HoMnO_3$ before (N_2) and after oxidation (O_2). The spectra of Mn_2O_3 and MnO_2 are shown as references.

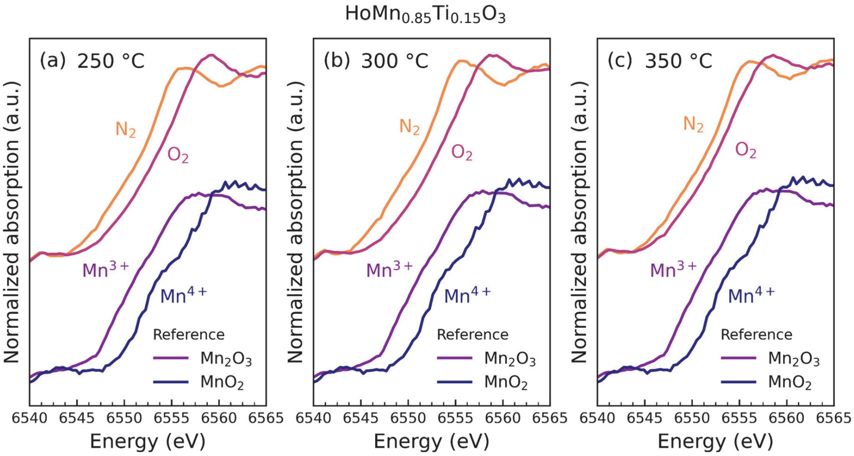

Figure S3: Normalized X-ray absorption near-edge structure (XANES) spectra at the Mn *K*-edge of $HoMn_{0.85}Ti_{0.15}O_3$ before (N_2) and after oxidation (O_2). The spectra of Mn_2O_3 and MnO_2 are shown as references.

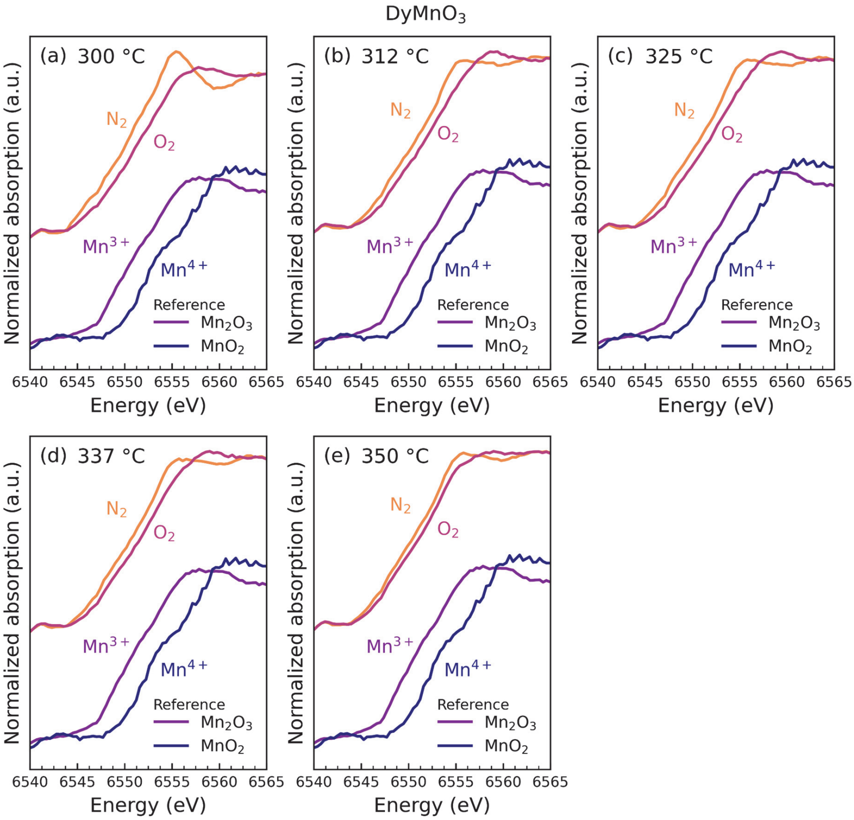

Figure S4: Normalized X-ray absorption near-edge structure (XANES) spectra at the Mn *K*-edge of DyMnO$_3$ before (N$_2$) and after oxidation (O$_2$). The spectra of Mn$_2$O$_3$ and MnO$_2$ are shown as references.

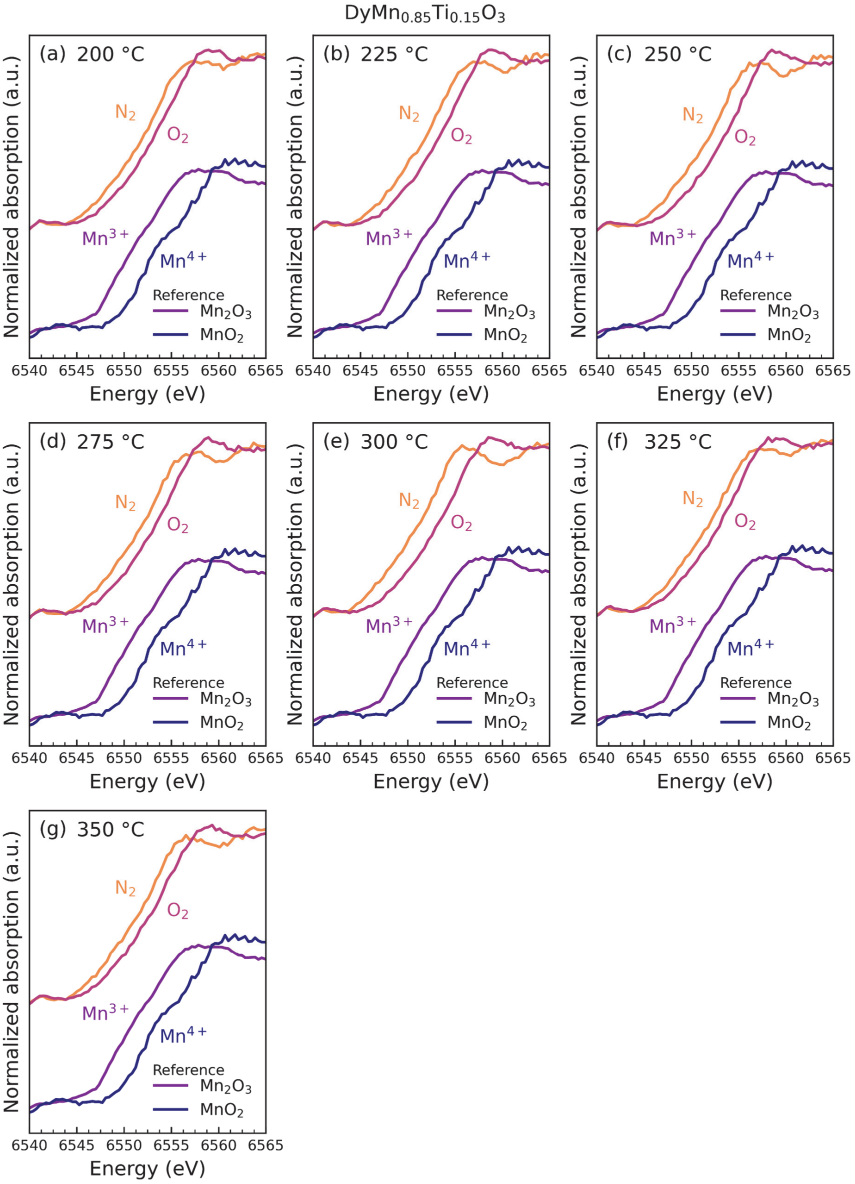

Figure S5: Normalized X-ray absorption near-edge structure (XANES) spectra at the Mn *K*-edge of DyMn$_{0.85}$Ti$_{0.15}$O$_3$ before (N$_2$) and after oxidation (O$_2$). The spectra of Mn$_2$O$_3$ and MnO$_2$ are shown as references.

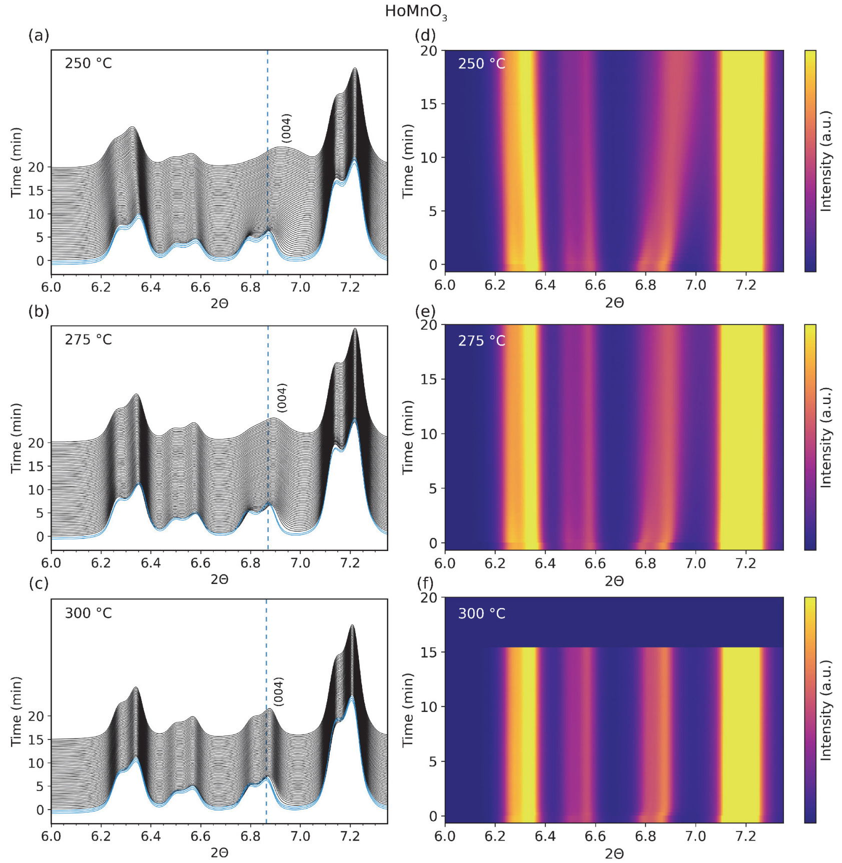

Figure S6: X-ray diffractograms and 2D contour plots of HoMnO$_3$ as a function of time after *in situ* switching of atmosphere from N$_2$ (blue) to O$_2$ (black) at different temperatures. The baseline intensity at 6.0° 2θ in (a)-(c) indicate the time in min. after switching from N$_2$ to O$_2$ purge gas. Vertical dashed lines (blue) indicate the initial position of the (0 0 4) reflection measured in N$_2$.

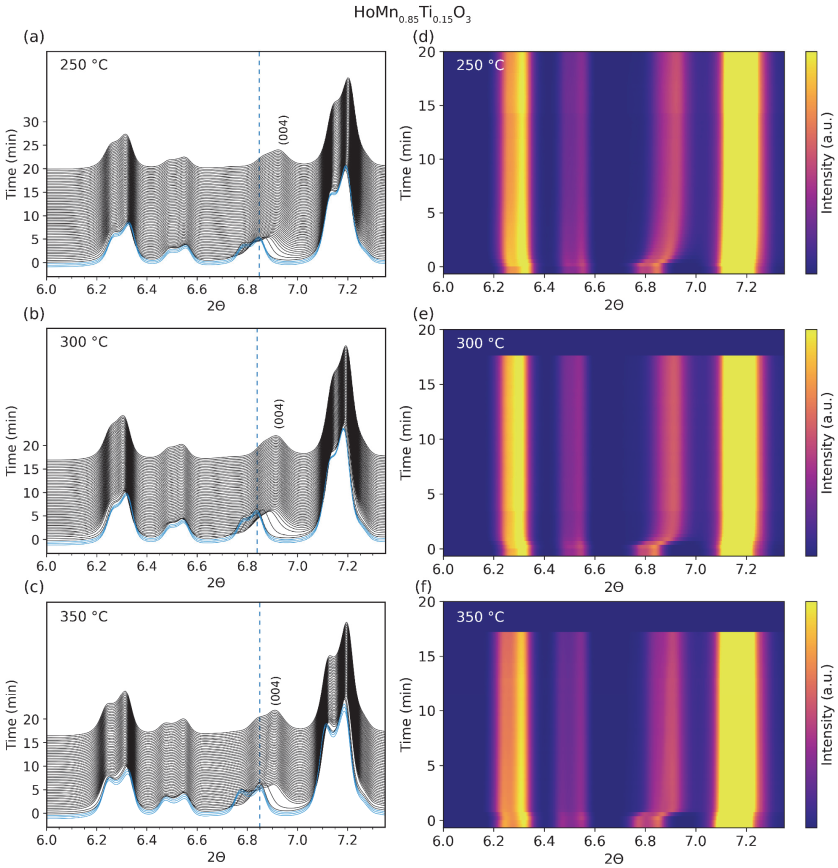

Figure S7: X-ray diffractograms and 2D contour plots of HoMn$_{0.85}$Ti$_{0.15}$O$_3$ as a function of time after *in situ* switching of atmosphere from N_2 (blue) to O_2 (black) at different temperatures. The baseline intensity at 6.0° 2θ in (a)-(c) indicate the time in min. after switching from N_2 to O_2 purge gas. Vertical dashed lines (blue) indicate the initial position of the (0 0 4) reflection measured in N_2.

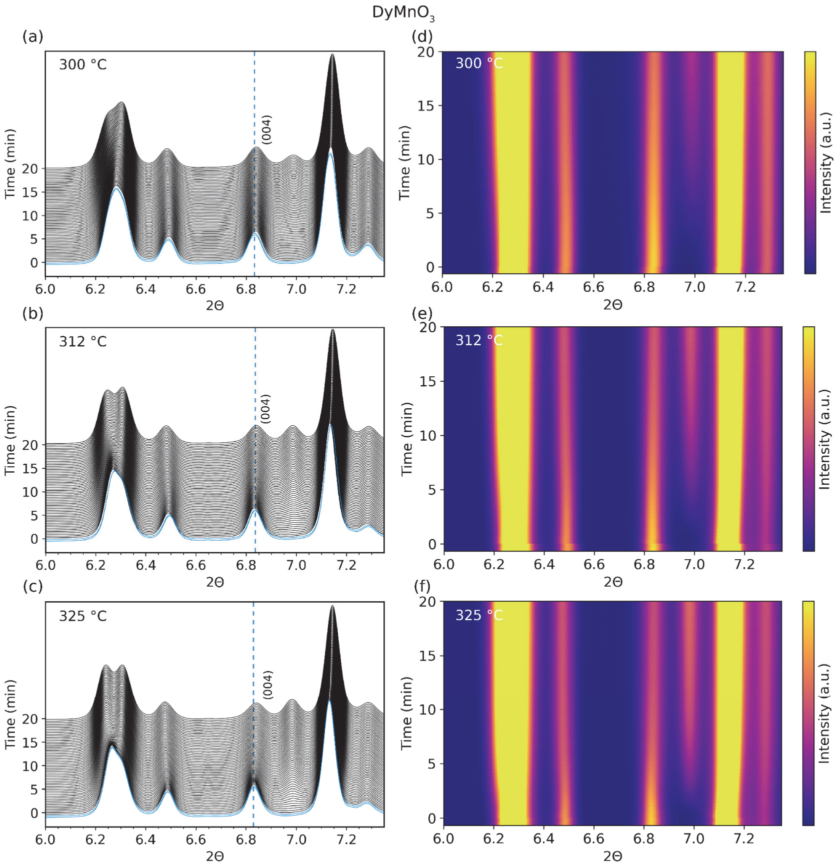

Figure S8: X-ray diffractograms and 2D contour plots of DyMnO$_3$ as a function of time after *in situ* switching of atmosphere from N$_2$ (blue) to O$_2$ (black) at different temperatures. The baseline intensity at 6.0° 2θ in (a)-(c) indicate the time in min. after switching from N$_2$ to O$_2$ purge gas. Vertical dashed lines (blue) indicate the initial position of the (0 0 4) reflection measured in N$_2$.

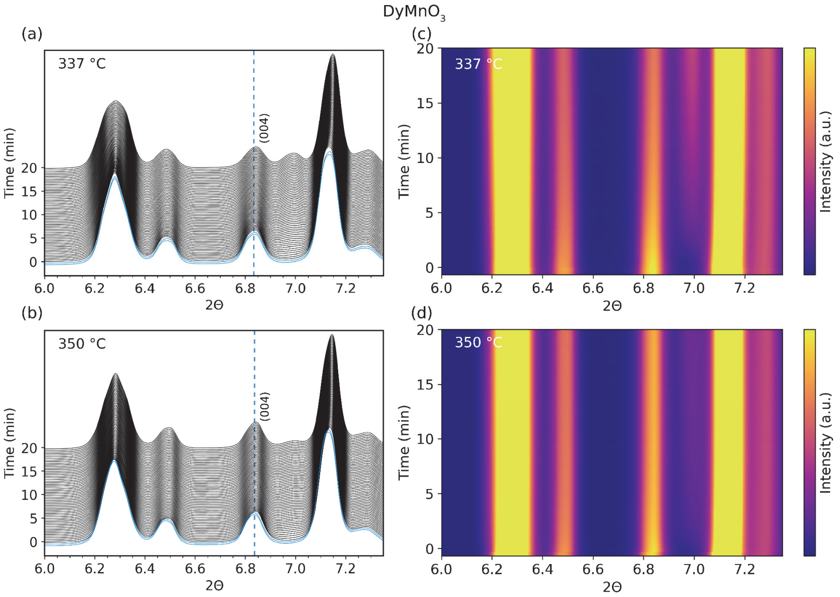

Figure S9: X-ray diffractograms and 2D contour plots of $DyMnO_3$ as a function of time after *in situ* switching of atmosphere from N_2 (blue) to O_2 (black) at different temperatures. The baseline intensity at 6.0° 2θ in (a)-(b) indicate the time in min. after switching from N_2 to O_2 purge gas. Vertical dashed lines (blue) indicate the initial position of the (0 0 4) reflection measured in N_2.

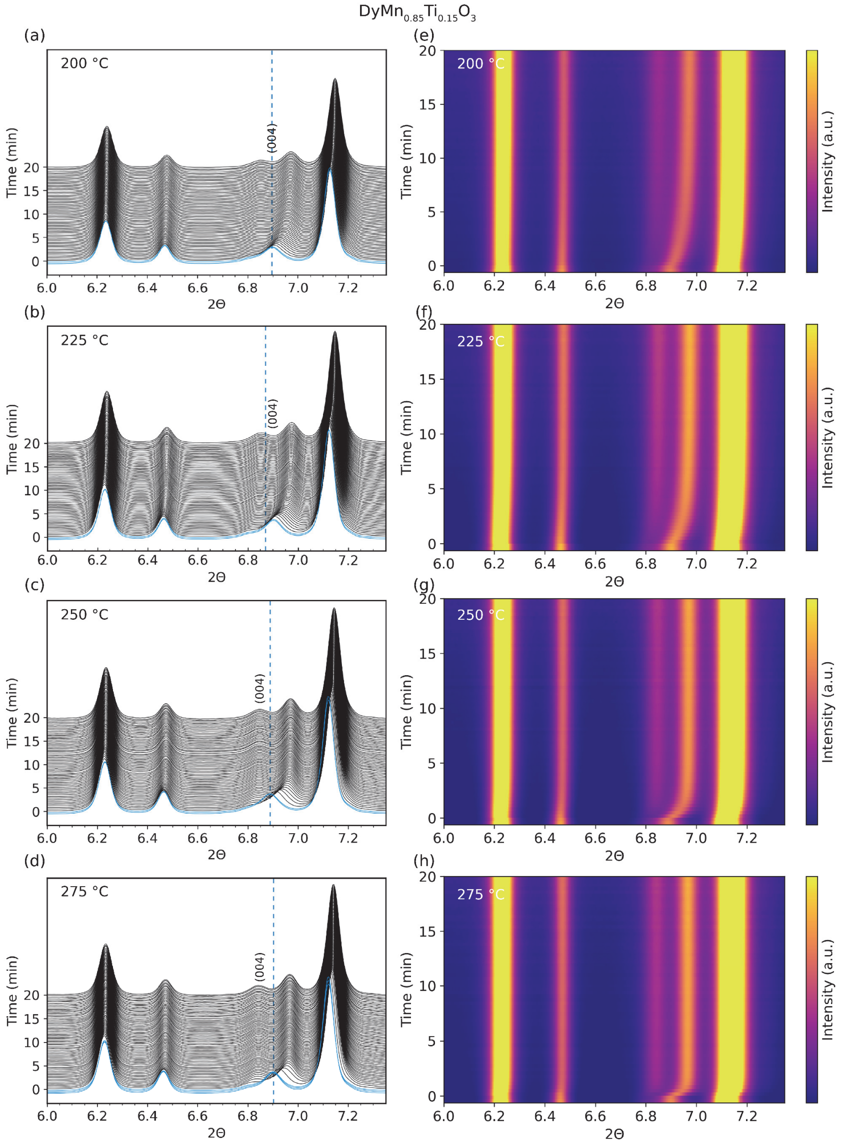

Figure S10: X-ray diffractograms and 2D contour plots of DyMn$_{0.85}$Ti$_{0.15}$O$_3$ as a function of time after *in situ* switching of atmosphere from N$_2$ (blue) to O$_2$ (black) at different temperatures. The baseline intensity at 6.0° 2θ in (a)-(d) indicate the time in min. after switching from N$_2$ to O$_2$ purge gas. Vertical dashed lines (blue) indicate the initial position of the (0 0 4) reflection measured in N$_2$.

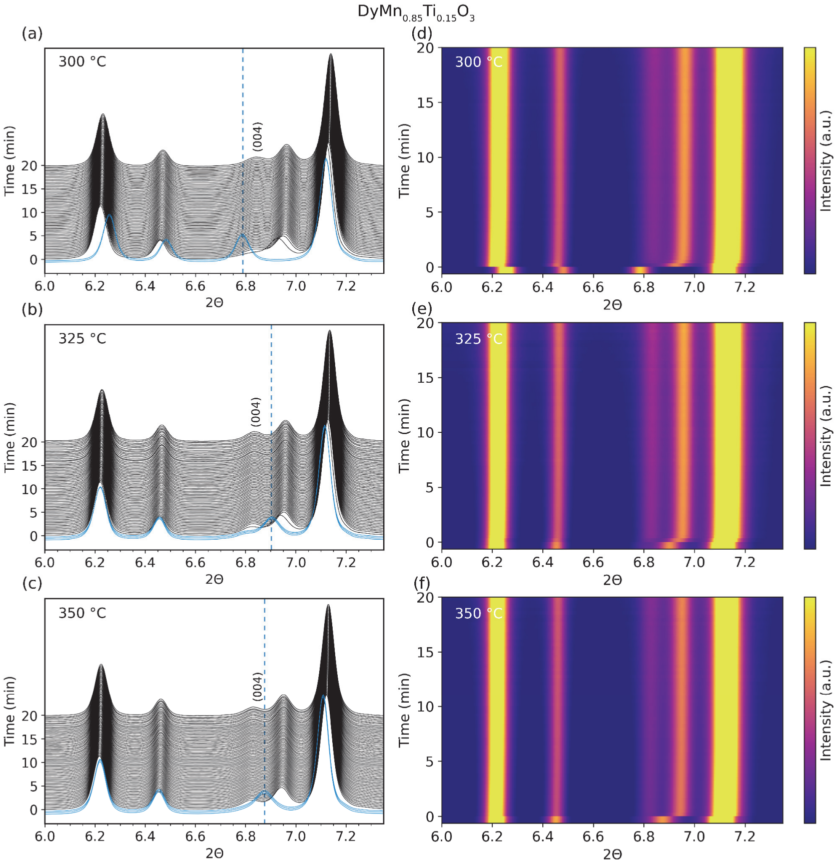

Figure S11: X-ray diffractograms and 2D contour plots of DyMn$_{0.85}$Ti$_{0.15}$O$_3$ as a function of time after *in situ* switching of atmosphere from N$_2$ (blue) to O$_2$ (black) at different temperatures. The baseline intensity at 6.0° 2*θ* in (a)-(d) indicate the time in min. after switching from N$_2$ to O$_2$ purge gas. Vertical dashed lines (blue) indicate the initial position of the (0 0 4) reflection measured in N$_2$.

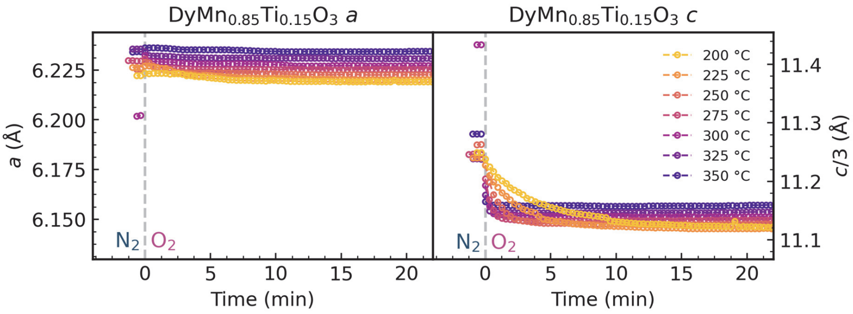

Figure S12: Refined lattice parameters *a* and *c* as a function of time after switching from N_2 to O_2 atmosphere for $DyMn_{0.85}Ti_{0.15}O_3$.

Manuscript III

High entropy hexagonal manganites for fast oxygen absorption and release

F. H. Danmo, A. Westermoen, K. P. Marshall, D. Stoian, T. Grande, J. Glaum, and S. M. Selbach, *Paper manuscript, to be submitted*

High entropy hexagonal manganites for fast oxygen absorption and release

Frida Hemstad Danmo,[1] Aamund Westermoen, [1] Kenneth Marshall,[2] Dragos Stoian,[2] Tor Grande,[1] Julia Glaum,[1] and Sverre M. Selbach[1,]*

[1]Department of Materials Science and Engineering, NTNU Norwegian University of Science and Technology, NO-7491 Trondheim, Norway.

[2]The Swiss-Norwegian Beamlines (SNBL), European Synchrotron Radiation Facility, Grenoble 38043, France

[*]E-mail: selbach@ntnu.no

ABSTRACT

Hexagonal manganites ($R\mathrm{MnO_3}$) display large capacity for oxygen storage and release at temperatures below 400 °C. A challenging trade-off is that larger R^{3+} cations improve both the absorption capacity and kinetics, but also destabilize the layered hexagonal structure with respect to orthorhombic perovskite. Here we combine 5 or 6 rare earth elements to stabilize the hexagonal phase through configurational entropy and report the resulting oxygen absorption capacity and kinetics of both bulk and nanocrystalline samples with composition $R\mathrm{Mn_{1-x}Ti_xO_3}$ where R = Y, Gd-Er and x = 0, 0.15. The oxygen absorption capacity is measured by thermogravimetric analysis (TGA), and the absorption kinetics was studied by high temperature X-ray diffraction (HT-XRD) and X-ray absorption near edge structure (XANES) upon *in situ* switching of atmosphere from N_2 to O_2. High-entropy compositions show similar oxygen storage capacity as the best known single or double R^{3+} compositions, and particularly Tb^{3+} and Ti^{4+} are found to improve the capacity. Importantly, the kinetics of oxidation is both strongly improved in high-entropy compositions and highly insensitive to the exact composition of the R^{3+} cations, profoundly enhancing the industrial potential of hexagonal manganites for oxygen storage and separation from air.

INTRODUCTION

Hexagonal manganites, $R\text{MnO}_{3+\delta}$ (R = Sc, Y, Ho-Lu), have been shown to incorporate large amounts of oxygen as interstitials at $T > 400$ °C,[1–5] and are therefore promising oxygen storage materials (OSMs) for oxygen separation applications such as chemical looping air separation (CLAS). These applications require materials with reversible oxygen incorporation and release, a high oxygen storage capacity (OSC), and fast ionic transport and surface exchange rates.[6–8] The OSC of hexagonal manganites have been shown to increase when using larger R^{3+} cations, either as the sole cation on the R site or as a substituted element in YMnO_3,[3,9–16] or by the addition of aliovalent dopants.[15–18]

The oxidation kinetics of these materials, however, are generally slow, with time to full oxidation being on the scale of several hours for some compositions.[11] This causes large drops in the available OSC when using short dwell times or quick heating and cooling rates,[4,9,11,12,14,15,19] which are necessary operation conditions for cyclic processes such as CLAS to produce O_2 gas efficiently.[7] The kinetics of oxidation has been shown to increase with the use of larger R^{3+} cations[12] and Ti^{4+} as a donor dopant on the Mn site,[16] indicating that further compositional tuning can make hexagonal manganites viable for oxygen separation processes. Unfortunately, the use of the larger rare earth cations is limited by the stability of the crystal structure of $R\text{MnO}_3$ compounds. Generally, the forming phase can be determined through the Goldschmidt tolerance factor $t = \frac{(r_R + r_O)}{\sqrt{2}(r_{Mn} + r_O)}$. For small rare earths ($r_R^{3+} \leq r_{\text{Ho}}^{3+}$) and tolerance factors $t \leq 0.855$, the hexagonal $P6_3cm$ structure is favored, while large rare earths ($r_R^{3+} \geq r_{\text{Dy}}^{3+}$, $t > 0.855$) are not stable within the hexagonal structure, and instead crystallize as the orthorhombic perovskite *Pnma*.

Many of the rare earth elements are also scarce, or expensive, and should be used in moderation. Rare earth elements have been categorized as critical raw materials by the EU, with large rare earths such as Nd, Pr, and Dy listed as having especially high economic importance as they are vital for magnets in wind turbine generators and electric vehicles.[20–23] Furthermore, the chemical similarity between the different rare earths also makes their isolation and purification expensive as they are generally mixed together in ore.

High entropy ceramics have emerged as a new and interesting direction of material design, due to high entropy materials displaying new or improved properties compared to their simpler, low entropy counterparts. This concept was first discovered for metal alloys, where the combination of 5 or more metals in equimolar amounts formed a single phase solid solution, with increased mechanical properties.[24,25] This has later been adapted to oxides and ceramics,[26–32] such as rock salt (Mg,Ni,Co,Cu,Zn)O,[33] perovskites,[34,35] oxyfluorides,[36] and carbides.[37] High entropy compounds are usually defined by having a configurational entropy, S_{config}, larger than 1.5R, where R is the universal gas constant.[38] As the high configurational entropy has been proven to stabilize multiple compounds within a single phase, even when some of the contributing compounds are not stable in this phase on their own,[25,33] this enables the use of elements that can contribute to interesting properties. High entropy ceramics have shown colossal dielectric constants,[29] proton conductivity,[39] and high ionic conductivity[28], demonstrating that this compositional design method shows potential for enhancing the properties of several material systems. Li-substituted high entropy oxides are promising for reversible energy storage as they display unusually high Li^+ conductivity.[27,28] The site disorder has been shown to increase Li-ion conductivity in solid electrolytes which can enhance ion diffusion,[40,41] and this could also be the case for other 2D and 3D ionic conductors with high configurational entropy as well.

Here we introduce high entropy compositions of hexagonal manganites as a new class of materials for fast oxygen absorption and release at low temperatures. High configurational entropy promotes formation of single-phase hexagonal materials and the oxygen storage capacity is high for all studied samples compared to reported data for single *R* compounds. Importantly, the oxidation kinetics is significantly improved in high-entropy samples compared to previous reports, and both the capacity and kinetics are insensitive to the exact rare earth cation composition. The improved properties are discussed in relation to structural disorder resulting from high configurational entropy, and the size of the R^{3+} cations causing an expansion of the *ab*-plane.

METHODS

Synthesis

Bulk samples of high entropy hexagonal manganites were prepared through solid state synthesis. Binary oxides Y_2O_3 (Aldrich), Gd_2O_3 (Aldrich), Tb_4O_7 (Alfa Aesar), Dy_2O_3 (Aldrich), Ho_2O_3 (TermoFisher), Er_2O_3 (Aldrich), Mn_2O_3 (Aldrich) and TiO_2 (Alrich) were stoichiometrically mixed and pressed into pellets. These were then fired at 1450 °C for 1 h in air, and subsequently crushed into powders. Nanocrystalline samples were prepared using a modified citric acid synthesis method previously reported by Bergum *et al.*[42] and Danmo *et al.,*[15,16] with composition and naming of all samples shown in Table 1. For the precursor solutions, metal acetates $Er(CH_3CO_2)_3 \cdot xH_2O$ (Aldrich), $Y(CH_3CO_2)_3 \cdot xH_2O$ (Aldrich), $Ho(CH_3CO_2)_3 \cdot xH_2O$ (AlfaAesar), $Dy(CH_3CO_2)_3 \cdot xH_2O$ (AlfaAesar), $Gd(CH_3CO_2)_3 \cdot xH_2O$ (Aldrich), $Tb(CH_3CO_2)_3 \cdot xH_2O$ (Aldrich), and $Mn(CH_3CO_2)_3 \cdot xH_2O$ (Riedel-de-Haën) were each dissolved in a mixture of citric acid and deionized water, and stirred on a hot plate set to 150 °C for 3 hours. The molar ratio between cation to citric acid was 1:20 for Er^{3+}, Y^{3+} and Ho^{3+}; 1:35 for Dy^{3+}, Tb^{3+} and Gd^{3+}; and 1:5 for Mn^{3+}. For the Ti^{4+} solution, titanium (IV) isopropoxide (TTIP) (Sigma-Aldrich) was added to a mixture of deionized water and citric acid in a ratio of 1:6.3 between Ti^{4+} and citric acid. The solution was stirred at 60 °C until clear. The precursor solutions were added in stoichiometric amounts, and ethylene glycol (EG) (Merck) was added with a 1:1 molar ratio with the citric acid in the solutions. This was kept on a hot plate at 150 °C for 24-48 hours until a viscous gel was formed. The gel was then dried at 120 °C for 3 days. This dried gel was calcined at 400 °C for 3 hours, and subsequently calcined at 600 °C for 6 hours, resulting in an amorphous powder. The powders were pre-reduced in 5 % H_2 in N_2 at 250 °C for 10 hours to promote formation of the desired hexagonal structure, and then crystallized at 900 °C in N_2 atmosphere for 1 hour.

Table 1: Composition, naming and tolerance factor of samples used in this study.

Composition	Nano-crystalline	Bulk	Goldschmidt tolerance factor
$Y_{0.167}Gd_{0.167}Tb_{0.167}Dy_{0.167}Ho_{0.167}Er_{0.167}MnO_3$	HEO1-n	HEO1-b	0.859
$Y_{0.167}Gd_{0.167}Tb_{0.167}Dy_{0.167}Ho_{0.167}Er_{0.167}Mn_{0.85}Ti_{0.15}O_3$	HEO2-n	HEO2-b	0.863
$Y_{0.167}Gd_{0.233}Tb_{0.167}Dy_{0.167}Ho_{0.167}Er_{0.1}Mn_{0.85}Ti_{0.15}O_3$	HEO3-n	-	0.865
$Y_{0.145}Gd_{0.210}Tb_{0.190}Dy_{0.165}Ho_{0.155}Er_{0.135}Mn_{0.85}Ti_{0.15}O_3$	HEO4-n	-	0.864
$Y_{0.2}Gd_{0.2}Dy_{0.2}Ho_{0.2}Er_{0.2}Mn_{0.85}Ti_{0.15}O_3$	HEO5-n	HEO5-b	0.860

Characterization

Phase purity of all samples, and lattice parameters of as prepared and oxidized nanocrystalline samples, were investigated using X-ray Diffraction (XRD) performed with a Bruker D8 Focus with Cu Kα radiation. The nanocrystalline samples were protected by a Kapton polyimide film, resulting in an increased background at lower angles. The Bruker AXS TOPAS 5 software[43] was used for Pawley refinement of lattice parameters and crystallite sizes (Table 2). Oxygen stoichiometry as a function of temperature when heating and cooling in O_2 atmosphere was studied by thermogravimetric analysis (TGA) with a Netzsch STA 449C Jupiter with 30 mL min^{-1} O_2 gas flow. The changes in weight were measured during heating to 800 °C and subsequent cooling to room temperature, using heating and cooling rates of 5, 10 or 20 °C min^{-1}. Calculations of δ were based on a reference point where all Mn is assumed to be found as Mn^{3+}, chosen as the point of lowest mass at

T > 700 °C. This corresponds to δ = 0 for undoped and δ = 0.075 for Ti-doped samples. The HEO1-n and HEO2-n samples were heated to 600 °C in N_2 atmosphere for 10 h prior to each measurement to remove excess oxygen. The other samples were heated to, and subsequently cooled down from, 800 °C using heating and cooling rates of 20 °C in O_2 within the TG instrument prior to the measurements, resulting in slightly oxidized states at the start of the measurements.

The particle size of the bulk powders was investigated using scanning electron microscopy (SEM), using a Hitachi S-3400 N scanning electron microscope with a secondary electron detector, and 5k voltage.

The effect of Ti-doping was addressed by studying the two nanocrystalline samples with equimolar amounts of all 6 *R* cations, HEO1-n and HEO2-n, without and with Ti-doping, respectively. Changes in lattice parameters with temperature and atmosphere were investigated using high-temperature X-ray diffraction (HT-XRD) with a Bruker D8 Advance with Cu Kα radiation. The samples were first measured in O_2 at 25 °C intervals during heating to 725 °C, subsequent cooling to 50 °C, and then during re-heating to 725 °C. This was then repeated in N_2 atmosphere. Samples were heated to 600 °C in N_2 atmosphere for 10 h prior to the first HT-XRD measurement in O_2. The lattice parameters were determined by Pawley refinement with TOPAS 5 in launch mode using Python with Jupyter Notebook.

HT-XRD and X-ray absorption near edge structure (XANES) measurements with *in situ* switching of atmosphere from O_2 to N_2 was performed at the Swiss-Norwegian Beamlines (SNBL) at the European Synchrotron Radiation Facility (ESRF) in Grenoble, France, using the BM31 beamline. Each sample was prepared in capillaries using quartz wool to secure the sample. A 10 mL min^{-1} gas flow was used for all experiments, and this was confirmed using a Pfeiffer Vacuum Omnistar spectrometer. A wavelength of 0.38591 Å and a Dexela 2923 area detector was used for diffraction measurements, while a Hitaxi Vortex single-element silicon drift detector was used to measure the XANES fluorescence signal of the Mn *K*-edge and the Tb L_3-edge. Due to transmission of Mn being weak because of heavy rare earth elements attenuating the signal, absorption measurements were performed in fluorescence mode. Diffraction measurements were performed with *in situ* switching of atmosphere at a chosen temperature, with XANES measurements performed prior to, and after, each set of diffraction measurements. XANES measurements were also carried out during oxidation as 200 °C with *in situ* switching of atmosphere. In between each set of measurements at a given temperature, the samples were heated to 500 °C in N_2 atmosphere to remove excess oxygen. Lattice parameters were refined with Pawley refinement using TOPAS 5 operating in launch mode with Jupyter Notebook. Larch[44] was used for normalization of XANES measurements.

RESULTS

All nanocrystalline samples were phase pure after synthesis and their diffractograms can be indexed with the hexagonal $P6_3cm$ space group, as illustrated in Figure 1. Trace amounts of the orthorhombic perovskite phase are found in some of the samples, as indicated by asterisks (*). The bulk HEO2-b and HEO5-b samples are also phase pure, while the HEO1-b sample was found to contain both the hexagonal $P6_3cm$ and the orthorhombic *Pnma* structure phases.

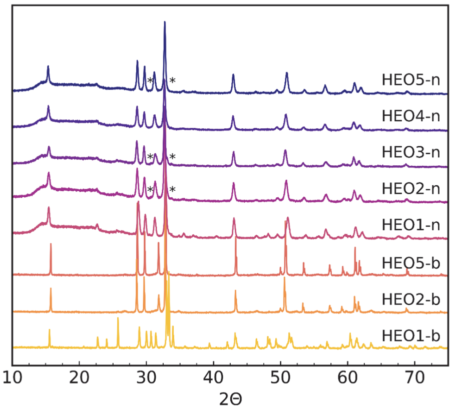

Figure 1: X-ray diffractograms for the as-prepared high entropy samples, with b denoting bulk samples and n denoting nanocrystalline samples, and asterisks (*) indicating reflections from trace amounts of the orthorhombic perovskite phase in the nanocrystalline samples. The HEO1-b sample contains approximately equal amounts of hexagonal and orthorhombic phase.

Lattice parameters (Table 1) for all the nanocrystalline materials show expansion of the unit cell compared to lattice parameters reported for undoped and single R^{3+} cation RMnO$_3$,[15,16,45] as expected from the larger average ionic radii of the cations incorporated in these compositions.[46] The increasing size of the *ab*-plane also corresponds well with increasing tolerance factors (Table 1). The nanocrystalline samples have crystallite sizes ranging from 23 to 31 nm, as expected from the citric acid synthesis method,[15,42] while SEM images of the bulk powders (Figure S1 and S2 in Supporting

Information) demonstrated that these samples had particles ranging from tens to hundreds of micrometers in size.

Table 2: Composition, sample name, and refined lattice parameters and crystallite sizes for as-prepared nanocrystalline materials. X-ray diffraction data were refined within the $P6_3cm$ space group in all cases.

Composition	Sample name	*a* (Å)	*c* (Å)	Crystallite size (nm)
$Y_{0.167}Gd_{0.167}Tb_{0.167}Dy_{0.167}Ho_{0.167}Er_{0.167}MnO_3$	HEO1-n	6.181(8)	11.412(0)	28 ± 1
$Y_{0.167}Gd_{0.167}Tb_{0.167}Dy_{0.167}Ho_{0.167}Er_{0.167}Mn_{0.85}Ti_{0.15}O_3$	HEO2-n	6.207(7)	11.382(2)	23 ± 1
$Y_{0.167}Gd_{0.233}Tb_{0.167}Dy_{0.167}Ho_{0.167}Er_{0.1}Mn_{0.85}Ti_{0.15}O_3$	HEO3-n	6.225(8)	11.374(0)	31 ± 1
$Y_{0.145}Gd_{0.210}Tb_{0.190}Dy_{0.165}Ho_{0.155}Er_{0.135}Mn_{0.85}Ti_{0.15}O_3$	HEO4-n	6.213(2)	11.411(6)	23 ± 1
$Y_{0.2}Gd_{0.2}Dy_{0.2}Ho_{0.2}Er_{0.2}Mn_{0.85}Ti_{0.15}O_3$	HEO5-n	6.189(9)	11.406(5)	30 ± 1

Oxidized HEO1-n and HEO2-n, measured after cooling the sample in O_2, both show a shift in the position of the (0 0 4) reflection from ~31.3 2θ to ~32.4 2θ (Figure 2), and the appearance of a second reflection at ~31.5 2θ. These two reflections, labeled as (1 0 10) and (0 0 12) in Figure 2, are characteristic for the *R3c* space group, which has a tripled *c* axis compared to the original $P6_3cm$ structure. The (1 0 10) reflection is less pronounced for the oxidized HEO2-n sample, as Ti-doping disrupts the *R*3*c* structure.[15,16]

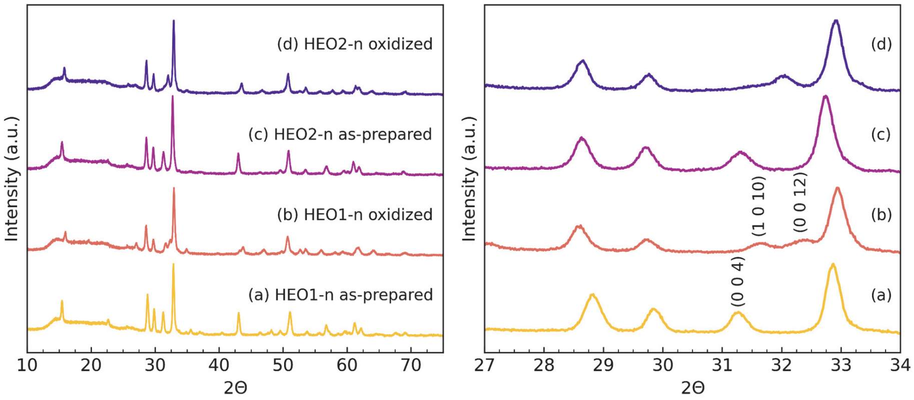

Figure 2: X-ray diffractograms for as-prepared and oxidized HEO1-n and HEO2-n.

Pawley refined lattice parameters for the as-prepared and oxidized nanocrystalline HEO1-n and HEO2-n samples are found in Table 2. The oxidized samples show an expansion of the *ab*-plane and a contraction along the *c* axis compared to the as-prepared samples, in agreement with previous work,[15] caused by interstitial oxygen entering the Mn-O layers. As the length of the *c* axis in the *R*3*c* space group is tripled compared to the original unit cell, values for the *c* lattice parameters for the oxidized samples refined within the *R*3*c* space group are divided by three for easier comparison between the two structures.

Table 3: Refined lattice parameters for as-prepared and oxidized $Y_xGd_xTb_xDy_xHo_xEr_xMnO_3$ (x=0.167) (HEO1-n) and $Y_xGd_xTb_xDy_xHo_xEr_xMn_{0.85}Ti_{0.15}O_3$ (x=0.167) (HEO2-n). The as-prepared samples were refined within the $P6_3cm$ space group, while the oxidized samples were refined within the $R3c$ space group. The *c* parameters marked with an asterisk (*) are divided by three for easier comparison between the $P6_3cm$ and the $R3c$ space groups.

Sample	Condition	*a* (Å)	*c* (Å)	Space group
HEO1-n	As-prepared	6.181(8)	11.412(0)	$P6_3cm$
HEO1-n	Oxidized	6.220(2)	11.035(6)*	$R3c$
HEO2-n	As-prepared	6.207(7)	11.382(2)	$P6_3cm$
HEO2-n	Oxidized	6.219(2)	11.152(9)*	$R3c$

All samples absorb large amounts of oxygen at temperatures below 400 °C in O_2 atmosphere, with $\delta \approx 0.30$ for HEO1-n, $\delta \approx 0.35$ for HEO2-n and HEO3-n, $\delta \approx 0.37$ for HEO4-n, and $\delta \approx 0.32$ for HEO5-n. Oxygen stoichiometry of nanocrystalline samples as a function of temperature measured during cooling using different cooling rates is shown in Figure 3. None of the samples show any significant decrease in OSC with increasing cooling rates, demonstrating that the oxidation kinetics are fast for all samples. The samples containing both Ti and Tb (Figure 3 (b)-(d)) show the highest oxygen storage capacities, as both elements are known to increase the oxygen storage capacity of hexagonal manganites.[12,15–17] The oxygen content for these samples is also above the $\delta = 0.33$ limit for oxidation of 2/3 of Mn only, giving 2 oxygen interstitials per 30-atom unit cell.[47] Oxidation of Tb^{3+} to Tb^{4+} can charge compensate incorporation of more oxygen interstitials than in samples without *R* cations which can be oxidized. In addition, the Ti-doped samples (Figure 3 (b)-(e)) show high oxygen content at T > 350 °C, as Ti increases the thermal stability of interstitial oxygen.[15,16] For calculating δ, a reference point at higher temperatures where all Mn and Tb are assumed to be found as Mn^{3+} and Tb^{3+} was chosen. This point was set at the minimum measured mass from TGA at T > 700 °C, giving $\delta = 0$ and $\delta = 0.075$ for the undoped and Ti-doped samples, respectively. It is observed that the Ti-doped samples do not reach a stable plateau at higher temperatures, indicating a small underestimation in the assumption of δ for these samples.

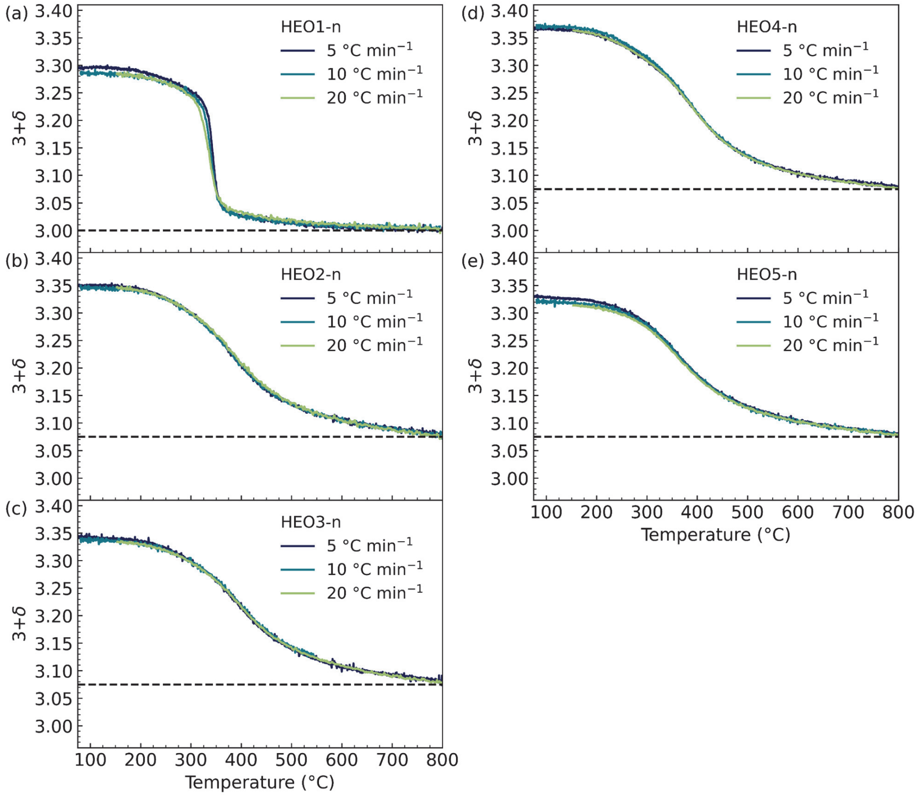

Figure 3: Oxygen stoichiometry during cooling as a function of temperature for nanocrystalline samples, measured using different cooling rates in O2 atmosphere. The dashed horizontal line indicates the oxygen stoichiometry were all Mn and Tb is assumed to be found as Mn^{3+} and Tb^{3+}, which corresponds to $\delta = 0$ and $\delta = 0.075$ for the undoped and Ti-doped samples, respectively.

Bulk HEO2-b and HEO5-b show a subtle decrease in oxygen storage capacity (Figure 4) compared to the corresponding nanocrystalline materials in Figure 2, with a decrease from $\delta = 0.35$ to $\delta = 0.27$ for HEO2, and from $\delta = 0.32$ to $\delta = 0.22$ for HEO5. There is also a small offset in the temperature ranges of oxidation and reduction for these samples, indicating that the samples are not fully oxidized due to kinetic limitations. HEO2-b has a subtly higher maximum oxygen content during cooling than HEO5-b, as this sample contains Tb which likely increase the total oxygen storage capacity of the material.[12] HEO2-b also shows less thermal hysteresis in oxygen content than HEO5-b, indicating slightly faster kinetics, which could also explain the higher oxygen content of this material.

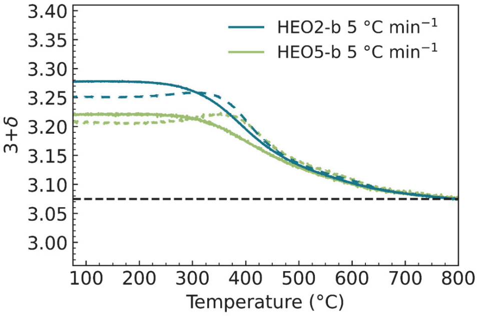

Figure 4: Oxygen stoichiometry as a function of temperature during heating (dashed lines) and cooling (solid lines) for the bulk HEO2-b and HEO5-b samples measured in O_2 atmosphere.

To investigate the differences between undoped and Ti-doped high entropy materials, the HEO1-n and HEO2-n samples were used for further measurements. Thermogravimetric measurements of oxygen stoichiometry as a function of temperature measured during heating and cooling in O_2 atmosphere using different heating and cooling rates are shown in Figure 5. HEO1-n shows a small oxygen absorption at 500 °C during heating, highlighted in the inset in Figure 5 (a), which may stem from oxidation of Tb^{3+} to Tb^{4+}. During heating, HEO1-n shows less oxygen absorption with increasing heating rates, with a decrease from $\delta = 0.21$ to $\delta = 0.17$ and $\delta = 0.13$ when increasing the heating rate from 5 °C min^{-1} to 10 °C min^{-1} and 20 °C min^{-1}, respectively. This sample also displays a visible hysteresis in oxygen content during heating and cooling, with a width of 20 °C. The width of the hysteresis does not change with heating rate, as observed for single *R* cation hexagonal manganites.[16] The temperature of maximum oxygen content during heating is subtly shifted upwards for both samples with increasing heating rates, with a shift from 320 °C to 350 °C for HEO1-n, and from 270 °C to 300 °C for HEO2-n.

The Ti-doped HEO1-n sample shows no thermal hysteresis in oxygen content, which is in accordance with previous findings for Ti^{4+} doped RMnO$_3$.[15–17] The oxygen absorption decreases subtly with faster heating rates for HEO2-n, but the change is less significant in value than for the undoped sample; for HEO2-n, the oxygen absorption drops from $\delta = 0.33$ to $\delta = 0.31$ when increasing the heating rate from 5 °C min^{-1} to 10 °C min^{-1}. No change in oxygen capacity is seen when increasing the heating rate further to 20 °C min^{-1} for HEO2-n.

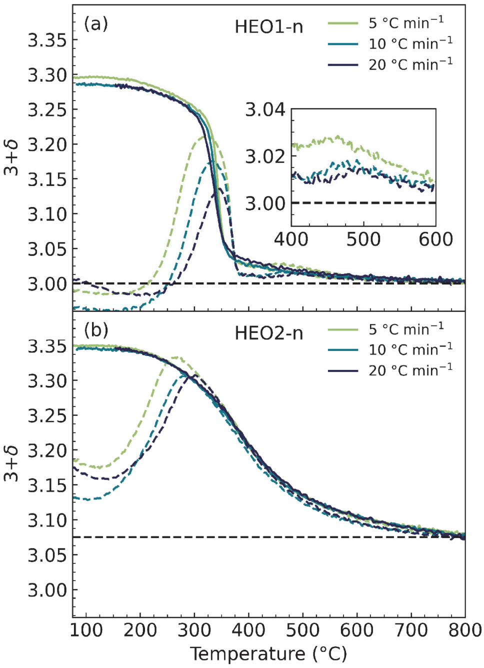

Figure 5: Oxygen stoichiometry measured during heating (dashed lines) and cooling (solid lines) using different heating and cooling rates in O_2 atmosphere for (a) HEO1-n and (b) HEO2-n. The horizontal dashed lines indicate the oxygen stoichiometry where all Mn and Tb are assumed to be found as Mn^{3+} and Tb^{3+}, respectively. The inset in (a) shows the small oxidation occurring at 500 °C during heating, which is believed to be due to oxidation of Tb^{3+} to Tb^{4+}.

When interstitial oxygen enters the crystal lattice, hexagonal manganites typically display an expansion in the *ab*-plane and a contraction in the *c* direction. Lattice parameters *a* and *c* of HEO1-n and HEO2-n from high-temperature XRD measurements performed during heating and cooling in O_2 and N_2 atmosphere are presented in Figure 6. The diffractograms for the HEO1-n sample were refined within the *R*3*c* space group, while the data from the Ti-doped HEO2-n sample was refined within the *P*6$_3$*cm* space group, as the reflections characteristic for the *R*3*c* space group are less pronounced for this sample when oxidized (Figure 2), hence the *P*6$_3$*cm* space group gave better fits. Both samples show a large contraction along the *c* axis at lower temperatures in O_2, which is a signature of the large oxygen absorption occurring for T < 400 °C. For the sample without Ti-doping, the largest changes in the *a* and *c* parameters occur between 325 °C and 350 °C, in accordance with the narrow temperature interval for oxygen absorption and release found from TGA (Figure 5). A small hysteresis in the *a* parameter is visible at ~150 °C, which may indicate some oxidation is taking place at a temperature below the bulk oxidation ~300 °C; this may be due to some oxidation of Tb^{3+} to Tb^{4+} occurring at lower temperatures in O_2. Only thermal expansion can be seen when heating and cooling HEO1-n in N_2 atmosphere.

The Ti-doped HEO2-n sample shows significant chemical expansion of the *c* parameter from oxygen incorporation and release up to 600 °C during heating and cooling in O_2, as expected from the increased thermal stability of O_i found through TGA. Above 600 °C, the increase in the *c* parameter becomes less distinct, but the continuous increase still indicates that the material has not reached a plateau at its assumed minimum oxygen content of $\delta = 0.075$, as hexagonal manganites nominally show a negative thermal expansion coefficient along the *c*-axis during heating.[48,49] The large gap between the *c* parameter values in O_2 and N_2 at higher temperatures also indicate that $\delta > 0$ at these temperatures. No large expansion of the *ab*-plane is visible during oxidation for this sample, instead a small contraction in the *a* parameter at T < 300 °C can be observed, similar to what has been reported for Ti-doped $DyMnO_3$.[15] A small contraction of the *c* parameter can be seen in N_2 atmosphere, indicating that some incorporation of interstitial oxygen also occurs at low pO_2 (nominally 5.0 purity, $\sim10^{-4}$–10^{-6} atm). No other changes in lattice parameters occur during heating and cooling in N_2 atmosphere, except what can be attributed to thermal expansion.

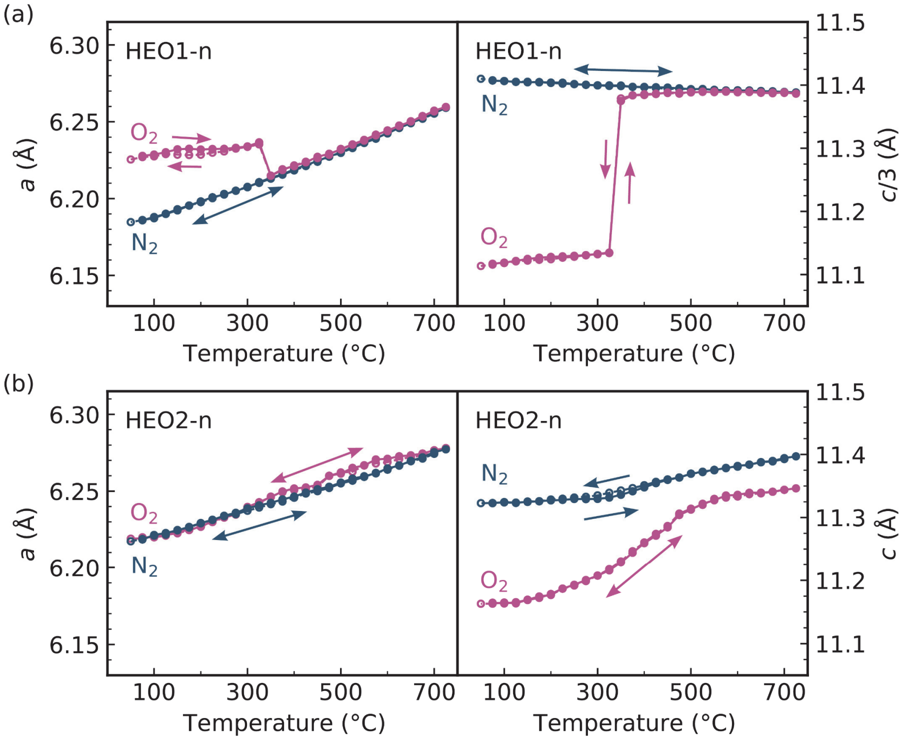

Figure 6: Refined lattice parameters *a* and *c* as a function of temperature for (a) HEO1-n and (b) HEO2-n found from high-temperature XRD during heating and cooling in O_2 and N_2 atmosphere.

Partial oxidation of both Mn^{3+} to Mn^{4+} and Tb^{3+} to Tb^{4+} occurs when exposing the HEO1-n and HEO2-n samples to O_2 atmosphere. Normalized X-ray absorption near-edge structure (XANES) spectra of the Mn *K*-edge and the Tb L_3-edge for both samples are presented in Figure 7, with spectra collected in N_2 atmosphere, and after stabilization in O_2 atmosphere. The Mn *K*-edge is shifted towards higher energy values, which indicates a partial transition from Mn^{3+} to Mn^{4+} when comparing to the reference spectra included in Figure 7 (a),(b). For Tb (Figure 7 (c),(d)), there is a decrease in absorption intensity of the peak at ~7522 eV after oxidation, and a second peak at ~7530 eV appears. This indicates the presence of Tb^{4+}, which has also been reported for other Tb-substituted $RMnO_3$ exposed to high pO_2.[12]

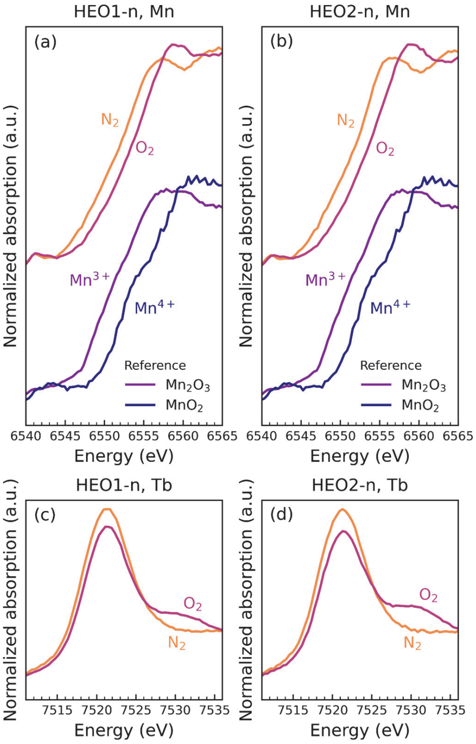

Figure 7: Normalized XANES spectra of HEO1-n and HEO2-n at the (a),(b) Mn *K*-edge and (c),(d) Tb *L*3-edge collected before (N_2) and after oxidation (O_2) at 200 °C, with Mn_2O_3 and MnO_2 spectra included as references in (a),(b).

XANES spectra collected during *in situ* switching of atmosphere from O_2 to N_2 (Figure 8) show that both the HEO1-n and HEO2-n samples oxidize quickly at 200 °C, with the Mn *K*-edge stabilizing at higher energies after ~15 minutes. The largest shift in edge position occurs during the first 5 minutes after switch of atmosphere, implying that the bulk of the oxidation process occurs in the beginning of the total equilibration time. The Mn *K*-edge of HEO2-n (Figure 8 (b)) shows a greater shift in energy compared to that of HEO1-n (Figure 8 (a)), indicating that more Mn^{3+} oxidizes to Mn^{4+} in the Ti-doped sample.

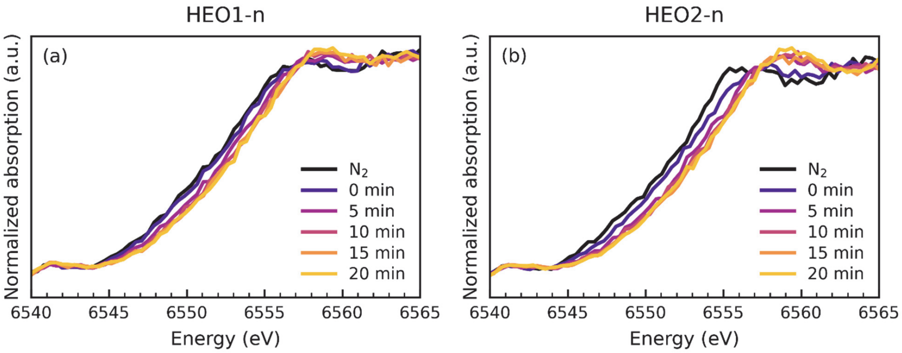

Figure 8: Normalized time-resolved XANES spectra of the Mn *K*-edge measured upon *in-situ* switching of atmosphere from N_2 to O_2 at 200 °C for (a) HEO1-n and (b) HEO2-n. Measurements done in O_2 are labelled as the time after switching atmosphere.

Synchrotron X-ray diffractograms measured upon *in situ* switching of atmosphere from N_2 to O_2 are shown for HEO1-n and HEO2-n in Figure 9 for measurements done at 200 °C and 300 °C, and for other temperatures in Figure S3 and S4. Both samples show shifts in peak positions after being exposed to O_2 atmosphere, demonstrating that interstitial oxygen is entering the lattice. The oxidation time decreases with increasing temperature for both samples, as expected. The Ti-doped sample also shows faster oxidation rates than the undoped sample, which agrees with previous findings for Ti-doped RMnO$_3$.[16] The visible $R3c$ reflections at ~6.8 2θ and ~6.9 2θ in N_2 atmosphere for HEO1-n indicate that the material contains significant amounts of interstitial oxygen even before being re-exposed to oxygen.

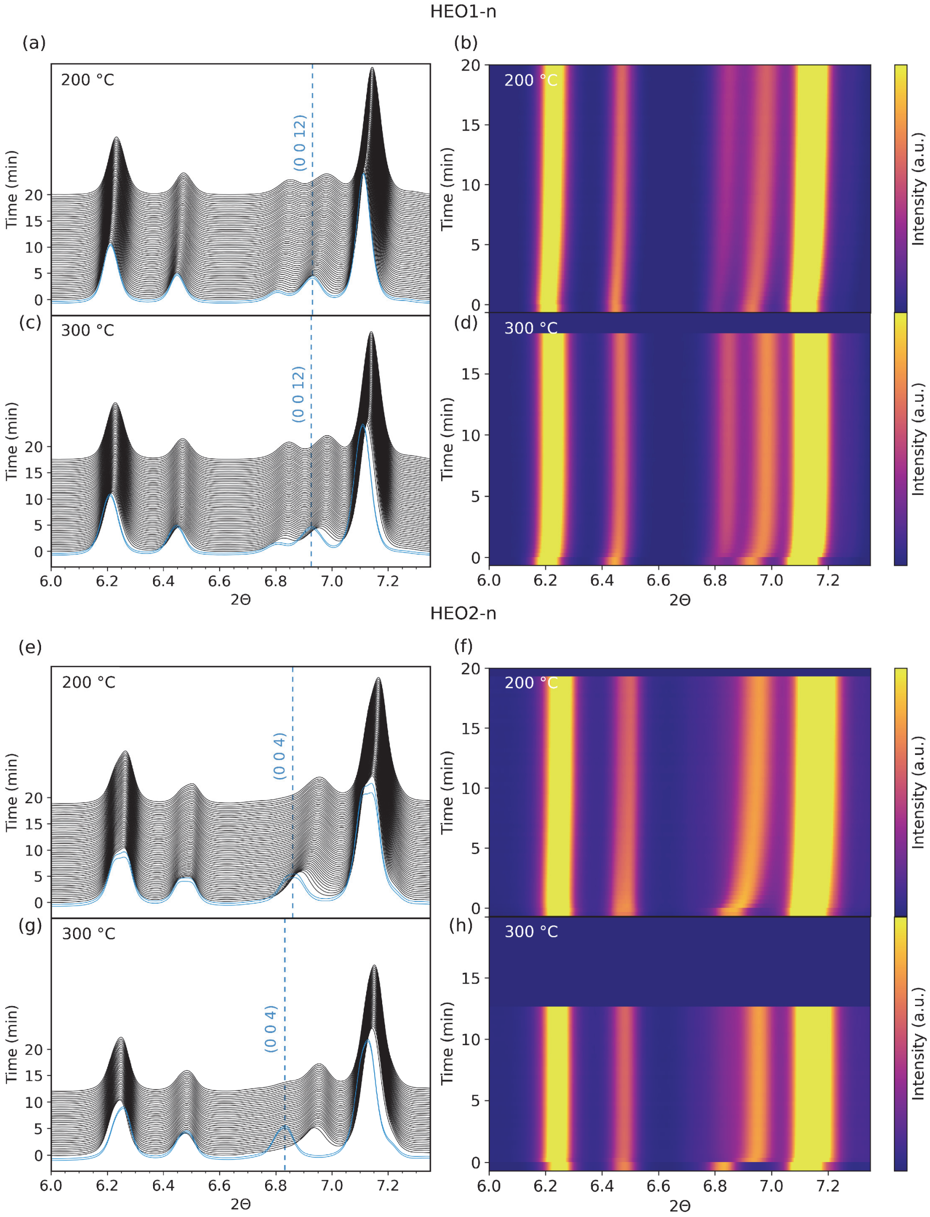

Figure 9: X-ray diffractograms and 2D contour plots of (a)-(d) HEO1-n and (e)-(h) HEO2-n measured at 200 °C and 300 °C as a function of time after *in situ* switching of atmosphere from N_2

(blue) to O_2 (black). The baseline intensity at 6.0° 2θ indicate the time in minutes after *in situ* switching from N_2 to O_2. Vertical dashed blue lines indicate the initial position of the $(0\ 0\ 4)_{185}$/$(0\ 0\ 12)_{161}$ reflection measured in N_2.

Since the degree of oxidation and changes in lattice parameters are closely linked, the time it takes for the lattice parameters to stabilize in the oxidized state can be used for investigating the oxidation kinetics. Refined lattice parameters as a function of time after *in situ* switching of atmosphere from N_2 to O_2 at different temperatures are shown in Figure 10. Both samples show a net contraction in the a and c axis during oxidation, and the time to reach equilibrium decreases with increasing temperatures. The contraction along c is lower in magnitude for HEO1-n than for HEO2-n, which is related to the former being slightly oxidized (indicated by appearance of the $R3c$ reflections in Figure 9) prior to exposure to O_2. The net contraction in c also decreases with temperature for HEO1-n, as TGA measurements (Figure 5) shows that the sample has a smaller OSC at $T > 350$ °C. When comparing the lattice parameters measured before oxidation in Figure 10 with the lattice parameters found for the as-prepared HEO1-n in Table 2 (a = 6.181(8) Å, c = 11.412(0) Å), we can see that the sample display a net *expansion,* not contraction, in the ab-plane during oxidation; during the first part of oxidation, the ab-plane expands, followed by a contraction during the final oxidation. This is also observed for the Ti-doped sample, which displays a slight expansion in the a parameter before contraction during oxidation.

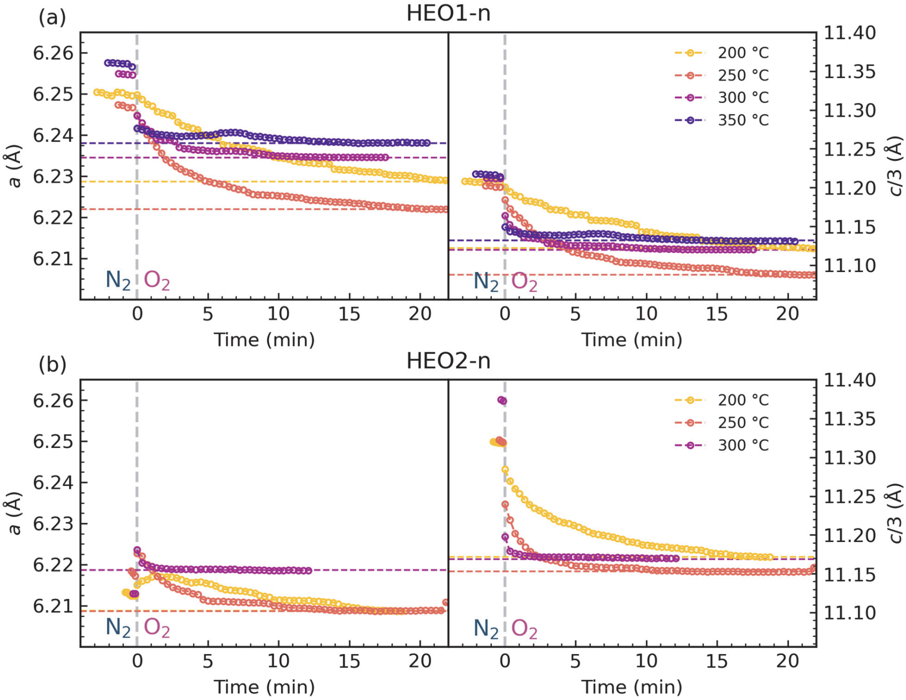

Figure 10: Refined lattice parameters as a function of time after in situ switching from N_2 to O_2 atmosphere for (a) HEO1-n and (b) HEO2-n. Both samples were refined within the $R3c$ space group. The colored horizontal lines indicate the value of the lattice parameters in the final oxidated state at the different temperatures.

DISCUSSION

Kinetics of oxidation. As evident from the thermogravimetric data in Figure 3 and Figure 5, all samples show fast oxygen incorporation and release rates, with no significant drop in oxygen storage capacity with increasing cooling rates, even as fast as 20 °C min^{-1}. In contrast, literature reports on undoped Y-, Ho- or Dy-based materials all show significant reduction in OSC during cooling even at 5 °C/min cooling rate.[11,12,16] $YMnO_3$ substituted with larger R such as Tb, Gd and Sm show no significant change in OSC when increasing the cooling rate from 1 to 5 °C min^{-1},[12] indicating that the larger R improves the kinetics of oxidation. However, these R-substituted samples also show a significant increase in thermal hysteresis with increasing cooling rates, implying significantly slower oxidation kinetics than for the high-entropy materials studied here. The lack of a thermal hysteresis in oxygen content for the Ti-doped HEO2-n samples (Figure 5) indicates that the addition of Ti^{4+} has further improved the kinetics of oxidation. Thermal hysteresis upon heating and cooling is an indication that the kinetics of oxygen exchange is too slow for continuous equilibration with the surrounding atmosphere. Hexagonal manganites substituted with large R^{3+} cations such as Gd^{3+} or Sm^{3+} have also shown indications of reduced oxygen release rates due to an increase in stability of the oxidized phase,[12] which could affect practical applications of the material. None of the samples in Figure 3 show signs of partial or delayed release of O_2 or shifts in temperature interval for reduction with increasing heating rates, indicating that reduction rates are still fast.

Both examined bulk samples show good oxygen absorption at 5 °C min^{-1} (Figure 4), indicating that the oxidation kinetics are fast enough for oxidation of bulk samples with large particles. With oxygen contents of $\delta = 0.28$ for HEO2-b and $\delta = 0.22$ for HEO5-b during cooling, these samples show comparable and better oxygen absorption properties than many nanocrystalline single R hexagonal manganites,[11,12] and significantly better than other reported bulk materials,[4,19] measured with equally fast cooling rates. This possibly enables the use of bulk materials prepared through solid state methods for oxygen separation applications, simplifying the material synthesis process significantly compared to sol-gel based methods.

The HEO1-n and HEO2-n samples oxidize fast (Figures 9 and 10) and reach fully oxidized states within 20 minutes or less at all temperatures, with increasing rates at higher temperatures. The Ti-doped sample is also subtly faster than the undoped sample, as expected as Ti^{4+}-doping is known to improve the oxidation kinetics.[16] As the oxidation time of HEO1-n (Figure 10) shows the transition from partially oxidized to fully oxidized (seen by the presence of $R3c$ before switching to O_2 in Figure 9), the actual full oxidation time starting from $\delta = 0$ is therefore believed to be longer compared to what has been observed here, but as the first stage of the oxidation is faster than the later stage, this should not increase the oxidation time significantly. The oxidation time for HEO1-n is substantially lower than what has previously been reported for $R\text{MnO}_3$ without aliovalent dopants, with $Y_{0.95}Pr_{0.05}MnO_3$ needing several hours to oxidize in air at different temperatures[11] and $HoMnO_3$ being far from fully oxidized after 20 minutes at 250 °C in O_2 atmosphere.[16] This strongly suggests that high entropy compositions greatly improves the oxygen incorporation rate of hexagonal manganites. This may be attributed to lattice site disorder causing overlap in site energies which promotes ionic transport.[41]

The changes along the c axis (Figure 10) can be directly correlated with the degree of oxidation, and the surface exchange rates of oxygen for the two samples can be calculated using the model developed by Moreno *et al.*[50] The calculated surface exchange rates are shown in Figure 11, with corresponding activation energies presented in Table 3. The surface exchange rates are higher for high entropy compositions compared to their undoped and Ti-doped counterparts, and comparable to values reported for perovskites and other oxides at several hundred degrees higher temperatures.[50–58] The surface exchange rates for HEO1-n are in addition likely an underestimation, as they are calculated from only the last, and slower, part of the oxidation process, as discussed earlier.

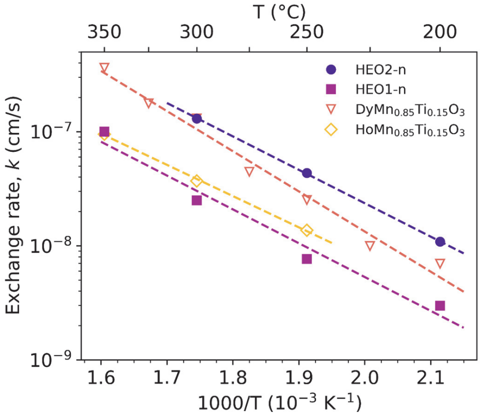

Figure 11: Surface exchange rate for HEO1-n and HEO2-n. Surface exchange rates for $HoMn_{0.85}Ti_{0.15}O_3$ and $DyMn_{0.85}Ti_{0.15}O_3$ from Danmo *et al.* are included for comparison.[16]

Table 3: Activation energies for different $RMnO_3$. Values marked with an asterisk (*) are from Danmo *et al.*[16]

Composition	Activation energy (eV)
HEO1-n	0.59
HEO2-n	0.58
$HoMn_{0.85}Ti_{0.15}O_3$*	0.54*
$DyMn_{0.85}Ti_{0.15}O_3$*	0.68*

Oxygen storage capacity. All samples show large oxygen storage capacities, with the highest OSC found for HEO4-n with $\delta = 0.37$ (Figure 3). Such high OSCs are common for hexagonal manganites that use large R^{3+} cations ($r_{R3+} \geq r_{Dy}$) on the *R* site,[9,11,12,14] and this can therefore not be attributed to high configurational entropy. The high OSC capacities can also be explained by Tb^{3+} oxidizing to Tb^{4+}, as confirmed by the XANES spectra in Figure 4, adding to the total amount of interstitial oxygen in the material.[9,12] As the OSC of the Ti-doped samples increases with increasing Tb-content (Figure 3), it is likely that the differences in OSC is mainly influenced by the amount Tb in each sample, and not only related to the other differences in composition (Table 1). A slight increase in oxygen content for HEO1-n can be observed during heating above T = 450 °C (Figure 5), which may also be related to oxidation of Tb. It is not known whether the O_i formed from charge compensation of Tb^{4+} enters the Mn-O layers through the interstitialcy mechanism, or if it enters other interstitial positions in the structure. If the latter is the case, then this oxidation mechanism will likely have other oxidation thermodynamics and kinetics than the oxidation of Mn, which is why it occurs at other temperatures. As Tb is known to exist as both Tb^{3+} and Tb^{4+} at T > 900 °C in high partial pressures of O_2,[59] it is likely that the amount of interstitial oxygen found in the materials at high temperatures is above what has been set as the "minima" (dashed line) in Figure 3-5; this line assumes that all Mn and *R* are found as Mn^{3+} and R^{3+}, which likely is not the case for Tb.

The thermal hysteresis found in the oxygen content during heating and cooling for HEO1-n is ~20 °C, which is on the smaller side of what has been reported for other $RMnO_3$ previously.[4,5,12] This makes the material well equipped for temperature swing absorption processes, as only a small change in temperature is needed for switching between complete oxidation and release. The temperatures for oxidation and reduction is comparable to what has been reported for $YMnO_3$ substituted with large *R*-cations such as Gd^{3+} and Sm^{3+}, which also display similarly narrow thermal hystereses in oxygen content.[12] This also indicates that using larger *R* shifts the temperature interval for oxidation during cooling towards higher temperatures, increasing the thermal stability of O_i. A further increase in thermal stability of interstitial oxygen is seen for Ti-doped samples. This makes the HEO2-n sample more viable for pressure swing absorption methods than temperature swing-based ones.

Phase stability. The presence of many elements may stabilize metastable structures as single-phase solid solution is favoured by configurational entropy. The hexagonal layered structure is stabilized even if some end-member hexagonal compounds would be metastable, or even unstable, in this structure, e.g. $TbMnO_3$[60] and $GdMnO_3$. Using high entropy compositions, such as the ones chosen for this study, is one way to enable the use of these larger rare earths while still maintaining the hexagonal manganite crystal structure. As all nanocrystalline samples show high phase purity, with only trace amounts of the orthorhombic phase found for HEO2-n, HEO3-n and HEO5-n, the differences in composition within the present study (Table 1) does not affect the phase stability of these samples significantly. This indicates that the high configurational entropy stabilizes the hexagonal structure even for tolerance factors as high as $t = 0.865$, much higher than the "limit" of $t = 0.855$ usually reported for these materials.[61]

The HEO1-b sample could not be prepared as phase pure, even though it has the lowest tolerance factor of all samples studied here (Table 1). This tolerance factor is determined by the size of the size of the cations in the material and was calculated by assuming the oxidation states of R and Mn to be R^{3+} and Mn^{3+}. As the oxidation states of Mn and Tb is known to change depending on both temperature and atmosphere, this is likely an imprecise assumption. In reducing conditions or at higher temperatures, Ti^{4+} can cause reduction of Mn to Mn^{2+} instead of being change compensated by excess O_i, which lowers the tolerance factor. It is therefore likely that the tolerance factor of Ti-doped samples is lower at the synthesis temperature (1450 °C for bulk samples) than that of undoped samples, which promotes formation of the hexagonal phase. For Tb, the opposite effect occurs; at higher temperatures, less Tb^{4+} will be present,[59] and the larger size of Tb^{3+} (0.98 Å) compared to that of Tb^{4+} (0.82 Å)[46] will then increase the tolerance factor, promoting formation of the orthorhombic perovskite phase. As the HEO1-b sample needs to be synthesized at higher temperatures through the solid-state synthesis method, and contains Tb but no Ti, the tolerance factor is likely too high to ensure a phase pure hexagonal manganite structure.

Structural changes. In addition to the site disorder caused by the high entropy composition possibly enhancing ionic diffusion in the material,[41] the large cations found in these samples may also be affecting oxygen transport properties. The larger R cations expand the *ab*-plane significantly, as can be seen from the lattice parameters in Table 2 and Figure 6. An expanded *ab*-plane has earlier been shown to increase both the OSC and the kinetics of oxidation in hexagonal manganites,[15,16] and this may also contribute to the improved properties found for the samples studied here.

Another effect of the of the expanded *ab*-plane is visible for the changes in lattice parameters occurring during oxidation (Figure 7); typically, hexagonal manganites display a contraction along c and an expansion in a during oxidation, but samples with larger a parameters, such as $DyMn_{0.85}Ti_{0.15}O_3$, show an expansion, followed by a contraction, along the a axis during oxidation.[15,16,62] This is also observed for both of the high entropy samples here, but the contraction along a when going from partially oxidized to fully oxidized (Figure 7) is more significant for HEO1-n. This is due to the HEO1-n sample having the largest a-parameter of the two before switching to O_2 atmosphere, and the HEO2-n sample shows only a slight expansion during the first stage of oxidation, before a slight contraction. This indicates that the rectification of the MnO_5 bipyramids that occurs during incorporation of O_i reaches a maximum during the first segment of oxidation, before contraction from electrostatic attraction between the negatively charged O_i and positively charged Mn (and Ti) starts to affect the structure for larger amounts of oxygen. Similarly, the expansion of the *ab*-plane found at low and medium O_i concentrations, and the following contraction found at higher O_i concentrations, is observable from Figure 3, showing the static HT-XRD measurements in O_2 and N_2; for the Ti-doped sample, the *a* parameter in O_2 is lower than that measured in N_2 at $T < 300$ °C, and higher at $T > 300$ °C. This can be related to the amount of oxygen present in the material at the different temperature ranges (Figure 2), as the oxygen content of HEO2-n is at its highest below $T = 300$ °C, and decreases with increasing temperatures.

As all high entropy samples studied here show excellent oxygen storage capacities of approximately the theoretical maximum of $\delta = 0.33$, with no large differences seen for different compositional variations, it is likely that the high configurational entropy increases oxygen storage capacity and oxygen transport properties of hexagonal manganites regardless of composition. This should enable the use of rare earth sources as raw materials for hexagonal manganite synthesis without the need for difficult and expensive process steps to separate the different rare earths. High entropy alloys have a high tolerance for impurity elements, which enables the use of scrap metals or recycled materials for synthesis,[24] and this likely applies to high entropy ceramics as well. One intriguing possibility is to use the remaining mix of rare earth elements left after critical elements such as Nd, Pr, and Dy are extracted. The tolerance factor of hexagonal manganites will benefit from using smaller, and cheaper, rare earth cations such as Er and Y, which combined with larger cations such as Gd, Ce and La, which are also comparatively cheaper, could result in an affordable material with excellent OSC and oxidation kinetics.[63,64] Cheaper raw materials, composed of several different rare earth elements, which also improve the properties compared to single *R* materials, would greatly improve the commercial potential of hexagonal manganites for oxygen storage and separation.

CONCLUSIONS

The oxygen absorption properties of high entropy hexagonal manganites have been studied, using thermogravimetric analysis (TGA), high-temperature X-ray diffraction (HT-XRD) in O_2 and N_2 atmosphere, and HT-XRD and X-ray absorption near-edge structure (XANES) with *in situ* switching of atmospheres. High configuration entropy materials were found to have improved kinetics of oxidation compared to typical hexagonal manganites, and to stabilize the hexagonal structure for large rare earth cations and high tolerance factors. The large *R* cations increased the size of the *ab*-plane of the samples, which also enhances surface exchange of oxygen. The oxygen storage capacity was found to be high ($\delta > 0.3$) for all nanocrystalline samples, with increased oxygen absorption with the addition of Ti and Tb. The bulk samples also displayed strongly improved oxygen absorption capacity and kinetics compared to previous reports. The oxygen absorption properties were found to be rather insensitive to variations in chemical composition, implying that structural disorder in itself is contributing to the improved oxidation kinetics. Improved properties and insensitivity to exact rare earth composition enhances the commercial potential of hexagonal manganites.

ACKNOWLEDGEMENTS

We would like to thank Elvia Anabela Chavez Panduro for help with the HT-XRD measurements. We would also like to thank the Swizz-Norwegian Beamlines (SNBL) and BM31 at the European Synchrotron Radiation Facility (ESRF) in Grenoble, France for providing the beamtime, and the staff for their support. Financial support from NTNU Norwegian University of Science and Technology is acknowledged.

REFERENCES

(1) Remsen, S.; Dabrowski, B. Synthesis and Oxygen Storage Capacities of Hexagonal $Dy_{1-x}Y_xMnO_{3+\delta}$. *Chem. Mater.* **2011**, *23* (17), 3818–3827.

(2) Remsen, S.; Dabrowski, B.; Chmaissem, O.; Mais, J.; Szewczyk, A. Synthesis and Oxygen Content Dependent Properties of Hexagonal $DyMnO_{3+\delta}$. *J. Solid State Chem.* **2011**, *184* (8), 2306–2314.

(3) Abughayada, C.; Dabrowski, B.; Kolesnik, S.; Brown, D. E.; Chmaissem, O. Characterization of Oxygen Storage and Structural Properties of Oxygen-Loaded Hexagonal $RMnO_{3+\delta}$ (R = Ho, Er, and Y). *Chem. Mater.* **2015**, *27* (18), 6259–6267.

(4) Świerczek, K.; Klimkowicz, A.; Nishihara, K.; Kobayashi, S.; Takasaki, A.; Alanizy, M.; Kolesnik, S.; Dabrowski, B.; Seong, S.; Kang, J. Oxygen Storage Properties of Hexagonal $HoMnO_{3+\delta}$. *Phys. Chem. Chem. Phys.* **2017**, *19* (29), 19243–19251.

(5) Abughayada, C.; Dabrowski, B.; Avdeev, M.; Kolesnik, S.; Remsen, S.; Chmaissem, O. Structural, Magnetic, and Oxygen Storage Properties of Hexagonal $Dy_{1-x}Y_xMnO_{3+\delta}$. *J. Solid State Chem.* **2014**, *217*, 127–135.

(6) Shah, K.; Moghtaderi, B.; Wall, T. Selection of Suitable Oxygen Carriers for Chemical Looping Air Separation: A Thermodynamic Approach. *Energy and Fuels* **2012**, *26* (4), 2038–2045.

(7) Krzystowczyk, E.; Haribal, V.; Dou, J.; Li, F. Chemical Looping Air Separation Using a Perovskite-Based Oxygen Sorbent: System Design and Process Analysis. *ACS Sustain. Chem. Eng.* **2021**, *9* (36), 12185–12195.

(8) Moghtaderi, B. Application of Chemical Looping Concept for Air Separation at High Temperatures. *Energy and Fuels* **2010**, *24* (1), 190–198.

(9) Klimkowicz, A.; Cichy, K.; Chmaissem, O.; Dabrowski, B.; Poudel, B.; Świerczek, K.; Taddei, K. M.; Takasaki, A. Reversible Oxygen Intercalation in Hexagonal $Y_{0.7}Tb_{0.3}MnO_{3+\delta}$: Toward Oxygen Production by Temperature-Swing Absorption in Air. *J. Mater. Chem. A* **2019**, *7* (6), 2608–2618.

(10) Klimkowicz, A.; Hashizume, T.; Cichy, K.; Tamura, S.; Świerczek, K.; Takasaki, A.; Motohashi, T.; Dabrowski, B. Oxygen Separation from Air by the Combined Temperature Swing and Pressure Swing Processes Using Oxygen Storage Materials $Y_{1-x}(Tb/Ce)_xMnO_{3+\delta}$. *J. Mater. Sci.* **2020**, *55* (33), 15653–15666.

(11) Cichy, K.; Świerczek, K.; Jarosz, K.; Klimkowicz, A.; Marzec, M.; Gajewska, M.; Dabrowski, B. Towards Efficient Oxygen Separation from Air: Influence of the Mean Rare-Earth Radius on Thermodynamics and Kinetics of Reactivity with Oxygen in Hexagonal $Y_{1-x}R_xMnO_{3+\delta}$. *Acta Mater.* **2021**, *205*.

(12) Otomo, M.; Hasegawa, T.; Asakura, Y.; Yin, S. Remarkable Effects of Lanthanide Substitution for the Y-Site on the Oxygen Storage/Release Performance of $YMnO_{3+\delta}$. *ACS Appl. Mater. Interfaces* **2021**, *13* (27), 31691–31698.

(13) Parkkima, O.; Malo, S.; Hervieu, M.; Rautama, E. L.; Karppinen, M. New $RMnO_{3+\delta}$ (R=Y, Ho; Δ≈0.35) Phases with Modulated Structure. *J. Solid State Chem.* **2015**, *221*, 109–115.

(14) Cichy, K.; Zając, M.; Świerczek, K. Evaluation of Applicability of Nd- and Sm-Substituted $Y_{1-x}R_xMnO_{3+\delta}$ in Temperature Swing Absorption for Energy-Related Technologies. *Energy* **2022**, *239*, 1–9.

(15) Danmo, F. H.; Williamson, B. A. D.; Småbråten, D. R.; Gaukås, N. H.; Østli, E. R.; Grande, T.; Glaum, J.; Selbach, S. M. Oxygen Absorption in Nanocrystalline H-RMnO3 (R=Y, Ho, Dy) and the Effect of Ti Donor Doping. *Under review.*

(16) Danmo, F. H.; Nylund, I.-E.; Westermoen, A.; Marshall, K. P.; Stoian, D.; Grande, T.; Glaum, J.; Selbach, S. M. Oxidation Kinetics of Nanocrystalline H-$RMn_{1-x}Ti_xO_3$ (R = Ho, Dy). *Submitted.*

(17) Levin, I.; Krayzman, V.; Vanderah, T. A.; Tomczyk, M.; Wu, H.; Tucker, M. G.; Playford, H. Y.; Woicik, J. C.; Dennis, C. L.; Vilarinho, P. M. Oxygen-Storage Behavior and Local Structure in Ti-Substituted $YMnO_3$. *J. Solid State Chem.* **2017**, *246* (November 2016), 29–41.

(18) Moreno Botello, Z. L.; Caneiro, A.; Roussel, P.; Gauthier, G. Synthesis and Preliminary Study of Pure and Zr-Doped YMnO3compounds as Solid Oxide Fuel Cells Electrode. *J. Alloys Compd.* **2017**, *690*, 348–355.

(19) Klimkowicz, A.; Świerczek, K.; Kobayashi, S.; Takasaki, A.; Allahyani, W.; Dabrowski, B. Improvement of Oxygen Storage Properties of Hexagonal $YMnO_{3+\delta}$ by Microstructural Modifications. *J. Solid State Chem.* **2018**, *258* (August 2017), 471–476.

(20) European Commission. *Study on the Critical Raw Materials for the EU*; 2023.

(21) Dang, D. H.; Thompson, K. A.; Ma, L.; Nguyen, H. Q.; Luu, S. T.; Duong, M. T. N.; Kernaghan, A. Toward the Circular Economy of Rare Earth Elements: A Review of Abundance, Extraction, Applications, and Environmental Impacts. *Arch. Environ. Contam. Toxicol.* **2021**, *81* (4), 521–530.

(22) Li, J.; Peng, K.; Wang, P.; Zhang, N.; Feng, K.; Guan, D.; Meng, J.; Wei, W.; Yang, Q. Critical Rare-Earth Elements Mismatch Global Wind-Power Ambitions. *One Earth* **2020**, *3* (1), 116–125.

(23) Blagoeva, D. T.; Alves Dias, P.; Marmier, A.; Pavel, C. C. *Assessment of Potential Bottlenecks along the Materials Supply Chain for the Future Deployment of Low-Carbon Energy and Transport Technologies in the EU.*; 2016.

(24) Yeh, J. W.; Chen, S. K.; Lin, S. J.; Gan, J. Y.; Chin, T. S.; Shun, T. T.; Tsau, C. H.; Chang, S. Y. Nanostructured High-Entropy Alloys with Multiple Principal Elements: Novel Alloy Design Concepts and Outcomes. *Adv. Eng. Mater.* **2004**, *6* (5), 299–303.

(25) Cantor, B.; Chang, I. T. H.; Knight, P.; Vincent, A. J. B. Microstructural Development in Equiatomic Multicomponent Alloys. *Mater. Sci. Eng. A* **2004**, *375–377* (1-2 SPEC. ISS.), 213–218.

(26) Musicó, B. L.; Gilbert, D.; Ward, T. Z.; Page, K.; George, E.; Yan, J.; Mandrus, D.; Keppens, V. The Emergent Field of High Entropy Oxides: Design, Prospects, Challenges, and Opportunities for Tailoring Material Properties. *APL Mater.* **2020**, *8* (4).

(27) Sarkar, A.; Velasco, L.; Wang, D.; Wang, Q.; Talasila, G.; de Biasi, L.; Kübel, C.; Brezesinski, T.; Bhattacharya, S. S.; Hahn, H.; Breitung, B. High Entropy Oxides for Reversible Energy Storage. *Nat. Commun.* **2018**, *9* (1).

(28) Bérardan, D.; Franger, S.; Meena, A. K.; Dragoe, N. Room Temperature Lithium Superionic Conductivity in High Entropy Oxides. *J. Mater. Chem. A* **2016**, *4* (24), 9536–9541.

(29) Bérardan, D.; Franger, S.; Dragoe, D.; Meena, A. K.; Dragoe, N. Colossal Dielectric Constant in High Entropy Oxides. *Phys. Status Solidi - Rapid Res. Lett.* **2016**, *10* (4), 328–333.

(30) Sarkar, A.; Breitung, B.; Hahn, H. High Entropy Oxides: The Role of Entropy, Enthalpy and Synergy. *Scr. Mater.* **2020**, *187*, 43–48.

(31) Oses, C.; Toher, C.; Curtarolo, S. High-Entropy Ceramics. *Nat. Rev. Mater.* **2020**, *5* (4), 295–309.

(32) Gild, J.; Zhang, Y.; Harrington, T.; Jiang, S.; Hu, T.; Quinn, M. C.; Mellor, W. M.; Zhou, N.; Vecchio, K.; Luo, J. High-Entropy Metal Diborides: A New Class of High-Entropy Materials and a New Type of Ultrahigh Temperature Ceramics. *Sci. Rep.* **2016**, *6* (November), 2–11.

(33) Rost, C. M.; Sachet, E.; Borman, T.; Moballegh, A.; Dickey, E. C.; Hou, D.; Jones, J. L.; Curtarolo, S.; Maria, J. P. Entropy-Stabilized Oxides. *Nat. Commun.* **2015**, *6*.

(34) Jiang, S.; Hu, T.; Gild, J.; Zhou, N.; Nie, J.; Qin, M.; Harrington, T.; Vecchio, K.; Luo, J. A New Class of High-Entropy Perovskite Oxides. *Scr. Mater.* **2018**, *142*, 116–120.

(35) Vinnik, D. A.; Zhivulin, V. E.; Trofimov, E. A.; Gudkova, S. A.; Punda, A. Y.; Valiulina, A. N.; Gavrilyak, M.; Zaitseva, O. V.; Taskaev, S. V.; Khandaker, M. U.; Alqahtani, A.; Bradley, D. A.; Sayyed, M. I.; Turchenko, V. A.; Trukhanov, A. V.; Trukhanov, S. V. A-Site Cation Size Effect on Structure and Magnetic Properties of Sm(Eu,Gd)Cr0.2Mn0.2Fe0.2CO0.2Ni0.2O3 High-Entropy Solid Solutions. *Nanomaterials* **2022**, *12* (1).

(36) Wang, Q.; Sarkar, A.; Wang, D.; Velasco, L.; Azmi, R.; Bhattacharya, S. S.; Bergfeldt, T.; Düvel, A.; Heitjans, P.; Brezesinski, T.; Hahn, H.; Breitung, B. Multi-Anionic and -Cationic Compounds: New High Entropy Materials for Advanced Li-Ion Batteries. *Energy Environ. Sci.* **2019**, *12* (8), 2433–2442.

(37) Zhou, J.; Zhang, J.; Zhang, F.; Niu, B.; Lei, L.; Wang, W. High-Entropy Carbide: A Novel Class of Multicomponent Ceramics. *Ceram. Int.* **2018**, *44* (17), 22014–22018.

(38) Miracle, D. B.; Miller, J. D.; Senkov, O. N.; Woodward, C.; Uchic, M. D.; Tiley, J. Exploration and Development of High Entropy Alloys for Structural Applications. *Entropy* **2014**, *16* (1), 494–525.

(39) Gazda, M.; Miruszewski, T.; Jaworski, D.; Mielewczyk-Gryń, A.; Skubida, W.; Wachowski, S.; Winiarz, P.; Dzierzgowski, K.; Łapiński, M.; Szpunar, I.; Dzik, E. Novel Class of Proton Conducting Materials - High Entropy Oxides. *ACS Mater. Lett.* **2020**, *2* (10), 1315–1321.

(40) Phani Dathar, G. K.; Balachandran, J.; Kent, P. R. C.; Rondinone, A. J.; Ganesh, P. Li-Ion Site Disorder Driven Superionic Conductivity in Solid Electrolytes: A First-Principles Investigation of β-Li3PS4. *J. Mater. Chem. A* **2017**, *5* (3), 1153–1159.

(41) Zeng, Y.; Ouyang, B.; Liu, J.; Byeon, Y. W.; Cai, Z.; Miara, L. J.; Wang, Y.; Ceder, G. High-Entropy Mechanism to Boost Ionic Conductivity. *Science (80-.).* **2022**, *378* (6626), 1320–1324.

(42) Bergum, K.; Okamoto, H.; Fjellvåg, H.; Grande, T.; Einarsrud, M. A.; Selbach, S. M. Synthesis, Structure and Magnetic Properties of Nanocrystalline $YMnO_3$. *Dalt. Trans.* **2011**, *40* (29), 7583–7589.

(43) Coelho, A. A. Topas Academic: General Profile and Structure Analysis Software for Powder Diffraction Data. *Bruker AXS, Karlsruhe, Ger.* **2007**.

(44) Newville, M. Larch: An Analysis Package for XAFS and Related Spectroscopies. *J. Phys. Conf. Ser.* **2013**, *430* (1).

(45) Gibbs, A. S.; Knight, K. S.; Lightfoot, P. High-Temperature Phase Transitions of Hexagonal $YMnO_3$. *Phys. Rev. B* **2011**, *83* (9), 1958.

(46) Shannon, R. D. Revised Effective Ionic Radii and Systematic Studies of Interatomic Distances in Halides and Chalcogenides. *Acta Crystallogr. Sect. A* **1976**, *32* (5), 751–767.

(47) Skjærvø, S. H.; Wefring, E. T.; Nesdal, S. K.; Gaukås, N. H.; Olsen, G. H.; Glaum, J.; Tybell, T.; Selbach, S. M. Interstitial Oxygen as a Source of P-Type Conductivity in Hexagonal Manganites. *Nat. Commun.* **2016**, *7*, 13745.

(48) Selbach, S. M.; Løvik, A. N.; Bergum, K.; Tolchard, J. R.; Einarsrud, M. A.; Grande, T. Crystal Structure, Chemical Expansion and Phase Stability of $HoMnO_3$ at High Temperature. *J. Solid State Chem.* **2012**, *196*, 528–535.

(49) Tomczyk, M.; Senos, A. M.; Vilarinho, P. M.; Reaney, I. M. Origin of Microcracking in YMnO3 Ceramics. *Scr. Mater.* **2012**, *66* (5), 288–291.

(50) Moreno, R.; García, P.; Zapata, J.; Roqueta, J.; Chaigneau, J.; Santiso, J. Chemical Strain Kinetics Induced by Oxygen Surface Exchange in Epitaxial Films Explored by Time-Resolved X-Ray Diffraction. *Chem. Mater.* **2013**, *25* (18), 3640–3647.

(51) Yang, Q.; Burye, T. E.; Lunt, R. R.; Nicholas, J. D. In Situ Oxygen Surface Exchange Coefficient Measurements on Lanthanum Strontium Ferrite Thin Films via the Curvature Relaxation Method. *Solid State*

Ionics **2013**, *249–250*, 123–128.

(52) Moreno, R.; Zapata, J.; Roqueta, J.; Bagués, N.; Santiso, J. Chemical Strain and Oxidation-Reduction Kinetics of Epitaxial Thin Films of Mixed Ionic-Electronic Conducting Oxides Determined by X-Ray Diffraction. *J. Electrochem. Soc.* **2014**, *161* (11), F3046–F3051.

(53) Chen, T.; Harrington, G. F.; Masood, J.; Sasaki, K.; Perry, N. H. Emergence of Rapid Oxygen Surface Exchange Kinetics during in Situ Crystallization of Mixed Conducting Thin Film Oxides. *ACS Appl. Mater. Interfaces* **2019**, *11* (9), 9102–9116.

(54) Bouwmeester, H. J. M.; Kruidhof, H.; Burggraaf, A. Importance of the Surface Exchange Kinetics as Rate Limiting Step in Oxygen Permeation through Mixed-Conducting Oxides. *Solid State Ionics* **1994**, *72*, 185–194.

(55) Skiba, E. J.; Chen, T.; Perry, N. H. Simultaneous Electrical, Electrochemical, and Optical Relaxation Measurements of Oxygen Surface Exchange Coefficients: Sr(Ti,Fe)O 3−d Film Crystallization Case Study. *ACS Appl. Mater. Interfaces* **2020**, *12* (43), 48614–48630.

(56) Stangl, A.; Riaz, A.; Rapenne, L.; Caicedo, J. M.; De Dios Sirvent, J.; Baiutti, F.; Jiménez, C.; Tarancón, A.; Mermoux, M.; Burriel, M. Tailored Nano-Columnar La2NiO4cathodes for Improved Electrode Performance. *J. Mater. Chem. A* **2022**, *10* (5), 2528–2540.

(57) Yang, G.; Kim, S. Y.; Sohn, C.; Keum, J. K.; Lee, D. Influence of Heterointerfaces on the Kinetics of Oxygen Surface Exchange on Epitaxial La1.85Sr0.15CuO4 Thin Films. *Appl. Sci.* **2021**, *11* (9), 1–9.

(58) Acosta, M.; Baiutti, F.; Wang, X.; Cavallaro, A.; Wu, J.; Li, W.; Parker, S. C.; Aguadero, A.; Wang, H.; Tarancón, A.; MacManus-Driscoll, J. L. Surface Chemistry and Porosity Engineering through Etching Reveal Ultrafast Oxygen Reduction Kinetics below 400 °C in B-Site Exposed (La,Sr)(Co,Fe)O3 Thin-Films. *J. Power Sources* **2022**, *523* (December 2021), 230983.

(59) Yo H., C.; Ryu S., K.; Lee S., E.; Kim H., K. Nonstoichiometry of the Terbium Oxide. *Bull. Korean Chem. Soc.* **1994**, *15* (1), 33–36.

(60) Lee, J. H.; Murugavel, P.; Ryu, H.; Lee, D.; Jo, J. Y.; Kim, J. W.; Kim, H. J.; Kim, K. H.; Jo, Y.; Jung, M. H.; Oh, Y. H.; Kim, Y. W.; Yoon, J. G.; Chung, J. S.; Noh, T. W. Epitaxial Stabilization of a New Multiferroic Hexagonal Phase of TbMnO 3 Thin Films. *Adv. Mater.* **2006**, *18* (23), 3125–3129.

(61) Bos, J.-W. G.; van Aken, B. B.; Palstra, T. T. M. Site Disorder Induced Hexagonal-Orthorhombic Transition in $Y^{3+}_{1-x}\,Gd^{3+}_{x}MnO_3$. *Chem. Mater.* **2001**, *13* (12), 4804–4807.

(62) Bergerud, A.; Selbach, S. M.; Milliron, D. J. Oxygen Incorporation and Release in Metastable Bixbyite V2O3 Nanocrystals. *ACS Nano* **2016**, *10* (6), 6147–6155.

(63) ISE. *Current prices of rare earths*. https://en.institut-seltene-erden.de/aktuelle-preise-von-seltenen-erden/ (accessed 2023-03-23).

(64) Shanghai Metals Market. *Daily Rare Earth Oxides Prices*. https://www.metal.com/Rare-Earth-Oxides (accessed 2023-03-23).

Supporting Information for:

High entropy hexagonal manganites for fast oxygen absorption and release

Frida Hemstad Danmo,[1] Aamund Westermoen, [1] Kenneth Marshall,[2] Dragos Stoian,[2] Tor Grande,[1] Julia Glaum,[1] and Sverre M. Selbach[1,]*

[1]Department of Materials Science and Engineering, NTNU Norwegian University of Science and Technology, NO-7491 Trondheim, Norway.

[2]The Swiss-Norwegian Beamlines (SNBL), European Synchrotron Radiation Facility, Grenoble 38043, France

[*]E-mail: selbach@ntnu.no

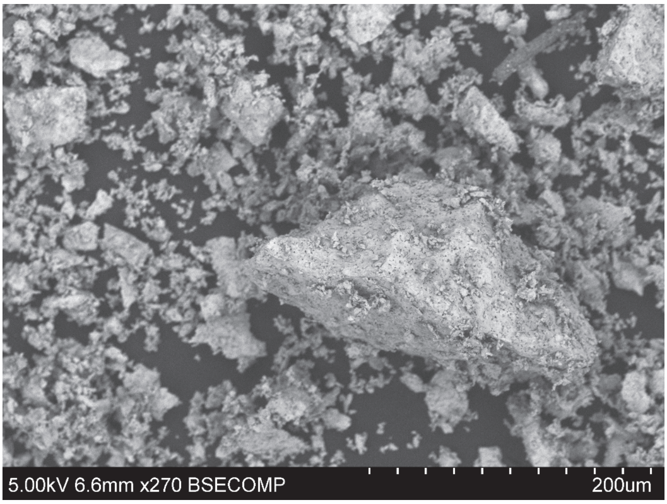

Figure 1: SEM image of the HEO2-b bulk powder.

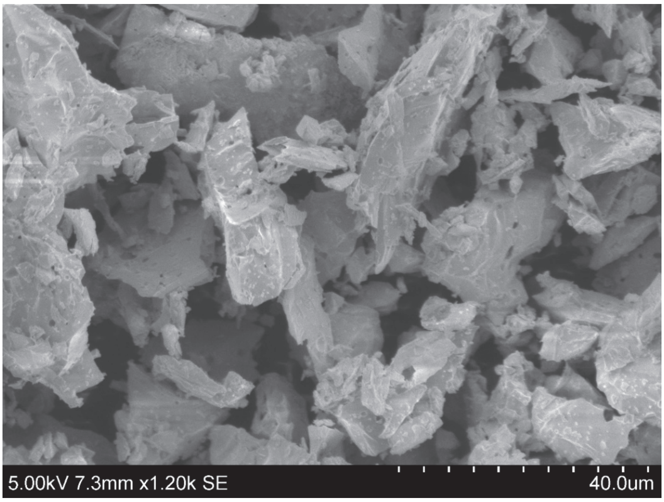

Figure 2: SEM image of the HEO5-b bulk powder.

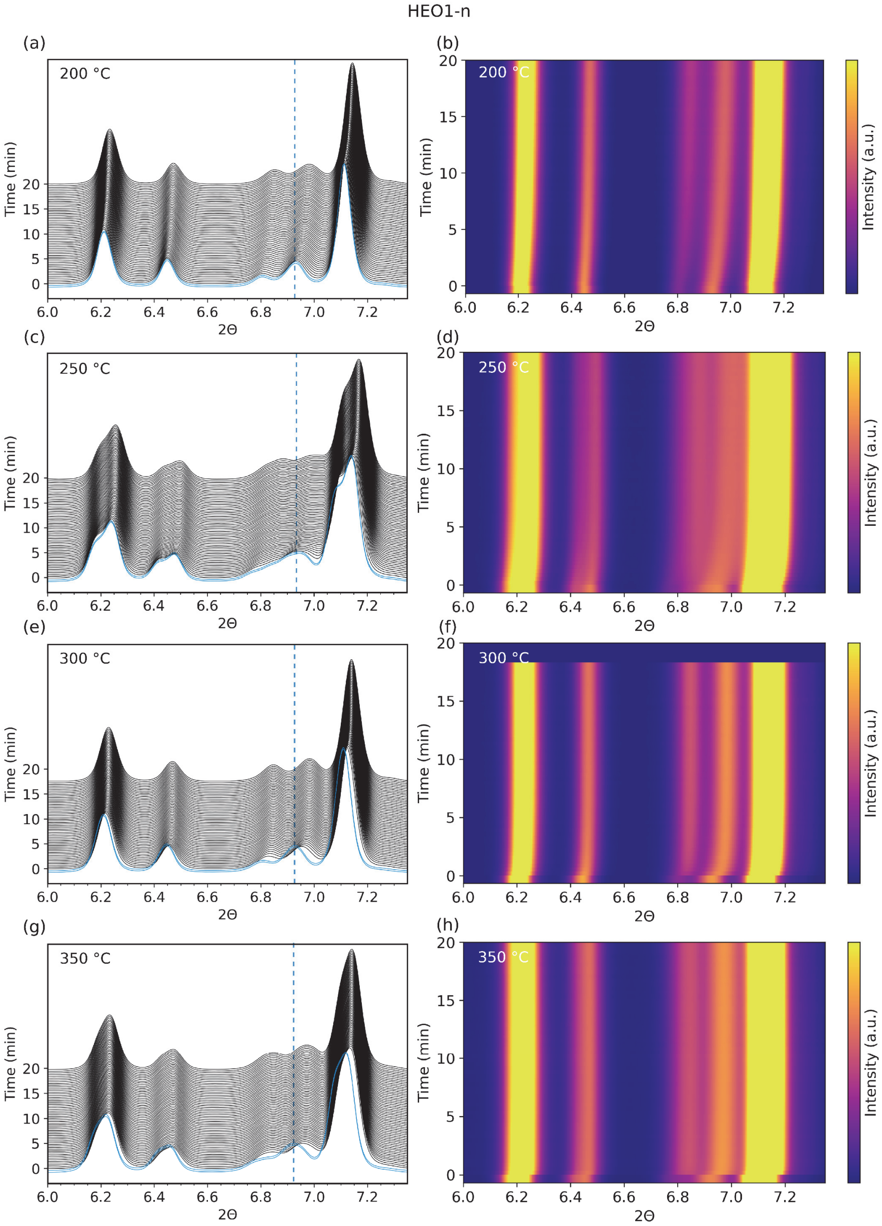

Figure 3: X-ray diffractograms and 2D contour plots of $Y_{0.167}Gd_{0.167}Tb_{0.167}Dy_{0.167}Ho_{0.167}Er_{0.167}MnO_3$ (HEO1-n) as a function of time after *in situ* switching of atmosphere from N_2 (blue) to O_2 (black).

The baseline intensity at 6.0° 2θ indicate the time in minutes after switching from N_2 to O_2 purge gas. Vertical dashed lines (blue) indicate the initial position of the (0012) reflection measured in N_2.

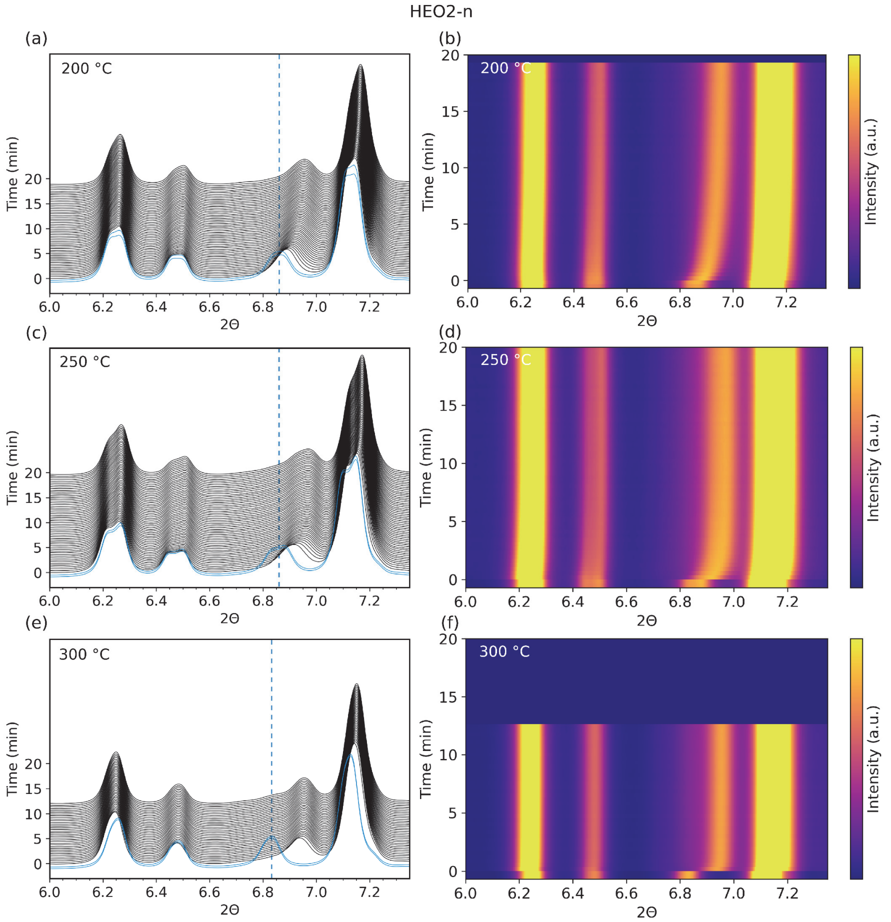

Figure 4: X-ray diffractograms and 2D contour plots of $Y_{0.167}Gd_{0.167}Tb_{0.167}Dy_{0.167}Ho_{0.167}Er_{0.167}Mn_{0.85}Ti_{0.15}O_3$ (HEO2-n) measured at 200 °C and 300 °C as a function of time after *in situ* switching of atmosphere from N_2 (blue) to O_2 (black). The baseline intensity at 6.0° 2θ indicate the time in minutes after switching from N_2 to O_2 purge gas. Vertical dashed lines (blue) indicate the initial position of the (004) reflection measured in N_2.

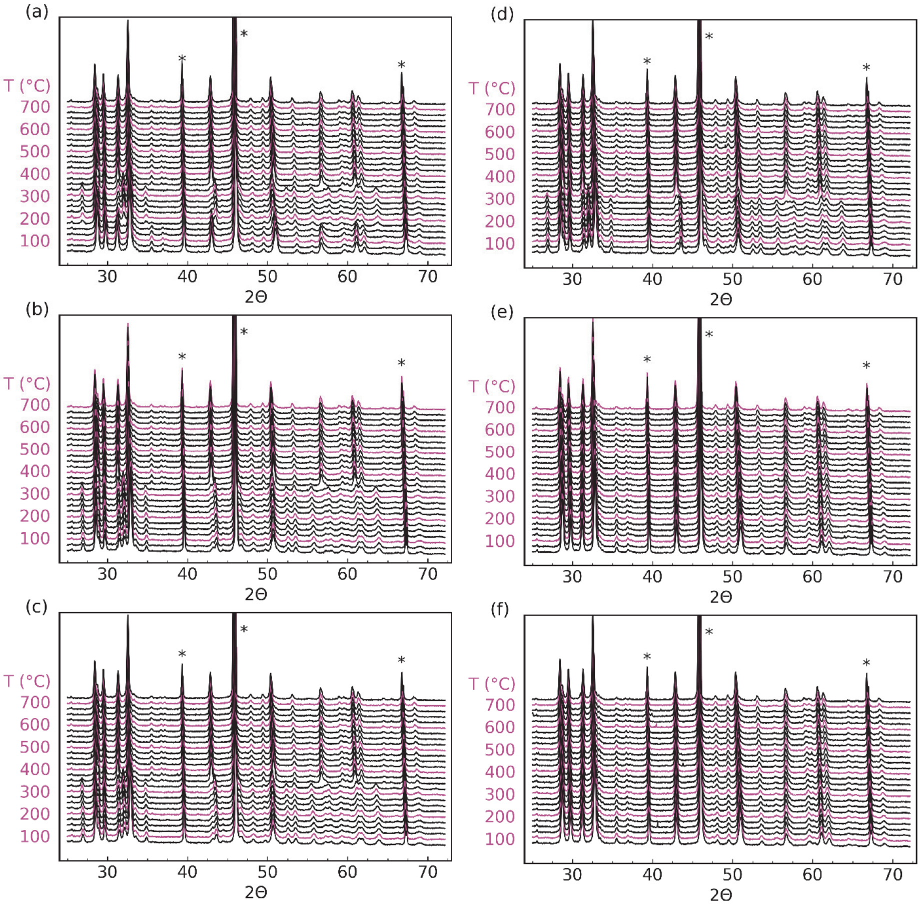

Figure 5: X-ray diffractograms for $Y_{0.167}Gd_{0.167}Tb_{0.167}Dy_{0.167}Ho_{0.167}Er_{0.167}MnO_3$ (HEO1-n) measured during (a) heating, (b) cooling, and (c) subsequent re-heating in O_2 atmosphere, and (d) heating, (e) cooling, and (f) subsequent re-heating in N_2 atmosphere. Asterisks (*) indicate reflections from the Pt-strip the sample was deposited on.

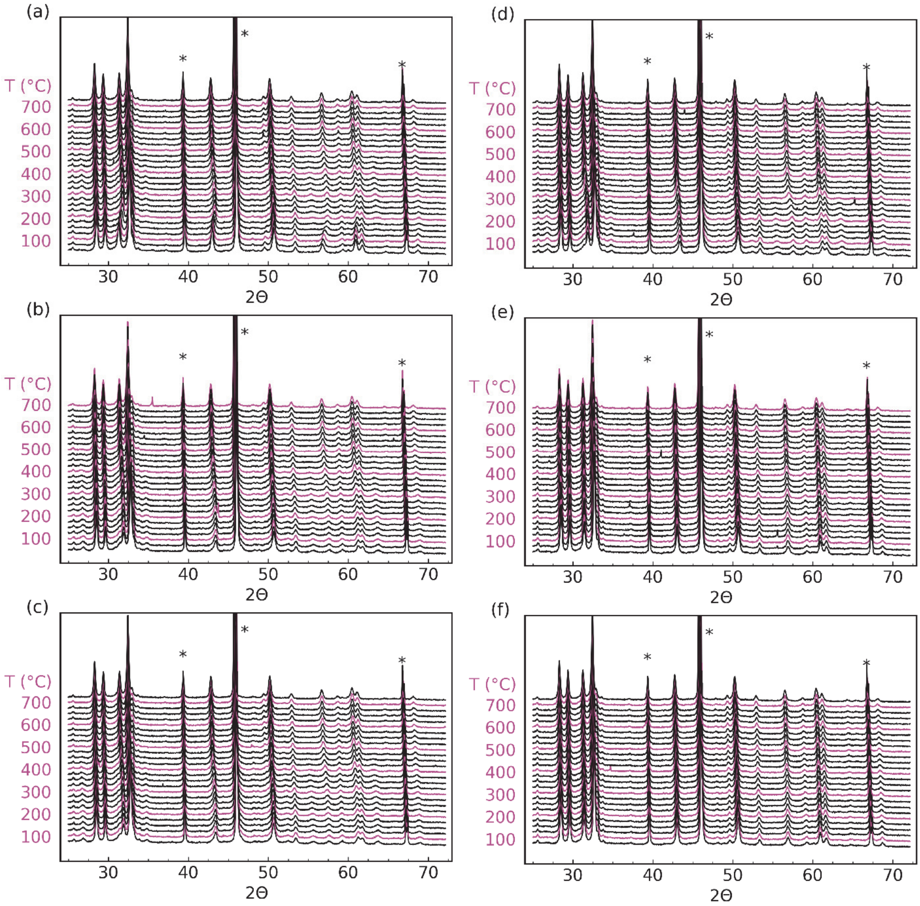

Figure 6: X-ray diffractograms for $Y_{0.167}Gd_{0.167}Tb_{0.167}Dy_{0.167}Ho_{0.167}Er_{0.167}Mn_{0.85}Ti_{0.15}O_3$ (HEO2-n) measured during (a) heating, (b) cooling, and (c) subsequent re-heating in O_2 atmosphere, and (d) heating, (e) cooling, and (f) subsequent re-heating in N_2 atmosphere. Asterisks (*) indicate reflections from the Pt-strip the sample was deposited on.

ISBN 978-82-326-7086-4 (printed ver.)
ISBN 978-82-326-7085-7 (electronic ver.)
ISSN 1503-8181 (printed ver.)
ISSN 2703-8084 (online ver.)

NTNU
Norwegian University of
Science and Technology